Fall 2013

Filter Synthesis and Design Techniques for Highly Adaptable Systems

Eric James Naglich
Purdue University

Recommended Citation

Naglich, Eric James, "Filter Synthesis and Design Techniques for Highly Adaptable Systems" (2013). *Open Access Dissertations*. 90.
https://docs.lib.purdue.edu/open_access_dissertations/90

Graduate School ETD Form 9
(Revised 12/07)

PURDUE UNIVERSITY
GRADUATE SCHOOL
Thesis/Dissertation Acceptance

This is to certify that the thesis/dissertation prepared

By Eric Naglich

Entitled
Filter Synthesis and Design Techniques for Highly Adaptable Systems

For the degree of Doctor of Philosophy

Is approved by the final examining committee:

WILLIAM J. CHAPPELL, Co-Chair
Chair

DIMITRIOS PEROULIS, Co-Chair

DAVID J. LOVE

JAMES V. KROGMEIER

To the best of my knowledge and as understood by the student in the *Research Integrity and Copyright Disclaimer (Graduate School Form 20)*, this thesis/dissertation adheres to the provisions of Purdue University's "Policy on Integrity in Research" and the use of copyrighted material.

Approved by Major Professor(s): WILLIAM J. CHAPPELL, Co-Chair

Approved by: V. Balakrishnan 11/27/2013
Head of the Graduate Program Date

FILTER SYNTHESIS AND DESIGN TECHNIQUES
FOR HIGHLY ADAPTABLE SYSTEMS

A Dissertation

Submitted to the Faculty

of

Purdue University

by

Eric J. Naglich

In Partial Fulfillment of the

Requirements for the Degree

of

Doctor of Philosophy

December 2013

Purdue University

West Lafayette, Indiana

ACKNOWLEDGMENTS

The work described in this dissertation would not have been possible without the support, efforts, and encouragement of several collaborators and family members. Specifically, I would like to thank my co-advisors, Dr. William J. Chappell and Dr. Dimitrios Peroulis, for guidance, encouragement, inspiration, and many thought-provoking discussions. I would like to acknowledge the current and former graduate students and post-doctoral researchers who have integrally contributed to the accomplishments of the past four and a half years: Dr. Hjalti Sigmarsson, Dr. Juseop Lee, Dr. Himanshu Joshi, Dr. Sungwook Moon, Dr. Xiaoguang Liu, Dr. Kenle Chen, Yu-Chen Wu, Trevor Snow, Yu-Ting Huang, Tsung-Chieh Lee, Mark Hickle, Mihal Sinani, and Wasim Irshad. Several funding sources have allowed the work to progress efficiently and under very professional guidance, including the Defense Advanced Research Projects Agency (DARPA), Office of Naval Research (ONR), and BAE Systems. Finally, I would like to thank my parents, Jim and Cindy Naglich, my sister, Kristie Naglich, and my entire family for their encouragement, assistance, and support in this endeavor.

TABLE OF CONTENTS

LIST OF TABLES

LIST OF FIGURES

ABSTRACT

Naglich, Eric J. Ph.D., Purdue University, December 2013. Filter Synthesis and Design Techniques for Highly Adaptable Systems. Major Professors: William J. Chappell and Dimitrios Peroulis.

Software defined radio and cognitive radio (SDR/CR) are promising concepts toward more optimally using the electromagnetic spectrum for communications and data transfer. These systems are highly agile in terms of modulation technique and frequency of operation due to early digitization and software processing of received radio frequency signals. However, the front ends of SDR/CR systems often use static antennas and switched banks of static, wide bandwidth filters before the digitization process. These components limit the ability of SDR/CR systems to operate in environments with high levels of interference and are therefore a bottleneck in the path to achieving optimal adaptation of wireless systems. This dissertation focuses on tunable and reconfigurable filter synthesis and design techniques that have the potential to alleviate the hardware adaptation bottleneck currently experienced by SDR/CR systems. The presented filter techniques and structures promise the capability to dynamically adapt the center frequency, order, response shape, bandwidth, group delay, passband insertion loss-stopband attenuation tradeoff, and transmission zero spectral location of a filter response in the field. Such reconfiguration capability is made possible through the use of new coupling relationships and structures that enable dynamic reconfiguration between electric, magnetic, and zero coupling values.

1. INTRODUCTION

Reconfigurable and high-performance high-frequency systems have received considerable attention over the last couple of decades due to exponentially-increasing wireless traffic [1], new semiconductor materials better suited to demanding system specifications such as Gallium Nitride (GaN) [2] and Indium Phosphide (InP) [3] that can change the required performance levels of front end filters, improvements in these materials processing yields and costs, ever-increasing success in applying silicon-based solutions to high-frequency problems [4], increased jamming threats both from co-site and external interference [5], and new system architectures, among other reasons. These systems are often called cognitive radio and/or software-defined radio [6]. The goal of these systems is to most optimally use the electromagnetic spectrum as well as increase the frequency at which systems operate. The electromagnetic spectrum is a finite resource, especially for wireless signal transmission, due to various noise sources at low frequencies and atmospheric absorption at higher frequencies [7].

Despite the recent interest in these systems, filters remain a bottleneck in cognitive radio system design due to low quality factor tuning elements, slow tuning speeds, control algorithm complexity, size, and power consumption depending on the type of filter used. In addition, many current multi-band systems use switched banks of static filters [8], which lowers the sensitivity and/or available power output of systems due to the loss of the switching elements. Systems that do currently employ tunable filters typically use Yttrium-Iron-Garnet (YIG) [9], switched capacitor [10], or solid-state varactor-tuned filters [11]. However, most of these filters typically only tune the center frequency of the filter and have high power consumption or insertion loss.

In order to more fully utilize the electromagnetic spectrum and the concept of cognitive radio, filter designs must progress beyond static and center-frequency tunable responses to a more generalized concept where the filter response characteristics can be specified in the field to respond to the current spectral environment. Such a generalized filter could be viewed as a bank of resonators that could be re-tasked to provide optimal front end performance for both the current spectrum and system function being executed for the number and quality of the resonators in the resonator bank. For example, a reconfigurable system may require a tunable, narrow-band bandpass filter in spectral environments with many interfering signals. However, implementing merely a narrow-band bandpass filter with only frequency tuning capability limits the reconfigurable system in several ways. First, a narrow-band bandpass filter will add insertion loss to the system that corresponds to the quality factor (Q) of the resonators used in the filter. In addition, if the reconfigurable system needed to change operating frequencies to a frequency out of the bandwidth of the narrow-band bandpass filer, the system would need to wait for the tunable bandpass filter to shift to the new desired frequency and optimize its shape. Depending on the amount of frequency hopping required, such a scheme could waste a lot of possible data throughput by often waiting for the tunable filter to catch up to the system. While the interference mitigation provided by such a tunable bandpass filter would outweigh the increased insertion loss and waiting times previously described in some spectral environments, in others it would unnecessarily limit system performance. Consider a spectral environment with low power interfering signals, or one with just a single interfering signal that would saturate a certain system. In such an environment, it would be better to have a tunable bandstop filter because its passband, which includes the operating frequency of the system, would have lower loss than the passband of a narrow-band bandpass filter. If the bandstop filter's passband was sufficiently wide, the system could reconfigure itself to operate at another frequency in the passband very quickly, without having to wait for tuning delays as in the tunable bandpass filter case. Later chapters of this dissertation will detail novel reconfigurable filter designs that can achieve in-field response shape tuning to benefit systems as in the example above.

As alluded to in the previous paragraph, bandstop filters with wide passbands can improve the performance of systems that used highly linear receivers and could only be saturated by few signals in the area. If the bandstop filter's passband is sufficiently wide, multiple tunable bandstop filters could be placed in cascade, providing anomalously wide notch frequency coverage. Such a front end configuration enables wide frequency range coverage systems to operate in spectral environments with interfering signals across their entire operating band. Narrow-band systems can also benefit from filter cascades. A bandpass filter in cascade with a bandstop filter or a cascade of bandstop filters can provide a narrow, low loss passband as well as a stop band with sub-bands with very high levels of isolation corresponding to the spectral location of the bandstop filter(s). If all of the filters in the cascade circuit are tunable, the passband and increased-isolation stopband regions can be positioned on-demand, subject to a few small limitations. Some of the work discussed in later chapters of this dissertation investigates some of the limitations associated with making tunable filter cascades for the first time. The remainder of this chapter will describe some alternative spectral isolation techniques currently in development, serve as an introduction to design and analysis methods that will often be used to describe filters in this dissertation, and provide an outline of this dissertation.

1.1 Alternative Spectral Isolation Techniques

While tunable and reconfigurable filters have been under development, other dynamic spectral isolation technologies have also been and continue to be investigated. Development of these technologies has been motivated by applications that require extreme amounts of isolation, such as the close physical proximity of airborne radars and satellite communication systems, as well as a desire to remove filters from RF front ends in applications that require minimum system size such as consumer electronics, where the cost of filtering off chip is also a major concern. Some of these technologies include antenna isolation baffles, mixer-first receiver designs, and self interference cancellation through beamforming.

Tunable antenna isolation baffles have been used to obtain up to 60 dB of narrowband isolation between co-located antennas and elements of an antenna array [12]. These devices are physically placed between antennas to shift the phase of coupling energy so that it destructively interferes at the receive antenna(s). The phase shift is made to be tunable through the use of varactors that load the baffles so that they are resonant near the frequency of interest. In [12], more than 40 dB isolation was achieved over 10 MHz bandwidths from 3.2 GHz to 3.4 GHz at a variety of scan angles. Such capability can be very useful to increase the transmit-receive isolation in microwave systems. However, due to its reliance on destructive interference, it is difficult to adjust the shape and bandwidth of the high isolation region of the spectrum that results from this technique. Therefore, such a concept could provide valuable supplemental isolation to a reconfigurable filter in diplexing applications, but it remains to be shown that it could replace filtering completely.

Mixer-first receiver designs that do not require RF filtering to operate in some environments are also under development [13], [14], [15], [16], [17]. These receivers use the impedance transformation property of passive mixers to implement high quality factor filtering by transforming low quality factor baseband impedances to RF. Such designs chop a cycle of the clock into multiple pieces with non-overlapping pulses and have distinct advantages over tunable and reconfigurable filters. For example, the center frequency of the passband response is directly controlled by a clock frequency, which is easier to control than most tunable resonators. In addition, the structures are implemented with switches and capacitors only, enabling them to be linear and designed in integrated circuit technology. Finally, since ideally no DC current passes through the switches, flicker noise is not a concern. However, receivers that implement mixer-first designs also have some limitations. First, many circuit parameters and performance metrics that are tied to them are in direct competition with each other. Some of these tradeoffs are similar to those of classical filters, such as bandwidth vs. insertion loss and selectivity vs. noise figure. However, some additional limitations exist. For example, an increase in selectivity can reduce the level of the stopband rejection or reduce the bandwidth over which the system's antenna can be instantaneously impedance matched because their parameters are linked [18]. In classical filters, stopband rejection is often limited by adjacent coupling paths and is less dependent on selectivity. In addition, there is a theoretical advantage to chopping a clock cycle into numerous short pulses. However, generating multiple non-overlapping pulses that are fractions of the clock frequency is difficult at high frequencies. With current technology, these systems show excellent performance below 1 GHz and degrade at higher frequencies. Nevertheless, mixer-first designs show great promise for filterless operation in some environments and as isolation supplements to reconfigurable filters.

Near field cancellation at receive antenna locations through beamforming has also been recently investigated as a method for increasing isolation between microwave systems. In these systems, antenna excitations are synthesized so that desired far field radiation patterns are maintained while near field patterns destructively interfere at the location of receive antennas. In [19], more than 50 dB isolation improvement was achieved over a 15 MHz bandwidth from 3.1 GHz to 3.6 GHz using beamforming techniques. However, these techniques are limited to narrow bandwidths and require multiple transmit antennas, which may not be possible to implement in some systems.

The techniques discussed above and others like them all add valuable isolation capability to microwave systems. However, their bandwidth limitations, linked parameters and specifications, difficulty/cost in implementation, and/or requirement for multiple antennas or circuit paths lead to capability levels that cannot replace conventional filtering in many applications. While these techniques are important options for supplementing filter technology, reconfigurable filters will remain an integral part of dynamic systems in high interference environments for the foreseeable future. The following sections will describe methods of filter synthesis that will be used in the description of the reconfigurable filters in this dissertation.

1.2 The Basic Coupling Matrix (M matrix)

In the early days of filter synthesis (1920's-1970), nearly all filter synthesis techniques involved the extraction of electrical elements (lumped capacitors and inductors, as well as transmission line lengths) from the polynomials that represented the filter's electrical performance mathematically [20]. This method was adequate for the technologies and synthesis demands of the era, but it involved element-by-element extraction of the circuit network and in many cases demanded starting over from the beginning when a characteristic of the network needed to be changed. As communication systems became more advanced and prolific, new filter synthesis techniques were developed in order to aid designers in meeting increasingly difficult specifications that included innovations like transmission zeros at designed frequencies and group delay equalization across the passband of bandpass filters. One of these advanced filter synthesis methods was developed in 1974 by Atia and Williams [21] to help design filters with difficult specifications associated with satellite communications. The coupling matrix provides a one-to-one correspondence between its elements and the physical resonators and coupling structures of the filter. This is a significant advancement beyond element-by-element extraction because it allows direct modeling of both the resonators (elements) of a filter and all of their couplings, enabling faster synthesis of advanced filtering functions. Cameron later developed general techniques to synthesize and generate the coupling matrix in an efficient fashion. This was performed in the low-pass domain, where different topologies may be conveniently obtained using similarity transformations [22], [23].

While the original coupling matrix assumes lossless, dispersion-free, synchronously-tuned resonators and frequency-independent coupling elements, these practical considerations can be added to different elements of the coupling matrix. Of particular interest to this dissertation is the ability to analyze and synthesize filters with asynchronously-tuned resonators, or resonators that are individually tuned to different frequencies. Doing so is becoming more practical with the recent increased attention given to tunable filters and resonators. Furthermore, if a system is using such tunable filters to change the center frequency of operation on demand, implementing synthesis concepts that require asynchronously tuned resonators to more optimally adapt to an interference scenario would require no additional hardware or cost. However, using dynamic, asynchronously-tuned resonators in filter synthesis is still an underdeveloped field with much room for contribution.

The coupling matrix is a representation of the relative strengths of coupling between the resonators or elements of a filter that can be derived from the voltage and current relationships between the elements of a generic equivalent circuit representation of the filter network. Such a generic equivalent circuit representation can be seen in Fig. 1.1. The circuit is driven by an open-circuit voltage source v_S with a source resistance of R_S and terminated by a load resistance R_L. Individual resonators are composed of 1 Henry (H) inductors and 1 Farad (F) capacitors, producing a normal-

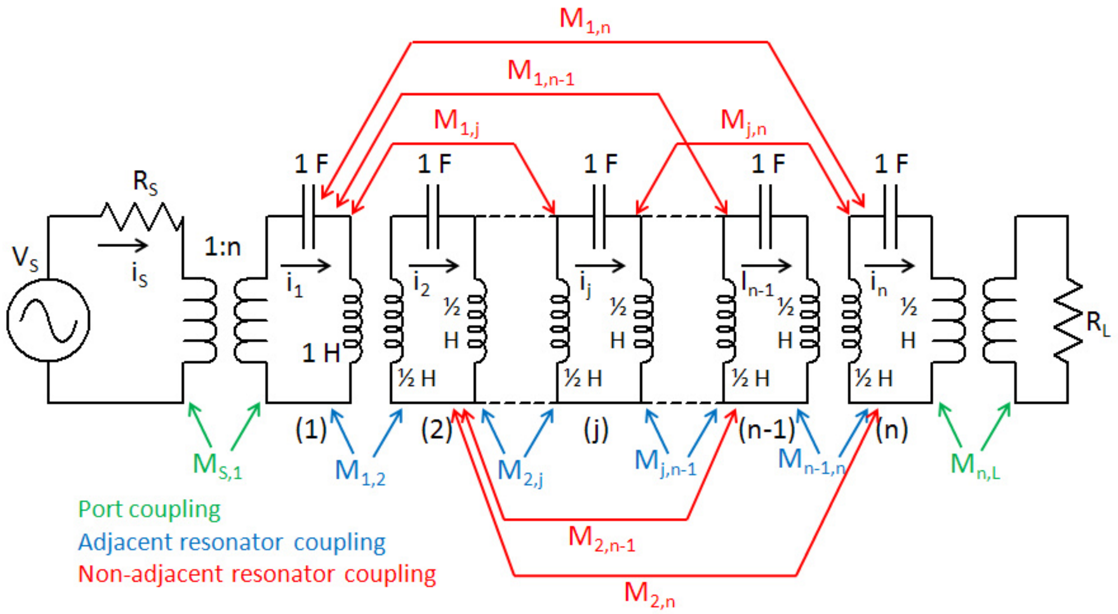

Fig. 1.1. Equivalent circuit model of series- and cross-coupled resonators and marked coupling (M) values.

ized resonant frequency of 1 radian/second (rad/s). The current in each resonator is labeled as i_n, where n denotes the resonator number. The resonators are coupled to each other, and each coupling is denoted as $M_{m,n}$, where m and n denote resonator numbers. These couplings are set such that the bandwidth of the filter is set to a normalized bandwidth from -1 rad/s to 1 rad/s and are assumed to be frequency-independent.

The voltage-current relationship in and between the ports and resonators of the network shown in Fig. 1.1 can be expressed in matrix form as shown in (1.1),

$$\begin{bmatrix} v_S \\ 0 \\ \vdots \\ 0 \\ 0 \end{bmatrix} = \begin{bmatrix} R_S + j(\omega - \frac{1}{w}) & jM_{0,1} & \cdots & jM_{1,n-1} & jM_{1,n} \\ jM_{0,1} & j(\omega - \frac{1}{w}) & \cdots & jM_{2,n-1} & jM_{2,n} \\ \vdots & \vdots & \ddots & \vdots & \vdots \\ jM_{n-1,1} & jM_{n-1,2} & \cdots & j(\omega - \frac{1}{w}) & jM_{n,n+1} \\ jM_{n,1} & jM_{n,2} & \cdots & jM_{n+1,n} & R_L + j(\omega - \frac{1}{w}) \end{bmatrix} \begin{bmatrix} i_1 \\ i_2 \\ \vdots \\ i_{n-1} \\ i_n \end{bmatrix}, \tag{1.1}$$

where $j(\omega - \frac{1}{w})$ is the bandpass transformation with center frequency and bandwidth normalized to 1 [24]. The voltage-current relationship in (1.1) can be written in simplified form as

$$\mathbf{v} = \mathbf{Zi} = (j(\omega - \frac{1}{w})\mathbf{U} + \mathbf{R} + j\mathbf{M})\mathbf{i}, \tag{1.2}$$

where $\mathbf{v}$ is the matrix on the left hand side of (1.1), $\mathbf{U}$ is the identity matrix except that $U_{S,S}$ and $U_{L,L}$ are equal to zero, and $\mathbf{i}$, $\mathbf{R}$, and $\mathbf{M}$ are

$$\mathbf{i} = \begin{bmatrix} i_1 \\ i_2 \\ \vdots \\ i_{n-1} \\ i_n \end{bmatrix} \tag{1.3}$$

$$\mathbf{R} = \begin{bmatrix} R_s & 0 & \cdots & 0 & 0 \\ 0 & 0 & \cdots & 0 & 0 \\ \vdots & \vdots & \ddots & \vdots & \vdots \\ 0 & 0 & \cdots & 0 & 0 \\ 0 & 0 & \cdots & 0 & R_L \end{bmatrix} \tag{1.4}$$

$$\mathbf{M} = \begin{bmatrix} 0 & M_{1,2} & \cdots & M_{1,n-1} & M_{1,n} \\ M_{2,1} & 0 & \cdots & M_{2,n-1} & M_{2,n} \\ \vdots & \vdots & \ddots & \vdots & \vdots \\ M_{n-1,1} & M_{n-1,2} & \cdots & 0 & M_{n-1,n} \\ M_{n,1} & M_{n,2} & \cdots & M_{n,n-1} & 0 \end{bmatrix}, \tag{1.5}$$

respectively. The **M** matrix in (1.5) is called the coupling matrix, and it can be used to completely specify the narrow-band behavior of a filter network assuming it is composed of synchronously-tuned similar resonators. Here, similar resonators are resonators with the same quality factor, coupling structures, and characteristic impedance. The coupling matrix is a mathematical representation of the coupling values between each of the similar resonators.

1.2.1 Coupling-Routing Diagrams

To aid in visualization of the mathematical coupling matrix representation of a given filter, it is common to draw coupling-routing diagrams. Coupling-routing diagrams are a visual representation of which nodes of the circuit are coupled to which other nodes of the circuit and the relative sign of the coupling values. Here, nodes of a filter network are the ports, resonators, and non-resonant nodes of the circuit. Relative signs of coupling values and non-resonant nodes will be described further in subsections below. An example of a coupling-routing diagram for a common 2-pole series-coupled bandpass filter topology can be seen in Fig. 1.2. Such a filter topology can produce a variety of filter responses depending on the coupling values, including Butterworth and Chebychev filter responses. Note that in Fig. 1.2, as will

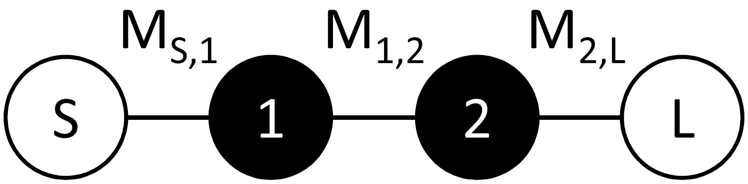

Fig. 1.2. Coupling-routing diagram for a common 2-pole series-coupled bandpass filter topology.

be the case in the remainder of this dissertation, the ports of the filter are represented by white circles. Here, S represents the source port, and L represents the load port. It is common to replace S and L with 0 and $n+1$, where n is the number of resonators in the filter network. Resonators in Fig. 1.2 are represented by black circles and are numbered sequentially. Coupling between ports and resonators is represented by solid black lines as all coupling values in this topology are positive. Negative coupling will be described in a subsection below. Note that the basic operation of the circuit can be intuitively understood from the coupling-routing diagram. For example, in Fig. 1.2, signal starts at the source (S) port. It progresses to resonator 1, which is a series-coupled resonator. A series-coupled resonator is a short circuit at resonance and an open circuit off resonance. Therefore, a signal at the resonant frequency of the resonators progresses through the circuit, while signals at frequencies away from the resonant frequency of the resonators are reflected back to the source port of the network. This creates a bandpass response, and the specific characteristics of the bandpass response are determined by the coupling (M) values.

Similar to Fig. 1.2, Fig. 1.3 shows the coupling-routing diagram for a common 2-pole shunt-coupled bandstop filter topology. Note that while the labeling and nomenclature is the same in both Fig. 1.2 and Fig. 1.3, Fig. 1.3 represents a different frequency response. There is no direct path between the resonators anymore, and a direct path between the source and load ports of the network was added. Therefore, an input signal at the resonant frequency of the resonators is reflected back to the source due to the short or open circuit input impedance of the resonators in the shunt

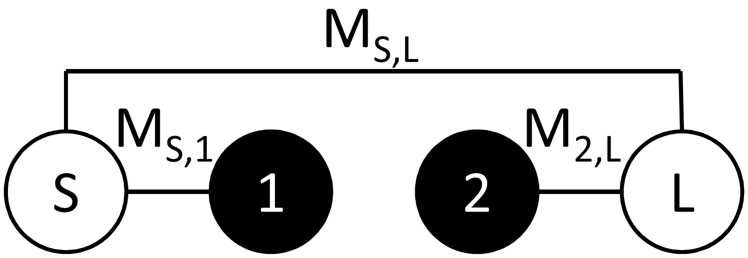

Fig. 1.3. Coupling-routing diagram for a common 2-pole shunt-coupled bandstop filter topology.

configuration and an input signal at a frequency away from the resonant frequency of the resonators passes directly from the source port to the load port, ideally unchanged other than a phase shift. Most if not all of more complicated resonator-based filters can be represented with coupling-routing diagrams by adding more resonators to the networks shown in Fig. 1.2 and Fig. 1.3 and other slight modifications. Therefore, the coupling matrix and coupling-routing diagram provide a mathematically rigorous and intuitive understanding of a narrow-band filter, respectively. Because of their complimentary nature, one is almost always shown with the other.

1.3 Additions to the Coupling Matrix for Synthesis of Advanced and Practical Filter Responses

While there are expansive tomes and dozens of scholarly articles on useful modifications to the coupling matrix [25], [26], here we will focus on four specific additions that are pertinent to the work described in the later chapters of this dissertation. These four additions are positive and negative coupling values, finite resonator quality factors, resonator frequency tuning, and non-resonating nodes, which are some of the most important modifications for having response design choices in the field. As will be shown, these additions enable advanced filtering functions with transmission zeros, accurate estimation of the amount of loss and band-edge sharpness that will be seen in a physically realized filter, using the off-resonance reactance of a resonator in the filter synthesis process, and accurate representation of resonators that are coupled through multiple coupling structures or over long electrical phase lenghts.

1.3.1 Positive and Negative Coupling Values

Positive and negative coupling values refer to the relative insertion phase difference between various coupling values. Because of the narrow-band, dispersion-free approximation that is made when using the **M** matrix method of filter synthesis, all coupling values are assumed to have either -90 electrical degrees or +90 electrical degrees insertion phase. Except in the case of acoustic or other types of non-electrical resonators, all coupling is achieved through magnetic (inductive) or electric (capacitive) fields. One field type is arbitrarily assigned to positive coupling, and the other is arbitrarily assigned to negative coupling. If only one of either electric or magnetic field coupling is used in a filter design, that type of coupling is often assigned to be positive coupling by convention. For example, a Butterworth response filter, represented by a single coupling matrix, can be implemented in two ways: with all electric field coupling or all magnetic field coupling. While the coupling matrix and coupling-routing diagram are the same for both cases, the out-of-band and tuning characteristics of both filters are different. This is a limitation of the basic coupling matrix method; it does not characterize behavior away from the center frequency of the filter very accurately. When both types of coupling are present in a filter design, as shown in the elliptic filter coupling matrix and frequency response shown below in Fig. 1.4 and (1.6) [27], it is the designer's choice whether to assign positive coupling to either electric or magnetic field coupling. The transmission zeros seen in the response in Fig. 1.4 are a result of having paths between the source and load ports of the filter utilizing both positive and negative coupling. When these two paths converge at the load port, destructive interference results at the frequency or frequencies where these paths are 180 degrees out of phase, creating the transmission zero(s).

Often, if all electric field coupling values are changed to magnetic field coupling values and all magnetic field coupling values are changed to electric field coupling values, the filter will have the same narrow-band response around its center frequency but different characteristics out of band. In a mixed-coupling topology with both electric and magnetic field coupling, it is common to assign positive coupling values to magnetic field coupling. This convention will be adopted for the remainder of this dissertation.

$$\mathbf{M} = \begin{bmatrix} 0 & 1.027 & 0 & 0 & 0 & 0 \\ 1.027 & 0 & 0.763 & 0 & -0.143 & 0 \\ 0 & 0.763 & 0 & 0.617 & 0 & 0 \\ 0 & 0 & 0.617 & 0 & 0.763 & 0 \\ 0 & -0.143 & 0 & 0.763 & 0 & 1.027 \\ 0 & 0 & 0 & 0 & 1.027 & 0 \end{bmatrix} \tag{1.6}$$

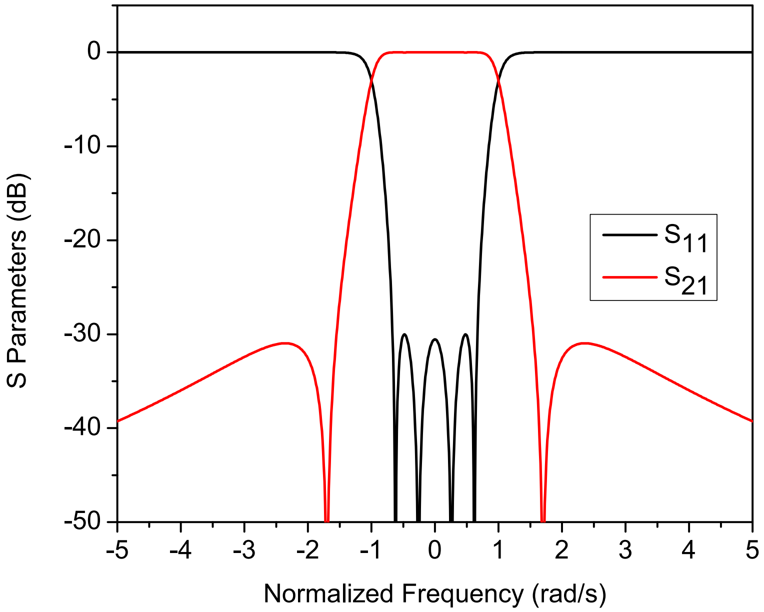

Fig. 1.4. Frequency response of a 4-pole elliptic bandpass filter with transmission zeros at ±1.7 rad/s and 30 dB equi-ripple return loss.

1.3.2 Finite Resonator Quality Factors

The basic **M** matrix filter synthesis method assumes lossless resonators. In any real filter implementation, the resonators will have loss that will affect the insertion loss of the filter and the sharpness of its band edges. Additionally, in some filter architectures such as absorptive bandstop filters [28], the quality factor (Q) is a design parameter that must be considered. In order to model these effects and filter topologies accurately, Q must be added to the **M** matrix. It is important to note that Q-related effects also frequently have a connection to the bandwidth of a filter. For example, a 2% fractional bandwidth n-pole filter with a given resonator Q will have significantly more insertion loss than a 10% fractional bandwidth n-pole filter with the same resonator Q. However, the **M** matrix filter synthesis method is normalized such that the filter response has a center frequency of zero rad/s and a bandwidth from -1 rad/s to 1 rad/s. The filter response is scaled in center frequency and bandwidth after the synthesis procedure is complete. In order to account for the Q-bandwidth relationship during the synthesis procedure, terms are added to the **M** matrix that depend on both Q and the fractional bandwidth of a filter. For a 4-pole series-coupled resonator bandpass filter topology with finite quality factor, the **M** matrix can be written as:

$$\mathbf{M} = \begin{bmatrix} 0 & M_{01} & 0 & 0 & 0 & 0 \\ M_{01} & \frac{-j}{Q\Delta} & M_{12} & 0 & 0 & 0 \\ 0 & M_{12} & \frac{-j}{Q\Delta} & M_{23} & 0 & 0 \\ 0 & 0 & M_{23} & \frac{-j}{Q\Delta} & M_{34} & 0 \\ 0 & 0 & 0 & M_{34} & \frac{-j}{Q\Delta} & M_{01} \\ 0 & 0 & 0 & 0 & M_{01} & 0 \end{bmatrix}, \tag{1.7}$$

where $\frac{-j}{Q\Delta}$ takes the Q and fractional bandwidth (Δ) into account. Finite Q responses can be synthesized using this term.

1.3.3 Resonator Frequency Tuning

Of particular interest to the work shown later in this dissertation is the ability to synthesize filter responses that composed of resonators that are tuned asynchronously, or tuned to different frequencies. Similar to how finite quality factor was added to the **M** matrix in (1.7), asynchronous tuning can be added to the **M** matrix synthesis procedure using the self-coupling terms (M_{nn}). A 4-pole series-coupled resonator bandpass filter topology with asynchronous resonator tuning has an **M** matrix of the form:

$$\mathbf{M} = \begin{bmatrix} 0 & M_{01} & 0 & 0 & 0 & 0 \\ M_{01} & M_{11} & M_{12} & 0 & 0 & 0 \\ 0 & M_{12} & M_{22} & M_{23} & 0 & 0 \\ 0 & 0 & M_{23} & M_{33} & M_{34} & 0 \\ 0 & 0 & 0 & M_{34} & M_{44} & M_{01} \\ 0 & 0 & 0 & 0 & M_{01} & 0 \end{bmatrix}. \tag{1.8}$$

It is important to note that the self-coupling terms (M_{nn}) in (1.8) are real numbers, where in (1.7) the self-coupling terms are imaginary. A real self-coupling term denotes frequency tuning of a specific resonator away from the center frequency of the filter response, while an imaginary self-coupling term denotes loss in a particular resonator. Note that the **M** matrix is multiplied by a factor of j in (1.2), reversing the real and imaginary roles of the self-coupling terms in the final voltage-current relationship in line with standard frequency domain analysis. Finally, the self-coupling terms can have both a real and imaginary part to model both finite Q and asynchronous tuning at the same time.

1.3.4 Non-Resonating Nodes

Because the **M** matrix filter synthesis method is a narrow-band approximation, all coupling values have a phase shift of exactly ±90 degrees. However, in some filter networks, there are coupling sections or transmission lines that have a phase shift that is an integer multiple of ±90 degrees as well as coupling sections or transmission lines that have a phase shift that is not an integer multiple of ±90 degrees. Non-resonating nodes are used to model coupling sections or transmission lines that have a phase shift that is an integer multiple of ±90 degrees. Coupling sections and transmission lines that have a phase shift that is not an integer multiple of ±90 degrees cannot be modeled by the **M** matrix synthesis method alone. Separate and hybrid analysis methods have been developed to deal with this situation [29]. One separate and one hybrid method will be shown later in this dissertation.

In this dissertation, non-resonating nodes will be used primarily in similar-resonator bandstop filters. To understand why they are needed, consider the 4-pole lumped element bandstop filter shown in Fig. 1.5 a). The filter shown in Fig. 1.5 a) is a completely lumped topology, but it has two resonator types. Often, it is most practical for all of the resonators in a filter to be the same. Therefore, it is common to transform the circuit to one with similar resonators using an impedance inverter, which

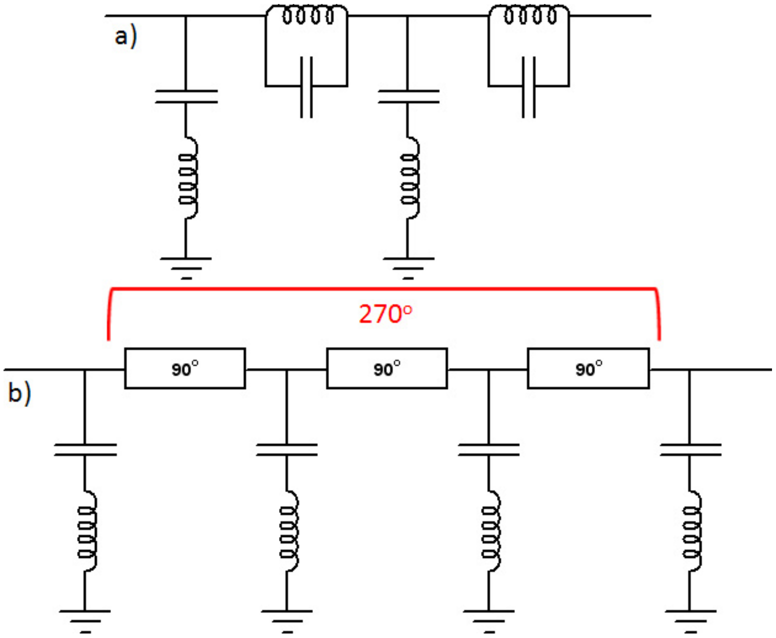

Fig. 1.5. Lumped element bandstop filters. a) Completely lumped with dissimilar resonators. b) Lumped element, similar resonators separated by 90 degree transmission lines.

can be implemented using a 90 degree transmission line. The resultant topology is shown in Fig. 1.5 b). Note that there are three connected 90 degree transmission lines that could be viewed as a single 270 degree transmission line. In the coupling-routing diagrams of Fig. 1.2 and Fig. 1.3, the only circuit elements that coupling values can span are ports and resonators. However, since coupling values in the **M** matrix method can only have an insertion phase of ±90 degrees, there is no way to represent three 90 degree transmission lines in series or a 270 degree transmission line. While a -90 degree transmission line would have the correct insertion phase, the topology of the circuit would not be upheld as the four resonators in Fig. 1.5 b) are not connected to the same points in the circuit. Non-resonating nodes fill this need. The coupling-routing diagram for the filter topology in Fig. 1.5 b) can be seen in Fig. 1.6. The non-resonating nodes (NRNs) allow a node for the connection of a 90 degree coupling element. The corresponding coupling matrix would have eight rows and eight columns. However, the **U** matrix from (1.2) is no longer the identity matrix with $U_{S,S}$ and $U_{L,L}$ equal to zero when NRNs are used. Instead of producing a frequency-dependent term in each non-port row as before ($j(\omega - \frac{1}{w})$ in (1.2)), the values in the **U** matrix corresponding to the rows of the NRNs must be changed to zeros as in (1.9) where the NRNs are given element numbers (2,2) and (4,4). Note that the NRNs can be given any diagonal element number in the **U** matrix as long as coupling values in the associated **M** matrix correspond to the chosen diagonal el-

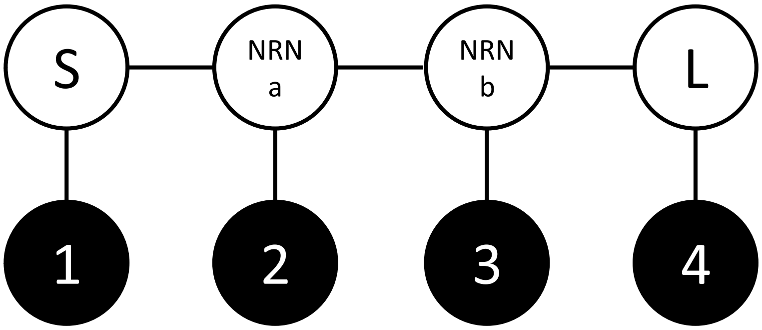

Fig. 1.6. Coupling-routing diagram for the filter topology shown in Fig. 1.5 b). NRN = non-resonating node.

ement numbers. The corresponding **M** matrix for (1.9) can be seen in (1.10), where the source is node 0, the load is node 7, and the NRNs are nodes a and b. The lack of resonance term in the chosen diagonal element numbers gives rise to the name ”‘non-resonating node.”’

$$\mathbf{U} = \begin{bmatrix} 0 & 0 & 0 & 0 & 0 & 0 & 0 & 0 \\ 0 & 1 & 0 & 0 & 0 & 0 & 0 & 0 \\ 0 & 0 & 0 & 0 & 0 & 0 & 0 & 0 \\ 0 & 0 & 0 & 1 & 0 & 0 & 0 & 0 \\ 0 & 0 & 0 & 0 & 0 & 0 & 0 & 0 \\ 0 & 0 & 0 & 0 & 0 & 1 & 0 & 0 \\ 0 & 0 & 0 & 0 & 0 & 0 & 1 & 0 \\ 0 & 0 & 0 & 0 & 0 & 0 & 0 & 0 \end{bmatrix} \tag{1.9}$$

$$\mathbf{M} = \begin{bmatrix} 0 & M_{01} & M_{0a} & 0 & 0 & 0 & 0 & 0 \\ M_{01} & M_{11} & 0 & 0 & 0 & 0 & 0 & 0 \\ M_{0a} & 0 & 0 & M_{a2} & M_{ab} & 0 & 0 & 0 \\ 0 & 0 & M_{a2} & M_{22} & 0 & 0 & 0 & 0 \\ 0 & 0 & M_{ab} & 0 & 0 & M_{b3} & 0 & M_{b7} \\ 0 & 0 & 0 & 0 & M_{b3} & M_{33} & 0 & 0 \\ 0 & 0 & 0 & 0 & 0 & 0 & M_{44} & M_{47} \\ 0 & 0 & 0 & 0 & M_{b7} & 0 & M_{47} & 0 \end{bmatrix} \tag{1.10}$$

1.4 Mixed Parameter Analysis

While the **M** matrix analysis method has many advantages and is applicable to a wide array of filter design problems, one of its limitations is analysis of filters that operate over wide frequency ranges relative to bandwidth and employ coupling structures that vary in electrical length as a function of frequency. In such cases, it is often simplest to use mixed parameter analysis, or the combination of ABCD, Y, and S parameters to yield transfer functions of a complex network. This technique allows for solving for a composite network transfer function from simpler element transfer functions and will be used in Chapter 9 of this dissertation to analyze a filter network capable of dynamically providing all pass or bandstop responses. A brief review and example follow.

Fig. 1.7 shows ABCD parameters for common circuit elements and configurations. From top to bottom, Fig. 1.7 shows ABCD parameters for a transmission line, a series impedance, a shunt admittance, an impedance inverter, and an admittance inverter. These element level ABCD parameters can represent most network components and can be matrix multiplied to determine composite ABCD parameters of a network composed of a series cascade of multiple instances of these basic elements [24]. ABCD parameters are not sufficient to analyze all networks though because they do not address parallel combinations of the elements shown in Fig. 1.7. Admittance or Y parameters are a convenient tool to use when this situation arises. Y parameters can be derived for an element or network by driving a port with a voltage, shorting

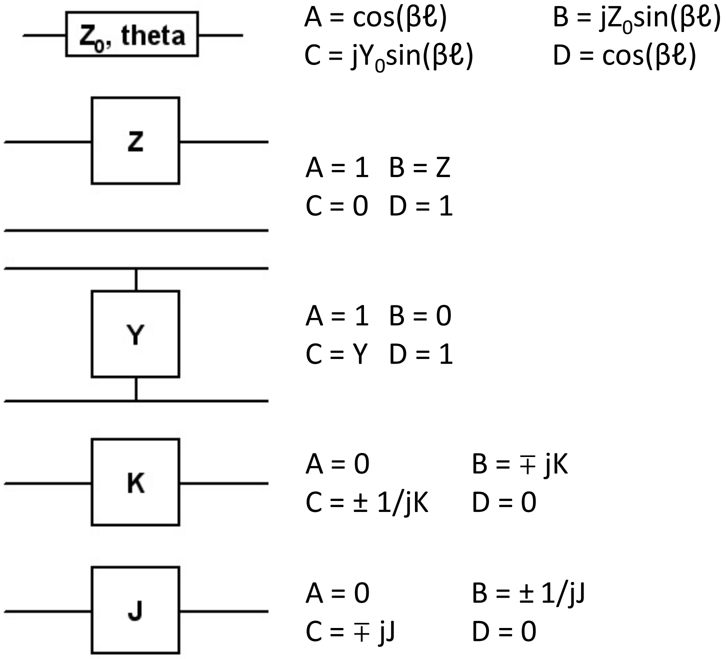

Fig. 1.7. ABCD parameters for common circuit elements and configurations.

all other ports, measuring the short circuit current at all ports that are not driven, and repeating the process after switching the driven port until all ports have been analyzed. (1.11) shows this concept mathematically.

$$Y_{ij} = \left.\frac{I_i}{V_j}\right|_{V_k=0 for k\neq j} \tag{1.11}$$

Alternatively, the Y parameters can be obtained from the ABCD parameters shown in Fig. 1.7 using the relationships shown in (1.12).

$$\begin{aligned} Y_{11} &= \frac{D}{B} \\ Y_{12} &= \frac{BC - AD}{B} \\ Y_{21} &= \frac{-1}{B} \\ Y_{22} &= \frac{A}{B} \end{aligned} \tag{1.12}$$

An advantage of Y parameter analysis is that the composite Y parameters of a set of parallel circuit elements is the matrix sum of the element Y parameter matrices. Once the composite Y parameters of a set of parallel circuit elements are found, they can be converted to ABCD parameters for further cascade analysis using the relationships shown in (1.13).

$$\begin{aligned} A &= \frac{-Y_{22}}{Y_{21}} \\ B &= \frac{-1}{Y_{21}} \\ C &= \frac{Y_{12}Y_{21} - Y_{11}Y_{22}}{Y_{21}} \\ D &= \frac{-Y_{11}}{Y_{21}} \end{aligned} \tag{1.13}$$

If the final network analysis step is a matrix multiply of ABCD submatrices, S parameters can be obtained from the relationships shown in (1.14).

$$\begin{aligned}
S_{11} &= \frac{A + B/Z_0 - CZ_0 - D}{A + B/Z_0 + CZ_0 + D} \\
S_{12} &= \frac{2(AD - BC)}{A + B/Z_0 + CZ_0 + D} \\
S_{21} &= \frac{2}{A + B/Z_0 + CZ_0 + D} \\
S_{22} &= \frac{-A + B/Z_0 - CZ_0 + D}{A + B/Z_0 + CZ_0 + D}
\end{aligned} \tag{1.14}$$

If the final network analysis step is a matrix addition of Y submatrices, S parameters can be obtained from the relationships shown in (1.15).

$$\begin{aligned}
S_{11} &= \frac{(Y_0 - Y_{11})(Y_0 + Y_{22}) + Y_{12}Y_{21}}{(Y_{11} + Y_0)(Y_{22} + Y_0) - Y_{12}Y_{21}} \\
S_{12} &= \frac{-2Y_{12}Y_0}{(Y_{11} + Y_0)(Y_{22} + Y_0) - Y_{12}Y_{21}} \\
S_{21} &= \frac{-2Y_{21}Y_0}{(Y_{11} + Y_0)(Y_{22} + Y_0) - Y_{12}Y_{21}} \\
S_{22} &= \frac{(Y_0 + Y_{11})(Y_0 - Y_{22}) + Y_{12}Y_{21}}{(Y_{11} + Y_0)(Y_{22} + Y_0) - Y_{12}Y_{21}}
\end{aligned} \tag{1.15}$$

As an example of mixed parameter analysis, consider the circuit shown in Fig. 1.8. This circuit is similar to a common 2-pole bandstop filter high pass prototype, but it has an additional admittance inverter that is for instructional purposes only. In order to find the S parameters of the circuit, a possible first step is finding the ABCD parameters of the six (three admittance inverters, two capacitors, and one transmission line) elements in the circuit, all of which can be found in Fig. 1.7. Next, both sets of shunt J_1 admittance inverters and capacitors C can be collapsed to a single shunt element by noting that the input admittance into admittance inverters is

$$Y_{in} = \frac{J^2}{Y_L}, \tag{1.16}$$

where Y_L is the load admittance beyond the admittance inverter. Therefore, both sets of shunt J_1 admittance inverters and capacitors C can be represented as the following single shunt element ABCD matrix

$$\begin{bmatrix} 1 & 0 \\ \frac{J^2}{sC} & 1 \end{bmatrix}, \tag{1.17}$$

where s is the frequency variable $j\omega$. Next, the parallel combination of the J_2 admittance inverter and the transmission line can be collapsed into a single series element by converting each element's ABCD parameters to Y parameters, adding the Y parameters, and converting back to ABCD parameters. Using this process, the ABCD parameters of the parallel combination of the J_2 admittance inverter and the transmission line are

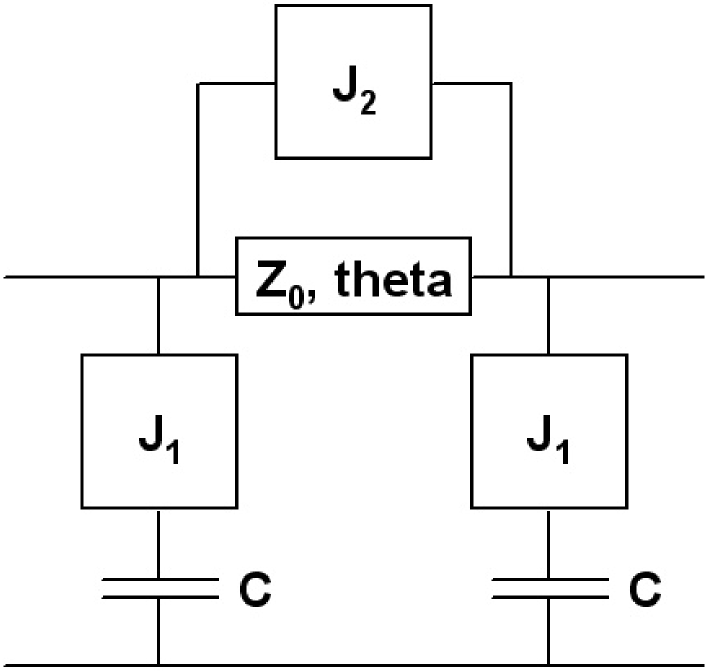

Fig. 1.8. Example circuit for mixed parameter analysis.

$$\begin{bmatrix} \frac{-cos(\theta)}{J_2 Z_0 sin(\theta)-1} & \frac{-jZ_0 sin(\theta)}{J_2 Z_0 sin(\theta)-1} \\ -jJ_2 - \frac{jsin(\theta)-jJ_2 Z_0}{Z_0(J_2 Z_0 sin(\theta)-1)} & \frac{-cos(\theta)}{J_2 Z_0 sin(\theta)-1} \end{bmatrix}. \tag{1.18}$$

Next, the ABCD parameters of the entire circuit in Fig. 1.8 can be found by matrix multiplying (1.17) by (1.18) and then by (1.17) again. Finally, the ABCD parameters of the entire circuit can be converted to S parameters using (1.14). If the values of the elements are set to $J1$=1, $J2$=0, $\theta=\pi/2$, Z_0=1, and C=1 so that the circuit in Fig. 1.8 represents a normalized high pass prototype, and the plotted S parameters are as shown in Fig. 1.9.

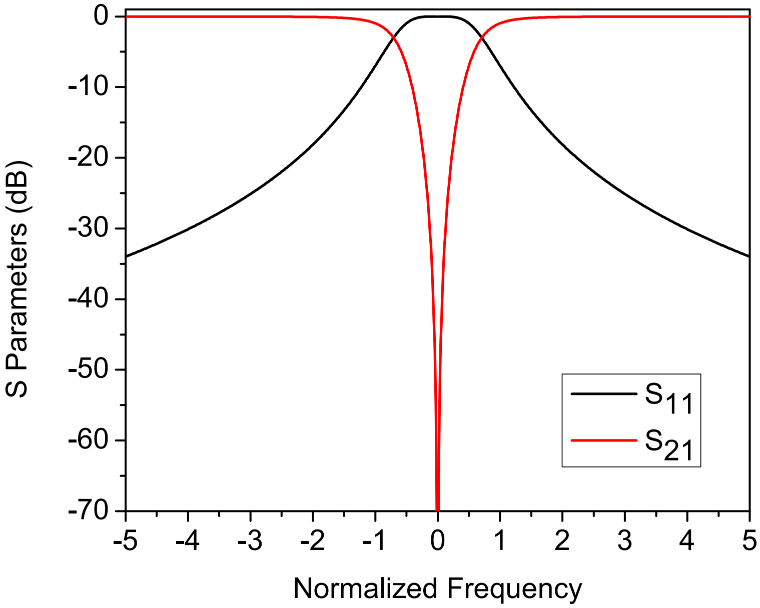

Fig. 1.9. S parameters of the circuit shown in Fig. 1.8 when the elements are set to give a normalized high pass response.

1.5 Organization of This Dissertation

This dissertation is organized as follows. First, high quality factor, tunable bandstop filters are presented in several frequency ranges. Next, cascades of such bandstop filters and enabling concepts for such cascades are discussed. These bandstop filter cascades extend the effective tunable range of individual tunable bandstop filters but are limited in this regard by the extent of their spurious-free upper passbands. Then, a tunable bandstop filter with an ultra-wide upper passband is presented as a method for alleviating the limitations of the previously presented bandstop filter cascades. Next, cascades of tunable bandpass filters and tunable bandstop filters are presented to leverage the adaptive rejection of bandstop filter cascades for narrow band systems. When in the skirt of a bandpass response, the bandstop filters add to the bandpass filter's rejection to produce over 100 dB isolation when the cascade is designed correctly. Filters that can convert their response shape on demand and in the field follows the bandpass-bandstop filter cascades. Bandpass-to-bandstop and all-pass-to-bandstop filters will be presented. Then, an inter-resonator coupling structure that enables inductive, capacitive, and zero coupling values is described. This structure is used in a resonator array with the capability of providing bandpass filter responses of different shapes, of different orders, and with and without transmission zeros. Next, analysis and design of a dual-band highly loaded coaxial cavity filter structure will be presented as well as a design method that enables cancellation of the first spurious mode of the structure. Finally, concepts for future work will be explained and conclusions will be drawn.

2. TUNABLE BANDSTOP FILTERS WITH RECONFIGURABLE NOTCH RESPONSES

2.1 Introduction

When implemented with tunable resonators, the bandstop filter network shown in Fig. 1.5 b) and Fig. 1.6 can provide response shapes with many bandwidth and equi-ripple attenuation options without any other tunable components. In other words, tunable bandstop filters have the unique advantage compared with tunable bandpass filters in that multiple, useful response shapes are possible when only the resonators of a filter are tunable. This distinction is important because radio systems in crowded, dynamic spectral environments will increasingly rely on tunable spectral isolation, especially as the spectrum is opened for cognitive radio operation [30]. In many systems, multiple adaptive bandstop filters will be used to filter out several of the most problematic interfering signals. Ideally, these filters would be able to re-task each of their individual resonators to create different filtering shapes across the spectrum. In addition, multiple notch filters could be created when needed, or the responses could be combined in order to create maximum spectral isolation over a single band. Fig. 2.1 shows three states of this concept using the bandstop filter network shown in Fig. 1.5 b) and Fig. 1.6. As shown in Fig. 2.1, this system of resonators is able to provide four 1-pole bandstop responses, two 2-pole bandstop responses, or one 4-pole bandstop response. This dynamic pole allocation capability becomes more powerful as resonator Q and tuning range are increased.

Several tunable bandstop filters have been created in recent history. It has been shown that very wide frequency tuning ranges can be achieved [31]. Bandstop filters have been shown with extended, resonance free passband responses [32], and others have MEMS tuning mechanisms [33]. A recent paper has shown a tunable level

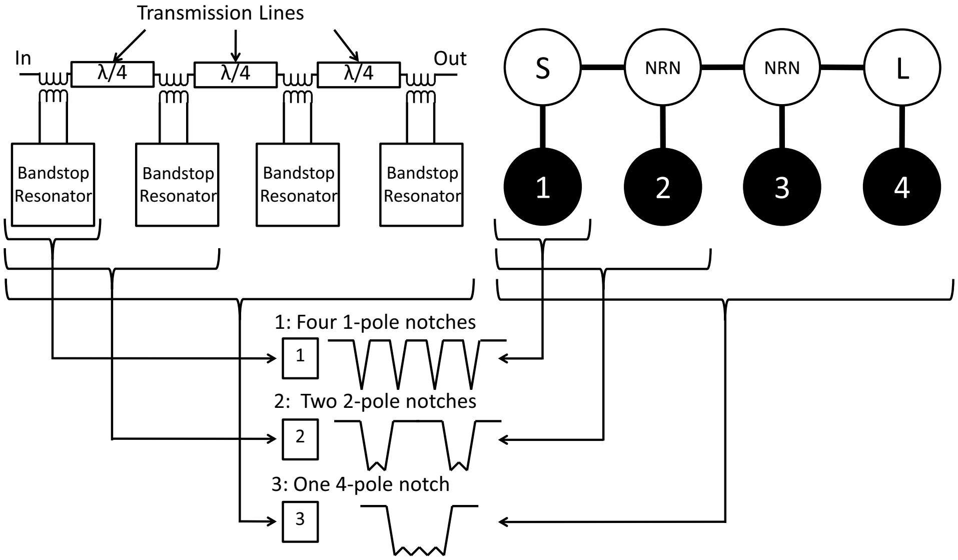

Fig. 2.1. Concept and coupling-routing diagram for a tunable four pole bandstop filter whose poles can tune independently to create four 1-pole notches, two 2-pole notches, or one 4-pole notch.

of attenuation [34]. However, none of the filters show dynamic pole allocation or have resonator Q higher than 150. In addition, some have limited bandwidths. A critical issue in creating wide bandwidth, high-Q filters is coupling into the resonators without excessively perturbing the feedline. Strong coupling into bandstop resonators can perturb the feedline and degrade the out-of-band response of the bandstop filter. In Fig. 2.1, the coupling mechanisms are depicted as transformers between sections of transmission lines which are ideally $\lambda/4$ in length. Traditionally, eliminating the perturbation to the feedline means reducing the external coupling which reduces the bandwidth and maximum attenuation of the filters. Preferably, one could find a mechanism to adjust the coupling by altering the dimensions of the resonator without impacting the transmission line. This concept will be a central focus of some of the work described in this dissertation.

In this chapter, a tunable 4-pole post-loaded cavity resonator bandstop filter is shown which can implement the capabilities shown in Fig. 2.1 and adjust its attenuation and bandwidth in response to the spectrum. This filter uses an in-cavity method for reducing the perturbation of the filter's passband response for a given amount of coupling, enabling large coupling values while retaining an unloaded Q that was measured as high as 450.

2.2 Resonator Structure For Reduced Out-Of-Band Perturbation Or Increased Coupling

Evanescent-mode cavity resonators have been extensively employed in widely frequency tunable filters [35]. Fig. 2.2 a) shows an example of a conventional substrate-integrated evanescent-mode cavity resonator with a straight loading post, but the technique discussed in this section could be applied to any type of post-loaded cavity. The side wall of the resonator is established by via-holes, and the resonant frequency of the resonator is controlled by the gap between the post and the conductor layer on the bottom side of the cavity. An actuator is usually attached to this conductor layer to adjust the resonant frequency. In tunable bandstop filter structures, a microstrip transmission line is usually attached to the top side of the resonator, and a coupling aperture in the conductor layer on the top side of the cavity provides coupling into the resonator. The geometry of this coupling aperture determines the amount of coupling with a given microstrip line. Only a small amount of coupling can be gained by increasing the size of the coupling aperture before it adds too much inductance to

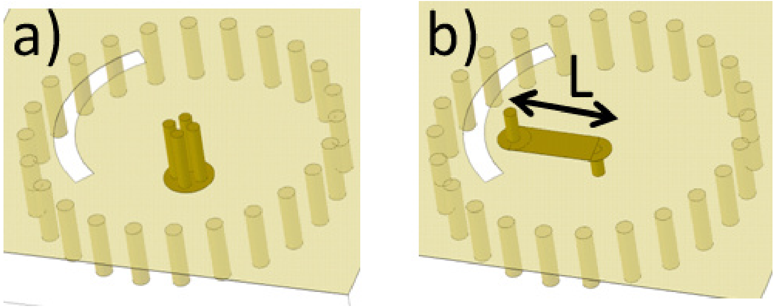

Fig. 2.2. a) Conventional resonator structure, b) proposed resonator structure.

the ground plane of the microstrip line, degrading the out-of-band return loss of the filter to unacceptable levels. The proposed structure in Fig. 2.2 b) is able to provide a given amount of coupling with a smaller coupling aperture than the conventional evanescent-mode cavity bandstop resonator. The loading post in the resonator is "bent" in order to redirect the current path inside the resonator closer to the sidewall of the cavity. The magnetic field is therefore asymmetric within the cavity and condensed in a region where a coupling aperture is placed. The external Q can be increased by simply increasing the length of the bent portion of the post (labeled 'L' in Fig. 2.2 b)), and therefore the coupling can be made larger for a given aperture size. This allows bandstop filters with less out-of-band response perturbation or bandstop filters with wider bandwidths than would be possible with the standard post configuration shown in Fig. 2.2 a). The other half of the bent post remains centered in the cavity in order to facilitate integration of electromechanical actuators for wide tuning ranges. The effect of the size of the coupling aperture on the filter transmission line can be understood with the model in Fig. 2.3 a). The coupling aperture adds inductance to the ground plane because it re-routes the current of the microstrip line mode. This increases the effective characteristic impedance of the line near the coupling aperture with a dependence on its size. The higher impedance cross section of the line near the coupling apertures can be modeled as an electrically short transmission line, which can be equivalently represented by a series inductance of impedance $Z\beta\ell$, where Z, β, and ℓ are the characteristic impedance, propagation constant, and physical length of the transmission line that represents the coupling aperture, respectively.

The full-wave simulated comparison of the coupling into the two resonators in Fig. 2.2 vs. coupling aperture sweep angle is shown in Fig. 2.3 b). The proposed structure provides notably more coupling for a given coupling aperture sweep angle. At a sweep angle of 25 degrees, the Q external for the bent post resonator is five times smaller than the Q external for the conventional post resonator. Similar resonators with both post types were fabricated with a 40 degree coupling aperture sweep angle.

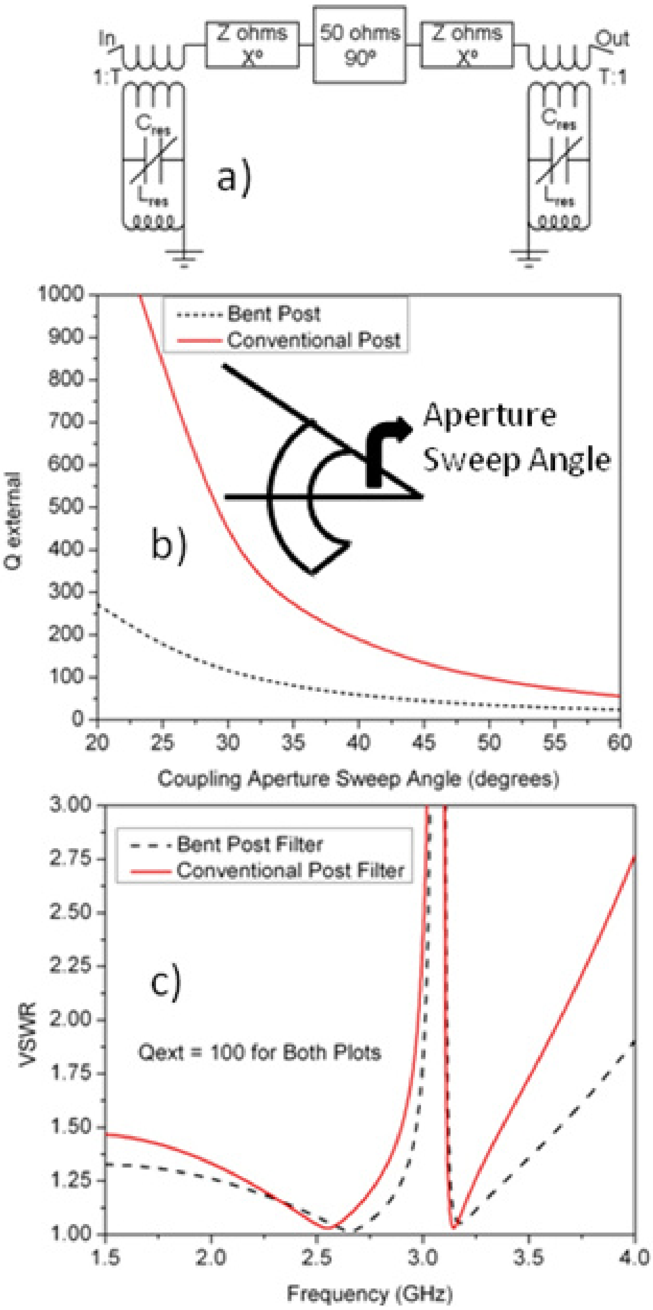

Fig. 2.3. a) Equivalent circuit model of coupling apertures and filter. b) Q external variation vs. aperture sweep angle for both loading post geometries. c) VSWR for both post geometries.

The measured Q external of the bent post resonator was 55.5, and the measured Q external of the straight post resonator was 172.8. These results are within 4.6% and

6.7% of the values in Fig. 2.3 b). Fig. 2.3 c) shows the full-wave simulated VSWR for 2-pole filters using both resonator types with a coupling aperture sweep angle set to provide an external Q of 100 in both cases (31.5° bent, 49° conventional). The VSWR of the proposed structure is lower than the VSWR of the conventional structure by up to 45% in the 1.5 to 4 GHz band. These results correspond to an equivalent series inductance of 1.18 nH for the bent post design versus 1.65 nH for the straight post design in the model of Fig. 2.3 a).

2.3 Filter Design

A 4-pole evanescent-mode cavity filter with the bent post structure was fabricated to show wide bandwidth and shape reconfiguration capability. A model of the fabricated filter with important dimensions specified can be seen in Fig. 2.4. The structure utilizes two layers of PCB material. The top layer contains the signal conductor of the filter's transmission line on one side, and bare dielectric on the other. This layer was fabricated on 0.254 mm thick Rogers Duroid 5880 material ($\epsilon_r = 2.2$, $\tan(\delta) = 0.0009$) and laminated to the second layer. The second layer contains the cavity resonators and coupling apertures. This layer was fabricated in 3.175 mm thick Rogers TMM3 material ($\epsilon_r = 3.27$, $\tan(\delta) = 0.002$). The coupling apertures were cut into the

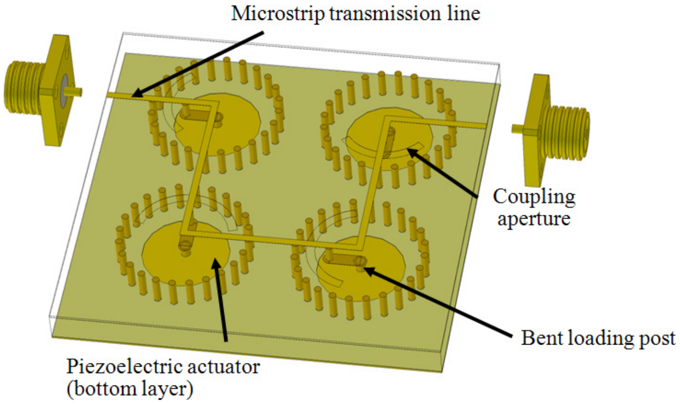

Fig. 2.4. Model of fabricated filter using the proposed resonator.

top conductor layer of the cavities. The coupling apertures are 1 mm wide and have sweep angles of 30 and 55 degrees to account for the different normalized low-pass prototype coupling values which are needed for this specific 4-pole filter. According to full-wave simulation of individual resonators, these sweep angles correspond to external Q values of 115 and 29, respectively. This layer of copper also serves as the ground plane for the transmission line on the 5880 layer. The cavity walls are defined by 0.8 mm diameter vias, and the cavity diameter from the center of one via to the center of the opposing via is 13.6 mm. A flexible copper membrane was laminated to the bottom layer of the cavities, and T216-A4NO-273X piezoelectric actuators from Piezo Systems, Inc. were attached to the membrane external to the cavities to allow electronic tuning of the gaps between the membrane and the loading posts, enabling frequency tuning of the resonators. The bottom half of the loading posts, which are centered in the cavity and responsible for the variable capacitances, are 1.25 mm tall and have diameters of 1.1 mm. In this case the diameters of the posts are equal. However, the diameters of the posts can be designed to be different, enabling different tuning ranges for each resonator. The distance from the centers of the bottom half of the loading posts and the centers of the coupling-enhancement vias is 3.5 mm. The coupling-enhancement vias have a diameter of 0.8 mm.

2.4 Measured Results

Measured results of the four pole filter described above can be seen in Figs. 2.5-2.7. Fig. 2.5 shows bandwidth and attenuation reconfiguration capability. The filter was able to be continuously tuned between a 126.2 MHz (3.9% fractional bandwidth (FBW)) 20 dB equi-ripple response and a 50.1 MHz (1.6% FBW) 40 dB equi-ripple response through electronic tuning of the resonant frequencies of the individual resonators, similar to the method introduced in [36]. It was also capable of a Butterworth-like filter shape with over 70 dB of attenuation. Fig. 2.6 shows the four pole filter tuning from 2.4 to 3.6 GHz with 20, 30, and 40 dB equi-ripple responses.

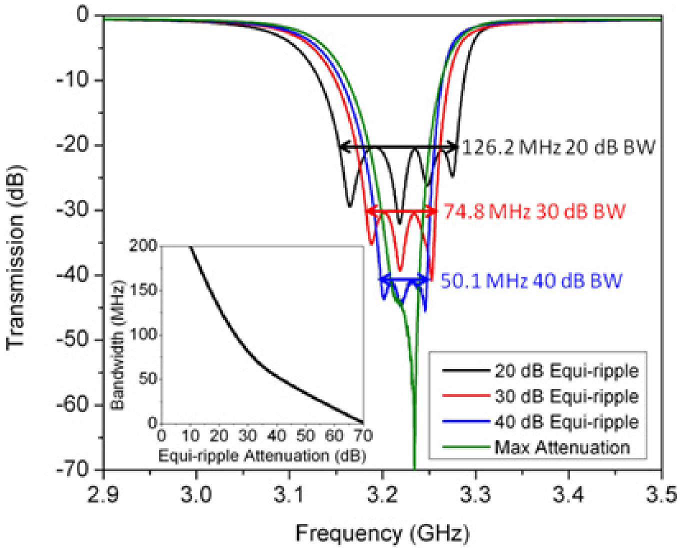

Fig. 2.5. Four measurements of the tunable filter in Fig. 2.4 showing BW control. Inset - Plot of bandwidth vs. equi-ripple attenuation.

The low passband loss varies from 0.24 dB to 0.53 dB in the 2 to 4 GHz frequency range due to the small perturbations caused by the relatively small coupling apertures utilized. Fig. 2.7 shows the filter exhibiting dynamic pole allocation capability. A 30 dB 4-pole response, two narrower 30 dB 2-pole responses, and four narrower 12-19 dB 1-pole responses are shown. Each resonator can be designed to have a different starting frequency without applied actuator voltage and can therefore cover different frequency tuning ranges. The total coverage of all resonators in this design is from 1.6 to 5.8 GHz. The range where all of the individual resonators overlap is 2.3 to 3.9 GHz. Therefore, a 4 pole filter can be formed from 2.3 to 3.9 GHz, while a 2-pole filter can be placed anywhere from 1.8 to 5.0 GHz, and a 1-pole filter can be placed anywhere from 1.6 to 5.8 GHz. Using this strategy, designers can trade total frequency coverage of a single pole filter for increased frequency coverage of 2-pole and 4-pole responses.

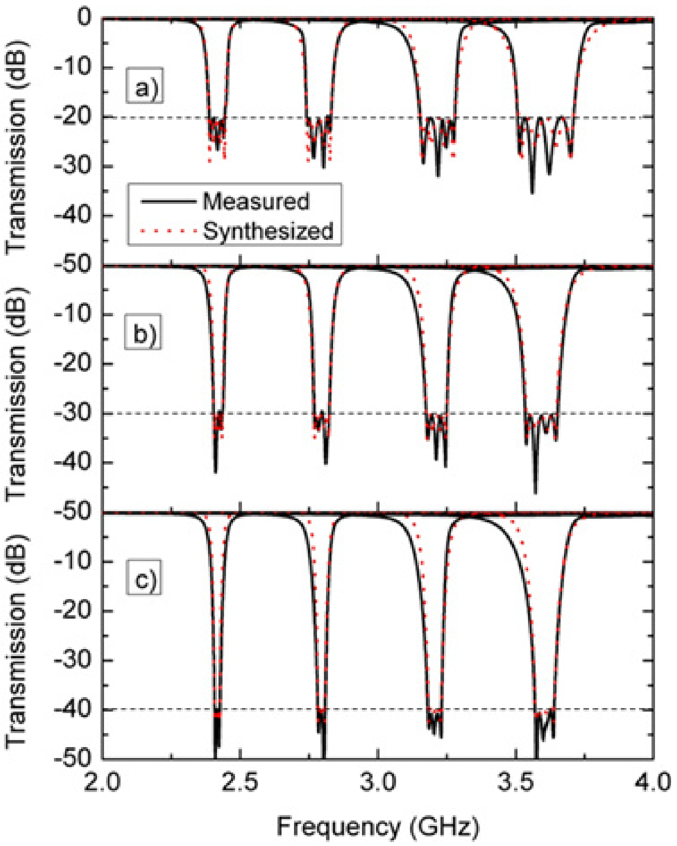

Fig. 2.6. Four measured and synthesized (with Q of 450) results of the filter in Fig. 2.4. a) 20 dB attenuation. b) 30 dB attenuation. c) 40 dB attenuation.

2.5 Conclusion

High Q tunable bandstop filters with variable bandwidth and dynamic pole allocation were designed. A novel post geometry for post-loaded cavity resonators was shown and applied to these tunable bandstop filters. This post geometry increased coupling into the resonators while reducing perturbation of the out-of-band response of the bandstop filter. Bandstop filters were simulated and measured to demonstrate the benefits of the new design and the concepts of tunable attenuation, tunable bandwidth, and dynamic pole allocation. These concepts are expected to be useful in the dynamic spectral environments of the future.

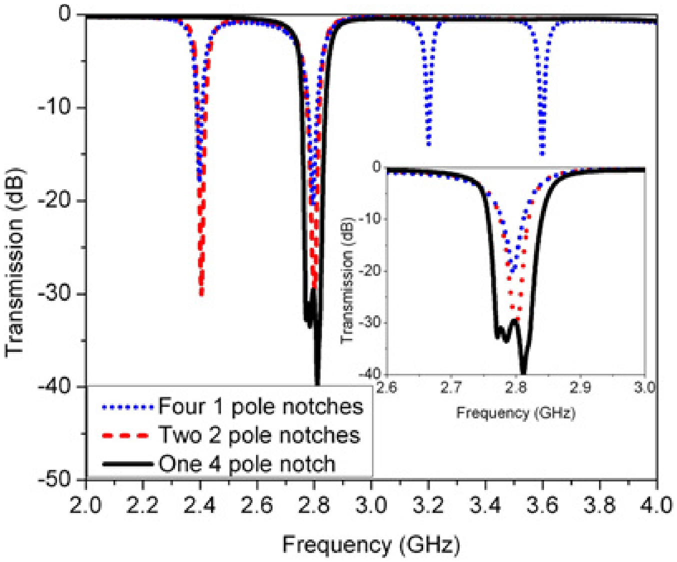

Fig. 2.7. Measurements showing adaptability for varying spectrums.

3. HIGH FREQUENCY TUNABLE BANDSTOP FILTERS WITH RECONFIGURABLE NOTCH RESPONSES FROM 6 GHZ TO 24 GHZ

3.1 Introduction

While the reconfigurable bandstop filter shown in the previous chapter has good performance, many systems operate at higher frequencies than it can cover, such as X band. Scaling the design to higher frequencies presents a significant design and fabrication challenge due to the combination of required feature sizes, tool and machine tolerances, and limitations in materials that are commercially available. Since the design concepts for the higher frequency bandstop filters to be shown in this chapter are very similar to the design concepts described in the previous chapter (bent loading post, aperture coupling, etc.), this chapter will only present some of the design and fabrication challenges, display the higher frequency filter designs, and show measured results.

3.2 High Frequency Bandstop Filter Design and Fabrication Challenges

There are two main design challenges associated with aperture-coupled, highly-loaded coaxial cavity bandstop filters in the 6 GHz to 24 GHz frequency range. First, as frequency increases, the feeding microstrip line must be physically closer to the cavity and coupling aperture for a given amount of coupling since the fields fall off faster in terms of physical length. Therefore, the substrate of the feeding microstrip line must get thinner as the operating frequency is increased. At a certain point, the substrate would be required to be so thin that it would affect the yield of some of the process steps associated with fabricating highly-loaded coaxial cavity filters. To compromise between coupling strength at high frequencies and ease of manufacturing, 10 mil (0.254 mm) thick Rogers' 5880 circuit board material was chosen for all high frequency designs shown in this chapter. This material was also chosen because it has a low loss tangent of 0.009 in the frequency range of interest. Restricting the microstrip line substrate to this material and thickness really shows the coupling strength advantage that can be achieved with the bend loading post structure at high frequencies. Fig. 3.1 shows a comparison of coupling into a highly-loaded coaxial cavity bandstop resonator using a straight loading post and a bent loading post. It is important to note that the resonators used in the simulations shown in Fig. 3.1 have the exact same coupling aperture, and the only difference between the two is the shape of the loading post. It can be seen that the bent loading post enables significantly more coupling, allowing easily-manufactured bandstop filters to be designed at frequencies higher than 6 GHz.

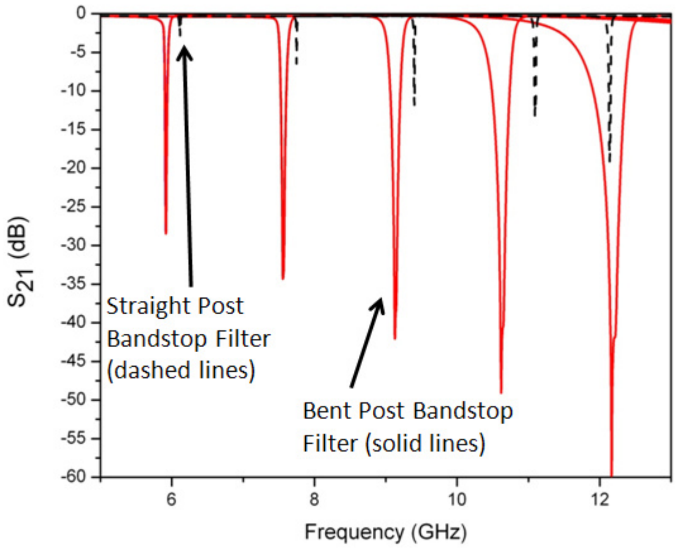

Fig. 3.1. Comparison of simulated coupling into a highly-loaded coaxial cavity bandstop resonator using a straight loading post (black, dashed lines) and a bent loading post (red, solid lines).

The requirement of a thin substrate for relevant coupling values brings about the second main design challenge associated with aperture-coupled, highly loaded coaxial cavity bandstop filters: a well-matched end-launch transition. End-launch connections were required by the sponsor of these higher frequency filters. The challenge is abruptly changing the electromagnetic field distribution from a coaxial one to a very thin microstrip one. In order to do this well, the extra capacitance of the end-launch connector's pin, extra inductance of the path through the connector to ground, and the thickness of the microstrip line's substrate relative to the radius of the connector's dielectric need to be taken into account. With thin substrates, the state-of-the-art transition has more than 1 dB/transition of insertion loss at 20 GHz [37].

3.3 Higher Frequency Bandstop Filter Designs

Three higher frequency bandstop filter designs will be shown in this section: a 6 GHz to 12 GHz tuning 2-pole filter, a 6 GHz to 12 GHz tuning 4-pole filter, and a cascade of a 6 GHz to 12 GHz tuning 2-pole filter and a 12 GHz to 24 GHz tuning 2-pole filter (4 total resonators). All of the designs use electrostatic-actuated silicon MEMS tuners [38].

3.3.1 6 GHz to 12 GHz Tuning 2-pole Bandstop Filter

A simulation model and photograph of the 6 GHz to 12 GHz tunable 2-pole filter can be seen in Fig. 3.2. The microstrip line is removed from the simulation model for clarity. The filter was designed to have a Butterworth shape and a 3 dB fractional bandwidth of 2% in the middle of the tuning range. Slight coupling between the resonators and ports skews the shape slightly and causes the reflection zeros seen in the figure, which are ideally not present in a Butterworth response. However, these reflection zeros only have a minimal effect on the performance of the filter. As can be seen, this filter is significantly smaller than the filter shown in the previous chapter due to the higher frequency of operation. Of particular interest is the diameter of the loading post, which is only 300 μm. The cavity layer is the same Rogers' TMM3 material shown in the previous chapter. Fig. 3.2 also shows measured results of the

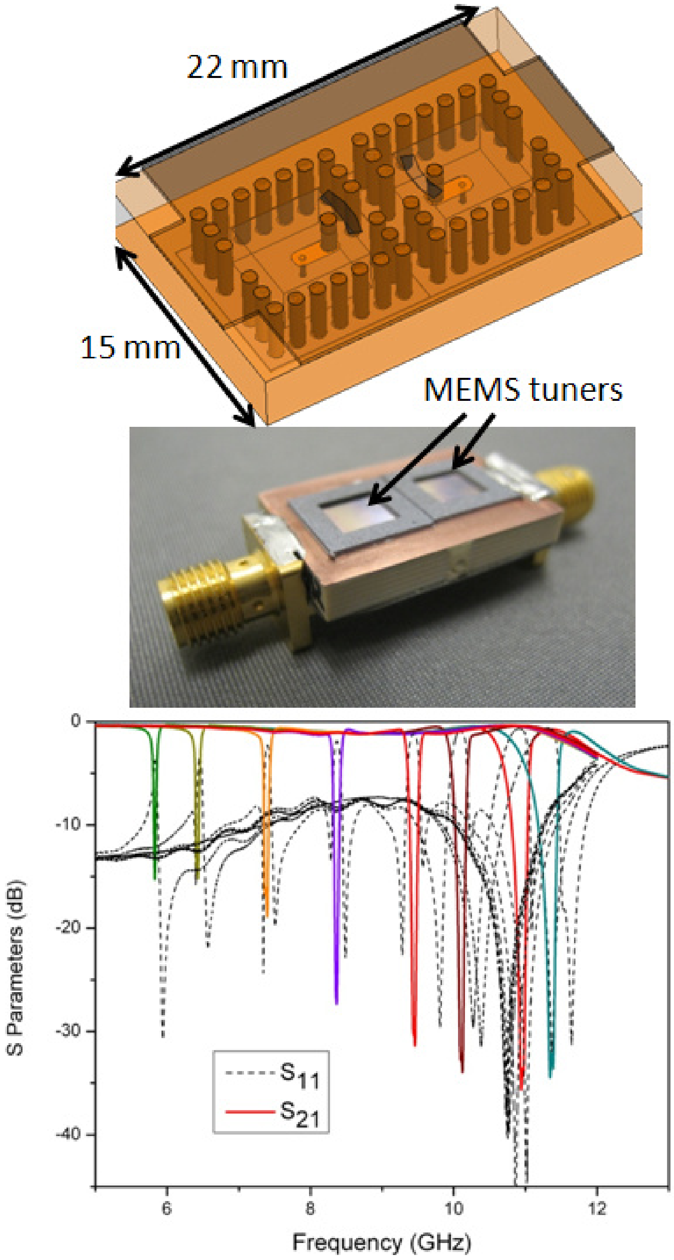

Fig. 3.2. Simulation model, photograph, and measured results of the 6 GHz to 12 GHz tunable 2-pole filter with MEMS actuators.

filter, with tuning from 5.8 GHz to 11.4 GHz and attenuation up to 34 dB. The measured frequency tuning range differed slightly from the designed frequency tuning range because the attachment process for the silicon MEMS tuners is still under development. The accuracy of the attachment of the MEMS tuners determines the initial frequency and tuning range of the resonators.

3.3.2 6 GHz to 12 GHz Tuning 4-pole Bandstop Filter

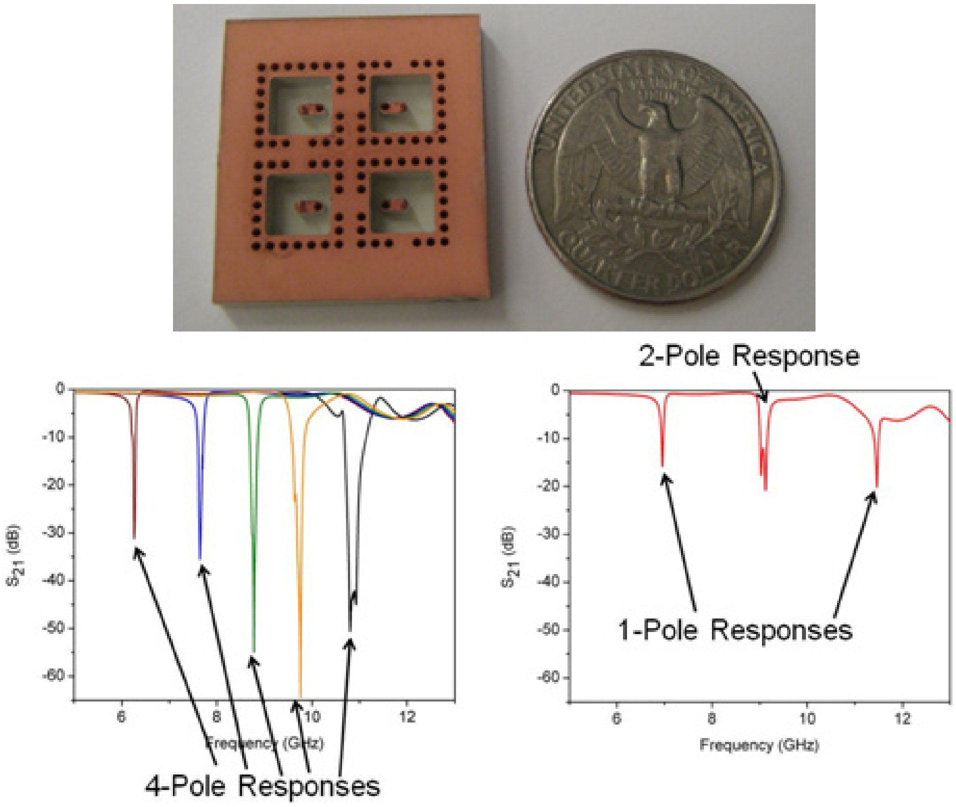

Fig. 3.3. Photograph and measured results of the 6 GHz to 12 GHz tunable 4-pole filter with MEMS actuators.

A photograph of the 6 GHz to 12 GHz tunable 4-pole filter can be seen in Fig. 3.3. This filter uses the same resonators as the 2-pole 6 GHz to 12 GHz tuning filter with different coupling values such that it can provide a 4% 3 dB fractional bandwidth 4-pole Butterworth response. The picture shows the filter without MEMS actuators to display the machined posts inside the cavity. A U.S. quarter is also in the picture for qualitative size comparisons. Fig. 3.3 also shows measured results of the 4-pole filter. In the left plot, the 4-pole response is tuned from 6 GHz to 11 GHz while providing a wider and deeper notch response than was possible with the 2-pole filter. Over 60 dB attenuation was measured. The right plot shows that this filter can also re-task its resonances in order to provide 1-pole and 2-pole responses in spectral environments with several relevant interfering signals. All three responses in the right plot are present at the same time, providing up to 20 dB attenuation at three seperate, dynamically-tunable frequencies.

It is of interest to note that in the 2-pole and 4-pole 6 GHz to 12 GHz tuning filters, the upper passband starts to degrade after 11 GHz, having 5 dB or more insertion loss. In addition, the 300 μm diameter loading posts in these two filter designs are the smallest posts that can be accurately fabricated in ceramic circuit board materials using current methods. Both of these traits are challenges to achieving operating frequencies higher than 12 GHz. The 6 GHz to 24 GHz tuning 4-pole bandstop filter cascade design of the next subsection addresses these challenges.

3.3.3 6 GHz to 24 GHz Tuning 4-pole Bandstop Filter Cascade

A simulation model and a photograph of the 6 GHz to 24 GHz tunable 4-pole bandstop filter cascade can be seen in Fig. 3.4. In order to have loading post diameters that are able to be manufactured, this design uses a thinner (0.762 mm vs. the previous 3.175 mm thickness) TMM3 substrate to host the cavities. This change results in lower resonator inductance. Reducing the inductance increases the resonant frequency and percent loading of the resonators. With the inductance reduction due to the change in substrate thickness, resonators could be designed with able-to-be-fabricated 300 μm diameter loading posts that operate up to 24 GHz. In order to make resonators that operate at frequencies as low as 6 GHz in the thinner substrate, the loading posts were made larger.

In order to address the passband degradation seen in the 6 GHz to 12 GHz tuning bandstop filters, the 5880 substrate was extended beyond the TMM3 substrate to facilitate proper grounding of the end-launch connectors. In addition, the previous

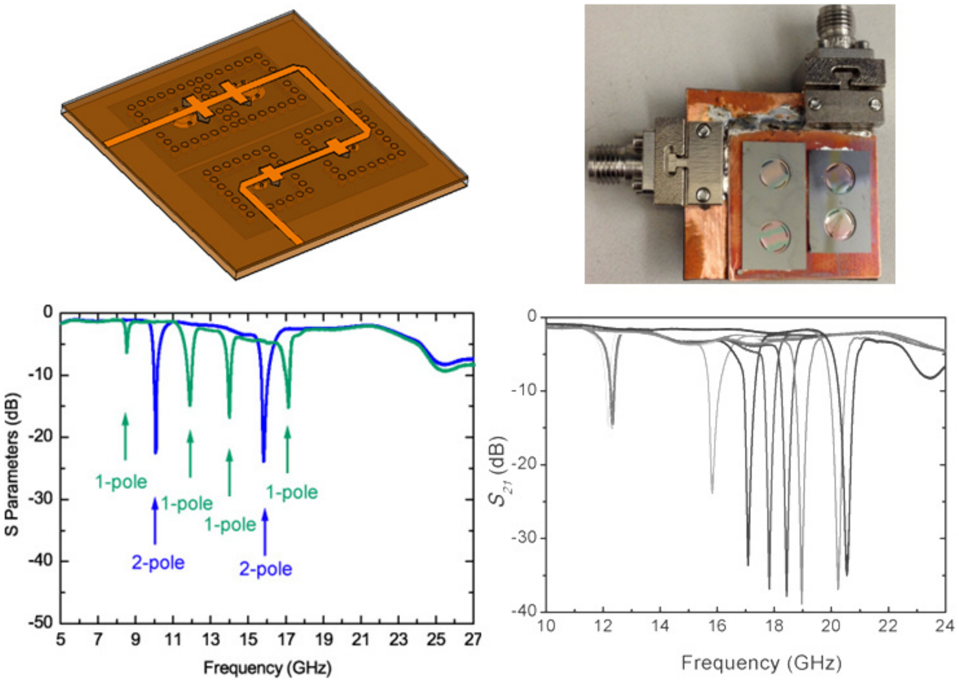

Fig. 3.4. Simulation model, photograph, and measured results of the 6 GHz to 24 GHz tunable 4-pole bandstop filter cascade with MEMS actuators.

SMA connectors were replaced with 2.92 mm connectors, which operate mode-free at higher frequencies. Capacitive patches were also added to the microstrip line over the coupling apertures, which can be seen in the simulation model in Fig. 3.4. The capacitive patches help to impedance match the coupling apertures, and their function will be explained in more detail in the next chapter of this dissertation. The improvements in the passband can be seen in the lower sub-figures of Fig. 3.4, where the passband extends to above 22 GHz. The left lower sub-figure shows tuning of the lower-frequency 2-pole filter from 8 GHz to 17 GHz. The measured values differed from the designed 6 GHz to 12 GHz because the MEMS actuator attachment method is still under development. The right lower sub-figure shows tuning of the higher-frequency 2-pole filter from 12 GHz to 20.5 GHz. This filter was unable to be tuned over an entire octave frequency range to 24 GHz due to issues with the MEMS actuator annealing process during their fabrication.

3.4 Conclusion

High frequency (6 GHz to 24 GHz) bandstop filter designs were shown in this chapter. These bandstop filters are the first to use silicon MEMS tuners, enabling compact, mass-producible designs. The filters showed dynamic pole allocation capability and provided up over 60 dB attenuation in some cases. A filter cascade was shown with a passband that extended from 6 GHz to 22 GHz, or a 3.67-to-1 ratio. For some systems, it would be useful to be able to cover a wider range than 3.67-to-1 while having continuous notch coverage. Since lower-frequency and higher-frequency bandstop filters have been shown that are well-matched out of band, it is theoretically easy to cascade these filters in order to create a continuous-coverage notch filter cascade with a very wide passband ratio. However, such capability is challenging due to coupling structure reactance and spurious resonator modes. The next chapter is focused on these challenges.

4. BANDSTOP FILTER CASCADES FOR WIDE COVERAGE RANGE INTERFERENCE MITIGATION

4.1 Introduction

The previous two chapters showed tunable bandstop filters that are capable of covering a relatively wide tuning range, up to an octave. However, even wider tuning microwave bandstop filters would be useful for systems that operate over very wide bandwidths, such as low probability of intercept communications [39], spectrum sensing [40], and dynamic spectral access systems [41]. Because of the wide operating frequency range of these systems, recent bandstop filter research has focused on creating filters that have an extended spurious-free upper passband. In [42], a 6 to 1 upper passband was shown, meaning that the first spurious resonance was at six times the bandstop filter center frequency. An 18 to 1 upper passband was shown in [43], but only in simulation. More recently, two methods to achieve an extended upper passband were shown in [44]. A tunable bandstop filter with an 8.9 to 1 upper passband was shown in [32]. Previous extended upper passband filters leave systems open to interference over a wide frequency range above the bandstop resonance by design, blocking interference at the notch frequency but leaving the system powerless against interference in the upper passband of the bandstop filter. In some applications, it would be advantageous to implement a bandstop filter with a wide upper passband that could tune over its entire upper passband. Currently, this functionality is usually implemented with yttrium iron garnet (YIG) filter [45] banks. However, YIG filters require a large amount of power ($\geq$1 Watt) and are physically large compared to some other tunable filter technologies. Solid state varactor-tuned bandstop filters have been shown to have low power consumption (mW) and very wide tuning ranges (4:1) [46]. However, the use of varactors results in low resonator quality factors (50 or less at microwave frequencies) and poor linearity. MEMS-tunable bandstop filters [47] offer low power consumption, higher quality factors (≥55 in X band), and increased power handling capability compared to some varactor-tuned filters. However, as of now there are no MEMS-tuned bandstop filters with wide upper passbands, and the frequency tuning range of these filters is often less than an octave. One method that has been used to provide a bandstop response over a frequency range wider than the tuning range of a single bandstop filter is a cascade of bandstop filters [48]- [52]. However, a high quality factor (≥400), low power consumption (≤10 mW), multi-octave, continuous frequency coverage bandstop filter cascade has not been demonstrated.

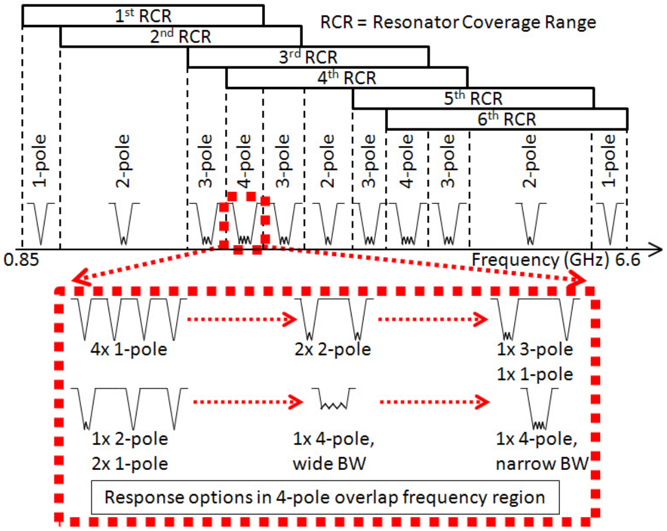

Fig. 4.1. Concept of a 6-resonator bandstop filter cascade using dynamic pole allocation and possible bandstop response orders over a wide spectrum. Examples of 6 reconfiguration possibilities of a 4-pole response are shown in the magnified window with the red-dotted outline. Such 4-pole responses could be obtained from a filter with the coupling-routing diagram shown in Fig. 1.6.

Evanescent-mode cavity based filters have been shown to meet most of these requirements [53]. However, past bandstop filters using aperture-coupled cavity resonators [54] do not have wide upper passbands due to the reactance of the coupling apertures. This chapter presents a novel method for increasing the spurious-free upper passband of an aperture-coupled cavity bandstop filter. The obtained 7.8 to 1 increased upper passband is combined with the octave tuning range of evanescent-mode cavity resonators to show a high quality factor ($\geq$400), low power consumption (μW), multi-octave, continuous frequency coverage bandstop filter cascade for the first time. In addition, the tuning ranges of the component filters of the cascade circuit overlap over designed frequency ranges, allowing higher-order notching capability in frequency bands where interference is most expected. This dynamic pole allocation concept is shown graphically in Fig. 4.1 for a 6-resonator bandstop filter cascade. Note that this concept only produces desired filter shapes if the resonators that form the 4-pole responses shown in the magnified window in Fig. 4.1, whose coupling routing diagram can be drawn as in Fig. 1.6, are designed with coupling values that are appropriate for all of the desired response shapes.

4.2 Motivation and Background

A conceptual image of a tunable evanescent-mode cavity resonator is shown in Fig. 4.2 with a piezoelectric actuator for electronic control of the gap between the flexible cavity sidewall and the loading element. In Fig. 4.2, the resonator is coupled into through an aperture in the ground plane of a microstrip transmission line. In most bandstop filters, the upper passband limiting factor is spurious higher order resonances of the filter's resonators [32]. Because evanescent-mode cavity resonators are very highly loaded, they have a very wide spurious-free frequency range above their fundamental resonance. This characteristic has been used to create bandpass filters using series-coupled resonators with very wide spurious-free frequency ranges of 10 to 1 or more [55].

When aperture coupling is used to couple a feeding transmission line to an evanescent-mode cavity resonator in a shunt configuration for a bandstop filter response, as shown in Fig. 4.2, the coupling apertures are an imperfection in the ground plane of the transmission line. This changes the local characteristic impedance of the trans-

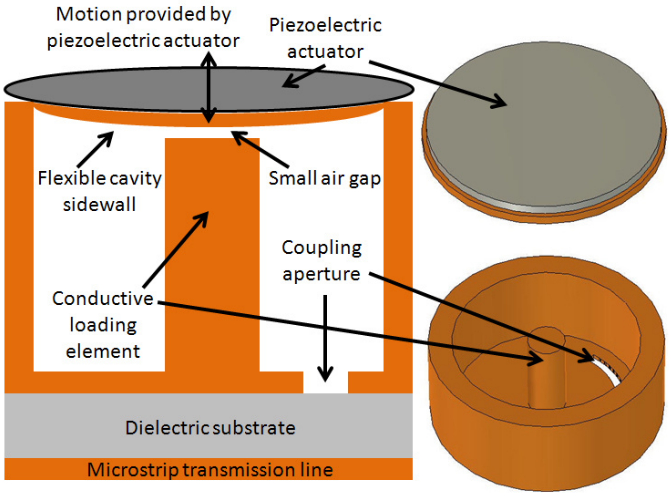

Fig. 4.2. Illustration of evanescent-mode cavity resonator coupled to a microstrip line through an aperture in the microstrip line's ground plane and a 3D model of an evanescent-mode cavity resonator.

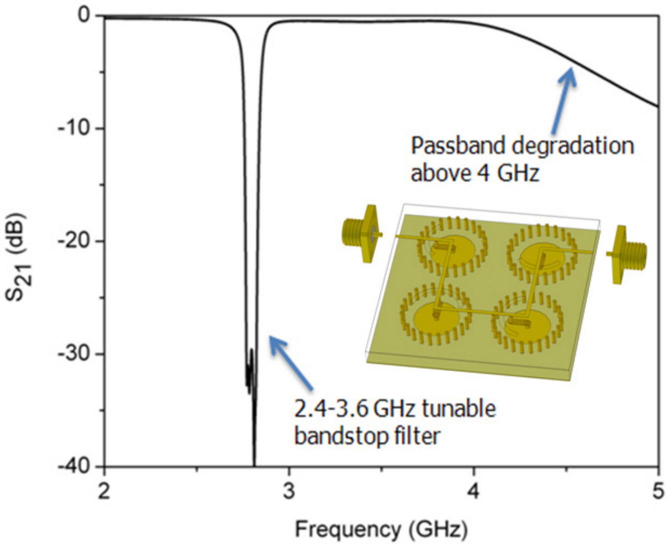

Fig. 4.3. Measured response of the bandstop filter described in [54] (inset) showing upper passband degradation above 4 GHz.

mission line. The local change in characteristic impedance causes reflection of signals at frequencies other than the bandstop filter center frequency, reducing the quality of the bandstop filter's passband. The reflections caused by the coupling apertures are the upper passband limiting factor of aperture-coupled evanescent-mode cavity resonator bandstop filters. An example of this effect can be seen in Fig. 4.3. Fig. 4.3 shows a measured response of the 4-pole tunable bandstop filter shown in [54] through 5 GHz. While the filter performs well and has a low loss passband over its tuning range of 2.4 GHz to 3.6 GHz, it can be seen that the passband degrades after 4 GHz. The following sections analyze this effect and provide a new design methodology for extension of the upper passband of aperture-coupled evanescent-mode cavity filters toward the goal of a multi-octave coverage bandstop filter cascade.

4.3 Design of Feeding Transmission Line and Coupling Apertures

To analyze the effect of the coupling apertures on the upper passband of aperture-coupled evanescent-mode cavity filters, we consider an example of a typical microstrip transmission line with two coupling apertures in its ground plane as shown in Fig. 4.4 a). Note that there are no evanescent-mode cavities represented in Fig. 4.4 a), and the coupling apertures in Fig. 4.4 a) are not the coupling apertures used in the filter shown in [54]. A microstrip line with apertures in its ground plane can be a bandstop filter itself because the coupling apertures have resonances. It is important to understand that in this chapter we are using this structure below the first resonance of the coupling apertures. In other words, the below-resonance impedance of the coupling apertures limits the upper passband of the coupling structure in Fig. 4.4 a) well before the resonances of the coupling apertures limit the upper passband of the structure.

An accurate equivalent circuit model of an aperture in the ground plane of a transmission line has already been presented [56]. The circuit model described in [56] is repeated in Fig. 4.4 b) for convenience. The circuit model in Fig. 4.4 b) models the first two resonances of the coupling aperture and their interaction, which was shown in [56] to accurately model the circuit below resonance. The model is asymmetric because the parallel combination of L_1 and C_1 model the first resonance of the coupling aperture, and the parallel combination of L_2 and C_2 model the second resonance of

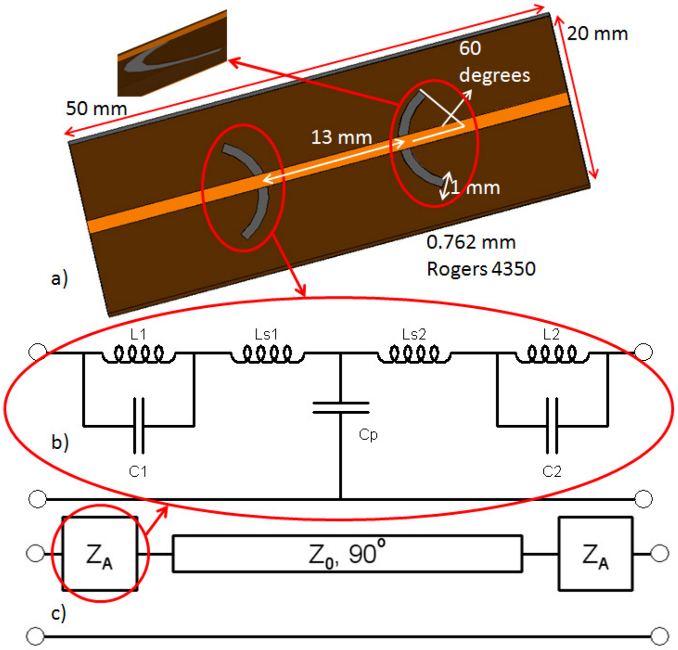

Fig. 4.4. a) Illustration of aperture coupling through the ground plane of a microstrip transmission line. b) Equivalent circuit model of a coupling aperture. c) Simplified equivalent circuit of the model in a).

the coupling aperture. Using this model of a single aperture, the structure in Fig. 4.4 a) can be represented as the circuit in Fig. 4.4 c). [56] describes a method to extract the lumped element values of the circuit model in Fig. 4.4 b) from full-wave simulation scattering parameter results, and relevant equations from [56] are in the appendix at the end of this chapter. Full-wave simulation of a single aperture and the entire structure in Fig. 4.4 a) was done, and lumped element equivalent circuit model values were extracted using the method described in [56] and the equations in the appendix of this chapter. The equivalent circuit model extracted values can be seen in Table 4.1. A comparison of the full-wave simulation and the extracted equivalent circuit lumped element model response for the models in Fig. 4.4 a) and Fig. 4.4 c) is shown in Fig. 4.5, and good agreement can be seen.

Fig. 4.5 shows that the microstrip line and coupling apertures shown in Fig. 4.4 a) have a passband that degrades after 3 GHz, and a spurious bandpass resonance

Table 4.1
Element values for equivalent circuit model shown in Fig. 4.4 b)

Inductor	Value (nH)	Capacitor	Value (pF)
L_1	0.501	C_1	0.469
L_2	0.031	C_2	0.301
L_{s1}	0.962	C_p	0.0561
L_{s2}	0.00165		

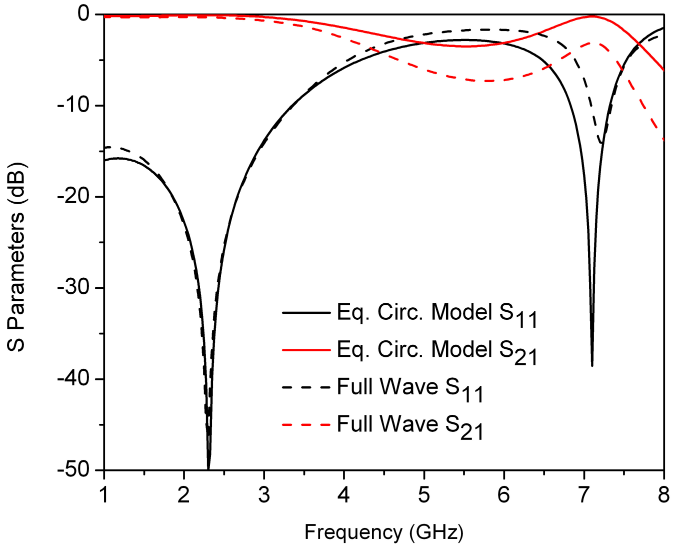

Fig. 4.5. a) Comparison of the lossless circuit level simulation of an optimized model of the coupling structure in Fig. 4.4 a) which uses the equivalent circuit model in Fig. 4.4 b) and a full wave simulation of the coupling structure in Fig. 4.4 a) (metal conductivity = 5.8e7 S/m, metal thickness = 35 μm).

can be seen at 7.1 GHz. Although the spurious bandpass resonance is at 7.1 GHz, its stopband degrades the passband of the coupling structure in Fig. 4.4 a) at frequencies as low as 3 GHz. This spurious bandpass resonance is at the frequency where the 13 mm transmission line between the coupling apertures in Fig. 4.4 a) is 180 electrical degrees long. While the transmission line has uniform width across the entire structure, the coupling apertures in its ground plane create inductive impedance boundaries that increase the local characteristic impedance of the transmission line. When a uniform 180 electrical degree transmission line is terminated in an impedance that does not match its characteristic impedance, a bandpass resonance results. The bandpass resonance at 7.1 GHz in Fig. 4.5 is due to this effect, and it must be mitigated in order to increase the upper passband of the coupling structure shown in Fig. 4.4 a).

The proposed method to mitigate the effect of the transmission line bandpass resonance described above is to capacitively load the transmission line section that causes the resonance. Capacitively loading the transmission line resonator reduces its resonant frequency and increases the coupling coefficient into the resonance, making it exhibit a broader response. If the resonance is lowered in frequency and broadened enough, it will become part of the passband of the coupling structure shown in Fig. 4.4 a). Since the resonance is due to a transmission line, one of the easiest and high quality factor methods to add shunt capacitance to the structure is to use an electrically short length of low characteristic impedance transmission line, similar to what is used in stepped impedance lowpass filters [24]. The susceptance of a short, relatively low characteristic impedance series patch is

$$B = \omega C \approx Y_0 \beta \ell_p. \tag{4.1}$$

where β is the propagation constant, ℓ_p is the length of the patch, C is the shunt capacitance, and Y_0 is the characteristic admittance of the patch.

Models of a transmission line over two coupling apertures with added shunt capacitance in the form of short, low characteristic impedance transmission line sections can be seen in Fig. 4.6, where Z_A is the same as it was in Fig. 4.4 c). The model in Fig. 4.6 a) has input impedance of

$$Z_{in} = \frac{Z_{TL} + Z_A + j\omega C Z_{TL} Z_A}{1 + 2j\omega C Z_{TL} - \omega^2 C^2 Z_{TL} Z_A + j\omega C Z_A}, \tag{4.2}$$

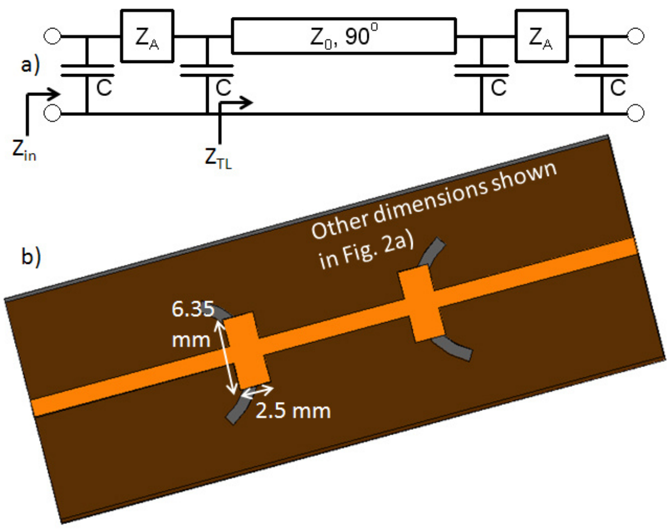

Fig. 4.6. a) Equivalent circuit approximation of aperture coupling through the ground plane of a microstrip transmission line with added shunt capacitance. b) Illustration of aperture coupling with added capacitive patches on the microstrip line.

where

$$Z_{TL} = Z_0 \frac{\dfrac{1 + j\omega C Z_A}{j\omega C(2 + j\omega C Z_A)} + jZ_0 tan(\beta\ell)}{Z_0 + j\dfrac{1 + j\omega C Z_A}{j\omega C(2 + j\omega C Z_A)} tan(\beta\ell)}, \tag{4.3}$$

where C is the shunt capacitance shown in Fig. 4.6 a), ω is the radian frequency, β is the propagation constant, Z_0 is the characteristic impedance of the transmission line, Z_A is the impedance of the coupling aperture, and ℓ is the length of the transmission line. All of the variables in this equation are known except for C from either the design of the coupling structure in Fig. 4.4 a) or parameter extraction from its simulation results. Therefore, (4.2) can be solved for the value of C that reduces the transmission line bandpass resonance, which occurs when $Z_{in} = \infty$, to a particular frequency through capacitive loading. The required capacitance can be realized as a low impedance section of transmission line using (4.1). Through optimization of (4.2) to yield an upper passband 1 dB roll-off frequency of 6.5 GHz with minimal passband ripple below 6.5 GHz, the capacitive patches were designed to be 2.5 mm long and 6.35 mm wide, corresponding to a capacitance of 0.85 pF at 4.2 GHz. Fig. 4.7 shows that the passband of the coupling structure now extends to 6.5 GHz before degradation occurs.

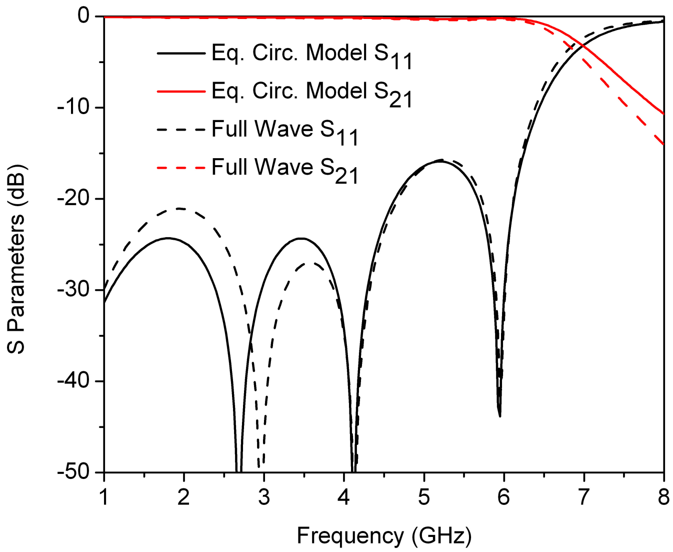

Fig. 4.7. a) Comparison of the circuit level simulation of an optimized model of the coupling structure in Fig. 4.6 a) which uses the model in Fig. 4.4 b) and a full wave simulation of the coupling structure in Fig. 4.6 b).

It can be seen that there are two reflection zeros shown in Fig. 4.5 while there are three reflection zeros shown in Fig. 4.7. While the reflection zero associated with the bandpass resonance of the transmission line between the coupling apertures (at 7.1 GHz in Fig. 4.5 and at 6.0 GHz in Fig. 4.7) is the focus of the proposed extended upper passband technique, the behavior of the other reflection zeros are also well-predicted by (4.2) and are a result of the interaction between the transmission lines of the circuit, the coupling apertures, and the capacitive patches. Since the lower frequency reflection zeros are not the limiting factor of the upper passband of a microstrip transmission line with coupling apertures in its ground plane, (4.2) provides enough information about their spectral locations in order to optimize the passband. Further understanding of the proposed extended upper passband technique can be gained from examining the passband response for several widths of the capacitive patches in Fig. 4.6. Fig. 4.8 shows the S parameter responses of the coupling structure in Fig. 4.6

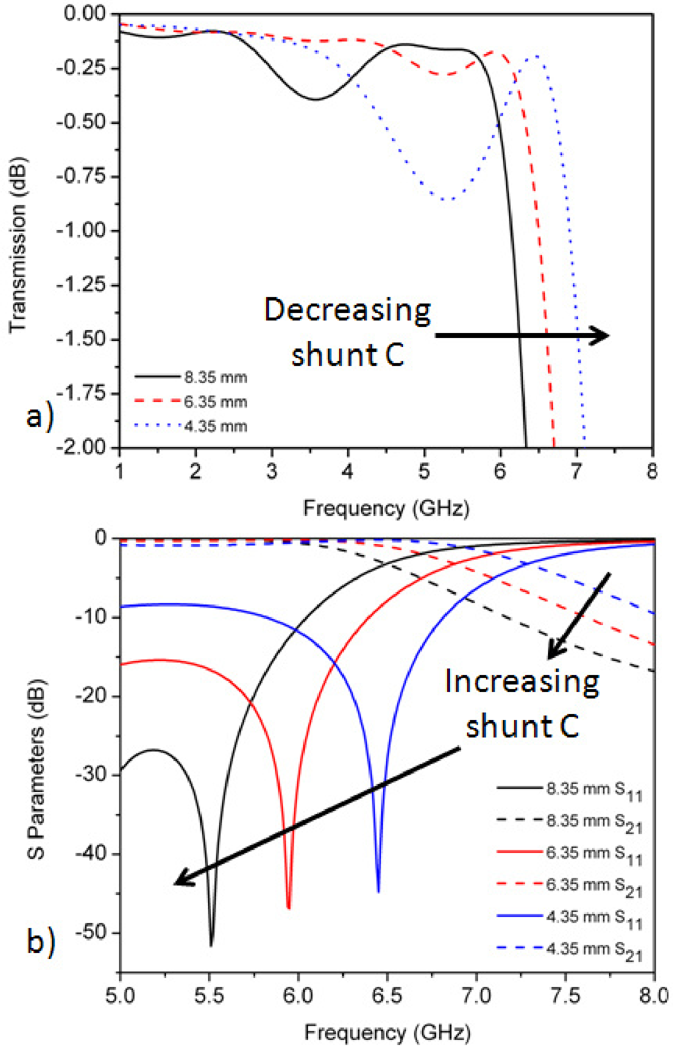

Fig. 4.8. a) Transmission response for three widths of the capacitive patch in Fig. 4.6 showing passband ripple vs. passband roll-off trade-off. b) S parameters for three widths of the capacitive patch in Fig. 4.6 showing the shift of the reflection zero frequency as shunt capacitance is added.

for capacitive patch widths of 4.35 mm, 6.35 mm, and 8.35 mm. In Fig. 4.8 a), the trade-off between passband ripple and passband roll-off frequency is shown. The 4.35 mm width case, which adds the least shunt capacitance to the coupling structure, has a higher frequency passband roll-off than the 6.35 mm width chosen in this design, but it also has higher passband ripple. The 8.35 mm width case, which adds the most shunt capacitance to the coupling structure, has more ripple in the passband than the 6.35 mm width case, as well as a lower frequency passband roll-off. Fig. 4.8 b) shows the shift of the reflection zero associated with the bandpass resonance of the transmission line between the coupling apertures as more shunt capacitance is added to the circuit. The location of this reflection zero can be designed to optimize the trade-off between passband ripple and passband roll-off frequency.

Consequently, the design methodology for the geometry of the proposed capacitive patches can be summarized as follows:

Step 1 Design a conventional aperture-coupled cavity bandstop filter to meet filter shape specifications.

Step 2 Extract the component values for the coupling structure model in Fig. 4.4 b) from measured or simulated scattering parameters using the method described in [56] and the equations listed in the appendix of this chapter.

Step 3 Determine the required value of C for the model in Fig. 4.6 a) to lower the first transmission line bandpass resonance using (4.2) so that the passband ripple and roll-off frequency is optimized.

Step 4 Design the capacitive patch dimensions to obtain the capacitance value required from the previous step using (4.1).

Step 5 Optimize the geometry of the capacitive patch in simulation to obtain the desired upper passband shape.

The geometry of the capacitive patch must be optimized in simulation because a low impedance section of transmission line is not a perfect capacitance. Alternatively, more advanced models of the capacitive patch could be used to further refine its geometry. The wide spurious-free coupling structure response shown in Fig. 4.7, in addition to the inherent wide spurious-free response of evanescent-mode cavity resonators, provides a path toward very wide frequency coverage bandstop filter cascades.

4.4 6-Resonator Bandstop Filter Cascade Design

Using the method described in the previous section to increase the upper passband of a microstrip line with apertures in its ground plane, an evanescent-mode cavity based 6-resonator bandstop filter cascade circuit was fabricated in order to provide complete notch coverage of the 0.85 to 6.6 GHz frequency range. In order to cover the entire frequency range, the 6 resonators of the structure were segregated into three sets of octave-tunable 2-pole filters that each cover a different frequency range. Because of the wide upper passband that is now possible with these filters, they can simply be cascaded. The resonators' tuning ranges were designed to have specific amounts of overlap so that certain portions of the spectrum are able to have 2-, 3-, and/or 4-pole responses. The regions with higher order filter capability can be designed to be in bands where high power or wide bandwidth interference is most expected. An illustration of the fabricated 6-resonator bandstop filter cascade can be seen in Fig. 4.9. The bandstop filter cascade uses three copper layers and two dielectric layers. The top copper layer, labeled Layer 1 in Fig. 4.9, contains the feeding microstrip transmission line. Capacitive patches can be seen along the length of the line. The top dielectric layer, labeled Layer 2 in Fig. 4.9, is 0.762 mm thick Rogers 4350 circuit board material (ϵ_r=3.66, tan(δ)=0.0037 @ 10 GHz). Rectangular regions of this dielectric layer were removed near the input and output ports of the circuit in order to facilitate grounding of the input and output SMA connectors. The middle layer of copper, labeled Layer 3 in Fig. 4.9, is below the 4350 dielectric layer and serves as the ground plane for the feeding microstrip transmission line. This layer of copper also has semi-circular apertures in it for coupling the microstrip transmission line to the evanescent-mode cavity resonators below. The bottom dielectric layer, labeled Layer 4 in Fig. 4.9, is Rogers TMM3 circuit board material (ϵ_r=3.27, tan(δ)=0.002 @ 10 GHz).

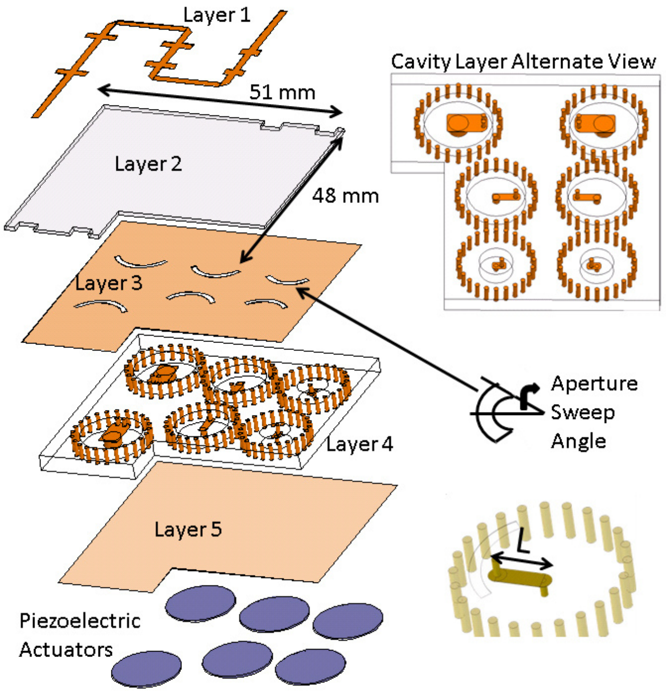

Fig. 4.9. Layer-by-layer view of the fabricated 6-resonator bandstop filter cascade.

The evanescent-mode cavity resonators are integrated into this dielectric layer. The outer walls of the resonators are defined by copper plated 0.8 mm diameter via holes that are spaced close enough together to approximate a solid wall over the circuit's operating frequency range. The resonators use the bent loading post geometry first shown in [54] to increase coupling for a given coupling aperture size and distance from the feeding microstrip transmission line. Some of the TMM3 material is removed from the interior of the cavity. These regions can be seen in Fig. 4.9 as transparent cylinders inside of the cavities and are 2.5 mm deep. The bottom copper layer, labeled Layer 5 in Fig. 4.9, is a flexible, thin sheet over the entire area of the circuit. The copper sheet is attached to the TMM3 dielectric layer everywhere except within the boundaries of the outer walls of the resonators, creating a bendable membrane over each bent loading post. 0.38 mm thick, 1/2 inch diameter piezoelectric actuators from Piezo Systems, Inc. are attached to the side of the bendable copper membranes external to the cavity using silver epoxy. The piezoelectric actuators allow electronic control of the gaps above the bent loading posts in the resonators and the bendable copper membrane.

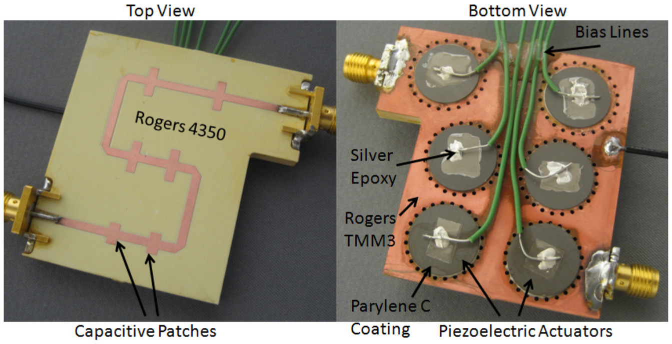

Fig. 4.10. Top and bottom views of the fabricated 6-resonator bandstop filter cascade.

Images of the fabricated evanescent-mode cavity bandstop filter cascade circuit can be seen in Fig. 4.10. The wires seen in Fig. 4.10 are the bias lines for the piezoelectric actuators, which use ±210 Volts to tune over their entire range of motion. The bias lines are connected to the piezoelectric actuators with silver epoxy external to the cavity. Other than a rectangular patch for connection of the bias lines, the top and sides of the piezoelectric actuators are coated in Parylene-C from Specialty Coating Systems in order to prevent shorting of the piezoelectric actuator bias voltages to the ground of the filter cascade circuit. In contrast to the 4-pole filter in [54] with four similar resonators, the 6-resonator cascade circuit shown in Fig. 4.9 and Fig. 4.10 is divided into three sets of two similar resonators that each focus on a subset of the entire frequency coverage range of the circuit. The dimensions of the resonators can be seen in Table 4.2. While each of the two similar resonators have the same outer diameter and loading post diameter, different nominal gaps between the loading post and the flexible copper membrane allow each resonator to have slightly different tuning ranges.

The length of the transmission lines between the coupling apertures for each of the three 2-pole filters are different as can be seen in Fig. 4.9. For a frequency-static

Table 4.2
Fabricated resonator dimensions (*: see Fig. 4.9 for definition)

Band	Low	Mid	High
Cavity Radius (mm)	7.5	7	6.75
Loading Post Radius (mm)	1.8	0.62	0.39
Aperture Width (mm)	1	1	1
Aperture Sweep Angle* (degrees)	60	60	50
Cavity Center to Aperture (mm)	5.5	5	5
L* (mm)	7.2	5	2.5
Design Butterworth 10 dB FBW	1%	2.5%	2.5%

bandstop filter that uses a transmission line as an inverter between similar resonators, the transmission line should be 90 degrees in electrical length. However, for tunable filters, a transmission line inverter between the resonators can only be 90 degrees in electrical length at one frequency. An asymmetric bandstop response is produced away from this frequency. The transmission line lengths between the resonators were designed in order to have a symmetric response at particular frequencies of interest. Additionally, since the 2-pole filters are matched to the system impedance in their passbands, the lengths of transmission line between each 2-pole filter do not have an appreciable effect on the cascade's response. Therefore, the transmission lines between each 2-pole filter should be kept as short as possible to reduce passband loss. Simulation results of the two lowest frequency resonators in the design, independent of the entire cascade circuit, can be seen in Fig. 4.11. The resonant frequencies overlap from 1-2 GHz while maintaining an almost 20 dB return loss from 0.5 to 6 GHz. Since the passbands of the individual 2-pole filters are able to be well matched over a wide frequency range, component filters of bandstop filter cascades can be designed as individual filters and then simply placed in series. This ease of integration lends itself to modular design, where resonators with a certain coverage range can

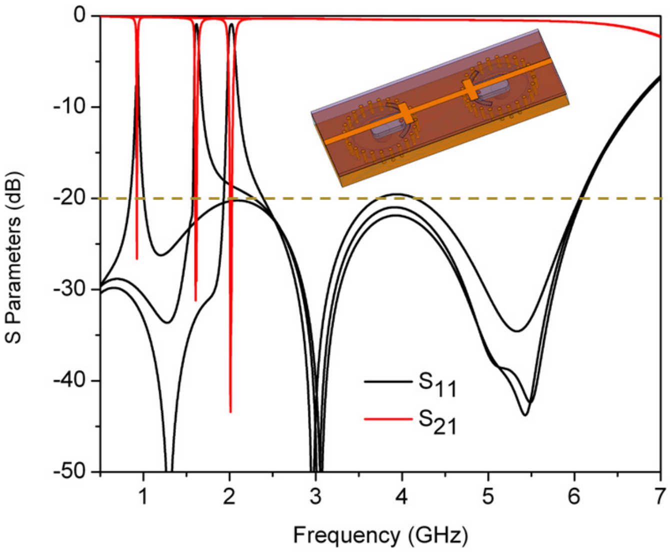

Fig. 4.11. Simulated superimposed responses of the two lowest frequency resonators of the cascade design tuning from 1 to 2 GHz while maintaining an almost 20 dB return loss from 0.5 to 6 GHz. The inset shows the simulated structure.

be dropped into and out of a design for different expected interference scenarios. In addition, it may be possible to increase the upper passband further than what is shown in this chapter. This concept in this chapter manipulates the first bandpass resonance of the transmission line between the coupling apertures in order to increase the upper passband. However, this transmission line has a bandpass resonance at each frequency for which its electrical length is an integer multiple of 180 degrees. If multiple bandpass resonances of this transmission line could be used to increase the upper passband, the passband could be extended to the first bandstop resonance of the coupling aperture, which is much higher than the current limit. For example, the first coupling aperture bandstop resonance for the structure in Fig. 4.4 a) is at 10.4 GHz. This is a subject of ongoing research.

4.5 Measured Results I

The response of the fabricated bandstop filter cascade was measured using an Agilent Technologies N5230C PNA. Bias voltages were applied to the piezoelectric actuators using Keithley 2400 Sourcemeter power supplies. The final structure was simulated using Ansoft HFSS. Measured vs. simulated S_{11} and S_{21} responses can be seen in Fig. 4.12 and Fig. 4.13, respectively. In both figures, the cascade is configured to produce three 2-pole responses. Good agreement can be seen between the measured and simulated data from DC to 6.5 GHz. From 6.5 to 10 GHz, the measured and simulated responses have similar shapes but slight discrepancies in frequency. These discrepancies can be explained by slightly smaller coupling apertures than desired and/or slightly smaller capacitive patches than desired according to the equivalent circuit model described in Section 4.3. In addition, measurement calibration was completed to the plane of the SMA connectors, where the simulation port was placed directly onto the filter substrate. Therefore, the simulations do not take the effect of the SMA to microstrip line transition. The notch responses were measured to have

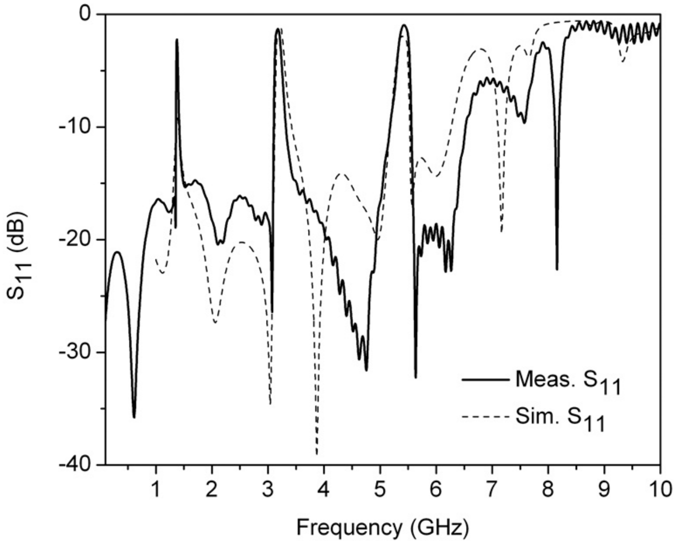

Fig. 4.12. Measured vs. simulated S_{11} response of the cascade circuit when it is configured to produce three 2-pole maximum attenuation responses. (static measurement).

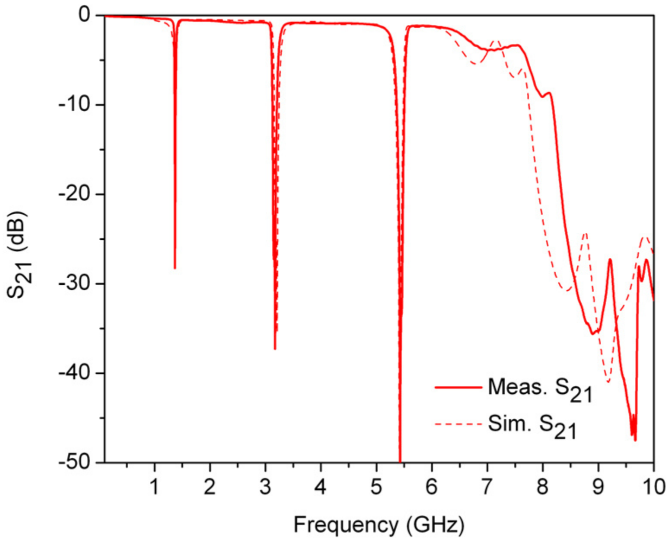

Fig. 4.13. Measured vs. simulated S_{21} response of the cascade circuit when it is configured to produce three 2-pole maximum attenuation responses. (static measurement).

10 dB fractional bandwidth (FBW) of 1.11% at 1.41 GHz, 2.70% at 3.2 GHz, and 2.57% at 5.41 GHz. The measured passband insertion loss was 0.065 dB at 100 MHz, 0.52 dB at 2 GHz, 0.88 dB at 4 GHz, 1.29 dB at 6 GHz, and 2 dB at 6.5 GHz.

Fig. 4.14 shows the six resonators tuned to independent frequencies, displaying the complete 1-pole coverage range of the bandstop filter cascade. The measured frequency tuning range of each resonator can be seen in Fig. 4.15. The tuning ranges in Fig. 4.15 result in frequency overlap ranges covered by multi-pole responses that can be designed to be in regions of expected interference. For example, the lower frequency range with 3- and 4-pole coverage is near long term evolution (∼1.6 and 2.0 GHz), cellular telephone (∼1.8 and 1.9 GHz), and ISM (∼2.4 GHz) signals, while the upper frequency range with 3- and 4-pole coverage operates in a common weather and aviation radar band (∼3.1 - 3.6 GHz). Fig. 4.16 shows the 2-pole coverage range of the cascade circuit, which is 1.03 to 6.4 GHz. Greater than 25 dB of attenuation is shown from 1.5 to 6.4 GHz. The bandwidth changes across the band from 1.0 to 4.8% 10 dB FBW due to the change in electrical length of the coupling apertures across

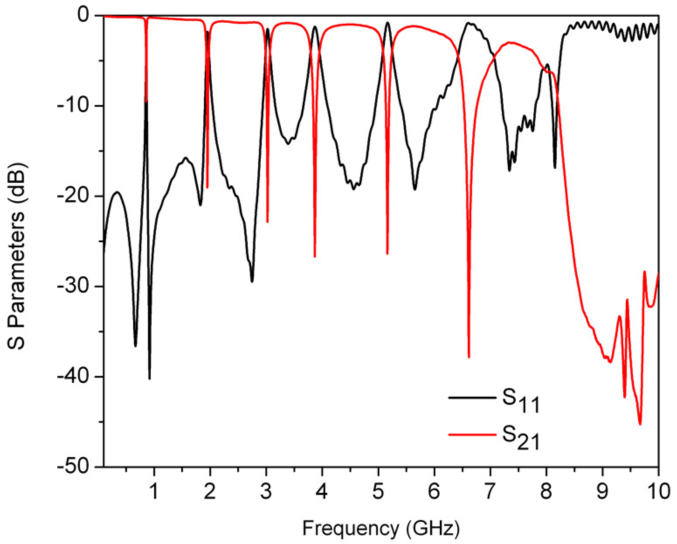

Fig. 4.14. Bandstop filter cascade circuit measured with all six resonators tuned to independent frequencies, showing the entire 1-pole coverage range. (static measurement).

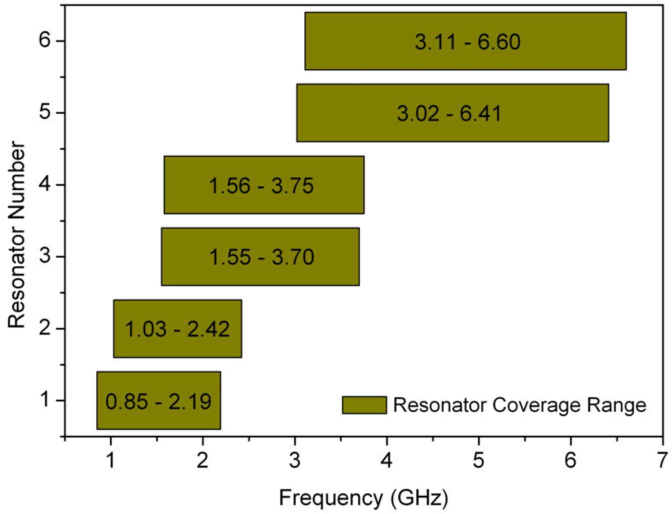

Fig. 4.15. Measured individual resonator tuning ranges.

the band. Fig. 4.17 shows the 4-pole coverage ranges of the cascade circuit, which are 1.56 to 2.19 GHz and 3.11 to 3.70 GHz. In these regions, multiple filter shapes are possible due to the widely tuning resonators. Fig. 4.17 shows a Butterworth-

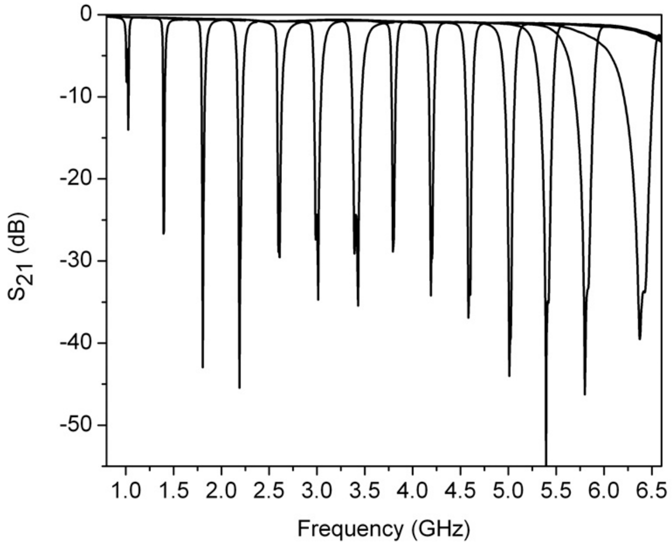

Fig. 4.16. Measured superimposed S_{21} responses showing continuous 2-pole coverage from 1.03 to 6.4 GHz. (tuning measurement).

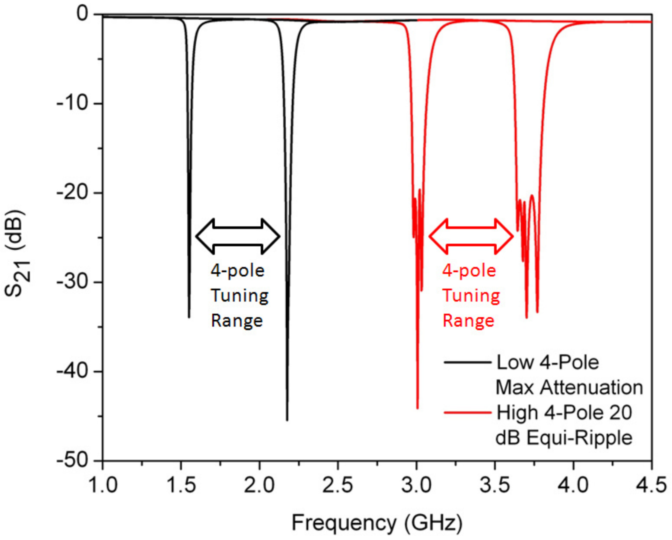

Fig. 4.17. Measured superimposed S_{21} responses showing the bandstop filter cascade circuit's measured tuning ranges in the 4-pole overlap frequency ranges. (tuning measurement).

like shape in the lower frequency 4-pole coverage range and a 20 dB equi-ripple shape in the higher frequency 4-pole coverage range. Any filter shape between the two shown, as well as split filter shapes such as two independent 2-pole filters, are

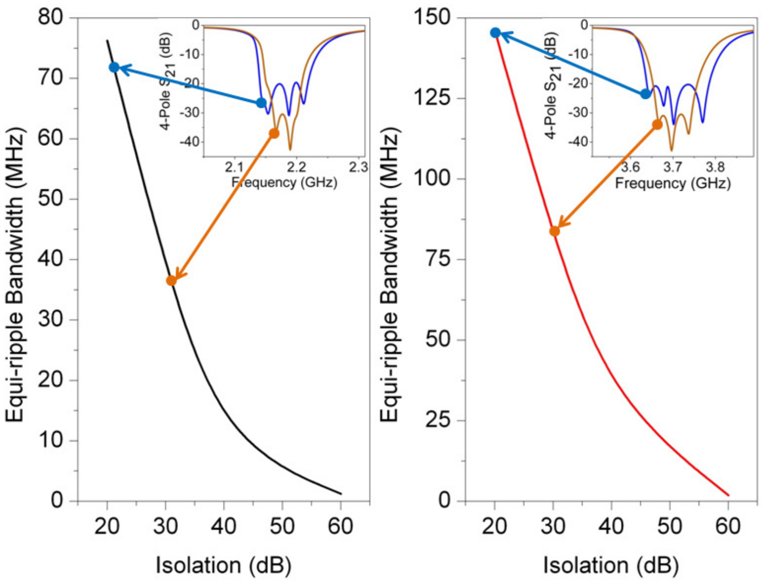

Fig. 4.18. Measured bandwidth vs. equi-ripple attenuation for different shapes of the 4-pole filter responses. Insets show examples of 20 and 30 dB levels of attenuation for the 4-pole overlap regions of the spectrum.

possible within a 4-pole coverage range. This shape reconfigurability allows a dynamic trade-off between bandwidth, attenuation level, and number of attenuated bands in the response. Measured results for the trade-off between bandwidth and equi-ripple attenuation for two frequency tunings of the 4-pole filter responses shown in Fig. 4.17 can be seen in Fig. 4.18. Examples of more of the possible filter shapes were shown in [54]. Combined with the wide passband and tuning ranges demonstrated in this chapter, this high level of filter shape reconfigurability enables unprecedented microwave system robustness in dynamic, noisy environments.

4.6 Ultra-Wide Upper Passband Bandstop Filters

While a 7.8 to 1 upper passband was obtained from the work described earlier in this chapter, some systems operate over an even wider frequency range. In addition, highly loaded coaxial cavities have been shown to have spurious free ranges of much more than 7.8 to 1 [55], so it would be valuable to determine a method and coupling structure that allows for even wider upper passbands. The challenge of designing such a structure is that energy must be coupled into the filter's resonators appropriately for the desired fractional bandwidth Δ and ratio of the resonator impedance Z_r to the system impedance Z_0 without creating a large impedance mismatch between the coupling structure impedance Z_C and Z_0. These concepts are shown in Fig. 4.19. This section presents a new coupling structure for highly-loaded coaxial cavity resonators that is well matched to the system impedance and enables a 17-to-1 upper passband ratio without strongly affecting their tuning range or quality factor, which is a 118% improvement of the state-of-the-art.

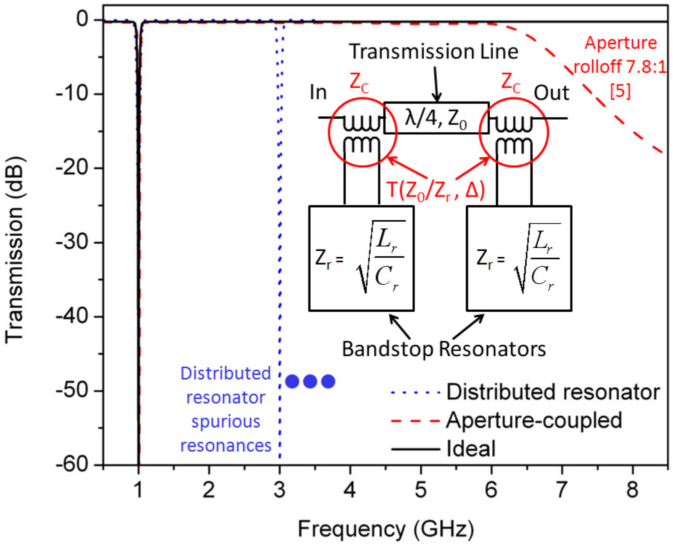

Fig. 4.19. Bandstop responses and common limiting factors of their upper passbands. Inset shows a schematic of a 2-pole bandstop filter. The coupling structure transformation ratio (T) depends on the ratio of the system impedance (Z_0) to the resonator impedance (Z_r), as well as the desired fractional bandwidth (Δ). With sufficient resonator spurious-free range, the upper passband is limited by the impedance mismatch between the coupling structure impedance (Z_C) and Z_0.

A two-pole, highly-loaded coaxial cavity resonator bandstop filter was designed to be tunable around a frequency of 1 GHz, and a model of the filter can be seen in Fig. 4.20. In contrast to previous filters that use these resonators, this design

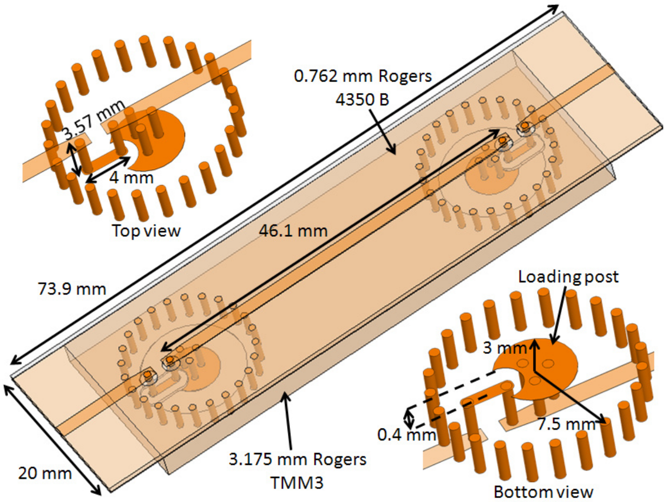

Fig. 4.20. Fabricated 2-pole filter structure. Top and bottom views of the external coupling structure are shown for clarity.

incorporates a ’U’ shaped external coupling structure that can be seen in Fig. 4.20. The structure couples the magnetic field of the source-to-load microstrip transmission line to the magnetic field of the cavity resonator and is formed by routing the source-to-load transmission line through the cavity. The structure can be designed to be well-matched up to relatively high frequencies, which produces a wide upper passband. The vertical sections of the coupling structure are made using 0.8 mm diameter plated vias that extend from the source-to-load microstrip line into the cavity resonator. Small apertures are cut into the microstrip line ground plane so that the vias are not shorted to ground. The horizontal part of the structure is a plate of copper offset in height from the loading post. The width of the copper plate, as well as the height offset from the loading post, allow it to be designed to act like a short section of microstrip transmission line that is matched to the system impedance. In the fabricated filter, the width of the horizontal section is 1 mm, the length is 4 mm, and the height offset from the loading post is 0.4 mm. In Rogers TMM3 material, this produces an approximately 50 ohm transmission line with an electrical length of approximately 7.8 degrees at 1 GHz.

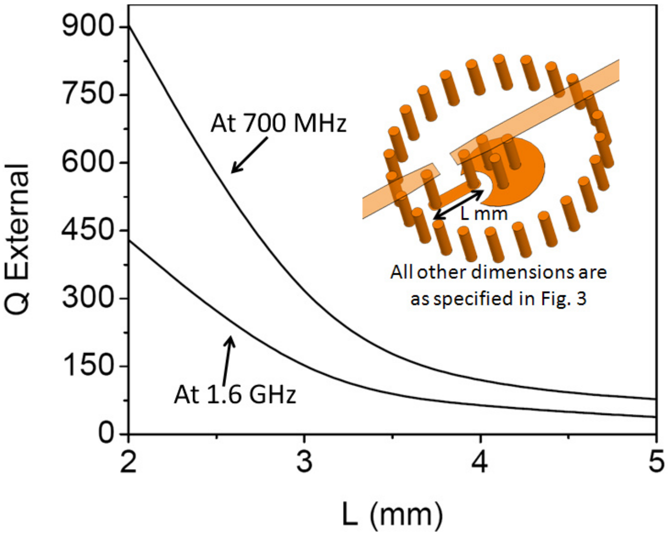

Fig. 4.21. Simulated external quality factor vs. coupling structure length.

The amount of coupling can be designed by adjusting the length of the horizontal part of the structure. The external quality factor (Q external) vs. the length of the horizontal part of the structure (L) can be seen in Fig. 4.21 for the design shown in Fig. 4.20. The external quality factors available in this particular design are relatively high, providing the ability to realize only narrowband bandstop filters. The challenge of getting Q external low enough to make wider and deeper bandstop filters is the difference between the system characteristic impedance and the resonator characteristic impedance. A 50 ohm system impedance was used in this design. However, the highly-loaded coaxial cavity resonators used in this design have a simulated characteristic impedance as low as 5.4 ohms due to the large amount of capacitive loading needed for a wide tuning range, which makes the required transformation ratio for a desired bandwidth filter very high and the challenge of low out-of-band reactance difficult.

It can be seen in Fig. 4.20 that the source-to-load transmission line substrate, which is 0.762 mm thick Rogers 4350B material (ϵ_r=3.66, tan(δ)=0.0037 @ 10 GHz), extends beyond the cavity substrate, which is 3.175 mm thick Rogers TMM3 material

(ϵ_r=3.27, tan(δ)=0.002 @ 10 GHz). This was done for better grounding of the SMA end-launch connectors and would not be part of an integrated design.

4.7 Measured Results II

Measured vs. simulated S_{11} and S_{21} responses can be seen in Fig. 4.22 a). Fig. 4.22 a) shows a measured 654 MHz, 15 dB attenuation, 1.2% 3 dB fractional bandwidth bandstop filter with a passband that extends to the 3 dB insertion loss point at 11.1 GHz, corresponding to a 17-to-1 ratio between the upper passband cutoff frequency and the notch center frequency. Note that the coupling structure reactance is what causes the passband to degrade, and the next higher-order mode of the filter is significantly higher in frequency than the 3 dB rolloff point of the passband. The full-wave simulations in Fig. 4.22 b) show that the input impedance of the coupling structure and resonator is approximately 50 ohms until the cutoff frequency.

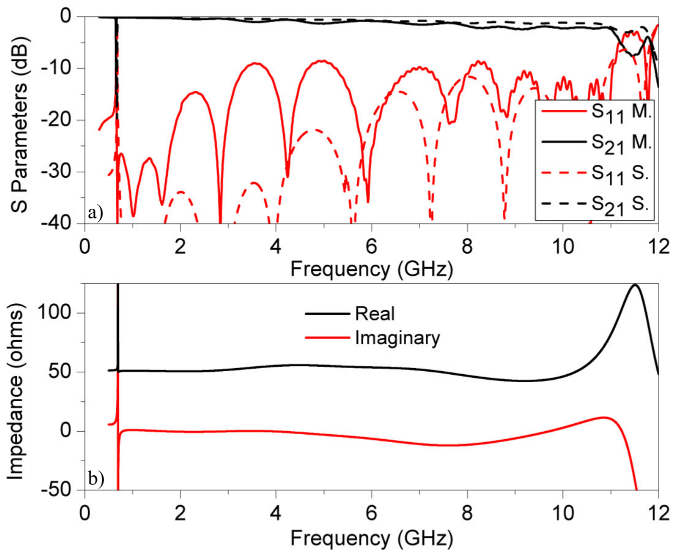

Fig. 4.22. a) Wideband simulated vs. measured results of the fabricated filter showing a 17-to-1 upper passband. S. = simulated, M. = measured. b) Simulated input impedance of coupling structure and resonator.

Agreement can be seen between measured and simulated results. However, the measured results have worse return loss than the simulated results and slight discrepancies with the simulated results in reflection zero location. This can be explained by inaccuracies in fabrication of the height of the coupling structure relative to the cavity loading post, mismatch at the coaxial-to-microstrip transition between SMA connectors and the filter that was not taken into account in calibration, and the extra length and loss due to the connectors.

Fig. 4.23 shows that the filter is tunable from 0.654 to 1.65 GHz while providing 15 dB to 35 dB of attenuation. The 3 dB fractional bandwidth varies from 1.2% to 3.2% across the tuning range. This tuning range makes the filter relevant for attenuating signals from television stations, cellular telephone towers, and LightSquared LTE [57] systems.

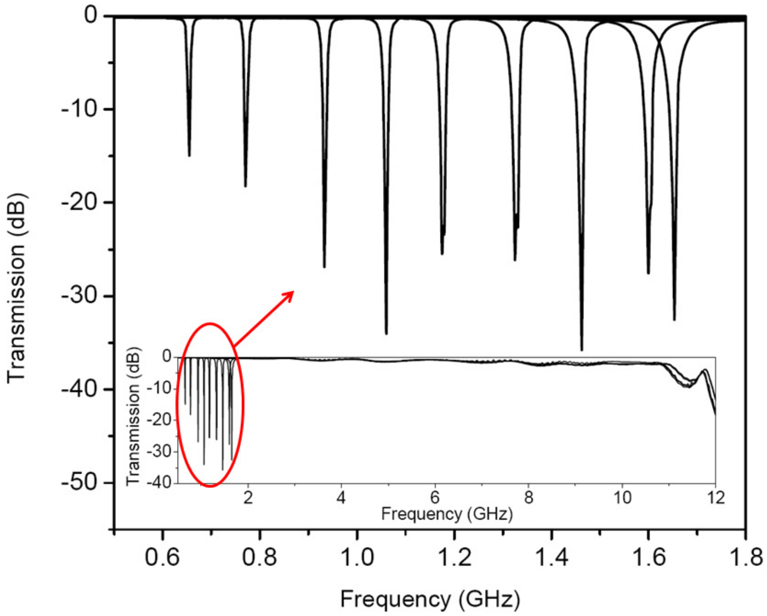

Fig. 4.23. Narrowband measured results of the fabricated filter showing the available tuning range. Inset shows wideband tuning measurement.

4.8 Conclusion

A method to increase the passband of aperture coupled cavity resonator bandstop filters was described which used resonances of the transmission lines between coupling apertures. A six-resonator bandstop filter cascade using this method was demonstrated, and a 7.8 to 1 upper passband was obtained. Continuous notch coverage of 0.85 to 6.6 GHz was achieved within the band. Enabled by the wide tuning ranges of evanescent-mode cavity resonators, the filter shapes and orders across the band could be tuned dynamically. These cascades can be modularly designed, with resonators of different frequency coverage ranges added to or subtracted from the circuit to trade off between attenuation level/response shape flexibility and passband insertion loss due to the length of the feeding transmission line. Bandstop filter cascades like the one demonstrated in this chapter are expected to be useful in systems that operate over wide frequency bands in spectral environments with dynamic interference.

A tunable bandstop filter with a 17-to-1 ratio between its upper passband roll-off frequency and its notch center frequency was also shown in this chapter. Such a wide upper passband will aid in the design of very wide coverage range bandstop filter cascades like the one shown in this chapter.

Cascades of bandpass and bandstop filters are also of interest to some systems. Bandpass-bandstop filter cascades provide the narrow passband of a typical bandpass filter with frequency ranges of very high isolation in the bandpass response's skirt due to the bandstop filters. However, since the bandpass filter is often not matched to the system impedance away from the passband, it is significantly harder to cascade a bandpass and bandstop filter than two bandstop filters because the bandstop filters are matched to the system impedance away from the notch response. Methods for properly designing tunable bandpass-bandstop filter cascades and practical limitations will be described in the next chapter.

4.9 Appendix: Coupling Aperture Parameter Extraction Formulas

The formulas for parameter extraction of the lumped element circle values in the model in Fig. 4.4 b) from measured or simulated S parameter results, originally derived in [56], are

$$C_i = \frac{1}{Z_0} \cdot \frac{1}{4\pi\Delta f_{3dB\_i}} \tag{4.4}$$

$$L_i = \frac{1}{(2\pi f_{0i})^2 C_i} \tag{4.5}$$

$$C_p = -\frac{1}{2\pi f_T X_{21}} \tag{4.6}$$

$$L_{si} = \frac{X_{ii} - X_{21}}{2\pi f_T} + \frac{L_i}{(\frac{f_T}{f_{0i}})^2 - 1} \tag{4.7}$$

where i = 1,2 to represent the first and second resonance of the coupling aperture, f_{01} is the center frequency of the first resonance of the coupling aperture, f_{02} is the center frequency of the second resonance of the coupling aperture, f_T is the frequency of the reflection minimum between the first and second resonance of the coupling aperture, Δf_{3dB_i} is the 3 dB bandwidth of the i^{th} resonance of the coupling aperture, and X_{ii} and X_{21} are the imaginary parts of three Z-parameters at f_T.

5. TUNABLE BANDPASS-BANDSTOP FILTER CASCADES FOR DYNAMIC HIGH ISOLATION BETWEEN ADJACENT BANDS

5.1 Introduction

The tunable bandstop filters described in the previous chapters would compliment wide bandwidth systems very well, allowing them to block dynamic, narrow bandwidth interfering signals while remaining open to the majority of the spectrum of interest. However, many systems are only interested in a narrow portion of the spectrum at any one instant in time, and they would ideally be able to block all other frequencies with infinite attenuation. The narrow band of interest may change in frequency over time, and infinite attenuation is not practical. However, as cognitive or spectrally aware radio architectures are advanced, they will become capable of determining the location of interfering signals in the spectrum that have the highest chance of saturating a receiver. Therefore, tunable, targeted, and deep transmission nulls are highly desirable in the stopband of the receiver's narrowband bandpass filter response to remove the interfering signals and eliminate nonlinearities in the receive chain. When such nulls are combined with a tunable passband response, the band of interest can be received with low loss while strong interfering signals are strongly attenuated. In contrast, a non-cognitive radio has to have the sharpest filter skirts possible by using as many poles in the filter response as allowed by the system because the location of the interference is undetermined. Such an approach adds often unnecessary insertion loss in the passband.

Dynamic, deep nulls in the spectrum, with 70 to 100 dB or more isolation, will allow for the possibility of simultaneous transmission and reception even in systems containing high power transmitters. Many current and future microwave applications would benefit from or even require these very high levels of isolation between certain, dynamic frequencies of interest. These applications include concurrent transmit-receive systems [58], shared antenna aperture systems [59], and co-site interference scenarios [60]. In some of these cases with high power transmitters, practical, tunable bandpass filters or bandstop filters alone cannot provide the isolation required for preventing self generated noise of a transmitter from leaking into the receiver path or even saturation of a receiver's low noise amplifier (LNA). Some cellular power amplifiers have output spectra with noise power that is only 50 dB down several MHz away from the edge of the bandwidth of the input signal [61]. Since such power amplifiers often output 33 dBm and the receive path is only further isolated from the transmit path by a diplexer that provides 50 dB isolation in some cases [62], noise leakage of -67 dBm or more is possible in an adjacent band, which is a significant amount of power compared to many wireless received signals. The result is a noisy receive signal or low resolution in a receivers analog-to-digital converter (ADC), and thus bit error rates (BER) that are higher than what is acceptable for the desired level of system performance. In order to attenuate the self generated noise below the -100 dBm level that is often approximately the noise floor in commercial silicon circuits, an additional 30 to 40 dB isolation is required. In order to obtain this level of isolation close to the passband, the system could employ a very high order bandpass filter or one with transmission zeros. However, these techniques add passband insertion loss or group delay variation. A Butterworth 0.5% 3 dB fractional bandwidth null with the required isolation could be created using resonators with a Q of 1200 that would not greatly increase passband insertion loss or group delay ripple by using a well designed cascade of bandpass and bandstop filters.

For example, it could be desired to have a high power, shared aperture antenna system that could transmit and receive at the same time on constantly varying frequency bands. Such a system could employ a tunable bandpass filter that tracks the receive band frequency. Many tunable bandpass filters that could be used in this case have been developed recently. Examples include filters with relatively high Q values that can tune over an octave [63] and others with reconfigurable shapes [64]. The widest-tuning bandpass filters are YIG (yttrium-iron-garnet) devices [65]. However, the high power signals involved could be too large for a bandpass filter to attenuate to a desired level, especially for a close transmit-receive band spacing. Conversely, the example system could use a tunable bandstop filter set the to receive band frequency range to attenuate the energy from the transmitter that is input to the receiver. Recent tunable bandstop filters are able to achieve up to 50 dB of attenuation [66], which could possibly reduce the power level difference between transmit and receive signals present at the LNA input to within the dynamic range of the system. However, using these bandstop filters will only enable the system to work well in a sparse spectrum without other interfering signals since it will not provide appreciable attenuation at frequencies other than the transmit frequency. Finally, the example shared aperture system could utilize an elliptic filter with a transmission null positioned at the transmitter frequency. However, implementing a tunable transmission null that is independent of the passband is difficult in elliptic filters, so the transmit frequency would have to be static, which is limiting.

A bandpass-bandstop filter cascade provides the benefits of all of the previously discussed filters, enabling the example shared aperture system to operate in most spectral environments. The frequency response of such a filter cascade using a second-order Butterworth bandpass filter and a second-order Butterworth bandstop filter can be seen in Fig. 5.1. Note that both the bandpass passband and bandstop stopband are independently tunable, so isolation on the order of 90 dB is possible between dynamic frequencies of interest. In this chapter, we show the capabilities of this filter system to demonstrate up to 120 dB of isolation when proper design rules are followed, but also that unwanted peaks will be generated in the frequency response that exacerbate the interference problem if the design rules are not followed. This potential for causing more harm than good by including the bandstop filter has not been described previously, and it is important to understand for the operation of widely tunable filters in cascade circuits. Before discussing these results and design rules, a

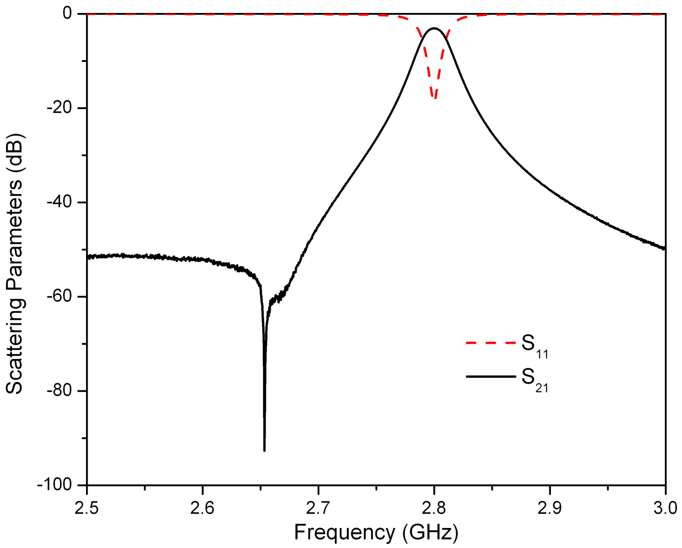

Fig. 5.1. Measured response of a tunable second-order bandpass filter cascaded with a tunable second-order bandstop filter. This cascade circuit allows high, dynamic isolation between two frequencies of interest.

novel bandstop filter design that will be used in measurement setups is presented in the next section.

5.2 Variable Bandwidth Bandstop Filter Design and Initial Filter Cascade Measurements

5.2.1 Variable Bandwidth Bandstop Filter Design

The proposed bandstop filter design and equivalent lumped element circuit are shown in Fig. 5.2. The shunt cavity resonators are coupled to using a varactor loaded transmission line, which will be called the inter-resonator transmission line to separate it from the inter-filter transmission line that is between the bandpass and bandstop filters in the cascade circuit to be shown. The high Q resonators are designed in 3.175 mm thick Rogers TMM3 substrate and defined by vias. The resonators capacitive posts are covered with a 1 μm layer of Parylene-N from Specialty Coating Systems to prevent shorting of the capacitor plates. A 0.38 mm thick commercially available

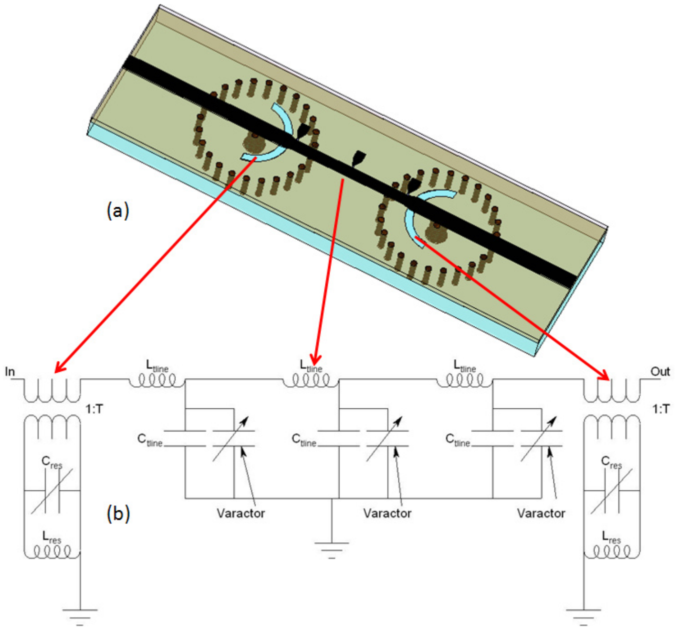

Fig. 5.2. a) 3-D layout of proposed bandstop filter. b) Equivalent circuit with lumped element transmission line approximation.

piezoelectric actuator from Piezo Systems Inc. is attached to the copper membrane to allow for frequency tuning. High resonator Q values in bandstop filters allow for deeper notches for a given bandwidth and less insertion loss in the pass band. The measured Q value for the resonators used in this design is 757 at 2.85 GHz.

The geometry of the slots in the ground plane for external coupling into the resonators was chosen to be semi-circular to align to the magnetic field pattern of the first mode of the resonator while minimizing the perturbation to the microstrip line. The size of the slots was chosen to achieve the transformer ratio that results in the desired bandwidth for a given post size that maximizes the resonator Q [67]. Ansoft HFSS and Agilent ADS software was used to find the optimal slot size, setting the transformer ratio such that the external Q is:

$$Q_{ext} = \frac{R}{\omega_0 L} = \frac{Z_0}{\omega_0 L T^2} = \frac{50}{\omega_0 (1.182 \times 10^{-9})(0.205^2)} = \frac{1.0 \times 10^{12}}{\omega_0}, \tag{5.1}$$

where T is the transformer ratio created by the slot in the ground plane.

The inter-resonator transmission line was fabricated using 0.787 mm thick Rogers Duroid 5880 material and laminated to the resonators. The length of the inter-resonator transmission line was chosen to be a quarter wavelength impedance transformer at the upper end of the tunable range. Therefore, the impedance transformer is a quarter wavelength or less over the tunable frequency range. As shown in [68], the resonators load the through line and the rate of change of their reactance is greater on the high frequency side of the notch than the low frequency side, producing asymmetry in the response. Shortening the transformer from its nominal quarter wavelength is a common way to mitigate this asymmetry.

The impedance of the inter-resonator transmission line impedance transformer was increased to a value of 66 ohms. This was done to reduce the nominal capacitance of the line because it is capacitively loaded with three varactors in order to tune the bandwidth of the filter. When transforming the first resonator of a low pass filter prototype to a parallel bandstop configuration, the bandwidth can be specified in terms of the inductance as [24]:

$$\Delta = \frac{\omega_0 L}{g_1 Z_0}, \tag{5.2}$$

where g_1 is the filter coefficient for a low pass filter proto-type and Δ is the fractional bandwidth of the filter. A similar expression can be derived in terms of the capacitance of the resonator that shows the same inverse relationship to system characteristic impedance. As seen in Fig. 5.2, these varactors can be thought of as an additional shunt capacitor in the lumped element equivalent of the inter-resonator transmission line. As the varactor capacitance is increased, the capacitance of the inter-resonator transmission line increases, decreasing its characteristic impedance and thus increasing the fractional bandwidth of the filter. The response of the filter away from the notch frequency degrades with increasing loading because of worsening return loss, so the value of 66 ohms was chosen as a trade-off between the out of band reflection and the bandwidth tuning range. A Microsemi MV20001-150A varactor with low absolute capacitance and high capacitance tuning range (0.15 pF-0.5 pF) was used as a loading element.

5.2.2 Initial Measured Results

Measured results showing the bandpass filter from [64] being tuned about the bandstop filter described in the above section when it is tuned to a static frequency are shown in Fig. 5.3. This would represent the case where the receive band is searching for a signal in the presence of a fixed interferer. Measured results showing the bandstop filter being tuned about a fixed bandpass filter are shown in Fig. 5.4, representing the case when an interferer is hopping through the spectrum around a fixed receive band. These plots show that isolation of 70-90 dB is possible between two spectrally close frequencies of interest over the 2.3 to 3.0 GHz band. Fig. 5.5 compares the cascaded result to the response of a simple two pole bandpass filter, showing the deep notch in the spectrum comes at the expense of 0.7 dB extra insertion loss in the pass band. The total pass band insertion loss of the four resonator chain increases to 3.4 dB. Fig. 5.6 a) shows that the bandpass and bandstop filters can be tuned within 55 MHz of one another around 2.63 GHz (2.1%). In Fig. 5.6 a), the bandpass filter is tuned to 2.595 GHz and the bandstop filter is tuned to 2.650 GHz. The bandpass filter insertion loss increases from 3.4 dB to 4.9 dB at this 2.1% spacing

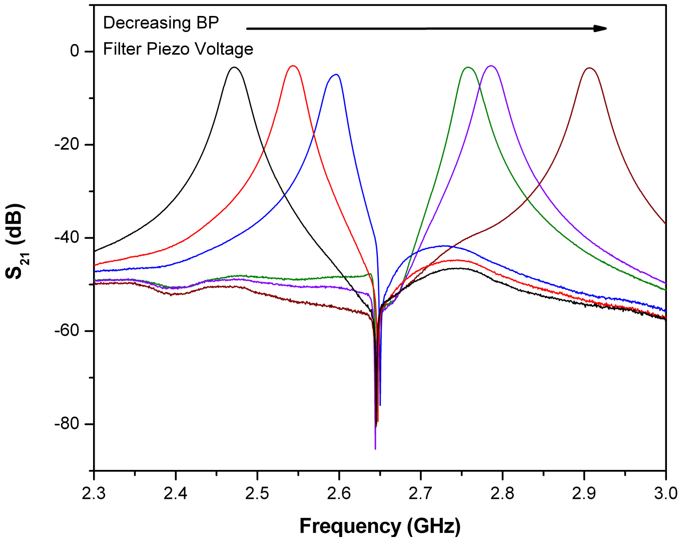

Fig. 5.3. Bandpass filter being tuned around a bandstop filter, useful in a situation with a constant interferer.

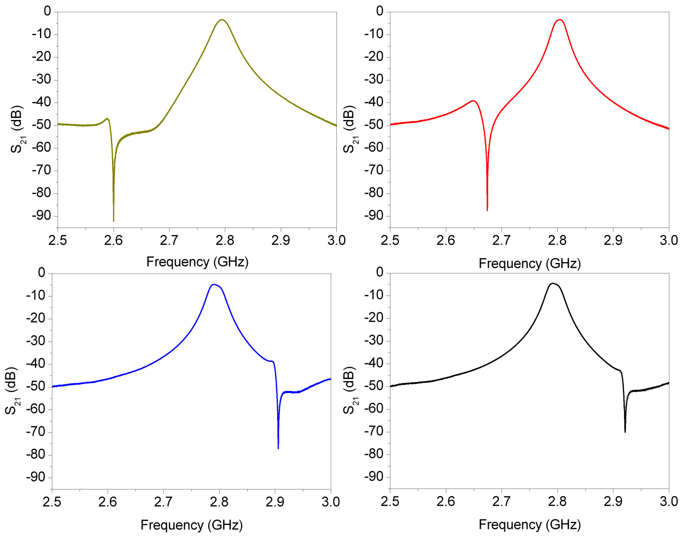

Fig. 5.4. Bandstop filter being tuned around a bandpass filter, useful in a situation with a hopping interferer.

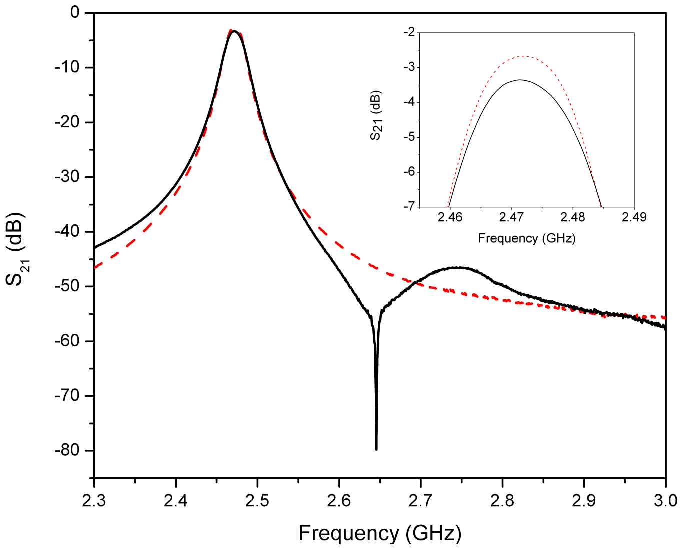

Fig. 5.5. Comparison of bandpass filter response (red dotted line) with response of cascaded bandpass and bandstop filters (solid black line).

and degrades further at lower spacings. Using the varactors on the inter-resonator transmission line, the bandstop filters -20 dB bandwidth was tunable with a width of 24.5 MHz to 41.0 MHz centered at 2.625 GHz using a varactor voltage range of 0 V to

5 V. A system of this configuration also presents many other useful possibilities. For example, while the filter cascade is designed to allow a two pole notch response on the skirt of a bandpass filter, the poles of the bandstop filter can be tuned to different frequencies to create notches at varying positions in the spectrum. Fig. 5.6 b) shows measured results of a tunable two pole bandpass filter cascaded with a tunable two pole bandstop filter where the two poles of the bandstop filter have been tuned to create dual notches about the bandpass filter pass band, resulting in a quasi-elliptic filter response for the entire circuit.

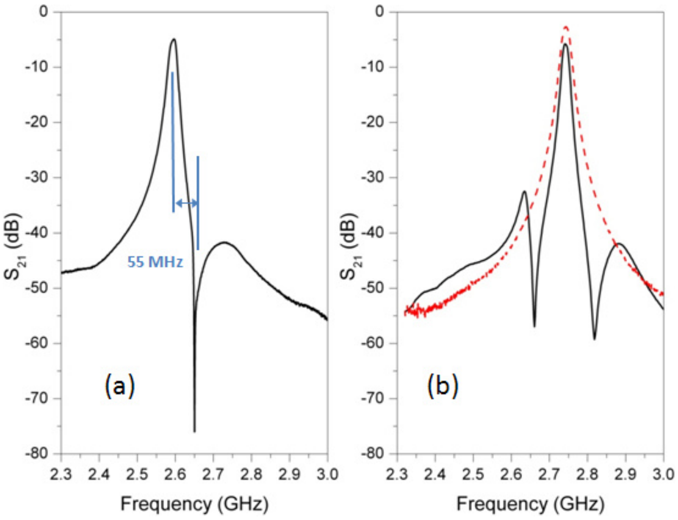

Fig. 5.6. a) Bandstop filter tuned within 55MHz of bandpass filter with minimal effect on bandpass filter insertion loss. b) Comparison of bandpass filter response (dashed red line) to response when bandstop poles are tuned to different frequencies about the bandpass response (solid black line).

5.3 Bandpass-Bandstop Filter Cascade Performance Over Wide Frequency Tuning Ranges

While the concept of a bandpass-bandstop filter cascade was shown in the previous section, the theoretical limitations of such a circuit were not analyzed. This section contains analysis of the theoretical limitations of bandpass-bandstop filter cascades over wide frequency tuning ranges.

5.3.1 Bandpass-Bandstop Filter Cascade Theory

General Coupling Matrix Model

For simplicity, a single bandpass filter in series with a single bandstop filter, both of second-order, will be analyzed. However, this method could be extended to higher-order filter cascades, with the only trade-off being more complicated equations. The filters will be connected using a transmission line of a certain length and characteristic impedance equal to the system characteristic impedance. An example of two of the possible coupling diagrams for the total circuit can be seen in Fig. 5.7.

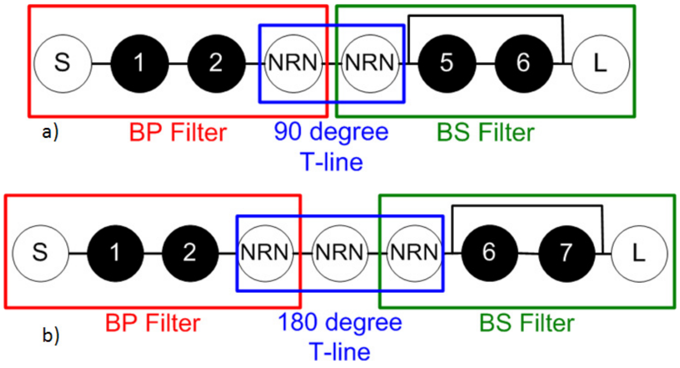

Fig. 5.7. Bandpass-bandstop filter cascade coupling diagrams. a) Bandpass filter connected to bandstop filter with 90 degree transmission line represented by the connection between two non-resonating nodes (NRN). b) Bandpass filter connected to bandstop filter with 180 degree transmission line represented by the connections between three NRNs.

For the second-order filter analysis in this chapter, both external coupling values will be equal to each other and symmetries such as the source-to-load coupling being the same as the load-to-source coupling can be taken advantage of to simplify the generalized second-order filter (N+2)x(N+2) coupling matrix M as

$$\begin{bmatrix} 0 & M_{0,1} & 0 & M_{0,3} \\ M_{0,1} & M_{1,1} & M_{1,2} & 0 \\ 0 & M_{1,2} & M_{2,2} & M_{0,1} \\ M_{0,3} & 0 & M_{0,1} & 0 \end{bmatrix}, \tag{5.3}$$

where the subscripts 0 and 3 correspond to the source and load, respectively, and subscripts 1 and 2 correspond to the first and second resonator, respectively.

It can be shown with coupling matrix methods [69] that the coupling matrix for a typical second-order 20 dB equi-ripple Chebychev bandpass filter is

$$\begin{bmatrix} 0 & 1.225 & 0 & 0 \\ 1.225 & 0 & 1.658 & 0 \\ 0 & 1.658 & 0 & 1.225 \\ 0 & 0 & 1.225 & 0 \end{bmatrix}, \tag{5.4}$$

and the coupling matrix for a second-order Butterworth bandstop filter is

$$\begin{bmatrix} 0 & 1.189 & 0 & 1 \\ 1.189 & 0 & 0 & 0 \\ 0 & 0 & 0 & 1.189 \\ 1 & 0 & 1.189 & 0 \end{bmatrix}. \tag{5.5}$$

These coupling matrices can be combined [70], along with non-resonating nodes (NRNs) that allow representation of a ninety degree inter-filter transmission line through their coupling mechanism, into the color-coded and line type segregated matrix in Fig 5.8 a). The color coding and line type corresponds to the component outlines in Fig. 5.7, where red solid represents the bandpass filter, blue dashed represents the ninety degree inter-filter transmission line, and green dotted represents the bandstop filter. α and γ represent scaling factors that allow the bandpass filter to have a different bandwidth than the bandstop filter, as only one frequency transformation can be used in the general coupling matrix method. Also, M_{11} represents

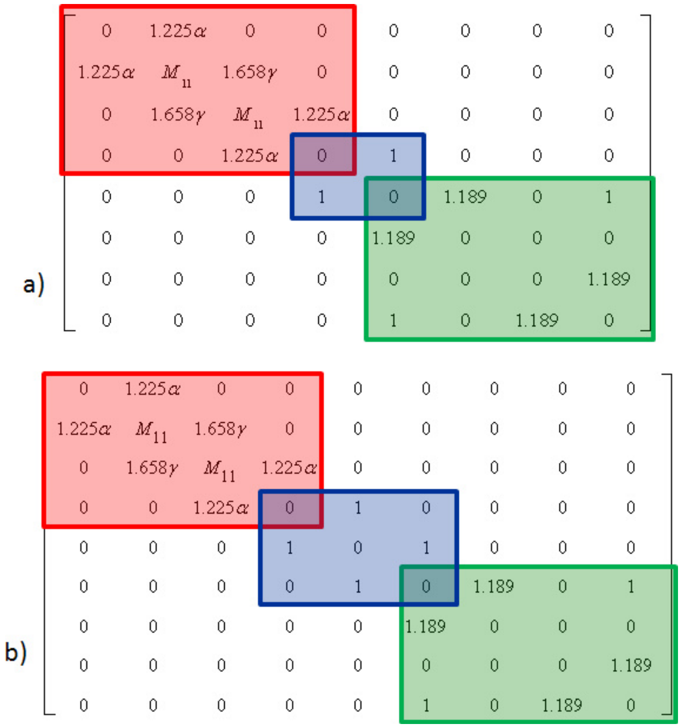

$$\begin{bmatrix} 0 & 1.225\alpha & 0 & 0 & 0 & 0 & 0 & 0 \\ 1.225\alpha & M_{11} & 1.658\gamma & 0 & 0 & 0 & 0 & 0 \\ 0 & 1.658\gamma & M_{11} & 1.225\alpha & 0 & 0 & 0 & 0 \\ 0 & 0 & 1.225\alpha & 0 & 1 & 0 & 0 & 0 \\ 0 & 0 & 0 & 1 & 0 & 1.189 & 0 & 1 \\ 0 & 0 & 0 & 0 & 1.189 & 0 & 0 & 0 \\ 0 & 0 & 0 & 0 & 0 & 0 & 0 & 1.189 \\ 0 & 0 & 0 & 0 & 1 & 0 & 1.189 & 0 \end{bmatrix}$$

$$\begin{bmatrix} 0 & 1.225\alpha & 0 & 0 & 0 & 0 & 0 & 0 & 0 \\ 1.225\alpha & M_{11} & 1.658\gamma & 0 & 0 & 0 & 0 & 0 & 0 \\ 0 & 1.658\gamma & M_{11} & 1.225\alpha & 0 & 0 & 0 & 0 & 0 \\ 0 & 0 & 1.225\alpha & 0 & 1 & 0 & 0 & 0 & 0 \\ 0 & 0 & 0 & 1 & 0 & 1 & 0 & 0 & 0 \\ 0 & 0 & 0 & 0 & 1 & 0 & 1.189 & 0 & 1 \\ 0 & 0 & 0 & 0 & 0 & 1.189 & 0 & 0 & 0 \\ 0 & 0 & 0 & 0 & 0 & 0 & 0 & 0 & 1.189 \\ 0 & 0 & 0 & 0 & 0 & 1 & 0 & 1.189 & 0 \end{bmatrix}$$

Fig. 5.8. a) Coupling matrix for 2-pole bandpass filter in series with a 2-pole bandstop filter, connected with a 90 degree transmission line. b) Coupling matrix for 2-pole bandpass filter in series with a 2-pole bandstop filter, connected with a 180 degree transmission line.

the frequency offset of the bandpass filter from the bandstop filter, where the bandstop filter is centered at 0 rad/s in the normalized frequency domain low pass filter prototype. Since the bandpass filter is synchronously tuned, $M_{22} = M_{11}$.

The frequency response in Fig. 5.9 results from the coupling matrix in Fig. 5.8 a). It can be seen that an unwanted peak appears at the bandstop filter frequency of operation, resulting in a reduction of attenuation of the undesired signal compared to using a bandpass filter alone. This unwanted peak is the result of a resonance created by the inter-filter transmission line. It can be understood by cutting the connection between the filters and the inter-filter transmission line at the filter ports and looking at the phase of the bandpass output impedance and the phase of the bandstop input impedance. This concept is shown graphically in the real frequency domain in Fig. 5.10. Fig. 5.10 shows a bandpass filter centered at 3 GHz and a

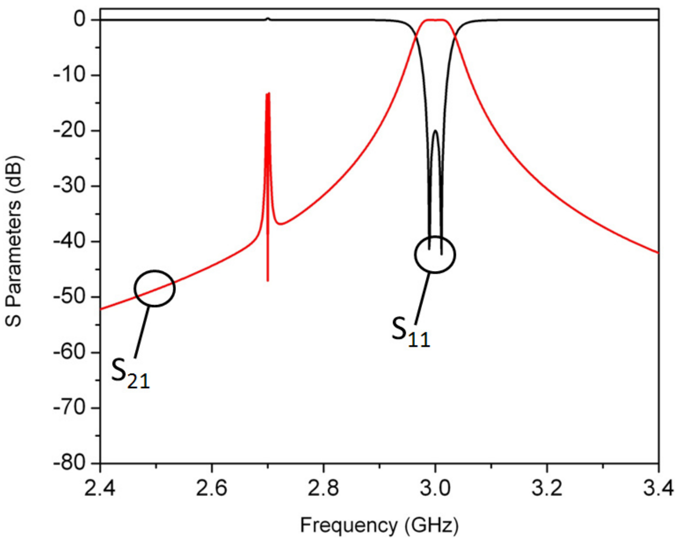

Fig. 5.9. Analytical response with unwanted peak that can result from improper design of a bandpass-bandstop filter cascade circuit. Reduction of attenuation at the bandstop filter frequency compared to using the bandpass filter alone is seen.

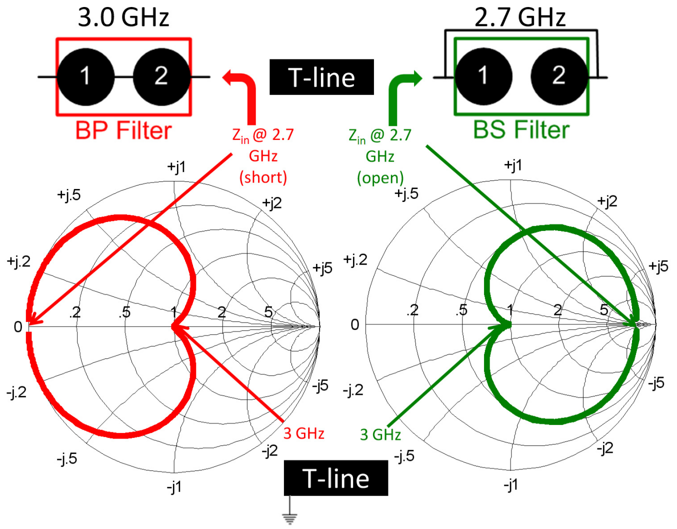

Fig. 5.10. Explanation of the unwanted peak seen in Fig. 5.9.

bandstop filter centered at 2.7 GHz. It can be seen that for a bandpass filter with parallel resonators, the phase response at 2.7 GHz (the bandstop filter frequency of operation) approaches that of a short circuit as the frequency decreases away from the passband. Similarly, it can be seen that for a bandstop filter with parallel resonators, the phase response at 2.7 GHz approaches that of an open circuit. This results in the inter-filter transmission line being terminated in an approximate short circuit on one side and an approximate open circuit on the other. When the electrical length is ninety degrees long at the bandstop filter frequency of operation, the inter-filter transmission line acts as a planar transmission line resonator.

The unwanted peak at the bandstop frequency of operation can be removed by changing the electrical length of the inter-filter transmission line. For example, the circuit in Fig. 5.7 b) employs a 180 degree transmission line, and it can be represented by the coupling matrix in Fig. 5.8 b), where the same color-coding and line type as in Fig. 5.8 a) applies. The frequency response in Fig. 5.11 results from the coupling matrix in Fig. 5.8 b). Note that the desired response is achieved, and the unwanted peak at the bandstop filter frequency of operation is gone. The coupling matrix model above shows that bandpass-bandstop cascade circuits will provide the desired response only if the filters are connected with the correct length of transmission line, which is

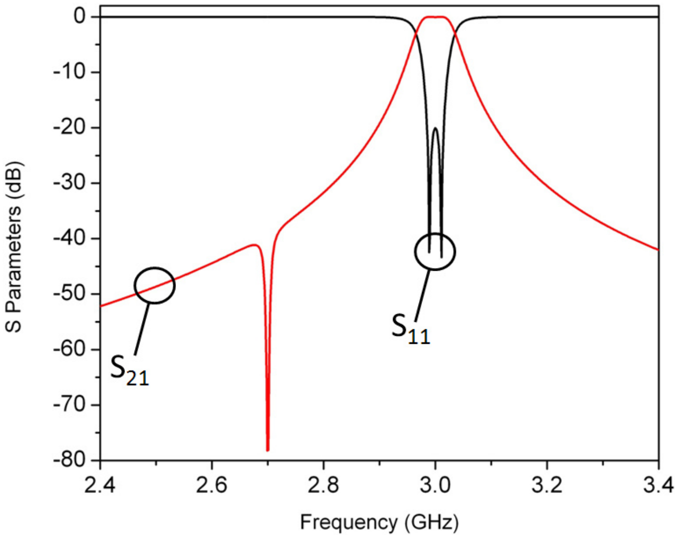

Fig. 5.11. Analytical response that can result from proper design of a bandpass-bandstop filter cascade circuit. An increase in attenuation at the bandstop filter frequency is seen compared to using the bandpass filter alone.

equivalent to saying that the circuits will only work if the filters are tuned to certain frequencies. This is limiting in a widely tunable system. In addition, the coupling matrix model assumes that the coupling values for the filters do not change when the filters are tuned over a wide frequency range. In practice, it is very difficult to fabricate a widely tunable filter with static coupling relationships. For this reason, the combined sub-matrix method discussed above is only an approximation that can be used to obtain estimations quickly. In order to determine the potential performance of a bandpass-bandstop filter cascade as it is tuned over a wide frequency range, a model that includes the length of the inter-filter transmission line as a parameter is needed. An ABCD matrix model of the circuit will accomplish this, as well as verify the estimation capability of the general coupling matrix model discussed above.

ABCD Matrix Model

The scattering (S) parameters of the bandpass filter and bandstop filter can be solved from their individual general coupling matrix models through standard methods [25]. The S parameters of the two filters can be converted to ABCD parameters, and the ABCD parameters of a transmission line are readily known [24]. The ABCD parameters of a transmission line are

$$\begin{bmatrix} cos(\beta\ell) & jZ_0 sin\beta\ell \\ \frac{jsin\beta\ell}{Z_0} & cos\beta\ell \end{bmatrix}, \tag{5.6}$$

where $\beta = 2\pi f/c$, f is frequency, c is the speed of light, ℓ is the physical length of the transmission line, and Z_0 is the characteristic impedance of the transmission line.

Note that (5.6) includes the length of the transmission line as a parameter that can be continuously varied. The three ABCD matrices for the bandpass filter, the inter-filter transmission line, and the bandstop filter can be matrix multiplied to obtain an ABCD matrix for the entire cascade circuit. Finally, the cascade ABCD matrix can be converted to an S parameter matrix for the entire cascade circuit that has the length of the inter-filter transmission line as well as the bandstop frequency of operation (through β) as continuously tunable parameters. This model can be used to determine the range of inter-filter transmission line electrical lengths over which acceptable performance is achieved. For example, if acceptable performance is defined as being within 20 dB of the maximum level of isolation that the bandpass-bandstop filter cascade circuit can produce, the circuit will meet specification as long as the inter-filter transmission line electrical length is between 99 and 261 degrees (or integer multiples). This can be seen graphically in Fig. 5.12. Frequency responses from the ABCD matrix model for thirty-two evenly spaced bandstop filter tuning frequencies are shown superimposed in Fig. 5.13. Fig. 5.13 is drawn with an inter-filter transmission line length of 46 mm and a relative dielectric constant of 2.1 to model the physical structure that will be described in the measured results section below. The largest increase in isolation (for parallel bandpass resonators and parallel bandstop resonators) is achieved with an inter-filter transmission line that is 180 degrees in electrical length at the bandstop filter frequency of operation, which corresponds to

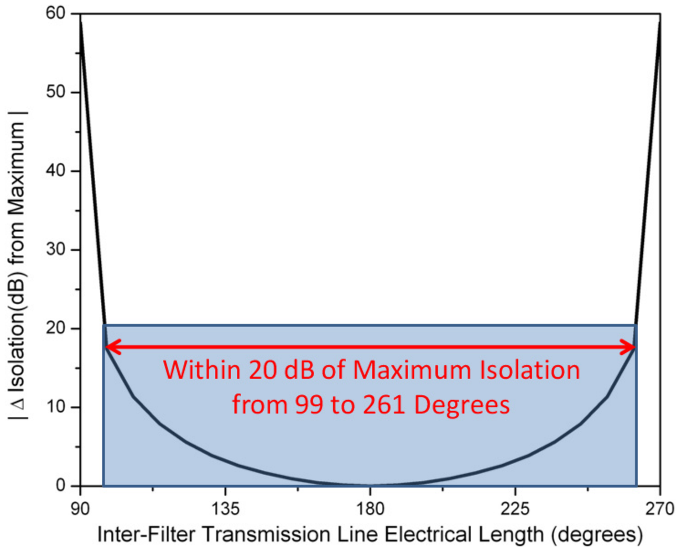

Fig. 5.12. Analytical results showing the range of inter-filter transmission line electrical lengths for which the bandpass-bandstop filter cascade circuit can provide within 20 dB of its maximum isolation level, which in this case occurs for an inter-filter transmission line electrical length of 180 degrees.

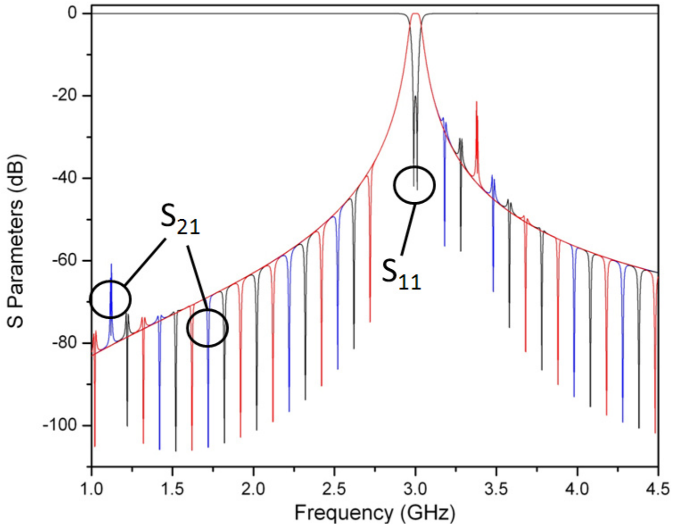

Fig. 5.13. Analytical response of bandstop filter being tuned about a static 3.0 GHz bandpass filter. Note the unwanted peaks seen at 1.12 and 3.36 GHz. These frequencies correspond to when the inter-filter transmission line is 90 and 270 degrees, respectively. Also note that the S_{11} is plotted for all 32 instances of the frequency response and that it stays at a constant 20 dB equi-ripple level as the bandstop filter is tuned about the bandpass filter.

2.24 GHz in Fig. 5.13. As the bandstop filter tunes and thus the electrical length of the transmission line at the bandstop filter frequency changes, the response slowly progresses toward the worst performance configuration, which can be seen at 1.12 GHz and 3.36 GHz in Fig. 5.13. These frequencies correspond to where the inter-filter transmission line is 90 and 270 degrees long, respectively. However, the takeaway from Fig. 5.13 is that good cascade circuit performance (high isolation) is possible over a wide variation in electrical lengths. This implies that dynamic, high isolation is possible over a wide frequency tuning range, beyond an octave.

Further Reconfigurability Through Bandstop Filter Shape Tuning

Many bandstop filters have been presented that have adjustable characteristics beyond being tunable in frequency. Some have a tunable level of attenuation [34], and others have constant bandwidth over wide tuning ranges [71]. All of this reconfigurability can be used in a bandpass-bandstop filter cascade to aid in blocking dynamic interference. Recently, a bandstop filter with the capability to tune its shape from a Butterworth to Chebychev response was proposed [36]. This second-order bandstop filter uses a non-zero inter-resonator coupling value and asymmetric tuning of the self coupling of its resonators to achieve its shape reconfiguring capability. A certain combination of inter-resonator coupling and resonator self-coupling values achieves a Butterworth response. A Chebychev response can be obtained from this Butterworth response merely by tuning the self coupling of the resonators. For example, a Butterworth bandstop filter is represented by (eq6-7)

$$\begin{bmatrix} 0 & 1.189 & 0 & 1 \\ 1.189 & 0.6663 & 0.9428 & 0 \\ 0 & 0.9428 & -0.6663 & 1.189 \\ 1 & 0 & 1.189 & 0 \end{bmatrix}, \tag{5.7}$$

where $M_{22} = -M_{11}$ here because the resonators are tuned asynchronously. An equiripple Chebychev bandstop filter shape can be obtained by tuning the resonator self coupling values away from the values in (5.7).

The shape changing capability of this filter is expected to be useful for trading stopband depth for width. For example, a bandstop filter could offer 40 dB of extra attenuation in a bandpass-bandstop filter cascade over a narrow bandwidth in Butterworth mode, or the filter could be reconfigured to Chebychev mode to maximize the bandwidth over which it provides 10 dB of extra isolation, depending on the spectral environment.

5.3.2 Comparison to Elliptic Filters

The frequency response of a bandpass-bandstop filter cascade looks very similar to what could be achieved with an elliptic filter. However, there are some important differences in capability and implementation between these two filter functions that make both valuable in different system applications. For this analysis, we will compare a fourth-order elliptic filter with two transmission zeros at one frequency with a second-order bandpass filter cascaded with a second-order bandstop filter. This comparison will use the same number of total resonators and the same number of transmission zeros in both cases.

The coupling diagram and frequency response of the fourth-order elliptic filter can be seen in Fig. 5.14. Two transmission zeros are set to a normalized frequency of -10. Compared to the filter cascade that will be shown below, this filter has a steeper roll-off adjacent to the passband, providing good selectivity. Elliptic filters can also be tuned over wide frequency ranges [72], providing adaptable selectivity.

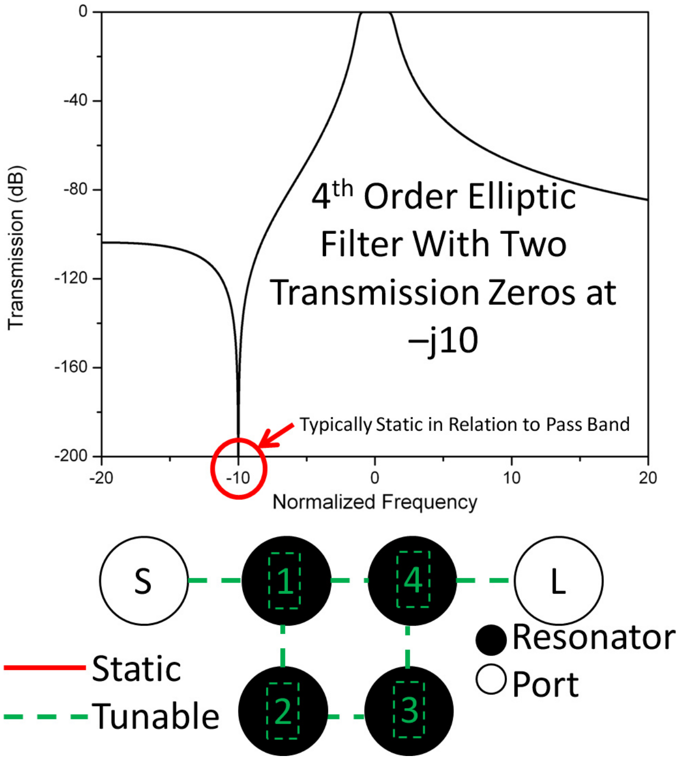

Fig. 5.14. Frequency response and coupling diagram for a fourth-order elliptic filter with two transmission zeros at j10 normalized frequency. Note that in order to tune the transmission null independently of the passband without affecting its shape, all resonators and coupling values must be tuned.

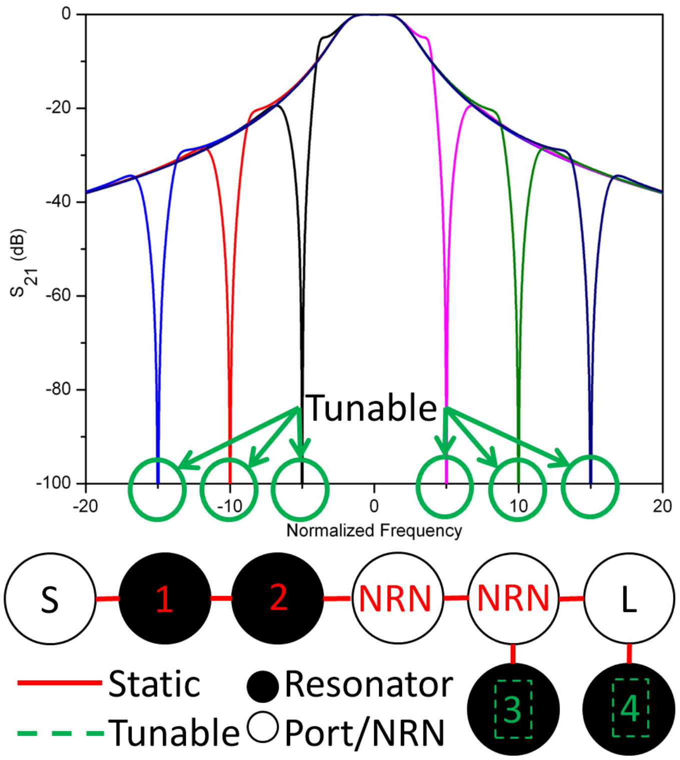

Fig. 5.15. Frequency response and coupling diagram for a second-order bandpass filter cascaded with a second-order bandstop filter at six separate bandstop tuning frequencies. Note that in order to tune the transmission null, only the resonators of the bandstop filter need to be tuned.

When the passband of an elliptic filter is tuned, the transmission zeros usually tune the same amount. For maximum flexibility, tuning the transmission zeros independently of the passband is desirable. However, this is very difficult to achieve in elliptic filters with two transmission zeros on one side of the passband because of the inherent dependencies of elliptic filter coupling coefficients. As can be seen in Fig. 5.14, all coupling values and resonator frequencies need to be tunable to enable an elliptic filter with independently tuning (non-symmetric about the passband) transmission zeros and a preserved passband shape. The transmission zero locations in this elliptic topology are also very sensitive to the M_{24} coupling coefficient. In some cases, deviation in M_{24} of 0.1% can split the transmission zeros to two separate frequencies, leaving very little additional attenuation at the desired transmission zero frequency. A filter with this level of reconfigurability and coupling coefficient control is extremely difficult to implement.

The benefit of using a bandpass-bandstop filter cascade is the ease of implementing transmission nulls that can tune independently of the filter passband. The coupling diagram and frequency response for six separate tunings of the bandstop filter are shown superimposed in Fig. 5.15. Note that in order to tune the transmission null, only the center frequencies of the bandstop resonators need to be tuned, and the passband shape is preserved throughout the tuning range. This is a much more easily realizable circuit if independently tuning transmission nulls are desired. However, the bandpass-bandstop filter cascade in this example provides a more gradual roll-off adjacent to the passband compared to the elliptic filter since it uses only a second-order bandpass filter.

5.3.3 Measured Results II

Highly loaded evanescent-mode cavity [64], [55], [73] bandpass and bandstop filters were fabricated and cascaded [74] for the purpose of verifying the theory above. A photograph of the measured filters can be seen in Fig. 5.16. The center frequencies of each resonator are tunable through the use of piezoelectric actuators. The piezoelectric actuators were biased using integrated connectors and bias lines fabricated on a 1 mil thick liquid crystal polymer (LCP) substrate. Several filter cascade circuit frequency response plots beyond what will be shown below can be seen in [74]. Methods for determining the physical size of the structures for bandpass inter-resonator coupling, the bandpass external coupling, and bandstop external coupling can be found in [25], [75], and [76] respectively. Piezoelectric actuator bias voltages ranged from -200 V to 200 V. Fig. 5.17 shows the measured frequency response for the situation where the inter-filter transmission line electrical length is 270 degrees at the bandstop filter frequency of operation. Note the unwanted peak in the S_{21} response at 3.36

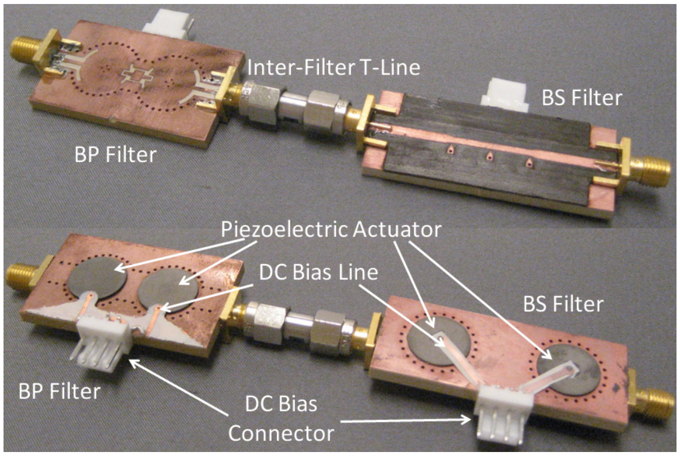

Fig. 5.16. Top and bottom view of measured devices connected by an SMA-to-SMA inter-filter adapter/transmission line. Biasing connectors and traces are integrated into the filter, and bias is applied using benchtop power supplies.

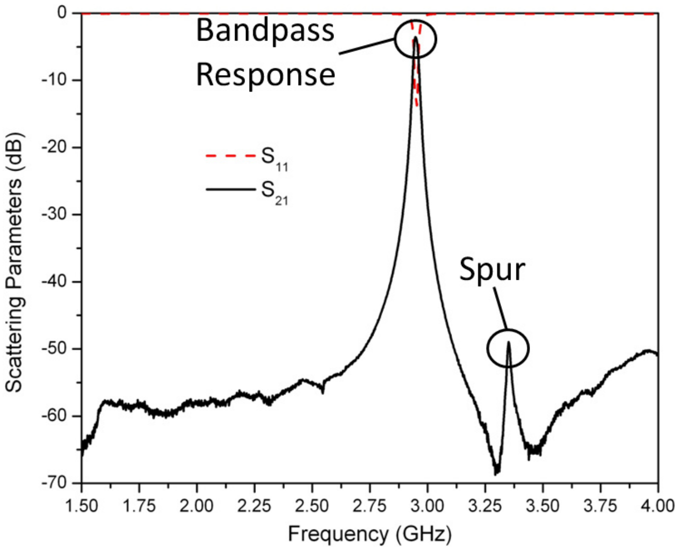

Fig. 5.17. Measured results showing the unwanted peak in the response formed when the bandpass filter is connected to the bandstop filter with a transmission line that is 270 degrees long at the bandstop filter frequency of operation.

GHz, which is the bandstop filter frequency of operation in this plot. Compared to the bandpass filter alone, the cascade circuit attenuates the signal about 20 dB less in this configuration. The theoretical unwanted peak in Fig. 5.13 predicts a 27 dB reduction in attenuation at the bandstop filter frequency. The 7 dB difference can be attributed to the finite Q of the filters, loss in the inter-filter transmission line, and interaction effects from the physical geometry of the filters that are not captured in the theoretical responses plotted in Fig. 5.13.

Additional measured results of the filter cascade can be seen in Fig. 5.18. It can be seen that the transmission null can be tuned about a static passband without affecting the passband shape unless a very small passband to transmission null spacing is employed. The transmission null is continuously tunable from 2.6 to 3.0 GHz when the bandpass filter is tuned to 2.8 GHz. This frequency range corresponds to where the inter-filter transmission line is an electrical length of 209 to 241 degrees long, showing that good performance can be achieved when the bandstop filter frequency of operation is well removed from where the inter-filter transmission line is 180 degrees, the ideal case. It can be seen that the shape of the transmission null is not symmetric like it is in the analytical response. Since open transmission lines (microstrip and

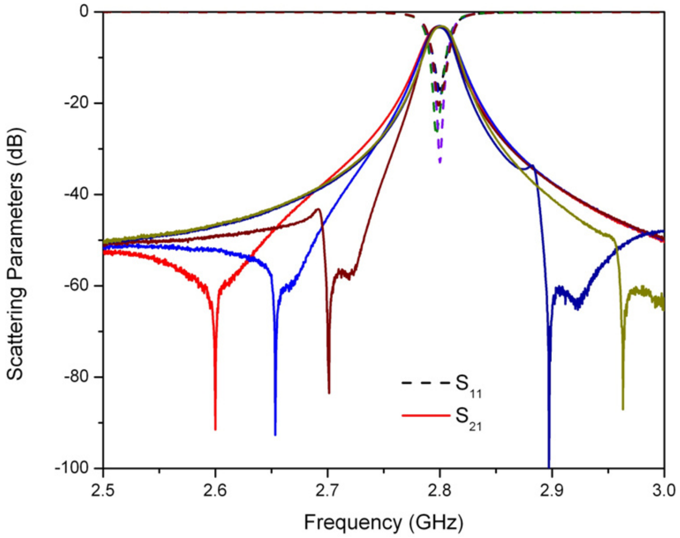

Fig. 5.18. Measured results of a bandstop filter tuning around a static bandpass filter. Up to 100 dB of isolation is shown between the passband and transmission null.

coplanar waveguide) and connectors were utilized, there was trace levels of radiation and substrate coupling on the order of -60 to -90 dB that is not included in the analytical filter models. This coupling affects the precise shape of the filter response, such as symmetry around the transmission null. A closed transmission line, such as a stripline, is recommended to reduce these trace level effects. Nonetheless, the response demonstrates that deep isolation is achievable even in a practical implementation that has stray coupling. The passband can also be tuned around a static transmission null as shown in Figs. 5.19 and 5.20, which show measured vs. simulated S_{11} and S_{21} data, respectively. Simulations for the bandpass filter and bandstop filter were performed

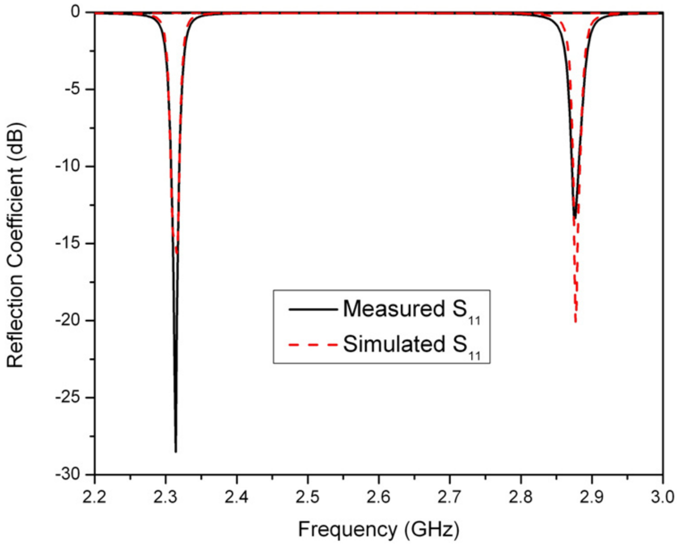

Fig. 5.19. Measured vs. simulated S_{11} results for the fabricated bandpass-bandstop filter cascade.

separately in Ansoft HFSS due to processing limitations. The results for each filter were then exported as s2p files to Agilent ADS and cascaded with a transmission line to simulate the entire measured circuit. It is important to understand that this simulation method does not completely capture stray coupling effects between the filters because they are modeled as isolated blocks in Agilent ADS. This, combined with fabrication tolerances and calibration only to the connectors of the cascade, is the cause of the slight variations seen in the measured vs. simulated data in Figs. 5.19 and

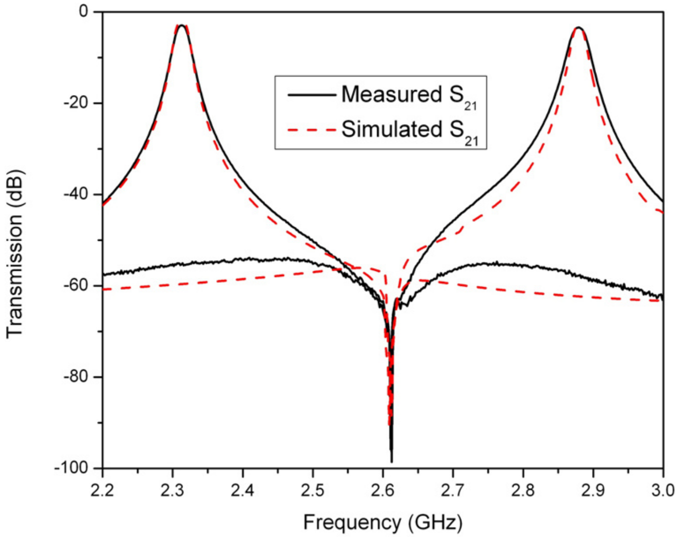

Fig. 5.20. Measured vs. simulated S_{21} results for the fabricated bandpass-bandstop filter cascade.

5.20. The insertion loss in the passband is 3.1 to 3.4 dB across the bandpass tuning range, and the passband has a 0.9% 3 dB bandwidth. Some of this loss is due to the connection between the filters, which includes two SMA connectors and an SMA-SMA adapter. Through measuring the bandpass and bandstop filter independently, it was deduced that this connection produced 0.4 dB of loss. In a system implementation of a bandpass-bandstop filter cascade, the connection between the filters would ideally have much lower loss. Since both the bandpass and bandstop filters are independently tunable, dynamic isolation from 80 to 100 dB is achieved between the passband and transmission null.

Using the Butterworth-to-Chebychev reconfigurable filter first demonstrated in [36], it is possible to implement a tunable transmission null shape on the skirt of the passband. This is shown in Fig. 5.21, where the filters are slightly tuned between the two shown states of the transmission null for clarity. The 55 dB bandwidth in the Butterworth case is 16 MHz, and the 55 dB bandwidth in the Chebychev case is 30 MHz, an increase of 87.5%. The ability to switch between Butterworth and

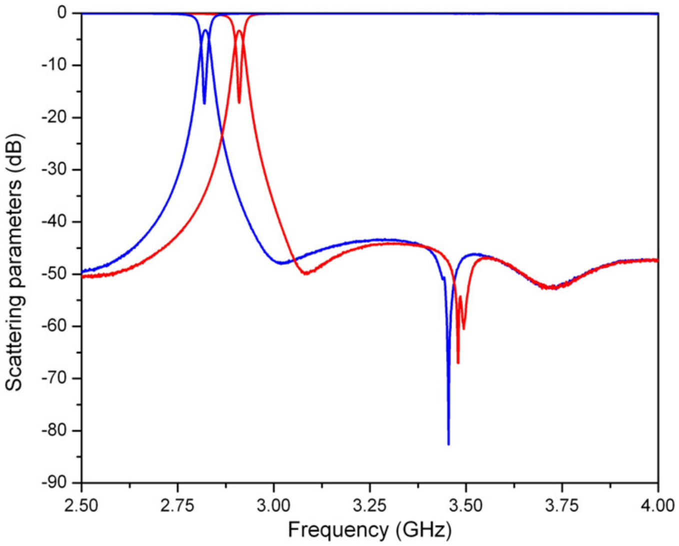

Fig. 5.21. Measured results showing tuning between a Butterworth and Chebychev bandstop response on the skirt of the bandpass filter. This ability promises to be useful in spectral environments with interferers of varying widths and shapes.

Chebychev responses is dynamic. This capability would be useful in system that operates in multiple spectral environments with interferers of varying bandwidths.

Instead of using the approach of the previous paragraph, it may be desirable in some systems to use a wider bandstop filter of higher order to provide deep isolation over a wider bandwidth than what is shown in this chapter. The evanescent-mode cavities used in this experiment are highly loaded, and it is difficult to obtain small external coupling values when using magnetic field external coupling with them. This limits the bandwidth that is achievable in a filter design. The concepts described in this chapter are applicable to bandstop filters of wider bandwidth, but there is a tradeoff in available tuning range. The reason for this tradeoff can be best understood by looking at Fig. 5.10. As the bandstop filter bandwidth widens, the frequency where the inter-filter transmission line will resonate if terminated correctly has a larger chance of being in the null of the bandstop filter. When the inter-filter transmission line resonant frequency is in the null of the bandstop filter, the bandstop side of the transmission line will be terminated with impedance that approaches an open circuit for parallel resonators. If the other side of the transmission line is terminated by a parallel resonator bandpass filter that is not tuned to the frequency where the transmission line is a resonator, it will be presented with impedance that approaches a short circuit for parallel resonators. For a ninety degree inter-filter transmission line, a resonance would occur over a wider range of bandstop tuning frequencies as the bandstop filter bandwidth widens. However, for fractional bandwidths less than 10%, the available theoretical tuning range is still very wide. An example of a wider-bandwidth null bandpass-bandstop filter cascade will be shown in the next section.

5.4 Higher-Order Bandpass-Bandstop Filter Cascades for Wider and Deeper Isolation

In order to show isolation over 100 dB over more significant bandwidths, a 2-pole tunable bandpass filter was cascaded with two 4-pole tunable bandstop filters for a total of 10 poles. A diagrams of this circuit can be seen in Fig. 5.22. The bandpass filter alone is able to provide 50 dB to 60 dB attenuation away from its passbands, and the 4-pole bandstop filters are also able to provide up to 60 dB attenuation. Because of the noise floor limitation of available network analyzers, the sensitivity of the measurement setup was limited to about 95 dB attenuation. Therefore, in order to show the full attenuation capability of the higher-order bandpass-bandstop filter cascades, the filters were measured individually and then cascaded in Agilent Advanced Design System (ADS) software using s2p file block circuit elements and

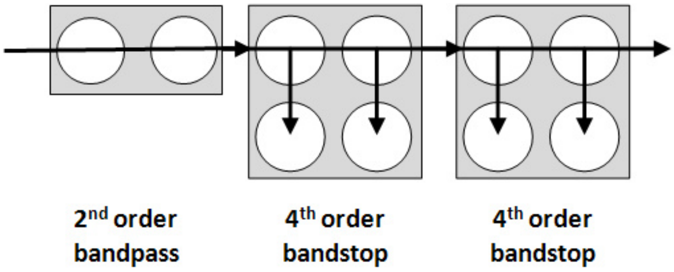

Fig. 5.22. 10–pole bandpass-bandstop filter cascade.

a transmission line. It is important to note that synthesizing final measurements

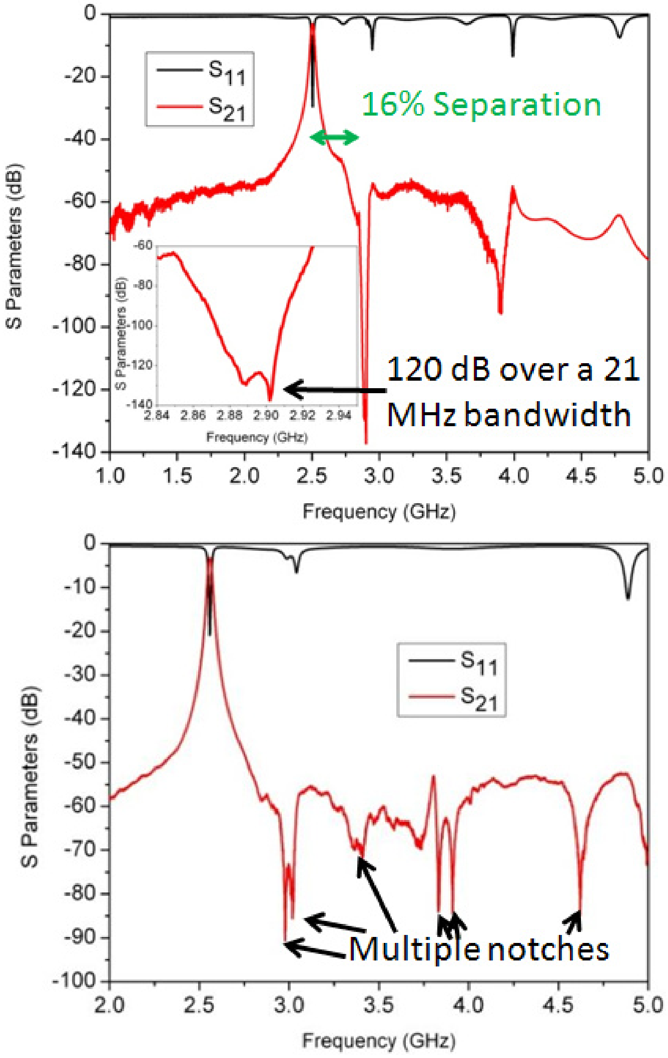

Fig. 5.23. Measured results of a cascade of a 2-pole bandpass filter with two 4-pole bandstop filters.

in this manner does not account for any stray coupling effects between the two filter structures and therefore ultimately needs to be verified by another means for complete certainty. For example, while the coupling apertures of the filters are operated well below the cutoff frequency where they are efficient radiators, they do still radiate at trace levels. Whether this trace radiation is enough to limit the isolation provided by the bandpass-bandstop filter cascade is implementation-specific and is yet to be tested.

Measured results of the 2-pole bandpass filter cascaded with two 4-pole bandstop filters can be seen in Fig. 5.23. The top picture shows a 2-pole bandpass filter response with 7 bandstop poles at 2.9 GHz and 1 bandstop pole at 3.9 GHz. 120 dB attenuation was achieved over a 21 MHz bandwidth at 2.9 GHz, which is a 0.72% fractional bandwidth. The bottom picture in Fig. 5.23 shows the same filter cascade with the bandstop resonators spaced over the upper stopband of the bandpass filter, selectively providing small bandwidths of additional attenuation. Such a response uses the dynamic pole allocation technique first descibed in Chapter 2. Such a configuration would be useful in an environment with several relevant interferers.

5.5 Conclusion

Tunable, substrate integrated, high Q bandpass-bandstop filter cascades were demonstrated that were capable of providing up to 120 dB isolation between two dynamically selectable frequencies of interest in synthesized measurements. Up to 100 dB isolation was measured real-time. It is shown that the bandpass and bandstop filters can be brought within 55 MHz of one another at 2.63 GHz (2.1% spacing) before they start to greatly affect each others responses. This capability would be useful in concurrent transmit-receive systems, shared aperture systems, and environments with strong co-site interference. Theory was developed through the use of general coupling matrix methods and ABCD parameter methods. The theory explains the behavior of the cascade circuit over wide frequency tuning ranges, and it was determined that good performance can be achieved over more than an octave. Measurements of evanescent-mode cavity filters were made to verify this theory, and good agreement was achieved.

Bandpass-bandstop filter cascade circuits were compared to elliptic filters due to the similarities in their filter functions. It was determined that elliptic filters of a given order have steeper roll-off from their passband, but less flexibility in tuning transmission zeros. The flexibility in transmission null placement obtained from using a bandpass-bandstop filter cascade is expected to be extremely useful in the open spectral environment of the future. Filter cascades of this type allow sensitive receivers to operate in the presence of spectrally close high power signals. The ability to do this is vital to optimize the capabilities of communication systems in spectrally dense environments. Systems having high power transmitters and sensitive receivers will be able to operate both concurrently instead of being constrained to use time division multiplexing, increasing system capability.

6. TUNABLE BANDPASS-TO-BANDSTOP RECONFIGURABLE FILTERS

6.1 Introduction

The bandstop filters and filter cascades described in previous chapters could enhance the interference immunity of wide bandwidth systems, and the bandpass-bandstop filter cascades described in the previous chapter could do the same for narrow bandwidth systems that experience high power interference. However, with the recent increased interest in reconfigurable integrated circuit technology, future systems may have the capability of converting from relatively wide bandwidth modes to narrow bandwidth modes. In addition, with the spectrum becoming more dynamic every day, interference profiles and power levels experienced by a system frequently change. Therefore, as modern microwave systems are progressed toward spectrally cognitive operation, more filter reconfigurability will be necessary to enable the full potential of these systems performance [6].

There has been much recent interest in tunable filters for cognitive and reconfigurable systems, especially tunable bandpass filters. Some of these filters demonstrate relatively high Q values and can tune over an octave [63], and some have reconfigurable shapes [64]. Recent progress has also been made in tunable bandstop filters [34]. These bandstop filters are important in spectrally dense environments where interference is a large concern. In an open spectrum with multiple cognitive radios simultaneously operating in it, an increasingly dynamic filter shape may be needed by a new radio for it to effectively join the environment. If this open environment contained several low-power interfering signals as in Fig. 6.1 a), this radio could most optimally benefit from a narrow-band bandpass filter centered at its receive frequency band to maximize the signal-to-noise ratio (SNR). If the environment changes so that

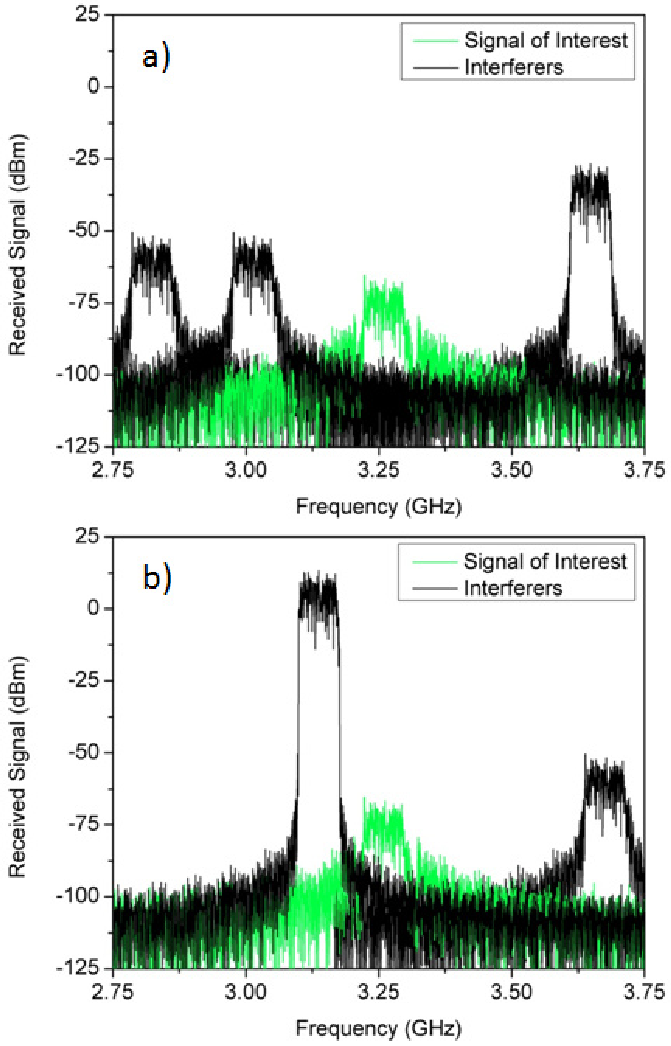

Fig. 6.1. a) Spectrum where a bandpass filter would be most useful for isolating a narrow band signal of interest. Note that a bandstop filter could be useful if a wide receive spectrum was desired. b) Spectrum where a bandstop filter would be most useful for isolating the signal of interest. These signals were adapted from an Agilent ADS example WCDMA project.

it includes a higher power interferer that is spectrally close to the receive band of the radio, as in Fig. 6.1 b), the radio may lose its ability to resolve desired signals well. In this situation, the SNR could possibly be maximized if the radio was able to place a deep bandstop filter response at the high-power interferer's frequency of operation. In addition, if the new radio has a high-power transmitter, the existing radios may need to dynamically place a transmission null at the new radio's operating frequency so that they can maximize their levels of performance in the changed spectral environment.

Filters occupy a relatively large amount of physical space in modern wireless systems compared with other typical radio components, most of which are now easily integrated on chip. In many cases, it would be impractical to implement both tunable bandpass filter banks and tunable bandstop filter banks in a system due to size constraints. A possible solution to this problem is to implement sets of coupled resonators whose response can be dynamically switched between a bandpass and bandstop shape, saving space while providing added flexibility to a system. This response reconfiguration concept is shown in Fig. 6.2. Fig. 6.3 shows that Chebyshev

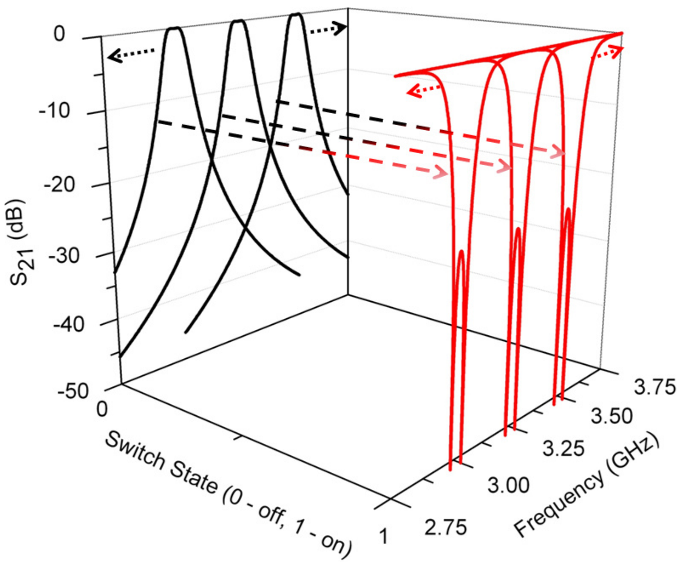

Fig. 6.2. Concept of a bandpass filter that can switch its response to that of a bandstop filter by toggling a switch.

bandpass, elliptic bandpass, and bandstop responses can be obtained from the same set of resonators if their coupling values are tunable. Note that Fig. 6.3 is theoretical, and the ability to achieve all three responses in Fig. 6.3 would require components that have wider tuning ranges than what is commercially available today. However, with the wide array of switches and varactors that are available today, the theory

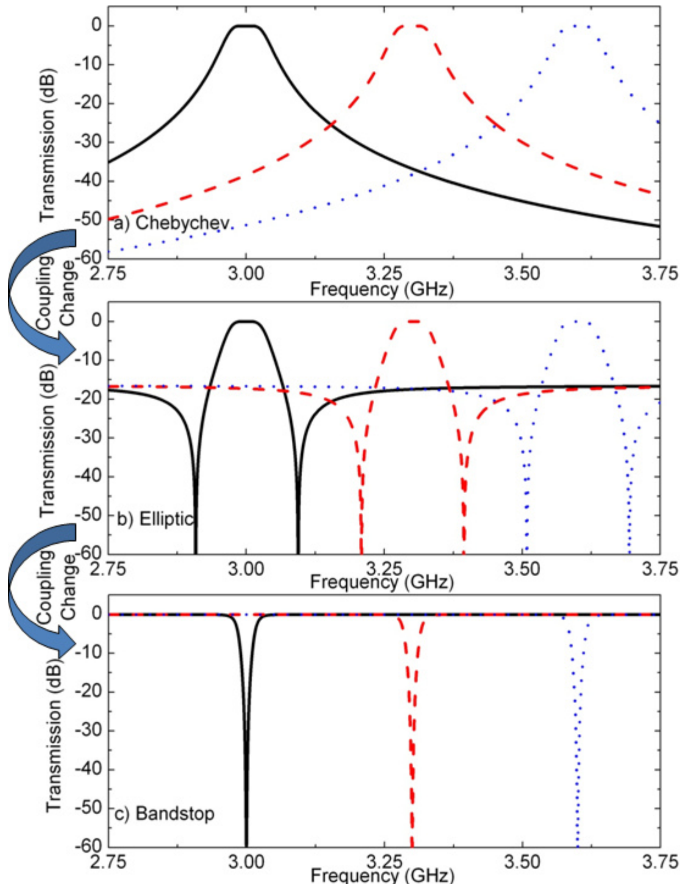

Fig. 6.3. Simulated results showing possible S_{21} responses of a set of two tunable resonators with tunable external and/or source-load coupling values.

presented below can be used to implement a filter that can transform between any single bandpass filter shape and any single bandstop filter shape. Fig. 6.4 shows the coupling diagram of the theoretical structure needed to implement the responses shown in Fig. 6.3. The dashed lines represent tunable or switchable coupling values, and the solid line represents static coupling.

A filter with the ability to switch between Chebyshev bandpass, elliptic bandpass, and "off" responses was shown in [77]. In contrast, the filter presented in this chapter switches between designed bandpass and bandstop filter responses, which is fundamentally different functionality. Bandpass-to-bandstop filter reconfigurability

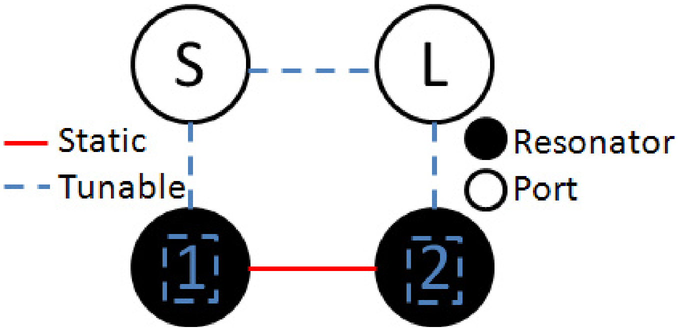

Fig. 6.4. Coupling diagram needed for implementation of a filter with responses shown in Fig. 6.3. Note that the resonant frequencies of the two resonators are independently tunable.

has been achieved in [78] and [79]. However, the filters demonstrated in these papers are not tunable and use relatively low Q resonators that result in spectrally wide responses. The filter in [78] uses the frequency-selective behavior of a cascade of unit electromagnetic bandgap (EBG) structures that can be switched to exhibit either a bandpass or bandstop response, and [79] demonstrates a bandpass-to-bandstop filter with a closed-ring resonator whose reconfigurability results from the perturbation effect on degenerate modes. In contrast, this chapter demonstrates a filter that can switch between many commonly prescribed narrow-band filter functions. For example, the theory described in this chapter could be used to create a filter that could switch between a Butterworth bandpass response and a Chebyshev bandstop response. In general, while the previous solutions are innovative, bandpass-to-bandstop reconfigurable filters suitable for integration into a tunable, narrow-band system have not been demonstrated. This chapter develops the theory of narrow-band, prescribed-response, bandpass-to-bandstop electronically reconfigurable filters and demonstrates a novel, high-Q , tunable, evanescent-mode cavity design with new capabilities not found in previous designs.

6.2 Bandpass-to-Bandstop Reconfigurable Filter Theory

The same geometry resonators can be used for a bandpass or a bandstop filter if the coupling relationships between the source, load, and resonators are changed appropriately. For the second-order filter analysis in this chapter, both external coupling values will be equal to each other, the resonator self-coupling values will have the same magnitude but opposite sign, and symmetries such as the source-to-load coupling being the same as the load-to-source coupling can be taken advantage of to simplify the generalized second-order filter (N+2)x(N+2) coupling matrix **M** to

$$\mathbf{M} = \begin{bmatrix} 0 & M_{01} & 0 & M_{03} \\ M_{01} & M_{11} & M_{12} & 0 \\ 0 & M_{12} & -M_{11} & M_{01} \\ M_{03} & 0 & M_{01} & 0 \end{bmatrix}, \tag{6.1}$$

where the subscripts 0 and 3 correspond to the source and load, respectively, and subscripts 1 and 2 correspond to the first and second resonators, respectively.

It can be shown with coupling matrix methods [69] that the coupling matrix for a typical second-order Butterworth bandpass filter is

$$\mathbf{M} = \begin{bmatrix} 0 & 0.8409 & 0 & 0 \\ 0.8409 & 0 & 0.7071 & 0 \\ 0 & 0.7071 & 0 & 0.8409 \\ 0 & 0 & 0.8409 & 0 \end{bmatrix}, \tag{6.2}$$

and the coupling matrix for a second-order Butterworth bandstop filter is

$$\mathbf{M} = \begin{bmatrix} 0 & 1.189 & 0 & 1 \\ 1.189 & 0 & 0 & 0 \\ 0 & 0 & 0 & 1.189 \\ 1 & 0 & 1.189 & 0 \end{bmatrix}. \tag{6.3}$$

Compared to the bandstop filter in (6.3), the coupling matrix in (6.2) has two main differences. Typical bandstop filters have a source-to-load coupling (M_{03}) value equal to one, which is commonly implemented as a 90 transmission line. Also, common bandstop filters have an inter-resonator coupling (M_{12}) value of zero, indicating that bandstop filters place the resonators in a shunt configuration, while bandpass filters, with a nonzero M_{12} and zero-valued M_{03}, place the resonators in a series configuration. In addition to these two differences, the M_{01} value changes slightly between the bandpass and bandstop cases. M_{01} becomes 1.189 in the normalized frequency Butterworth bandstop case, compared with 0.8409 for the Butterworth bandpass case.

It is straightforward to change the zero-valued M_{03} of a bandpass filter to a value of one through the use of switches with high isolation which switch in a 90° transmission line between the resonators. In addition, a uniquely designed coupling structure will be shown below that allows for the switching of M_{01} between the bandpass and bandstop modes of the filter. However, changing from a nonzero M_{12} value to an M_{12} value of zero is difficult in practice, since it is difficult to fully block the coupling mechanism between resonators. Fortunately, it is possible to synthesize a bandpass-to-bandstop reconfigurable filter with a nonzero M_{12} value if the resonators of the filter can be tuned asynchronously [36].

The analysis in [36] begins with the general coupling matrix for a conventional bandstop filter with synchronously tuned resonators. An example can be seen in (6.3) for a synchronously tuned Butterworth bandstop filter. However, [36] shows that (6.3) is just one of many possible Butterworth bandstop filter coupling matrices. If (6.3) is allowed to have nonzero M_{11} and M_{12} values as in (6.1), an infinite number of Butterworth bandstop filter coupling matrices is possible. Reference [36] shows that, as long as

$$M_{01}^2(M_{12} + M_{12}^{'}) + M_{12}^2 > M_{12}^{'} \tag{6.4}$$

is satisfied, where primed quantities correspond to the new, asynchronously tuned filter and unprimed quantities correspond to the original, synchronously tuned filter, the same frequency response can be achieved with an arbitrary $M_{12}^{'}$ value if

$$M_{11}^{'} = \pm\sqrt{M_{01}^{'2}(M_{12} + M_{12}^{'}) + M_{12}^2 - M_{12}^{'2}} \tag{6.5}$$

is satisfied and $M_{01}^{'} = M_{01}$. In this example, M_{12}, which is the inter-resonator coupling for the synchronously tuned bandstop filter in (6.3), is zero. For an $M_{12}^{'}$ of one, an M_{11} of 0.643 produces the Butterworth response of the original synchronously tuned filter.

In most cases, the desired bandpass and bandstop response **M** matrices will have different M_{12} values. However, it is possible to implement both matrices without a tunable physical inter-resonator coupling structure in a filter. In a physical filter implementation at microwave frequencies, the inter-resonator coupling coefficient k_{12} can sometimes describe coupling values between resonators more clearly since it accounts for bandwidth explicitly. This is especially appropriate in a filter with two modes of operation, where each mode has different semi-arbitrary fractional bandwidths. In this case, k_{12} will be constant between filter modes of operation for a static physical inter-resonator coupling structure, but M_{12} will change due to differing fractional bandwidths in each mode of filter operation. In other words, using k_{12} instead of M_{12} will more clearly show that the inter-resonator coupling is static throughout the synthesis process. Because of this, the remainder of the theoretical analysis in this chapter will be done using the coupling coefficients k_{01} and k_{12} along with M_{01} and M_{12} as follows:

$$k_{01} = \sqrt{\Delta} \cdot M_{01} \tag{6.6}$$

$$k_{12} = \Delta \cdot M_{12} \tag{6.7}$$

where Δ is fractional bandwidth. It is to be understood that k_{01} represents external coupling to both of the filters ports because both coupling values will always be equal in this analysis.

Using the k values in (6.7) to represent coupling values at the actual design fractional bandwidths will allow straightforward synthesis of a bandpass-to-bandstop reconfigurable filter with independent bandwidths for each mode of operation without a tunable k_{12} value. It will be shown that a bandpass-to-bandstop reconfigurable response can be synthesized by enabling tunable coupling values for k_{01}, M_{11}, and M_{03}

only and that k_{12} can be static and arbitrary as long as (6.4) is satisfied. It is also possible to change M_{03} to produce an elliptic response in the bandpass case. First, the novel coupling structure used in the proposed filter will be explained.

6.2.1 Novel Coupling Structure for Simultaneous k_{01} and M_{03} Switching

The novel coupling structure designed for bandpass-to-bandstop reconfigurable filters is a transmission line of electrical length L degrees over a coupling aperture in the wall of the first resonator, followed by a switch, followed by a transmission line of length $270 - 2 \cdot L$ degrees, followed by a switch, followed by a transmission line of length L degrees over a coupling aperture in the wall of the second resonator. A model of such a structure can be seen in Fig. 6.5, where the resonators have been omitted for clarity.

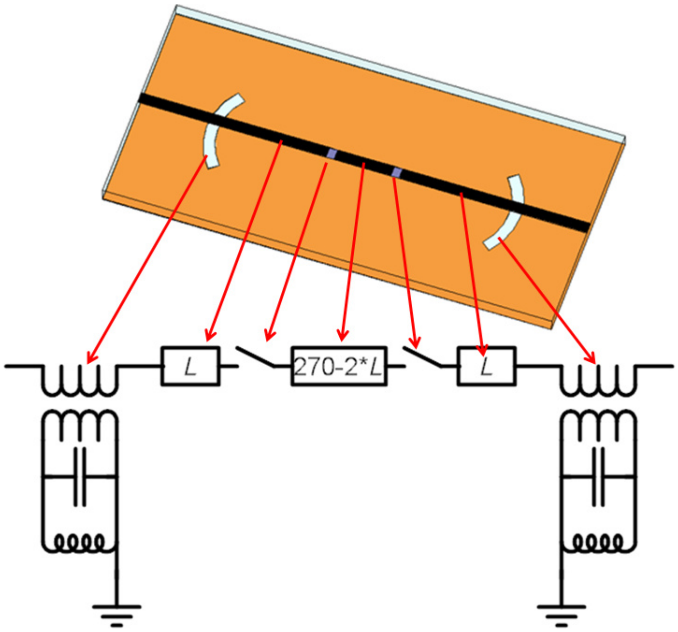

Fig. 6.5. Novel coupling structure designed for bandpass-to-bandstop reconfigurable filters.

This coupling structure has three modes of operation. First, in the bandstop mode of the filter, the switches are closed, and the coupling structure becomes a 270°

transmission line over coupling apertures in the resonators. A 270° transmission line has a positive coupling value in this analysis. This positive insertion phase allows for a bandstop response with a nonzero k_{12} value. The coupling apertures in the walls of the resonators are sized to provide the appropriate k_{01} value for the bandstop mode of the filter. An equivalent circuit model of this mode of operation can be seen in Fig. 6.6 a).

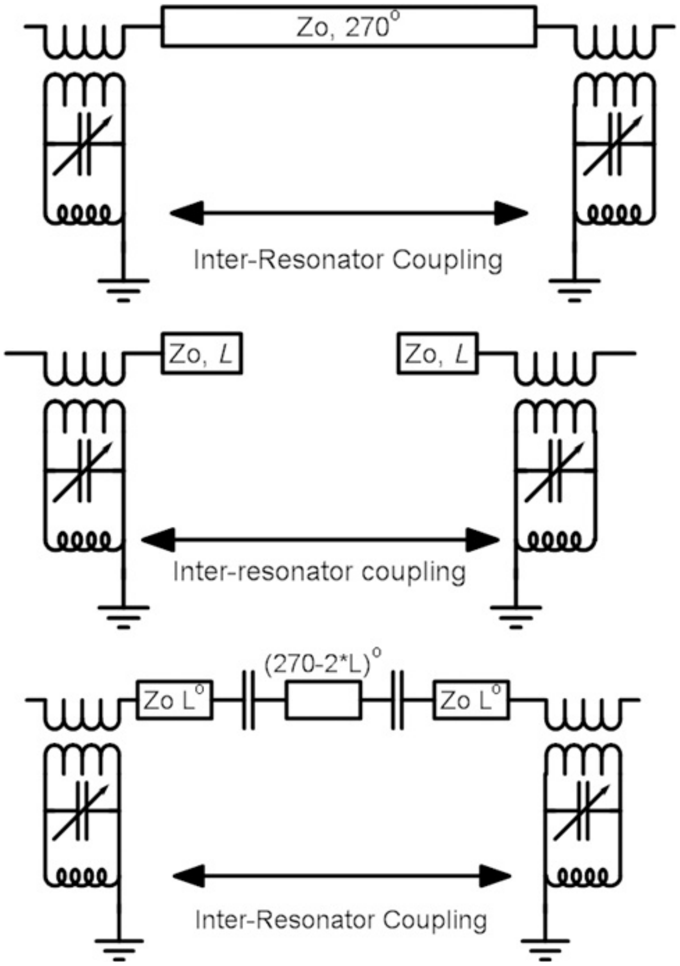

Fig. 6.6. a) Coupling structure in the bandstop mode of the filter. b) Coupling structure in the bandpass mode with very high isolation switches. c) Coupling structure in the bandpass mode with medium isolation switches, enabling an elliptic response.

The coupling structures second mode of operation requires very high isolation switches. In this mode, the switches are open, and the coupling structure becomes a transmission line of length L degrees over a coupling aperture in the in the wall of the first resonator. The transmission line between the two switches is not coupled to, therefore the source-to-load coupling is removed. Symmetry allows similar coupling into resonator 2 as resonator 1. The transmission lines of length L are approximately open at their interior ends if high-isolation switches are utilized. The length of the transmission line from the coupling aperture to the open end transforms the impedance seen at the coupling aperture. Therefore, k_{01} also changes accordingly, and different k_{01} values are possible between the bandpass and bandstop modes of the filter. An equivalent circuit for this mode of operation can be seen in Fig. 6.6 b).

The coupling structure's third mode of operation requires a switch with a medium level of isolation, similar to the level found in common solid-state RF switches. Variable isolation switches or varactors could also be used for even more flexibility. In this mode, the switches are in their off-state but have significant capacitance. An equivalent circuit for this mode of operation can be seen in Fig. 6.6 c). For a certain range of small switch capacitance values, the capacitance shown in Fig. 6.6 c) adds approximately two more 90° phase shifts into the circuit. Considering that 270 electrical degrees are already present from the transmission lines, the total insertion phase in this mode of the coupling structure becomes 450°. This is a significant result because the 450° of insertion phase is the sign opposite of the 270° of insertion phase obtained in the bandstop mode of operation, and this allows for negative source-to-load coupling. Negative source-to-load coupling results in an elliptic response [80], [81], providing a third useful mode of operation for the proposed filter.

6.2.2 Analysis of Bandpass-to-Bandstop Reconfigurable Filter

In the typical bandpass mode of the filter, the second mode of operation of the coupling structure defined in Fig. 6.6 above is given by

$$k_{01BP} = \sqrt{\Delta_{BP}} \cdot M_{01BP} \tag{6.8}$$

$$k_{12BP} = \Delta_{BP} \cdot M_{12BP} \tag{6.9}$$

where the subscript BP denotes quantities associated with the bandpass mode of the filter. As stated previously, it is desired to synthesize a bandpass-to-bandstop reconfigurable filter with a static k_{12} value. Therefore, in the bandstop mode of the filter,

$$k_{01BS} = \sqrt{\Delta_{BS}} \cdot M_{01BS} \tag{6.10}$$

$$k_{12BS} = k_{12BP} \tag{6.11}$$

where the subscript BS denotes quantities associated with the bandstop mode of the filter. This corresponds to the first mode of operation of the coupling structure defined in Fig. 6.6. Setting k_{12BP} equal to k_{12BS} is possible if the resonators of the filter are can be tuned asynchronously [36]. For an arbitrary k_{12BS}, the resonators must be tuned asynchronously according to the relationship in (6.12) and (6.13), which are modified versions of (6.5). These expressions must produce a real number value for M_{11} as follows:

$$M_{11BS} = \sqrt{M_{01BS}^2 M_{12BS} - M_{12BS}^2} \tag{6.12}$$

or

$$M_{11BS} = \sqrt{M_{01BS}^2 \frac{k_{12BP}}{\Delta_{BS}} - (\frac{k_{12BP}}{\Delta_{BS}})^2}. \tag{6.13}$$

The bandstop k and $\mathbf{M}$ values in (6.11)(6.11) produce a bandstop filter which has a fractional bandwidth (FBW) lower limit of

$$FBW_{BSmin} = \frac{k_{12BP}}{M_{01BS}^2} = \frac{\Delta_{BP} \cdot M_{12BP}}{M_{01BS}^2}. \tag{6.14}$$

Since $\frac{M_{12BP}}{M_{01BS}^2} = 0.5$ using the values in (2) and (3), the bandstop filter must be at least half as wide in bandwidth as the bandpass filter for the case of switching a

Butterworth bandpass filter to a Butterworth bandstop filter. However, other filter shapes can be used to produce different bandwidth limitations between each mode of operation.

6.3 Bandpass-To-Bandstop Reconfigurable Filter Design

An evanescent-mode cavity-resonator-based bandpass-to-bandstop reconfigurable filter was fabricated with a static inter-resonator coupling structure for measurement. A model of the fabricated filter can be seen in Fig. 6.7. An expanded view of each layer of the structure is shown in Fig. 6.8. The evanescent-mode cavity resonators were designed in 3.175-mm-thick Rogers TMM3 printed circuit board material and defined by plated vias. The cavities have semi-circular apertures cut into their surface to enable magnetic field coupling. Single, weakly coupled resonators were fabricated out of the same TMM3 board as the filter cavities presented in this chapter, and the unloaded Q was measured to vary from 608 to 650 across the frequency range from 2.75 to 3.75 GHz.

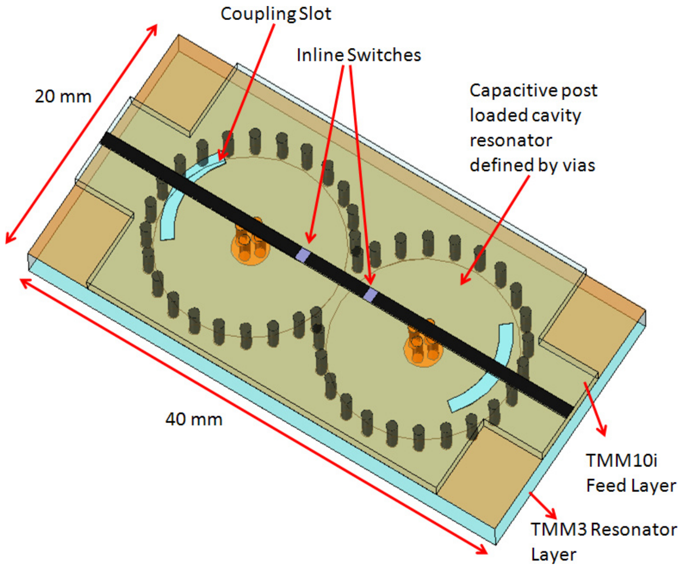

Fig. 6.7. Filter simulation model showing geometry and materials used in the fabricated filter.

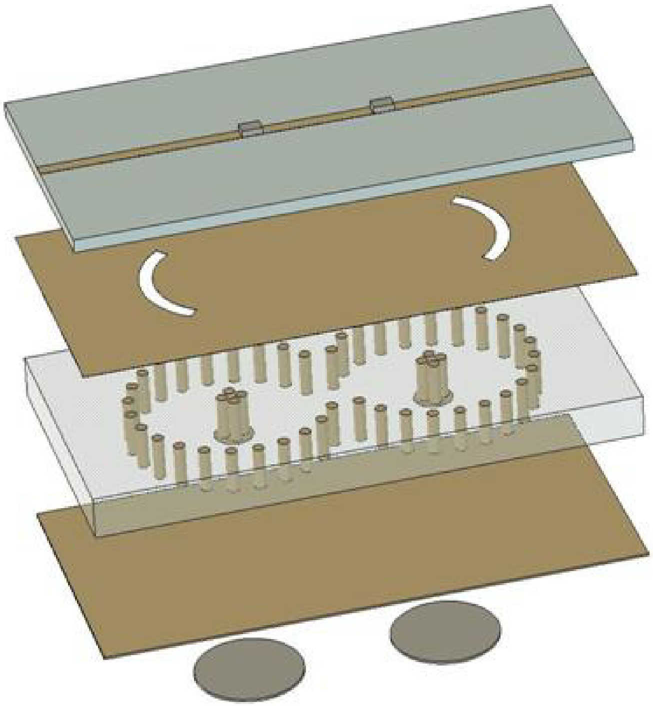

Fig. 6.8. Layer-by-layer expanded view of filter. From top to bottom, the layers are TMM10i, thin copper, TMM3, and thin copper. The disks represent the actuators. Note that there are switches in line with the transmission line shown above on the top layer.

A copper membrane was laminated onto the substrate to close the cavity and form the bottom plate of the capacitor inside of the resonator. Commercially available 0.38-mm-thick piezoelectric actuators from Piezo Systems, Inc. were attached to the copper membrane to allow for electronically controllable deformation of the membrane. Capabilities of these resonators with associated bias voltages and capacitive gap dimensions can be seen in [55]. The cavity feeds were fabricated on 1.27-mm-thick Rogers TMM10i material and laminated to the cavities. The feeds were fabricated on this high-dielectric material to reduce the size of the 270° transmission line for source-to-load coupling described above.

The bandwidths of the bandpass and bandstop modes of the filter are somewhat independent. Each can be designed within the fractional bandwidth range of 0.5% to

5.0%. The design of a second-order, independent-bandwidth, bandpass-to-bandstop reconfigurable filter like the one presented in this chapter can be completed by following the procedure outlined below. It is assumed at the start of this procedure that adequate resonators have already been designed and that magnetic coupling is used to physically implement M_{01}, such as the aperture coupling into the resonators shown in Fig. 6.8. Example values for a 1.2% fractional bandwidth Butterworth bandpass to 0.9% fractional bandwidth Butterworth bandstop reconfigurable filter will be given to aid understanding.

Step 1 Design the coupling between the two resonators, k_{12}, as required by the bandpass shape that is desired [25]. This should be carried out as if only a bandpass filter was being designed. For example, in a second-order Butterworth bandpass filter as in 6.2, M_{12} is 0.7071. For a 1.2% fractional bandwidth, this results in a k_{12} of 0.008485.

Step 2 Implement a source-to-load coupling value, M_{03}, of one with a phase of 270° degrees. A 270° transmission line whose characteristic impedance matches that of the system can be used to accomplish this.

Step 3 Now, assuming a k_{12} value of zero, design the external coupling, k_{01}, as required to meet the bandwidth specification of the bandstop filter [76]. Use the M_{01} value from (6.3) for the normalized Butterworth bandstop filter, 1.189. For a 0.9% fractional bandwidth filter, this results in a k_{01} of 0.1128.

Step 4 The k_{12} value is fixed by the bandpass mode of the filter at 0.008485. Since the bandstop filter has a 0.9% fractional bandwidth, an M_{12} value of 0.9428 describes the inter-resonator coupling in the bandstop mode.

Step 5 To achieve the desired bandstop response, tune the resonators asynchronously according to (6.12) and (6.13). With the coupling values above, an M_{11} value of 0.6663 describes the resonator self-coupling for the bandstop mode of the filter.

Step 6 Design the location of the switches along the 270° transmission line to enable switching between the k_{01} needed for the bandstop mode [step 3] and the k_{01} needed for the bandpass mode [see (6.2) and (6.9)] [75]. When the switches are placed directly after the magnetic coupling structures for k_{01}, the minimum in external coupling is achieved for the case when the switch is open because the coupling structure is adjacent to a current minimum on the transmission line. When the switches are placed 90° in electrical length after the coupling structures for k_{01}, the maximum in external coupling is achieved for the case when the switch is open because the coupling structure is adjacent to a current maximum on the transmission line. The switches are closed in the bandstop mode, resulting in a 270° transmission line.

Step 7 Determine the switch type and amount of switch isolation needed for the prescribed bandpass filter shape.A very high isolation switch with low off-state reactance will provide a Butterworth or Chebyshev response, as shown in Fig. 6.3 a). Isolation on the order of 4050 dB is required for this example design. However, a lower isolation reflective switch with capacitive reactance in the off state will create an elliptic response, as shown in Fig. 6.3 b). The isolation level of the switches will be the limit of the out of band isolation in the elliptic bandpass case unless the design has high source-to-load coupling through another mechanism. An absorptive switch will provide inductive reactance in its off state, and this will produce the response of a self-equalized filter. A theoretical progression of filter responses in the normalized frequency domain for changing switch isolation types and levels is shown in Fig. 6.9. Note that the location of the transmission zeros in the elliptic state of the filter can be designed through the choice of switch isolation, with the tradeoff being less filter isolation beyond the transmission zeros the closer the transmission zeros are to the filter passband.

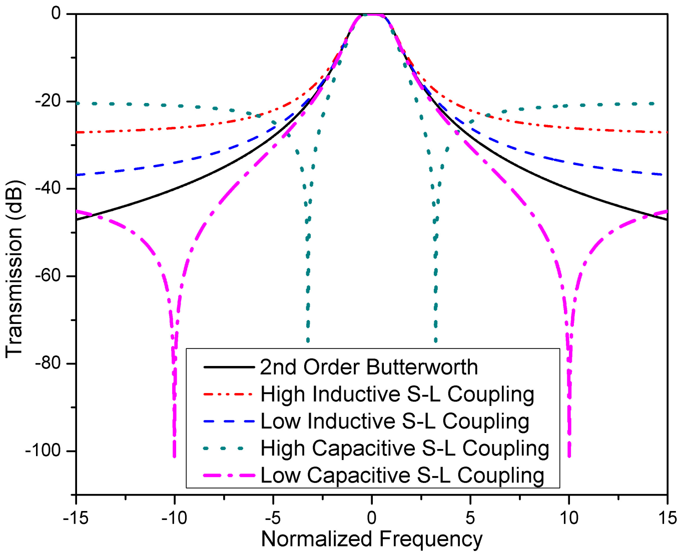

Fig. 6.9. Theoretical progression of filter responses in the normalized frequency domain for four different source-to-load coupling structure switch isolation levels. The second-order Butterworth response has zero source-to-load coupling.

In the 1.2% fractional bandwidth bandpass mode of the filter, the coupling matrix in (6.2) will describe the filter, and the k values will be

$$k_{01BP} = 0.09212 \tag{6.15}$$

$$k_{12BP} = 0.008485. \tag{6.16}$$

In the 0.9% fractional bandwidth bandstop mode of the filter, the coupling matrix

$$\mathbf{M} = \begin{bmatrix} 0 & 1.189 & 0 & 1 \\ 1.189 & 0.6663 & 0.9428 & 0 \\ 0 & 0.9428 & -0.6663 & 1.189 \\ 1 & 0 & 1.189 & 0 \end{bmatrix} \tag{6.17}$$

will describe the filter.

The k values for the bandstop mode of the filter will be

$$k_{01BS} = 0.11280 \tag{6.18}$$

$$k_{12BS} = 0.008485. \tag{6.19}$$

Notice that the k_{12} value in both modes of the filter is the same, enabling a static inter-resonator coupling structure. The difference in k_{01} between filter modes is designed for by the correct placement of the switches in the source-to-load coupling structure described above. Finally, the difference in M_{11} values can be implemented as long as the filter's resonators are independently tunable. Therefore, a tunable bandpass filter can be made a bandstop filter by simply putting a switch on the feed line structure, but only if the proper design rules are followed.

6.4 Measured Results

A labeled photograph of the device can be seen in Fig. 6.10. The ideal synthesized response in Fig. 6.11 a) shows a theoretical second-order Butterworth bandpass filter with no stray coupling between source and load ports. It is valuable to do a measurement of the fabricated filter without switches in the source-to-load coupling

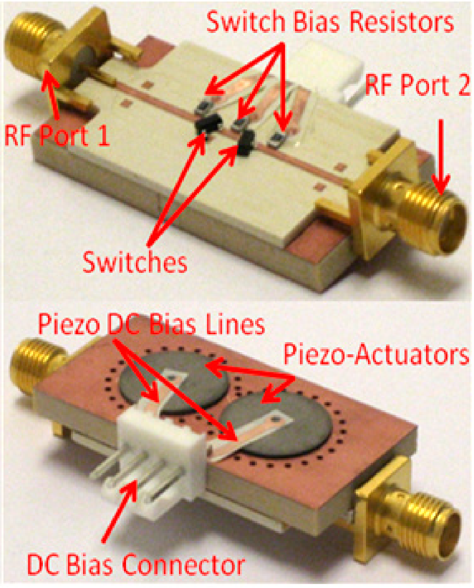

Fig. 6.10. Labeled photograph of both sides of the fabricated filter. For measurements, a network analyzer was connected to the RF ports, and dc power supplies were connected to the dc bias connector. The dc traces were fabricated on a 25.4 μm liquid crystal polymer (LCP) substrate.

structure to observe the amount of coupling due to radiation and substrate paths for comparison. This measurement can also be seen in Fig. 6.11 a). This response is the optimal limit of what could be achieved with this design. While this response is shown for reference, it may be possible to achieve a similar response with high-quality microelectromechanical systems (MEMS) switches [82] in the near future. The response of this filter in both bandstop and bandpass modes can be seen over a wider

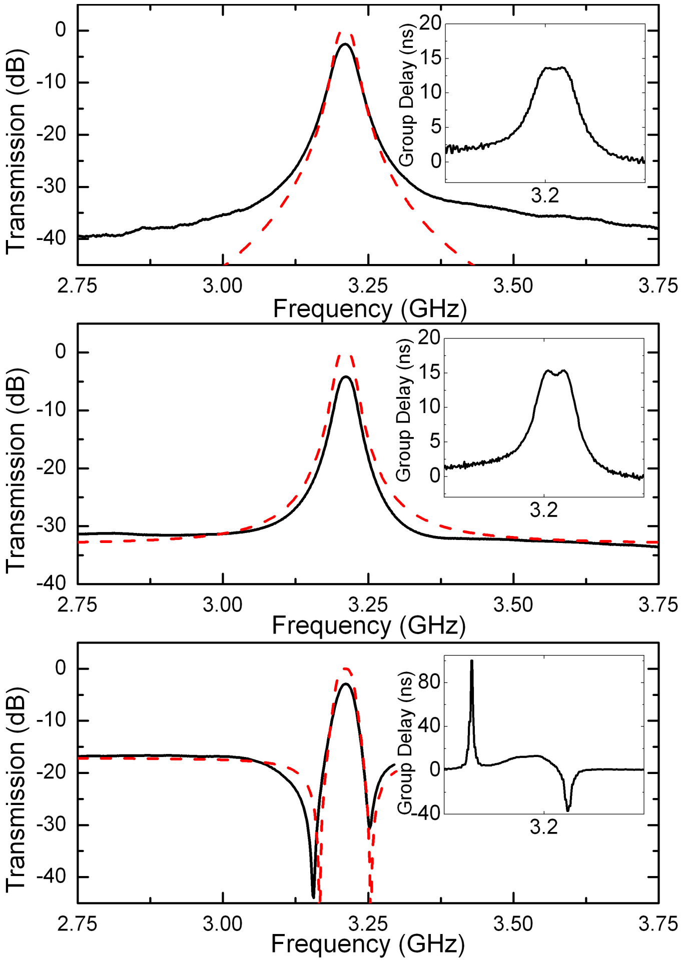

Fig. 6.11. Measured and synthesized S_{21} responses of the filter in the bandpass mode. a) Response with no switches (open) compared with the ideal Butterworth filter. b) Response with absorptive switches compared with the ideal self-equalized filter. c) Response with reflective switches compared to ideal elliptic filter. Note that loss was not included in synthesis.

frequency range in Fig. 6.12. A zero-ohm resistor was used in the bandstop case in Fig. 6.12 to simulate a perfect switch and show the optimal limit of the design. The bandstop mode shows good performance up to 6 GHz, where an unwanted resonance starts to appear. The bandpass mode has 20 dB or greater out-of-band attenuation across the entire frequency range. Because of the extended upper stop band in the bandpass case, no spurious passband circuitry would be required in most systems. A self-equalized filter response was produced by using state-of-the-art, absorptive,

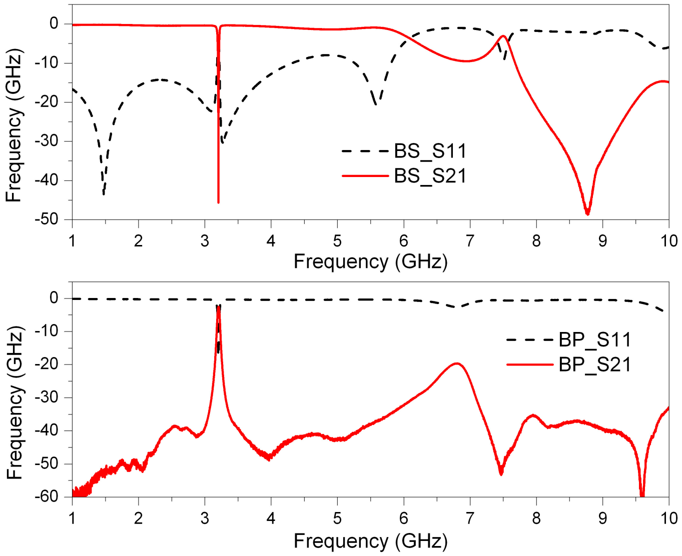

Fig. 6.12. Measured S_{11} and S_{21} responses of the filter in the bandpass and bandstop modes from 1 to 10 GHz. a) Bandstop mode. b) Bandpass mode.

solid-state switches [83] with high isolation and low insertion loss. Synthesized and measured examples can be seen in Fig. 6.11 b). The measured plot in Fig. 6.11 c) was obtained using medium isolation reflective switches [84], resulting in an elliptic response. For the ideal case in Fig. 6.11 a), the filter is centered at 3.21 GHz and exhibits 2.6 dB insertion loss in the passband. Of this loss, 0.12 dB is due to the fact that the filter has stronger external coupling than was designed for due to fabrication tolerances of the circuit board plotter used. Accounting for the mismatch loss, a 1% fractional bandwidth filter with 2.5 dB of insertion loss has a Q of 457 based on gain bandwidth product. Also, according to simulation, 0.1 dB of the loss was due to radiation from the coupling apertures. It can be seen that synthesis lines up well with measurement, noting that loss was not included in synthesis.

Group delay for each filter case can also be seen in Fig. 6.11. The filter in Fig. 6.11 a) has a 13.5 ns group delay in the middle of the passband, with 0.4 ns variation across the band. The filter in Fig. 6.11 b) has a 14.7 ns group delay in the middle of the passband, with 0.6 ns variation across the band. The self-equalized case has a greater group delay than the Butterworth case because it has a narrower bandwidth. The narrower bandwidth is a result of a reduction in M_{01} due to the use of an absorptive switch. For comparison, according to Agilent ADS, a Chebyshev filter with similar bandwidth as the self-equalized filter in Fig. 6.11 b) has a group delay of 18.2 ns in the middle of the passband.

Measured results showing a tunable elliptic bandpass S_{21} response and a tunable bandstop S_{21} response are shown in Fig. 6.13. Note that all traces in the plot are S_{21}.

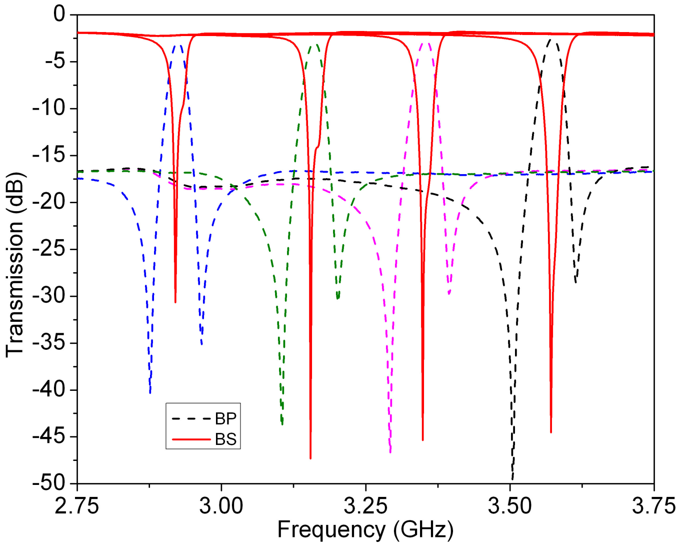

Fig. 6.13. Measured S_{21} response of the filter in bandpass and bandstop modes, tuned across the available tuning range.

The responses in Fig. 6.13 were obtained using a solid-state reflective RF switch [84] in line with the transmission line between the resonators. While the loss is higher when using a solid-state switch, the filter can be switched between modes very quickly in this configuration, on the order of 10 ns. Comparatively, many MEMS switches have switching speeds on the order of 10 μs. Fast switching speed between modes could be important in some situations, because the filter takes roughly 1 ms to tune across the tuning range. For example, if a receiver was using the filter in bandpass mode at 3.5 GHz, and a signal appeared at 2.9 GHz that needed to be sensed quickly, the filter could switch to bandstop mode in 10 ns to make the receive path a through line at 2.9 GHz instead of taking 1 ms to tune that bandpass filter to 2.9 GHz. This opens the receiver to a much wider frequency range, but in some situations the trade-off would be justified.

In bandpass mode, the filter has less than 2.9 dB insertion loss in the passband over the tuning range, which was 2.9 GHz to 3.6 GHz. Up to 50 dB isolation is demonstrated in the out-of-band transmission nulls, which are 1.5% away from the center of the passband. Beyond the transmission zeros, the out-of-band attenuation was 17 dB. In bandstop mode, the filter produces up to 45 dB isolation at its center frequency and has the same tuning range as in the bandpass case. Due to the higher resistance of the solid-state switches in their on state, the filter shows 1.8 dB to 2.4 dB insertion loss across the passband in the bandstop state.

Simulated versus measured data for the 3.35-GHz responses in Fig. 6.13 can be seen in Fig. 6.14. It can be seen that the simulated and measured responses are similar with only minor variation. The insertion loss and transmission zero locations relative to the passband in the bandpass mode were predicted very well. Similarly, the out-of-band loss in the bandstop mode of the filter lines up very well between measured and simulated data. However, there are a few discrepancies that warrant discussion. In the bandpass data, the measured S_{11} away from the passband is 1.7 dB lower than the simulated S_{11}. It is hypothesized that this is due to the finite off-state resistance of the switches on the source-to-load coupling transmission line. In the simulated bandpass data, the switches were modeled as 0.3 pF capacitors in the off-state as a first-order approximation according to the component datasheet. The

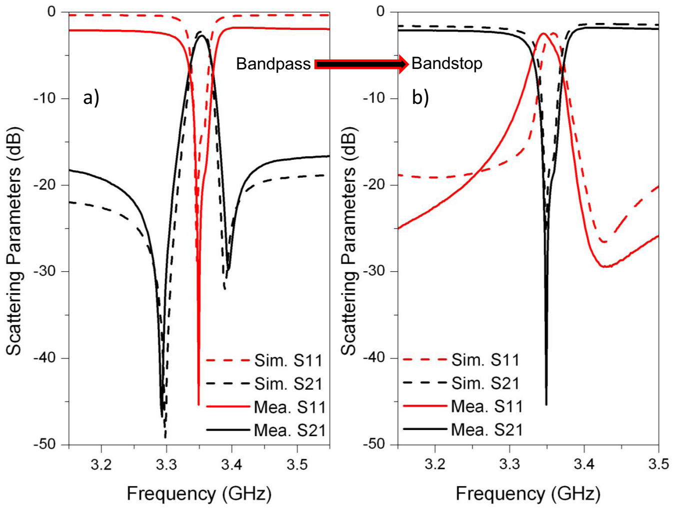

Fig. 6.14. Simulated versus measured data for the 3.35-GHz responses in Fig. 6.13. a) Bandpass data. b) Bandstop data.

finite resistance of the switches in their off-state causes the discrepancy in out-of-band isolation in the bandpass mode. In the bandstop mode, the switch was modeled as a 6-Ω resistor as a first-order approximation according to the component datasheet. The discrepancy in filter bandwidth can be attributed to the fact that the external coupling apertures were cut slightly too large by the circuit board plotter.

6.5 Performance Improvement Through the Use of State-of-the-Art MEMS Switches

In contrast to previous bandpass-to-bandstop reconfigurable filters, the narrowband bandpass-to-bandstop filter described above integrated mode-switching components in its coupling structures, as opposed to in the resonators of the filter. This prevents the switching components from reducing the quality factor (Q) of the filter's resonators, but it relies on the switching components' isolation level in bandpass mode and insertion loss in bandstop mode. In bandpass mode, the isolation of the switch limits the out-of-band isolation of the filter. In bandstop mode, the on-state loss of the switch increases the out-of-null insertion loss of the filter. Many commercially available solid state switches offer high isolation or low on-state loss, but none offer both at the levels required for implementing a low loss, high isolation, narrow-band bandpass-to-bandstop filter. However, the latest MEMS switches, in this case Radant MEMS RMSW303 switches, promise up to 70 dB isolation and as low as 0.3 dB insertion loss at 2 GHz. This increased level of switch performance opens up new uses for bandpass-to-bandstop filters in practical communications systems.

6.5.1 Filter Design

The bandpass-to-bandstop filter that used solid-state switches and was described above was redesigned to use an advanced series-shunt configuration MEMS switch from Radant MEMS. Fig. 6.15 compares the transmission responses of the solid-state switch bandpass-to-bandstop filter (Fig. 6.15 a)), the zero ohm and open circuit response, approximating a perfect switch, of the previously described filter (Fig. 6.15 b)), and the new MEMS switch bandpass-to-bandstop filter (Fig. 6.15 c)). The re-

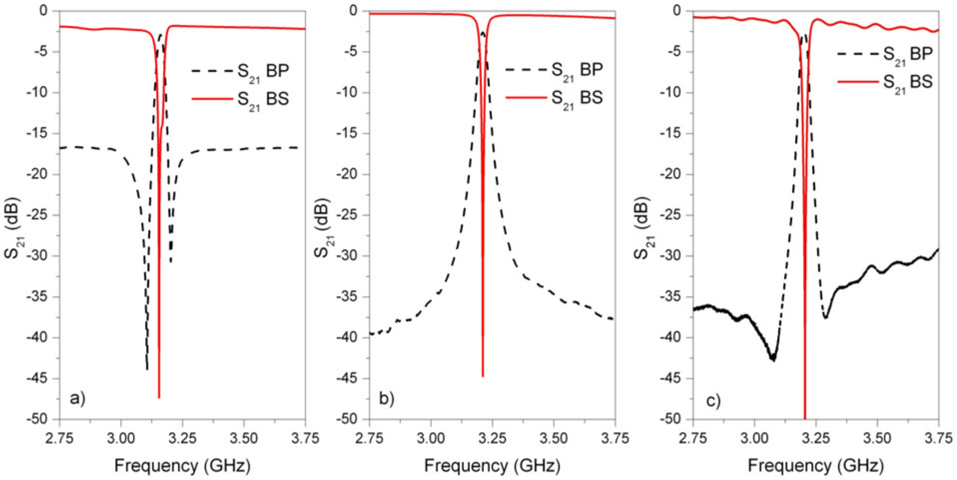

Fig. 6.15. a) Measured BP-BS filter S21 responses using a common, solid state switch (on-bandstop, off-bandpass). b) Measured BP-BS filter S21 responses using a zero ohm resistor (bandstop) and an open circuit (bandpass). c) Measured BP-BS filter S21 responses using Radant MEMS switch.

sponse in Fig. 6.15 c) is much closer to the optimal performance shown in Fig. 6.15 b) than the result for the solid state switch shown in Fig. 6.15 a) due to the increased performance of the MEMS switch. An image of the filter and its model can be seen in Fig. 6.16. While some of the design parameters are slightly different, the construction methods are the same as what is described above for the solid-state switch bandpass-to-bandstop filter. Note that in contrast to the solid-state switch filter described above, a single MEMS switch is used instead of two solid state switches. Using a single MEMS switch reduces the away-from-stopband insertion loss in the bandstop mode of the filter (switch on). This can be done because the isolation of the switch in its off-state (bandpass mode) is very high. In fact, measurements and simulations show that the switch isolation is higher than the substrate and slot radiation coupling

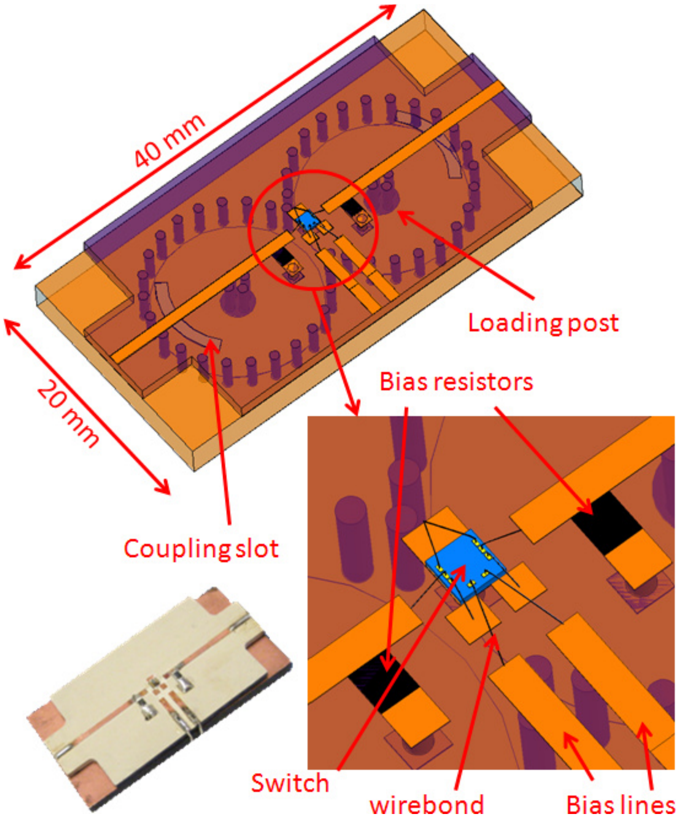

Fig. 6.16. Image of the model and fabricated filter with an integrated MEMS switch and bias control circuitry.

of the filter structure itself. Therefore, using one MEMS switch should not degrade the bandpass out-of-band isolation of the filter.

However, using a single MEMS switch does introduce one constraint compared to a two-switch filter configuration. The strength of the external coupling into each resonator is set by the coupling slot geometry and the strength and distribution of the magnetic field of the wave on the microstrip line. In the bandstop mode of the filter, assuming a perfect switch, the coupling into the resonators is primarily determined by the slot geometry. In the bandpass mode of the filter, assuming a perfect reflective switch is used, an open circuit occurs at the switch location. This open circuit results in reflections which change the magnetic field strength in the vicinity of the coupling slot compared to the bandstop (switch on) state of the filter. Therefore, with one switch, the relationship between the external coupling in the bandpass mode and the external coupling in the bandstop mode is fixed. If two switches are used, the locations of the switches can be chosen to create open circuits at locations on the transmission line which will give a desired difference in external coupling between the two modes of operation, resulting in the ability to design different filter shapes in the bandpass and bandstop modes of operation. In the design presented next, one switch was used in order to minimize bandstop mode insertion loss away from the null.

6.5.2 Integrated MEMS Filter Performance Enhancements

Measured results of the filter can be seen in Fig. 6.17. Fig. 6.17 a) shows the transmission and reflection responses of the filter in the bandpass state. The filter has a passband insertion loss as low as 2.4 dB, can continuously tune over a 1.95 GHz to 3.8 GHz frequency range, and has a 1.06% FBW. Compared to the solid state switch bandpass response shown in Fig. 6.15 a), the isolation level far from the passband was improved from 17 dB to as high as 37 dB. Fig. 6.17 b) shows the transmission response of the filter in the bandstop state. The reflection response was omitted for clarity, but it shows no abnormalities. In the bandstop mode, the filter

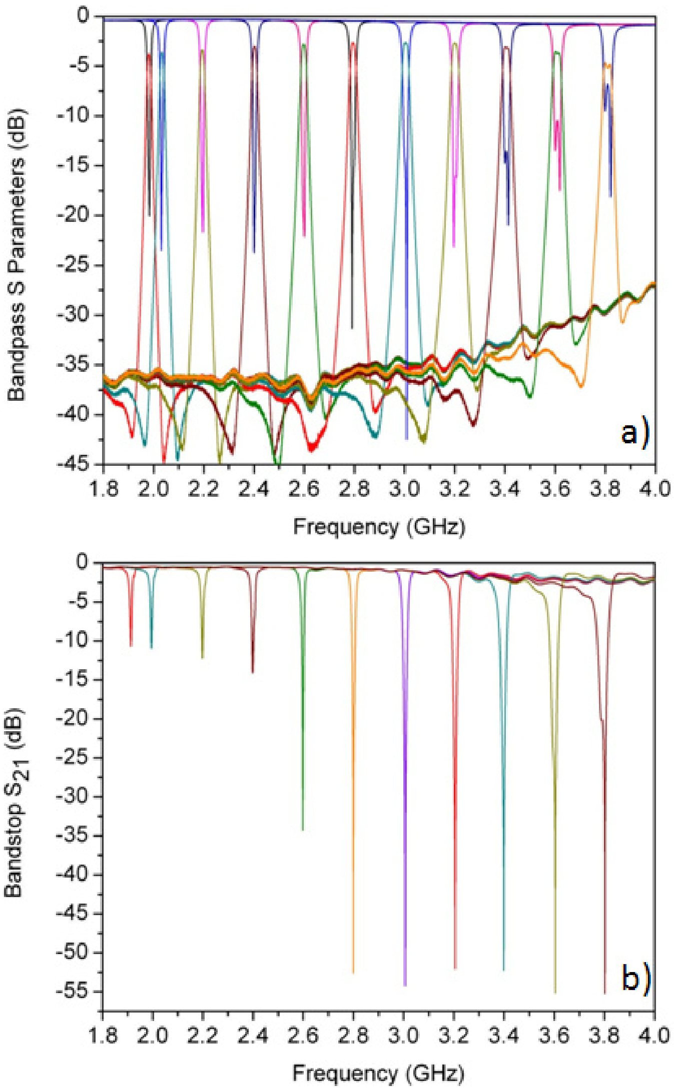

Fig. 6.17. Measured response of MEMS-integrated filter in a) bandpass mode and b) bandstop mode.

can tune over the same frequency range as in the bandpass mode, provides up to 55 dB of attenuation, and has a 0.82% FBW. Compared to the solid state switch bandstop response shown in Fig. 6.15 a), the insertion loss away from the stopband is lower, especially in the lower end of the frequency range (0.5 dB at 2 GHz).

The performance of the filter in both states starts to degrade in the higher end of the frequency tuning range. This is possibly an effect of the grounding and wire bonding techniques used to attach the MEMS switch. As can be seen in Fig. 6.16, 1 mm long wire bonds were used to connect the filters microstrip line to the switch, which has a co-planar waveguide (CPW) port. Ideally, the wire bond would be shorter and connect a CPW transmission line to the CPW switch port. Additionally, a single plated via was placed under the switch for grounding. Ideally, the grounding strategy would use several distributed vias to reduce undesired inductance. While making these design changes might improve the filter performance, the measurements in Fig. 6.17 are the best narrow-band bandpass-to-bandstop filter response shown to date in terms of insertion loss and tuning performance.

6.5.3 Dynamic Spectrum Utilization of Bandpass-to-Bandstop Filters

Bandpass-to-bandstop filters offer microwave systems interesting, new reconfiguration trade-offs. Many of these trade-offs involve consideration of the delays during switching between modes and tuning to varying frequencies. Three particularly interesting spectrum sequences that are well-served by the capabilities of a tunable bandpass-to-bandstop filter will be discussed. The first is when the bandpass-to-bandstop filter is in bandpass mode, centered at frequency f_0 as in Fig. 6.18 a). If a high priority signal suddenly appears at $f_0 + \Delta f$, it may not be desirable to wait until the bandpass filter can tune to $f_0 + \Delta f$ because important information would be lost. In this case, the filter can quickly switch to bandstop mode to receive the signal at $f_0 + \Delta f$ at the cost of the receiver being open to a wide range of spectrum as shown in Fig. 6.18 b). The opposite situation is also interesting. If the filter is set at f_0 in bandstop mode, and a high power signal appears at $f_0 + \Delta f$, the filter could switch to bandpass mode quickly to protect and retain the dynamic range of the system while still listening to a part of the spectrum. It will take a finite amount ot time to tune the bandpass filter to the desired band, but the system will be protected during this process by the out of band attenuation in the bandpass mode. Finally, the third interesting spectral sequence that will be investigated also involves the bandpass-to-bandstop filter starting in bandstop mode at f_0. If the signal at

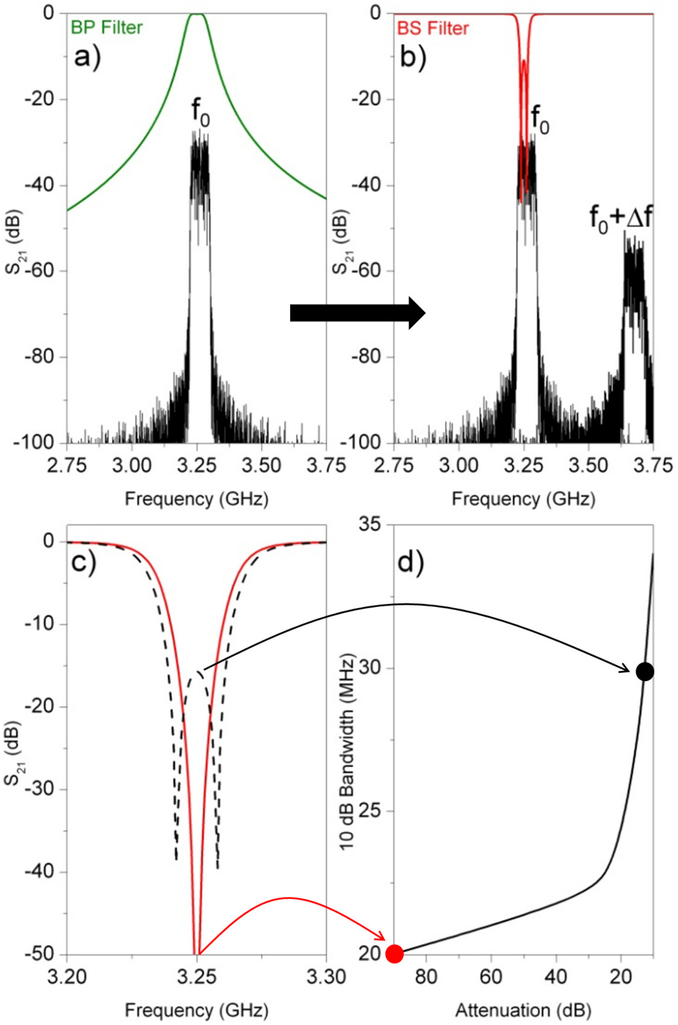

Fig. 6.18. a-b) Switching from BP to BS mode to quickly allow a new, high priority signal into the receiver. c-d) Trading notch depth for width to attenuate a spectrally wider interferer.

f_0 becomes wider than the bandwidth of the filter, energy could still get through to the receiver and degrade system performance. However, the MEMS-integrated bandpass-to-bandstop filter in bandstop mode is capable of tuning its frequency response between a Butterworth and Chebychev filter shape. In effect, this allows it to optimize its "attenuation-bandwidth product" for a given interfering signal. For example, the filter could be designed to provide 10 dB of attenuation over a 20 MHz bandwidth with high attenuation at f_0, but then could be electronically reconfigured to provide 10 dB of attenuation over a 30 MHz bandwidth. Both cases are shown in Fig. 6.18 c). Fig. 6.18 d) shows the trade-off trend between 10 dB bandwidth and equi-ripple attenuation with the cases in Fig. 6.18 c) indicated. This concept is described in [36].

6.6 Conclusion

An electronically reconfigurable bandpass-to-bandstop filter was shown that can utilize the same set of coupled resonators and switch the feeding structure to change between different modes of operation. For example, the filter can exhibit Butterworth and elliptic bandpass responses as well as a Butterworth bandstop response by changing the state of the feed network and slightly adjusting the center frequencies of the resonators. The theory of such a filter was developed through the use of coupling matrices and coupling coefficients such that the inter-resonator coupling remained unchanged. A detailed bandpass-to-bandstop filter design process was also presented. In bandpass mode, the fabricated filter had less than 3 dB of insertion loss for a 1.06% 3-dB bandwidth filter, and, in bandstop mode, the filter provided greater than 45 dB of isolation. A second bandpass-to-bandstop filter that used a single MEMS switch to transform its response between bandpass and bandstop shapes was also designed. Compared to previous designs that used solid-state switches, the filter showed increased out-of-band attenuation in its bandpass mode and decreased insertion loss away from the stopband in its bandstop mode.

Benefits and applications of a bandpass-to-bandstop reconfigurable filter are envisioned to include general system flexibility at no cost of physical space, concurrent transmit and receive schemes, and multi-element antenna systems, but there are many other possible uses. In cognitive radio environments, these filters would be valuable to radio systems to isolate signals of interest or attenuate interfering signals, depending on the environment or mode of operation of the radio. This flexibility will be required since the electromagnetic environment of the future will be open and constantly changing.

7. SWITCHLESS TUNABLE BANDSTOP-TO-ALL-PASS RECONFIGURABLE FILTER

7.1 Introduction

The use of the bandstop filters, filter cascades, and shape reconfigurable filter described in previous chapters all assume that interference mitigation will be required by the systems that employ them. However, in systems that have high dynamic range analog to digital converters, front ends made of materials with high heat conduction and dielectric breakdown voltage, use cases in sparse signal environments, and/or the cognitive capability to determine the location of interfering signals, the need for interference mitigation could be significantly reduced or dependent on the presence very large, intermittent signals. In some situations, the presence of pre-LNA filters only increases insertion loss or decreases sensitivity with no corresponding performance advantage. For example, most past and current microwave front ends are primarily designed with bandpass filters for protection from generating or receiving unwanted interference [85]. One reason for the ubiquity of bandpass filters is that most microwave systems are unaware of the spectrum in which they are operating. This creates a need for a fear-based front-end architecture that attenuates all frequencies except the band of interest. However, a front-end architecture based on bandpass filters can result in significant insertion loss in the frequency band of interest, limiting system performance. For a given resonator quality factor (Q), there is a trade-off between bandpass filter bandwidth, order, and passband insertion loss [68]. Therefore, the greater the protection from generating or receiving interference in adjacent frequency bands, the higher the insertion loss in the band of interest.

A microwave system that is cognizant of the spectrum in which it is operating [6] would not need to operate in the fear-based mode of operation described above.

In fact, it could use no filtering if there was not strong interference present. This would have the benefits of lower insertion loss than bandpass-centric front ends and much greater operating frequency flexibility. For example, a bandpass-centric system would need to switch between static filters in a bank [86], [87] or employ a tunable filter [88]- [91] to change operating frequencies. These methods involve a further increase in insertion loss due to the switch or a time delay due to filter tuning and shape adjustment, respectively. A front end without filtering has neither of these issues. In the event that interference became a concern, the spectrally aware system would know its frequency and could place a tunable bandstop filter [33]- [52] in its front end frequency response to attenuate it. Employing tunable bandstop filters in spectrally aware systems minimizes insertion loss in the band of interest and maximizes the frequency range in which the system can instantaneously operate. Wideband systems [94] and systems with highly linear LNAs [95] could benefit most from such an interference mitigation strategy. Allowing a receiver to take advantage of the benefits of a bandstop filter-centric front end while dynamically allowing for a mode of operation which allows signals at all frequencies to be received in low power environments is the motivation of this chapter.

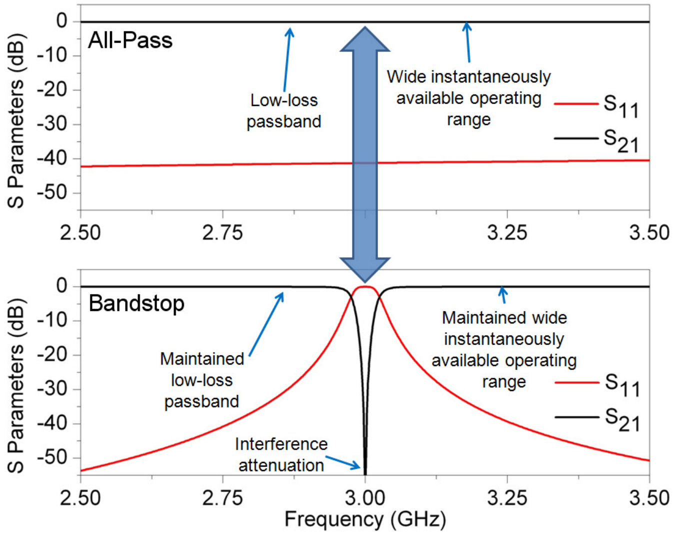

Fig. 7.1. Concept and benefits of a bandstop-to-all-pass filter.

One way to have an open front end frequency response in which bandstop filters can be added to on demand is to use bandstop filters that have a mode of operation that allows all frequencies to pass. This concept is shown in Fig. 7.1. Bandstop filters with this capability were shown in [96], [97], and [98]. However, [96] uses superconducting structures and switches, which are not practical in some situations due to large volume and power requirements. [97] also used switches in order to selectively add a parallel bandpass filter to the circuit which had a passband over the same frequency range as the stopband of the bandstop filter. [98] achieves the desired effect without using switches for single bandstop resonators which are twice-coupled to a through transmission line. Multi-pole filters are demonstrated in [98] by cascading the single resonator structures. While the method in [98] achieves superior all-pass state insertion loss, it requires the use of long transmission lines and two tuning elements with each resonator. This chapter presents the theory and measurement of switchless second-order bandstop filters that use series-coupled resonators to achieve bandstop-to-all-pass operation and attenuation level tuning, as well as the effect of finite resonator Q values on the all-pass response. In contrast to [98], the filter theory presented in this chapter does not require coupling over large phase lengths of distributed resonators and can achieve a bandstop-to-all-pass response using a single tuning element per resonator. However, as noted above, the method in [98] produces less all-pass state insertion loss. This tradeoff between tuning complexity and all-pass state insertion loss makes both methods valuable. The measured filter was implemented with tunable highly-loaded coaxial cavity resonators. These resonators have been used extensively by the authors and others to implement bandpass [38]- [99] and bandstop [54], [100] filters. However, it is important to note that the filter theory presented in this chapter is applicable to filters using any type of tunable bandstop resonator.

7.2 Bandstop-To-All-Pass Filter Theory

7.2.1 Bandstop And All-Pass State Responses

For the filters described in this chapter, both external coupling values will be equal to each other, the resonator self-coupling values will have the same magnitude but opposite sign, and symmetries such as the source-to-load coupling being the same as the load-to-source coupling can be taken advantage of to simplify the generalized second order filter $(N+2)\times(N+2)$ coupling matrix $\mathbf{M}$ to

$$\mathbf{M} = \begin{bmatrix} 0 & M_{01} & 0 & M_{03} \\ M_{01} & M_{11} & M_{12} & 0 \\ 0 & M_{12} & -M_{11} & M_{01} \\ M_{03} & 0 & M_{01} & 0 \end{bmatrix}, \tag{7.1}$$

where the subscripts 0 and 3 correspond to the source and load, respectively, and the subscripts 1 and 2 correspond to the first and second resonator, respectively. (7.1) corresponds to the coupling routing diagram shown in Fig. 7.2.

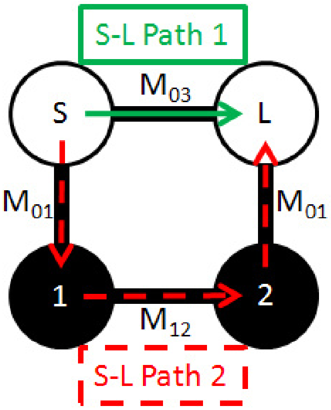

Fig. 7.2. Coupling routing diagram. S = source, L = load, 1 = resonator 1, 2 = resonator 2.

In [36], it was shown that a Butterworth bandstop filter response can be obtained from a structure with the coupling relationships in Fig. 7.2 if the correct relationship between M_{11} and M_{12} is maintained and M_{12} and M_{03} have the same sign. After substituting a value of positive one for M_{03} to represent coupling through a source-to-load inverter, the coupling relationships in (7.1) produce the transmission response

$$|S_{21}| = \left|\frac{s^2 + M_{11}^2 + M_{12}^2 - M_{01}^2 M_{12}}{s^2 + M_{01}^2 s + \frac{1}{2}M_{01}^4 + M_{11}^2 + M_{12}^2 - M_{01}^2 M_{12}}\right|, \tag{7.2}$$

where s is the normalized frequency variable and is equal to $j\omega$ where j is the square root of -1 and ω is radian frequency. In [36], the transmission response in (7.2) was set equal to zero at a normalized frequency of zero to solve for the required relationship between M_{11} and M_{12} to produce a Butterworth bandstop response. If (7.2) is set equal to one, a solution exists not only at a normalized frequency of zero, but also at all frequencies if the resonators are synchronously tuned. In (7.1), synchronously tuned resonators are represented by an M_{11} value of zero. One set of solutions that results from setting (1.2) equal to one at all frequencies is

$$\begin{gathered} M_{01} = Arbitrary \\ M_{12} = \frac{M_{01}^2}{2} \\ M_{11} = 0. \end{gathered} \tag{7.3}$$

With the relationship between M_{01} and M_{12} in (7.3) in place, the transmission response in (7.2) becomes

$$|S_{21}| = \left|\frac{s^2 + M_{11}^2 - \frac{M_{01}^4}{4}}{s^2 + M_{01}^2 s + M_{11}^2 + \frac{M_{01}^4}{4}}\right|, \tag{7.4}$$

which has a magnitude of one for all values of $s = j\omega$ if M_{11} is zero. In other words, the magnitude of the numerator in (7.4) equals the magnitude of the denominator in (7.4) for all frequencies if the resonators are synchronously tuned. This is the all-pass state of the bandstop-to-all-pass filter.

However, the magnitude of (7.4) is not equal to one at all frequencies if M_{11} is set to a value other than zero. In addition, if (7.4) is set equal to zero at a normalized frequency of zero, there is a solution for M_{11}. The solution is

$$M_{11} = \frac{M_{01}^2}{2}, \tag{7.5}$$

which yields the bandstop state of the bandstop-to-all-pass filter. In order for the bandstop state of the bandstop-to-all-pass filter to have the correct bandwidth in the normalized frequency domain, M_{01} should be set to a specific value for the desired filter shape. Any desired filter shape can be implemented since M_{01} can be arbitrary in the all-pass state of the filter according to (7.3). Therefore, setting M_{01} to correctly implement the bandstop filter state has no effect on the all-pass filter state.

In summary, if the relationship between M_{01} and M_{12} is designed correctly in a tunable second order bandstop filter, the filter response can be switched between bandstop and all-pass states by merely tuning the resonant frequencies of the resonators so that M_{11} varies between zero and the value in (7.5). Frequency-scaled versions of the ideal synthesized bandstop and all-pass state responses according to the theory above can be seen in Fig. 7.1, where a second-order Butterworth response shape was chosen for the bandstop state of the filter. A second-order Butterworth bandstop filter requires an M_{01} of 1.189 [101].

7.2.2 Variable Attenuation and Bandwidth

If M_{11} is set to a value other than zero or the value in (7.5), other states of the filter are possible. If M_{11} is varied between zero and the value in (7.5), a bandstop filter response with variable bandwidth and attenuation results. This response could be useful in applications that require signal equalization. Additionally, if several filters of this type with different frequency tuning ranges were cascaded, the cascade could be dynamically reconfigured to provide frequency equalization, selective attenuation, or an all-pass response over very wide frequency ranges. If M_{11} is increased beyond the value in (7.5), a variable attenuation and bandwidth equi-ripple shape is achieved. The equi-ripple shape offers a wider bandwidth for a given level of attenuation than the Butterworth response, and the response can be tuned between these two states dynamically if tunable resonators are used. This greatly increases the flexibility of the filter. Example synthesized transmission responses and the associated M_{11} values can be seen in Fig. 7.3. The inset shows that the 10 dB bandwidth of the transmission response varies almost linearly with the scaling factor of M_{11} relative to the value in (7.5) over the range shown.

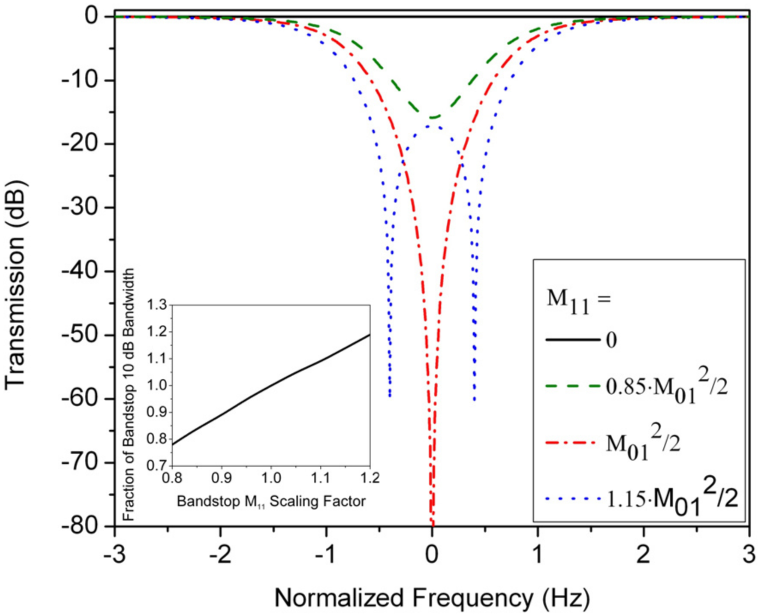

Fig. 7.3. Synthesized bandstop state response shapes as M_{11} is varied from the value in (7.5) by a scaling factor. Inset shows fraction of 10 dB bandwidth relative to the ideal Butterworth case (when M_{11} equals the value in (7.5)) vs. M_{11} scaling factor relative to the M_{11} value in (7.5).

7.3 Effect of Filter Bandwidth and Finite Unloaded Quality Factor on All-Pass State Response

The bandstop-to-all-pass capability described in the previous section results from changing the value of the self-coupling, M_{11}, in the coupling matrix. Physically, this adjusts the phase response of the resonators by tuning along the reactance slope of their resonances. These changes in phase tune the interference between the filter's two source-to-load signals paths between constructive and destructive interference at the output port. The two signal paths can be seen in Fig. 7.2. In the ideal synthesis described in the previous section, there was no loss in either of the source-to-load signal paths. Therefore, both perfect constructive and destructive interference were achieved in the synthesis equations. However, loss will exist in both signal paths in a fabricated filter, and the loss of each of the signal paths will not be equal in most real implementations. Different losses in the two source-to-load signal paths will have two main effects on a bandstop-to-all-pass filter's response. First, in the bandstop state, the filter will not produce infinite attenuation. This is the case for any real bandstop filter. Second, in the all-pass state, the signals from the two source-to-load paths will not perfectly reproduce the input signal at the output port. This lack of perfect signal reconstruction results in an unwanted all-pass state difference in passband insertion loss at the resonant frequency of the filter relative to non-resonant frequencies that is proportional to the difference in losses between the two source-to-load signal paths. The effect of imperfect signal reconstruction at the output port can be analyzed using a modification to (7.1). If the coupling mechanism that implements M_{03} in Fig. 7.2 is assumed to be lossless, a difference in loss between the two source-to-load signal paths can be completely modeled by assigning a finite resonator unloaded Q. A finite resonator unloaded Q can be added to (7.1) as

$$\mathbf{M} = \begin{bmatrix} 0 & M_{01} & 0 & M_{03} \\ M_{01} & -\frac{j}{Q_u\Delta} & M_{12} & 0 \\ 0 & M_{12} & -\frac{j}{Q_u\Delta} & M_{01} \\ M_{03} & 0 & M_{01} & 0 \end{bmatrix}, \tag{7.6}$$

where Q_u is resonator unloaded Q and Δ is the 3 dB fractional bandwidth. The larger Q_u and Δ are, the closer the response of (7.6) will become to the ideal response of (7.1). Although this analysis uses a lossless coupling mechanism for M_{03}, it approximates reality well because M_{03} is frequently implemented with a low-loss transmission line in bandstop filters.

While (7.6) shows that Δ and/or Q_u can be increased in order to improve the all-pass state response of a bandstop-to-all-pass filter, Δ is usually set by specific application requirements. Similarly, specific application requirements will require a maximum all-pass state insertion loss, which dictates the Q_u needed. The second-order Butterworth filter equation of the required Q_u for a specified Δ and a desired level of all-pass state insertion loss can be derived from (7.6), and it is

$$Q_u = \frac{1}{1.414\Delta\left(\frac{1}{\left|S_{21(0)}\right|+1} - \frac{1}{2}\right)}, \tag{7.7}$$

where $S_{21(0)}$ is the insertion loss at $s = 0$ in linear scale. For example, if Δ is required to be 2%, (7.6) produces the normalized frequency domain all-pass state transmission responses in Fig. 7.4 as Q_u is varied. Note that all of the responses in Fig. 7.4 have a theoretically perfect impedance match to the ports of the system. Fig. 7.4 shows that with very high Q_u values the response approaches the ideal lossless case described in the previous section. As Q_u is lowered, the all-pass state has more and more insertion loss until a special case is reached. This special case is an absorptive bandstop filter [102]- [104], which has theoretically infinite attenuation in its stopband and is perfectly impedance matched at all frequencies. The high Q_u examples are

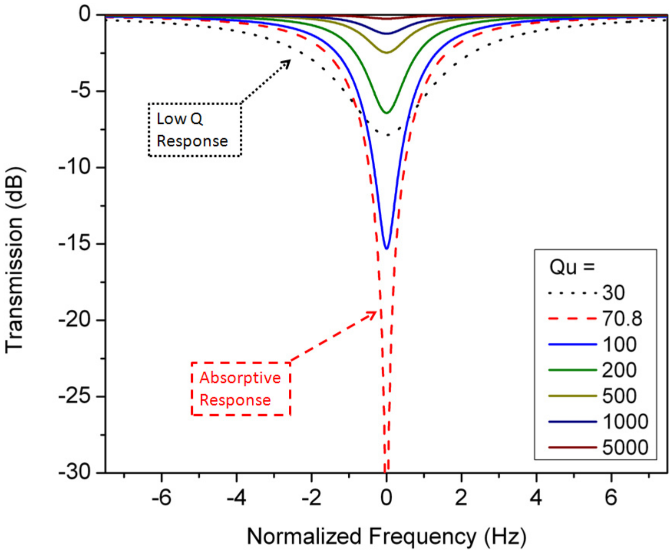

Fig. 7.4. Synthesized all-pass state responses for a 2% fractional bandwidth bandstop filter for various unloaded Q values. In all responses, the return loss is 0 (-∞ dB).

shown with solid traces in Fig. 7.4, while the absorptive case is designated by a dashed trace. The dotted trace in Fig. 7.4 shows an example of the wide, shallow response that occurs when Q_u is below the value that produces the absorptive response. The responses in Fig. 7.4 demonstrate that in order to implement a bandstop-to-all-pass filter with the best all-pass state for a given Δ, high-Q tunable resonators are required. Finally, while this chapter presents theory for a two-pole bandstop filter, the analysis for higher-order filters is similar. It is important to note that the all-pass state insertion loss due to finite-Q_u resonators described above accumulates for higher-order filters.

7.4 Filter Design and Fabrication

Evanescent-mode cavity resonators have been shown to have wide tuning ranges while retaining high Q values [38], [64], [55]. These traits make them very well suited for use in realizations of bandstop-to-all-pass filters. In order to verify the theory presented above, an evanescent-mode cavity based, second-order filter was designed and fabricated. A model of the filter with dimensional annotations can be seen in Fig. 7.5. The filter includes three copper layers and two dielectric layers. The top copper layer in Fig. 7.5 is the source-to-load transmission line. In this implementation, a 270 degree transmission line at 3 GHz was chosen in order to match the sign of its coupling to the sign of the inter-resonator coupling as required by (7.1). The inter-resonator coupling and its sign will be explained further below. The source-to-load transmission line also employs capacitive patches to improve impedance matching in the filter's upper passband as described in [100]. The top dielectric layer of the filter structure is a 0.762 mm thick sheet of Rogers 4350B material (ϵ_r=3.66, tan(δ)=0.0037 @ 10 GHz) that has rectangles cut out of it to facilitate grounding of the input and output connectors.

The second copper layer of the structure is the ground plane for the source-to-load transmission line. This copper layer also contains coupling apertures that couple the

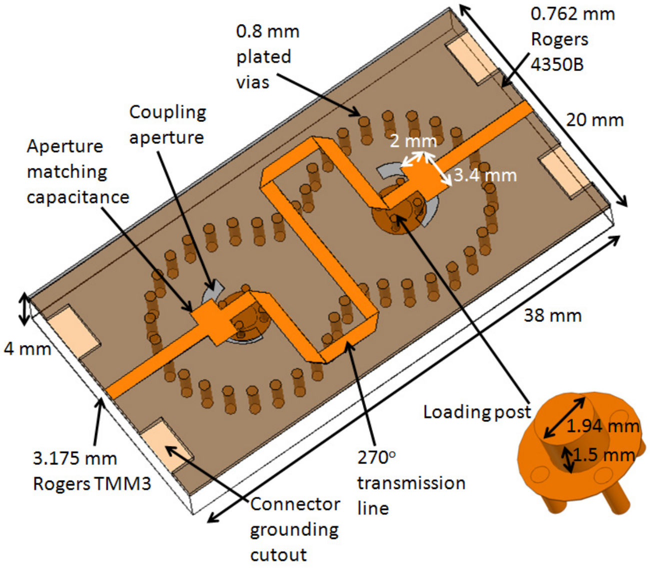

Fig. 7.5. Simulation model of the fabricated bandstop-to-all-pass filter.

mode of the source-to-load transmission line to the mode of the cavity resonators. These coupling apertures were sized and optimized in simulation to produce the correct amount of coupling for a 2.5% fractional bandwidth Butterworth response [76]. The second dielectric layer of the structure is a 3.175 mm thick sheet of Rogers TMM3 material (ϵ_r=3.27, tan(δ)=0.002 @ 10 GHz) that contains the evanescent-mode cavity resonators. The two dielectric layers of the structure were bonded together using DuPont Pyralux LFO100 adhesive. The cavity walls are formed by 0.8 mm diameter copper-plated vias, and the cavity diameter is 13.6 mm from the center of one via to the center of the opposite via. The cavities have copper-plated loading posts that are 1.94 mm in diameter and 1.5 mm tall. These loading posts are supported on a copper platform that is connected to the top of the cavity in Fig. 7.5 by four plated vias. The inset in Fig. 7.5 shows the geometry of the loading posts inverted with respect to their orientation in the full structure shown in Fig. 7.5 for clarity.

Inter-resonator coupling is implemented through an iris between the two cavities. The iris was designed in simulation to produce the correct M_{12} value according to (7.5) [105]. Iris coupling, which is predominantly magnetic field coupling, was chosen

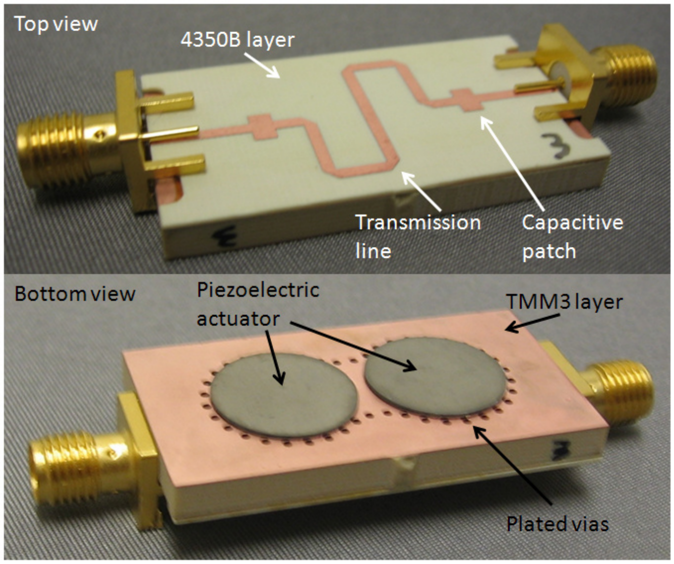

Fig. 7.6. Top and bottom views of the fabricated bandstop-to-all-pass filter.

because of the field distribution in evanescent-mode cavities. Since most of the electric field in the cavity is concentrated in the gap above the loading post, the magnetic field is much more accessible. The inter-resonator coupling can be modeled as an inductive T network that has an insertion phase that approaches 90 degrees. This requires a 270 degree electrical length source-to-load transmission line in order to properly implement (7.1) and have the same sign coupling for both M_{03} and M_{12}. However, evanescent-mode cavity compatible inter-resonator coupling structures that provide the opposite sign coupling compared with the iris implemented in this chapter exist [27]. The third copper layer of the structure is a thin copper membrane that is laminated to the TMM3 layer everywhere except within the boundaries of the cavity walls. This allows the thin copper membrane to flex above the loading posts. 0.38 mm thick, 1/2 inch diameter piezoelectric actuators from Piezo Systems, Inc. are attached to the side of the flexible copper membranes external to the cavity using silver epoxy. Images of the fabricated filter can be seen in Fig. 7.6. Fig. 7.6 clearly shows the positioning of the piezoelectric actuators.

7.5 Measured Results

Measured results of the bandstop and all-pass states of the fabricated filter can be seen in Fig. 7.7. Fig. 7.7 shows a 2.1 dB insertion loss in the all-pass state at 3.05 GHz. When the resonators are tuned away from 3.05 GHz, the response has insertion loss of 0.4 dB. Therefore, the all-pass state resonances provide an additional insertion loss of 1.7 dB at 3.05 GHz in the all-pass state. A 15 dB or greater return loss is maintained from 1 GHz to 4.25 GHz, and the response approximates a through transmission line. In the bandstop state, attenuation of 69 dB is shown, and the 3 dB fractional bandwidth is 2.7%. According to the theory described above, this fractional bandwidth and all-pass level of attenuation corresponds to a resonator Q of 540, which is in line with Q's of previously-reported, similarly sized evanescent-mode cavity resonators [55]. The response is also able to be tuned to any attenuation level between the 2.1 dB and 69 dB shown in Fig. 7.7 by tuning the resonant frequencies of the resonators. For example, tuning M_{11} to the value in (7.5) results in the 69 dB attenuation response. Fig. 7.8 shows the 2.1 dB, 10 dB, 20 dB, 30 dB, and 70 dB

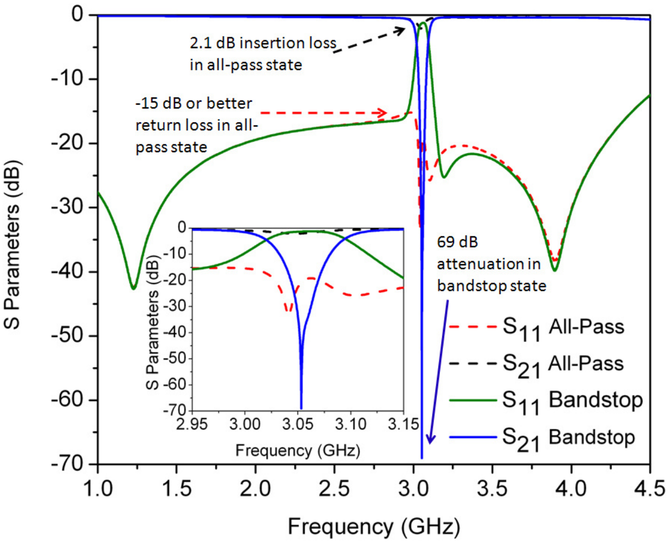

Fig. 7.7. Measured bandstop and all-pass states of the fabricated bandstop-to-all-pass filter.

attenuation responses of the fabricated filter. This functionality would be useful in applications that require signal equalization.

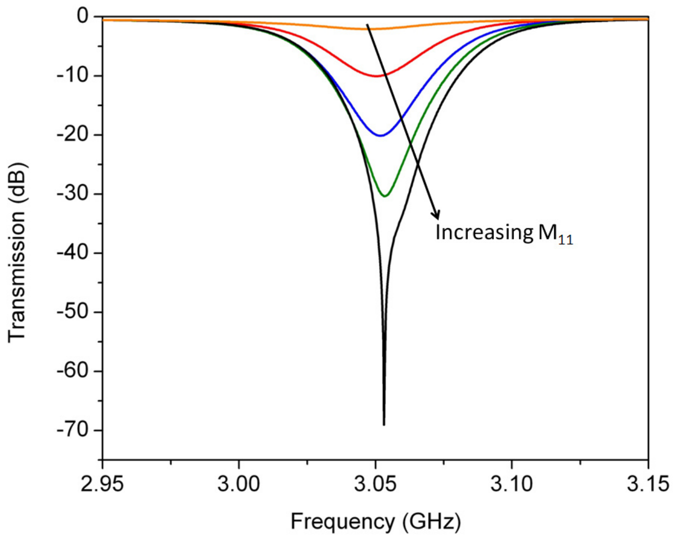

Fig. 7.8. Measured 2.1 dB, 10 dB, 20 dB, 30 dB, and 70 dB attenuation states of the fabricated bandstop-to-all-pass filter.

Measured vs. simulated S_{11} and S_{21} responses can be seen in Fig. 7.9. In the all-pass state, the measured insertion loss at the resonant frequency of the resonators is 2.1 dB vs. a simulated value of 1.8 dB. This difference is due to the lower quality factor of the fabricated resonators compared to the simulated resonators which can result from copper surface roughness and oxidation. Connector losses also contribute to the difference in insertion losses. The measured filter's upper passband starts to degrade at lower frequencies compared with the simulated filter. The degradation is the result of an impedance mismatch caused by the coupling apertures in the ground plane of the source-to-load transmission line. Imperfections in the size of the coupling apertures or the capacitive matching patches in the feeding microstrip transmission line relative to the simulated geometry produce lower frequency passband degradation like what is shown in Fig. 7.9 a). However, the measured performance matches the simulated performance well in the band of interest. In the bandstop filter state shown in Fig. 7.9 b), the measured 3 dB fractional bandwidth was 2.7% vs. a simulated value of 2.5%.

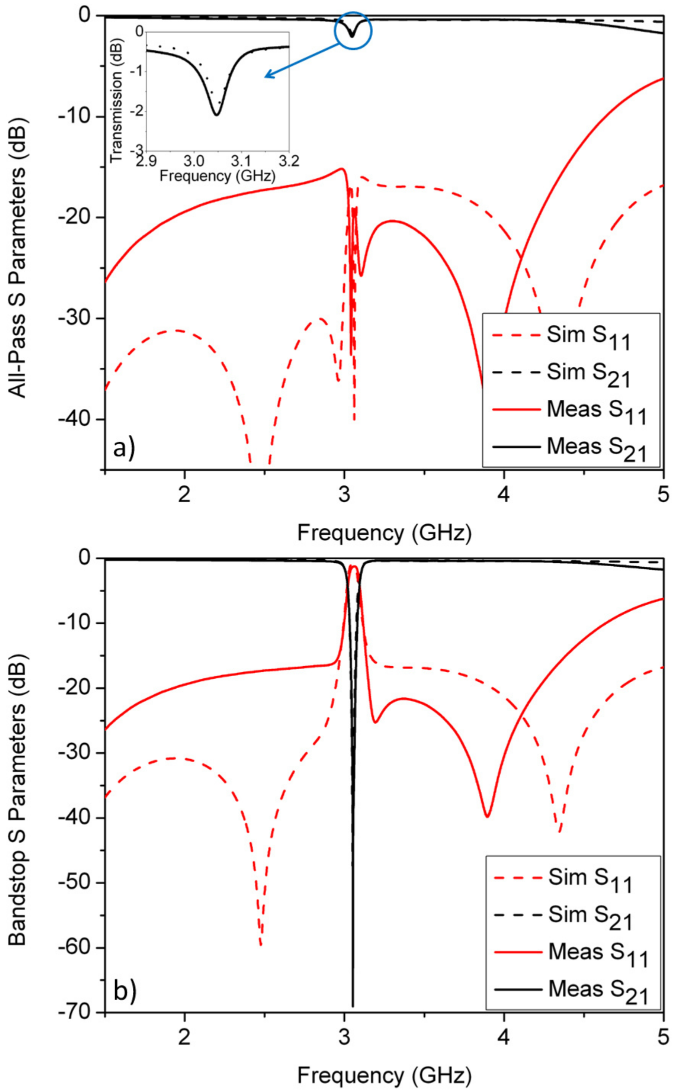

Fig. 7.9. Measured vs. simulated S parameters for the bandstop-to-all-pass filter: a) All-pass state b) Bandstop state.

This difference supports the theory above that the coupling apertures may have been fabricated to be a slightly incorrect size. In addition, the measured reflection zeros are not at the same frequencies at which they appear in the simulated response, further supporting an unmodeled impedance mismatch at either the coupling slots or the connector-to-microstrip transition. While fabrication process limitations resulted in 50 to 200 μm of inaccuracy, the shape and attenuation levels of the measured bandstop response still match simulated results well and prove the bandstop-to-all-pass concept. Standard professional fabrication facilities would be able to reduce these inaccuracies greatly.

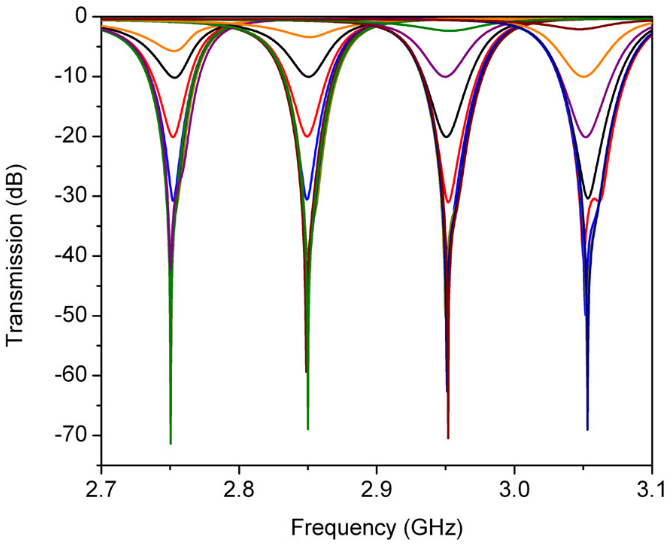

Fig. 7.10. Several measured response states of a single filter tuning from 2.75 GHz to 3.1 GHz. Less than 4 dB, 10 dB, 20 dB, 30 dB, 40 dB, 50 dB, 60 dB, and 70 dB attenuation states are shown. Note that the center frequency of the filter is continuously tunable over the entire range.

The lowest measured all-pass state insertion loss, 2.1 dB, was achieved at 3.05 GHz. However, the all-pass response, as well as the variable attenuation capability shown in Fig. 7.8, can be continuously tuned over the range of 2.75 GHz to 3.1 GHz with insertion loss less than 4 dB in the all-pass state. Fig. 7.10 shows measurements of many of the possible response shapes in this band. The filter is continuously tunable in both frequency and attenuation from 2.75 GHz to 3.05 GHz and from 2.1 dB to 70 dB, respectively. In addition to the many shapes shown in Fig. 7.10, equi-ripple responses were also measured. 10 dB and 20 dB equi-ripple responses can be seen in Fig. 7.11. These responses were obtained through tuning M_{11} beyond the value in (7.5), and a larger M_{11} resulted in a wider bandwidth response. Such equi-ripple responses can be achieved by many tunable bandstop filters when the resonances are

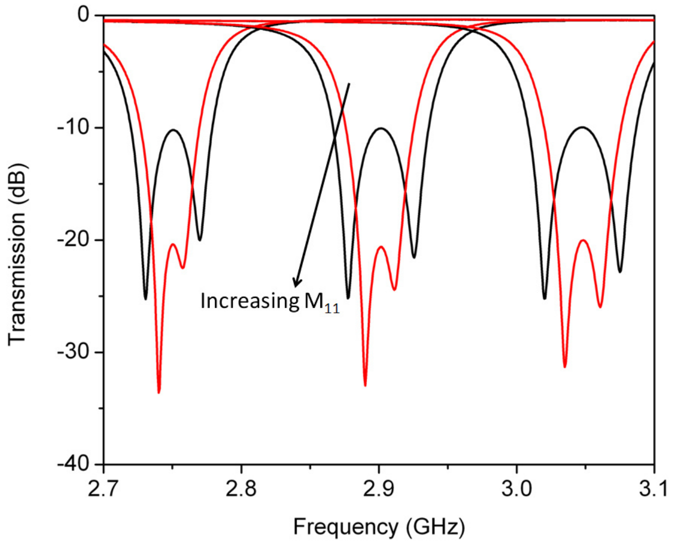

Fig. 7.11. Measured 10 dB and 20 dB equi-ripple responses. The capability to provide this response shape allows a trade-off between attenuation level and bandwidth.

slightly offset from each other in frequency, and they are not a unique aspect of the bandstop-to-all-pass filter. The equi-ripple responses result from interaction of the edges of the stopbands of the resonances. The 3 dB fractional bandwidth of the 3.05 GHz 10 dB equi-ripple response is 3.8%, and that of the 3.05 GHz 20 dB equi-ripple response is 3.1%. Since these responses are wider than the responses shown above, this capability allows a dynamic trade-off between filter bandwidth and level of attenuation. The measured responses in Fig. 7.7-Fig. 7.11 are comparable to the theoretical responses in Fig. 7.3 and Fig. 7.4, proving the effect of finite resonator Q and tuning of M_{11} for the bandstop-to-all-pass filter theory presented in this chapter. It is important to note that changing between all-pass, Butterworth bandstop, and equi-ripple bandstop filter shapes requires only very slight frequency tuning of the resonators. Subject to the tuning speed of the resonators used in a particular implementation of a bandstop-to-all-pass filter, the filter shape could be reoptimized very quickly should the spectrum or signals of interest change.

7.6 Conclusion

An electronically reconfigurable bandstop-to-all-pass filter was shown that can provide numerous response shapes for spectrally aware systems. The theory of such a filter was developed through the use of coupling matrices such that only the resonator center frequencies need to be tuned in order to achieve bandstop-to-all-pass reconfiguration. In the filter's bandstop state, 70 dB of attenuation was measured with a 3 dB bandwidth of 2.7%. The attenuation level was able to be continuously varied over a very wide range, and equi-ripple responses were also demonstrated. In the filter's all-pass state, the filter had 0.14 dB to 0.74 dB of passband insertion loss from 1 GHz to 4.25 GHz and an insertion loss of 2.1 dB at the filter's center frequency.

Applications of a bandstop-to-all-pass reconfigurable filter are envisioned to include wide operating bandwidth, cognitive systems. With bandstop-to-all-pass filters, a system could configure its front end response to the all-pass state when interference was limited, reducing insertion loss compared to bandpass filter front end designs. When interference started to affect performance, the system could place bandstop responses in its front end response at the frequencies of the interference. In addition, a cascade of bandstop-to-all-pass filters could provide the functionality described in this chapter over multi-octave frequency ranges. The filtering capability and flexibility provided by bandstop-to-all-pass filters enables new high-frequency front end strategies featuring very low passband insertion loss.

8. FIELD PROGRAMMABLE FILTER ARRAY ENABLED BY WIDE SPURIOUS FREE RANGE POSITIVE-TO-NEGATIVE INTER-RESONATOR COUPLING STRUCTURE

8.1 Introduction

The bandstop, bandpass-to-bandstop, and bandstop-to-all pass reconfigurable filters presented in previous chapters used offset-tuned resonators to achieve their reconfiguration capability. This technique adds a shift in attenuation and phase to signals relative to the synchronously tuned resonator case with inter-resonator coupling, but it is not equivalent to tuning the inter-resonator coupling. It can be used to compensate for the effects of inter-resonator coupling in bandstop filter configurations, as it was in the bandpass-to-bandstop filter design. However, there are filter response effects, such as bandwidth and filter order tuning in bandpass filters, that cannot be achieved through the use of asynchronous tuning. In addition, asynchronous resonator tuning can provide the ability to add multi-order stopband-enhancing nulls in the skirts of bandpass filter responses that are not possible to achieve through the tuning of inter-resonator coupling. Therefore, it is desirable to have a separate technique for tuning the inter-resonator coupling that is isolated from the resonator spectral position.

Several frequency- and shape-tunable filters have been shown recently [77], [106], [107] as well as tunable inter-resonator coupling [108]. However, these filters are not capable of changing the sign and magnitude of coupling values on demand, which is a limitation to the reconfiguration capability of cross-coupled filters. Filters with innovative inter-resonator coupling structures that enable near-zero coupling states [109] and positive-to-negative (including near-zero) states [27] have also recently been shown. A particularly interesting reconfiguration capability that is enabled by tunable inter-resonator coupling is the ability to reconfigure the order of a filter on demand through setting desired coupling values to zero, isolating resonators from the response. Such capability enables a system to trade passband insertion loss for stopband selectivity as needed, minimizing insertion loss for a given interference scenario. However, the structure in [109] is not capable of providing negative coupling, and the structure in [27] has spurious resonances near the filter passband in some states due to its use of a resonance to obtain positive-to-negative tuning.

This chapter presents an inter-resonator coupling structure that provides positive, negative, or near-zero coupling. In contrast to the structure in [27], the proposed approach uses current redirection as opposed to coupling through a tunable resonance, leading to a wide spurious-free range. It also provides digital addressability to coupling values as opposed to the analog tuning of [27], simplifying potential control algorithms and enabling a single amplifier and switch matrix to control many coupling structures. This is significant because generating unique, precise voltages to control analog-tuned coupling may become too complex to be practical as reconfigurable resonator arrays are scaled to a large number of resonators. Such simplicity enables the first demonstration of a 6-resonator reconfigurable array.

As the number of resonators in such reconfigurable resonator arrays grows in order to provide increased filtering capability as needed, more resonators will be unused when low-order responses are optimal for the current spectrum. The resonator arrays in [27] and [110] have ports at every resonator and can be configured such that adjacent resonators are used to provide filtering for additional system channels. However, in single channel systems or systems where channels are isolated, adjacent resonators that are not required for the desired filter response will almost always go unused, wasting volume, cost, weight, and control voltages for both the unused resonators and their respective coupling structures.

In [110], it was shown that adjacent paths through resonators that are not used to create the passband response can be used to enhance the zero coupling state of a switchable coupling structure by creating a coupling null between a port of the filter and a desired-to-be isolated port. The second part of this chapter presents a way in which adjacent, previously unused resonators in reconfigurable resonator arrays can be used to add notches to the stopband of low-order filter responses using signal interference techniques. Such capability enables low passband insertion loss while still providing high attenuation of a few targeted interfering signals, which would be useful when system sensitivity must be maximized in the presence of a small number of high power interfering systems.

Signal interference techniques have previously been used to create notches [111], [52]. In [111], signal interference is obtained through source-to-load coupling in order to improve the selectivity of low-order bandpass filters. In [52], signal interference is used between a path including narrowband resonators and an all-pass path to create an active bandstop filter with low passband distortion. Additionally, configurations such as the triplet [112] create transmission zeros through the use of adjacent resonant paths. In contrast to [52], the method shown in this chapter uses signal interference to add notches to the stopband of a narrowband bandpass response instead of a wide passband, taking into account the off-resonance reactance in the stopband of the bandpass response. In contrast to other narrowband bandpass filters with transmission zeros like the triplet, the method shown in this chapter is the first to use adjacent resonant paths where the adjacent resonators can contribute or not contribute to the filter passband, giving more adaptation capability. This chapter also shows that analog control of resonant frequencies and digital control of coupling structures provides all of the benefits that analog control of all parameters would add to this response enhancement technique while making control of the resonator array simpler. Finally, the chapter shows additional analysis of the effects of parasitic switch parameters on the performance of the reconfigurable resonator array in [110].

8.2 Positive-To-Negative Coupling Structure

When two loaded cavity resonators are coupled to one another using a waveguide iris, the sign of the coupling is dependent on the relative orientations of the loading elements and charge on the cavity walls [113]. Examples can be seen in Figs. 8.1 a) and b). In [114], it was shown that a probe connecting the top wall of the iris to the bottom wall of the iris over a distance can provide negative inter-resonator coupling relative to the coupling of the waveguide iris through effectively reversing the direction of the coupled current. In the proposed concept, several of these probes are used inside each waveguide iris. A switch is placed between one end of each probe and the iris wall, expanding the concept to provide coupling value switching capability. Such a coupling structure can be seen in Fig. 8.1 c). With the switches off, the coupling structure is approximately equivalent to a waveguide iris with positive coupling as in Fig 8.1 a). With the switches on, the negative coupling provided by the probes overtakes the positive coupling of the waveguide iris as long as the probes are large enough. With some switches on and some off, other positive, negative, and near-zero coupling values result. The structure effectively twists the configuration in Fig. 8.1 a) into the configuration in Fig. 8.1 b) as more switches are turned on. In addition, the current distribution across the width of the iris varies, so altering switch states in different probe locations results in different coupling values. Therefore, 2^N

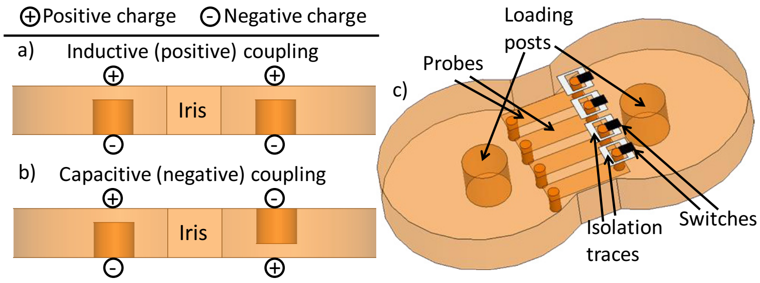

Fig. 8.1. a) Side view, + coupling (like charge on each cavity side). b) Side view, - coupling (opposing charge on each cavity side). c) Switchable coupling structure for positive-to-negative coupling.

coupling states exist, where N is the number of probes. This allows each coupling structure to be addressed as a digital N-bit word, with each bit representing the state of a switch, on or off. Although discrete, the coupling values available can be varied enough to facilitate the design of highly reconfigurable filters.

8.3 Switch Parasitic Analysis

Any type of switch or PIN diode could be used to adjust inter-resonator coupling values in such a coupling structure, and therefore it is important to understand the effects of parasitic switch parameters on insertion loss and spurious free range. Switch on resistance will increase the loss of the inter-resonator coupling structure and therefore the filter. In order to gain insight into how a particular amount of switch resistance affects filter insertion loss, a two-pole simulation was performed where all materials except for the inter-resonator coupling structure switches were lossless. The switch resistance was swept from 0 to 10 ohms using three different lengths of coupling probes, and the simulated results of two-pole insertion loss vs. switch resistance can be seen in Fig. 8.2 for two inter-resonator coupling structure states and three probe lengths [110]. It can be seen that setting the switches that control inner probes (defined in Fig. 8.2) to the on state results in higher loss than setting the switches that control outer probes to the on state. However, switching inner probes also results in larger changes in coupling values. Both effects are due to the sinusoidal field distribution in the transverse direction of the waveguide iris between the resonators. It can also be seen that longer probes result in more insertion loss. Longer probes also result in larger coupling changes as they are switched on. Both effects are due to the exponentially decaying field distribution in the longitudinal direction of the below-cutoff waveguide iris between the resonators. Note that modern switches [115]- [117] have on state resistances near 1 ohm, and therefore this switchable inter-resonator coupling method can be used with minimal additional insertion loss.

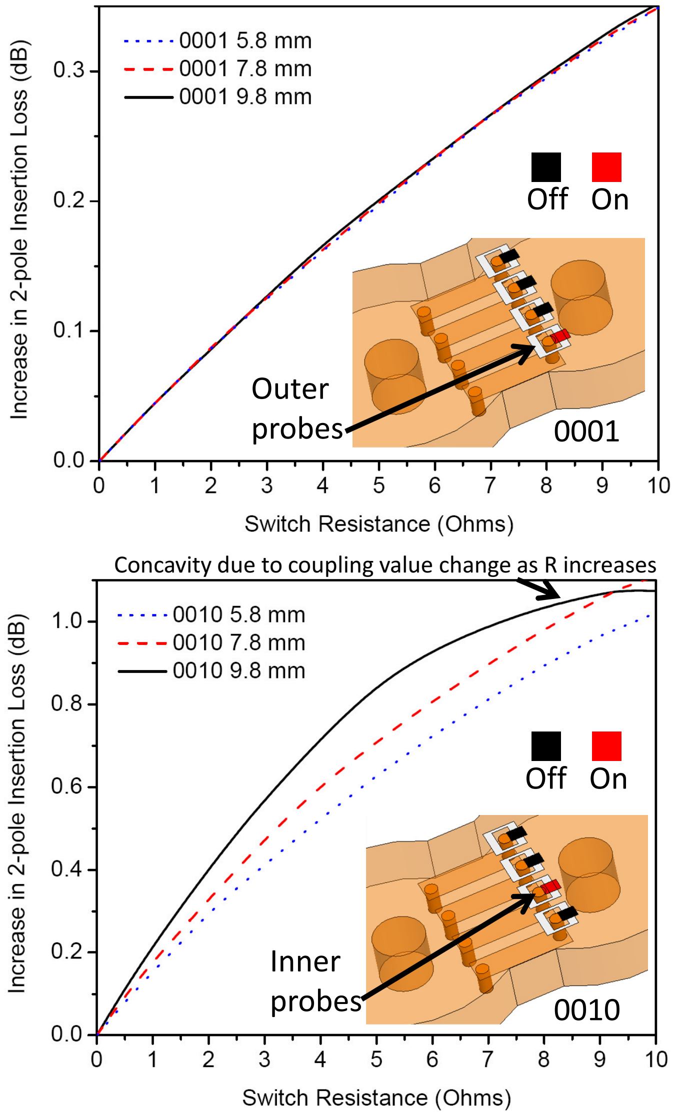

Fig. 8.2. Simulated increase in two-pole insertion loss vs. switch resistance for two inter-resonator coupling structure states and probe lengths of 5.8 mm, 7.8 mm, and 9.8 mm. Increase in insertion loss is relative to the lossless case with ideal switches.

The spurious free range of such a filter can also be impacted by switch selection. Most reflective switches have significant capacitance in their off state. This capacitance loads the primarily inductive reactance of the inter-resonator coupling structure probes. Therefore, the probes will have resonances that appear as spurious peaks in the filter response. Fig. 8.3 shows simulated results of the first spurious resonance

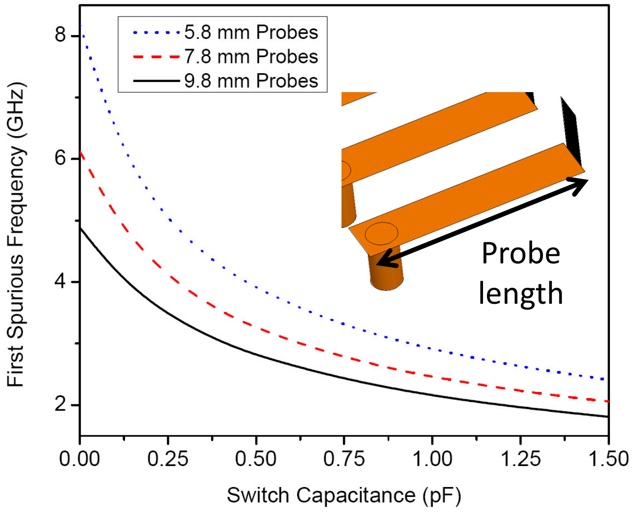

Fig. 8.3. Simulated first spurious resonance frequency vs. switch capacitance for probe lengths of 5.8 mm, 7.8 mm, and 9.8 mm.

frequency vs. switch capacitance for three probe lengths. It can be seen that higher switch off state capacitance or longer probes reduces the first spurious resonance frequency. Probe length is a design tradeoff because longer probes result in a larger change in coupling as the probes are switched in for a given iris length. Using shorter, narrower irises can increase the spurious frequency at the cost of reduced probe count for a given manufacturing capability and higher sensitivity to probe manufacturing tolerances due to the more rapid change in field intensities. Minimal switch capacitance is optimal for a wide spurious free range. The reconfigurable resonator array shown in [110] uses 7.8 mm probes and switches with 0.3 pF off state capacitance. The measured first spurious frequency was 3.86 GHz, which closely matches the simulations in Fig. 8.3.

8.4 Response Enhancements Enabled By Positive-To-Negative Inter-Resonator Coupling

When used in a multi-resonator array, positive-to-negative inter-resonator coupling enables reconfiguration between several filter response types that are not possible otherwise. In addition, it can enhance more standard responses and increase isolation between resonators that are desired to be isolated. Such capability will be shown in the following subsections.

8.4.1 Zero Net Coupling State Enhancement Using Destructive Interference

Due to manufacturing tolerances and environmental effects, the zero net coupling state will often not provide exactly zero coupling. However, the structure is resilient against these nonidealities in rectangular arrays of resonators due to destructive interference paths within the circuit. The destructive interference provided by these additional paths can be enhanced through intelligent selection of coupling values between the resonators that are to be isolated from the circuit. For example, consider four resonators in an X-port, X-resonator (where X is an integer ≥ 4) array whose coupling-routing diagram is in Fig. 8.4 a). Suppose that a 2-pole response using res-

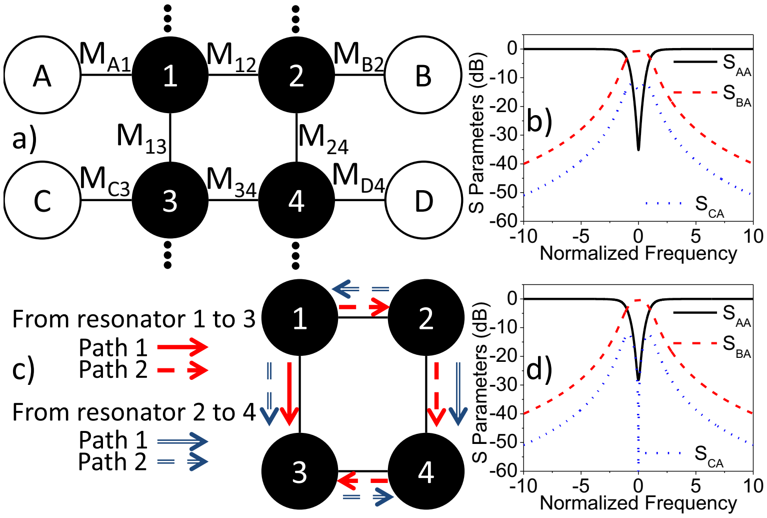

Fig. 8.4. a) Coupling-routing diagram of 4 resonators in an array. Resonators are black, ports are white. b) Response when M13 = M34 = M24 = 0.2. c) Paths for destructive interference between resonators 1 & 3 and 2 & 4. d) Improved response when M34 = 0.764.

onators 1 and 2 is required by the system containing the filter because the spectral conditions call for the lowest possible insertion loss. If $M_{A1} = M_{B2} = M_{C3} = M_{D4} = 0.841$, $M_{12} = 0.707$ for a 2-pole Butterworth shape, and $M_{13} = M_{34} = M_{24} = 0.2$ is the smallest obtainable M value (a conservative estimate, as will be shown later), the synthesized response from port A to ports B and C is as shown in Fig. 8.4 b). The response has 0.66 dB more insertion loss than the ideal 2-resonator-only case at the center frequency of the filter, and the passband shape is slightly changed due to the -14 dB transmission coefficients from port A to port C and port B to port D. While this may be acceptable in many applications, optimizing the destructive interference between the paths shown in Fig. 8.4 c) can further isolate resonators 3 and 4. If M_{34} is set to

$$M_{34} = \frac{M_{A1}^4 + M_{13}^2}{M_{12}}, \tag{8.1}$$

destructive interference is maximized at the center frequency of the filter, and the result is the response in Fig. 8.4 d) with 0.34 dB insertion loss. In the example above, $M_{34} = 0.764$ is the ideal value. While the proposed coupling structure cannot dial in an exact M_{34} value, setting M_{34} to the closest available value still significantly aids in isolating adjacent resonators. If the resonators are tunable, tuning the to-be-isolated resonators far from the passband further increases isolation.

8.4.2 Local Stopband Attenuation Enhancement Technique

Concept

Adjacent resonators that are not in use to create the current passband response required from a reconfigurable resonator array can be used to enhance the filter response by adding transmission zeros to the filter stopband. Transmission zeros locally enhance the stopband isolation in a filter response. This is especially valuable in low-order filters due to their more gradual stopband slopes but is applicable to all filter orders and shapes. For example, consider the coupling-routing diagram shown in Fig. 8.5 a) with six resonators and two ports. Such a coupling-routing diagram could

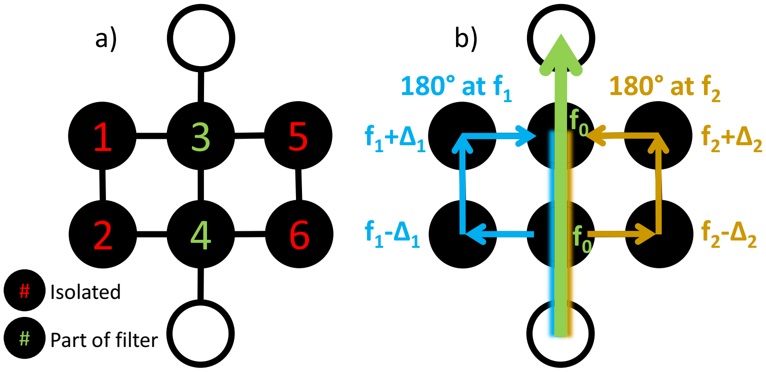

Fig. 8.5. Example coupling-routing diagrams of a reconfigurable resonator array section with six resonators. a) Two-pole filter response at f_0 obtained by isolating resonators 1, 2, 5, and 6. b) Resonant destructive interference paths that create transmission zeros at f_1 and f_2.

represent a reconfigurable resonator array with six resonators or a subset of resonators in a larger array. In [110], it was shown that a two-pole filter response could be obtained from such a reconfigurable resonator array if the appropriate coupling values are set to zero so that resonators 1, 2, 5, and 6 are isolated from the circuit. This configuration would be valuable when minimum insertion loss is required by the system that hosts the resonator array. However, resonators 1, 2, 5, and 6 and their associated inter-resonator coupling structures are not adding any performance to the response in this configuration while consuming valuable resources.

If the coupling to and between resonators 1, 2, 5, and 6 is instead set to non-zero values, resonant destructive interference paths can be created at targeted frequencies. This concept is shown in Fig. 8.5 b). In Fig. 8.5 b), resonators 3 and 4 produce a 2-pole response at f_0. Energy at frequencies f_1 and f_2, the frequencies in the 2-pole response stopband at which increased attenuation is desired, also leak through the path that contains resonators 3 and 4 due to the finite stopband attenuation of the 2-pole response. An equal magnitude and opposite phase signal at f_1 can be leaked through the adjacent path that contains resonators 1 and 2 if the coupling values and/or resonant frequencies associated with resonators 1 and 2 are set properly, creating a resonant transmission zero path. A similar effect can be achieved at f_2 using the adjacent path through resonators 5 and 6. A particularly attractive trait of the proposed method to create transmission zeros is that the zeros are created on demand using paths composed of multiple resonators as opposed to the conventional method of using reactive cross-coupling [118], [119], [120]. Using paths composed of multiple resonators enables the design of the shape, tuning range, and bandwidth of transmission zeros, similar to how these parameters can be designed in conventional bandstop filters that use multiple resonators [121], [122].

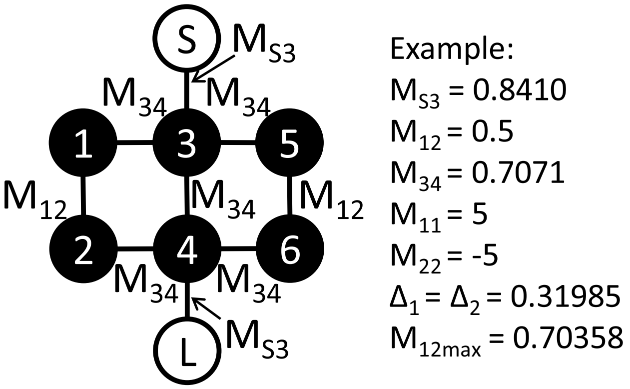

Fig. 8.6. Simplified example coupling-routing diagram and coupling values for a two-pole Butterworth response with 2nd order transmission zeros at -5 and 5 normalized frequency.

Numerical Example

Fig. 8.6 shows a simplified example coupling-routing diagram and coupling values. Coupling values are repeated in this example to allow for simpler equations that are possible to display neatly in this format. However, all analysis techniques shown in this example will be applicable to structures with unique coupling values for each coupling structure. The N+2 x N+2 coupling matrix [69] for the coupling-routing diagram in Fig. 8.6 is

$$\begin{bmatrix} 0 & 0 & 0 & M_{S3} & 0 & 0 & 0 & 0 \\ 0 & M_{11+} & M_{12} & M_{34} & 0 & 0 & 0 & 0 \\ 0 & M_{12} & M_{11-} & 0 & M_{34} & 0 & 0 & 0 \\ M_{S3} & M_{34} & 0 & 0 & M_{34} & M_{34} & 0 & 0 \\ 0 & 0 & M_{34} & M_{34} & 0 & 0 & M_{34} & M_{S3} \\ 0 & 0 & 0 & M_{34} & 0 & M_{22+} & M_{12} & 0 \\ 0 & 0 & 0 & 0 & M_{34} & M_{12} & M_{22-} & 0 \\ 0 & 0 & 0 & 0 & M_{S3} & 0 & 0 & 0 \end{bmatrix}, \tag{8.2}$$

where M_{11-} is M_{11} - Δ_1, M_{11+} is $M_{11} + \Delta_1$, M_{22-} is M_{22} - Δ_2, and M_{22+} is $M_{22} + \Delta_2$. Δ_1 and Δ_2 represent asynchronous tuning of resonators 1 & 2 and 5 & 6, respectively. In this example, M_{S3} and M_{34} are set to the values required for a Butterworth 2-pole filter, but any two-pole filter shape can be used. The remaining unique coupling value, M_{12}, is semi-arbitrarily set to 0.5 with the assumption that some type of tunable inter-resonator coupling structure is used. However, there is a limit to the maximum value of M_{12} relative to the other coupling values that will be shown later. For this example, resonant transmission zeros will be placed at normalized frequencies of -5 and 5. However, these frequencies can be arbitrarily assigned.

In the conventional coupling matrix synthesis method [25], equations are solved to determine the coupling M values to fit a desired passband polynomial shape. When resonant transmission zero paths are desired, additional equations must be simultaneously solved in order to ensure that the transmission coefficient is zero at the desired frequencies. In the example shown in Fig. 8.6, Δ_1 and Δ_2 are the parameters for which equations must be solved. Note that if M_{12} and M_{34} are set to specific values, it is possible to make Δ_1 and Δ_2 zero and therefore the resonators will all be synchronously tuned. However, asynchronous tuning allows for semi-arbitrary values of M_{12} and M_{34} while still creating deep resonant transmission nulls. Also note that the adjacent paths in Fig. 8.6 are symmetric. This will lead to Δ_1 and Δ_2 being equal and the equations that determine them significantly simpler. However, in general, this is not a requirement. Δ_1 and Δ_2 can be found by solving

$$\begin{aligned}\Delta_1 &= \mathrm{Solve}(\mathrm{S}_{21} = 0)|_{\mathrm{s}=-\mathrm{M}_{11}} \\ \Delta_2 &= \mathrm{Solve}(\mathrm{S}_{21} = 0)|_{\mathrm{s}=-\mathrm{M}_{22}}\end{aligned}, \tag{8.3}$$

where s is the frequency variable $j\omega$. Since the adjacent paths are symmetric in this example, Δ_1 and Δ_2 are the same value and are equal to

$$\begin{aligned}&\Delta_1 = \Delta_2 = \\ &\sqrt{\frac{4M_{11}^2M_{12}^2M_{34} - 4M_{11}^2M_{12}M_{34}^2 - M_{12}^4M_{34} + 2M_{12}^3M_{34}^2}{-M_{34}(4M_{11}^2 - M_{12}^2 + M_{34}M_{12})}}.\end{aligned} \tag{8.4}$$

For the example values shown in Fig. 8.6, Δ_1 and Δ_2 are equal to 0.31985. Note that in this symmetric example, $M_{22} = -M_{11}$.

The additional requirement of a solution for (8.3) leads to a constraint on the maximum value of M_{12} that can be used to obtain Butterworth-like resonant transmission zero paths with theoretically infinite attenuation at one frequency. This constraint can be found by rearranging (8.3) to solve $S_{21} = 0$ at $s = -M_{11}$ and $s = -M_{22}$ for M_{12} when both Δ_1 and Δ_2 are zero. In the example shown in Fig. 8.6, the maximum M_{12} value is 0.70358. This value represents the M_{12} inter-resonator coupling value that requires no asynchronous tuning (Δ_1 and Δ_2) in order to create resonant transmission zero paths. However, the ability to asynchronously tune the resonators greatly relaxes the required accuracy of M_{12} to obtain resonant transmission zero paths, leading to the ability to obtain deep notches with only discrete control of inter-resonator coupling values as in [110].

Notch Response Adjustment

The response of the network shown in Fig. 8.6 can be seen in Fig. 8.7 with ideal infinite resonator quality factor (Q) and a Q-bandwidth product of 15, which could represent a Q of 500 and a fractional bandwidth of 3%. In the ideal case, the transmission coefficient response at the resonant frequencies of the adjacent resonators (1,

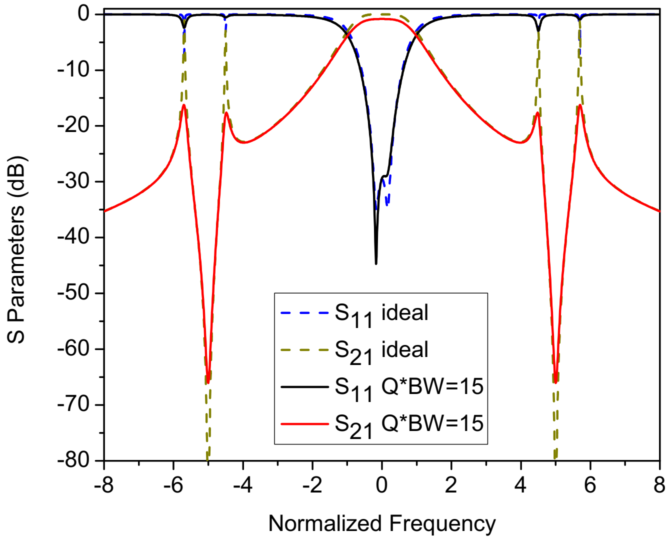

Fig. 8.7. Synthesized response of the network and coupling values shown in Fig. 8.6 for ideal and finite Q cases. BW = fractional bandwidth, Q = unloaded quality factor. Q*BW = 15 could represent, for example, Q = 500 and BW = 3% (insertion loss = 0.83 dB).

2, 5, and 6) is relatively high, leading to spurious peaks at the edges of the resonant transmission zeros at -5 and 5 normalized frequency. However, with finite quality factor and bandwidth it can be seen that the magnitude of these spurious peaks is greatly reduced. It can also be seen that in both cases the passband return loss deviates from an ideal Butterworth shape due to the band edge reactance of the notch responses. However, even with the close frequency spacing between the passband and notches shown in this example, better than 25 dB return loss is maintained throughout the passband.

The notch shape and bandwidth can be controlled by adjusting the inter-resonator coupling values and asynchronously tuning the adjacent resonators. Fig. 8.8 shows the synthesized variation of the bandwidth of the notch at -5 normalized frequency from the example network in Fig. 8.6 as M_{12} is varied from 0.1 to 0.6, which could be done with an inter-resonator coupling structure such as the one shown in [110]. The notch bandwidth is maximized as M_{12} approaches its maximum value for this family of shapes, which in this example is 0.70358 as stated above. However, the

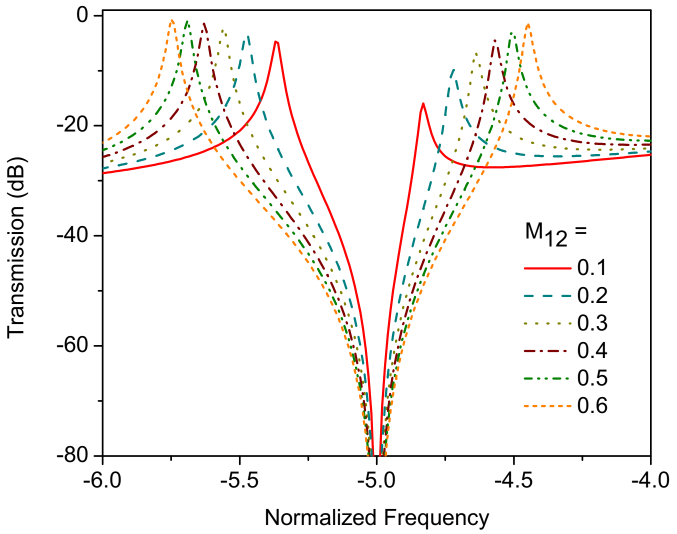

Fig. 8.8. Synthesized infinite-Q response of the transmission zero at -5 normalized frequency from the network shown in Fig. 8.6 for varying M_{12} values. Note that Δ_1 & Δ_2 are found for each response shown here using (8.3). In this example, Δ_1 & Δ_2 are only zero when M_{12} = 0.70358.

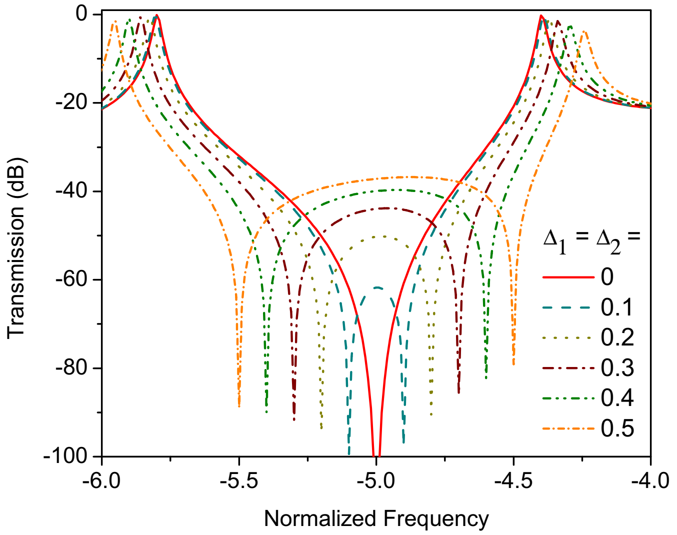

Fig. 8.9. Synthesized infinite-Q response of the transmission zero at -5 normalized frequency from the network shown in Fig. 8.6 when M_{12} is set to 0.70358 and Δ_1 & Δ_2 are varied.

bandwidth can be further increased if an equi-ripple shape is formed by increasing Δ_1 and Δ_2 beyond the value solved for in (8.4). Such synthesized responses can be seen in Fig. 8.9 for the case when M_{12} is set to 0.70358 and Δ_1 & Δ_2 are varied from 0 to 0.5, which could be done by asynchronously tuning the resonators in adjacent paths. Note that when M_{12} is 0.70358 in this example, Δ_1 and Δ_2 should be zero according to (8.4) to obtain a Butterworth-like deep notch.

The synthesized responses shown here are similar to those that resulted from the cascades of bandpass and bandstop filters shown in Chapter 5 because they have a narrow band passband and deep nulls in the stop band. As for those responses, these responses are valuable for attenuating both external and self interference. For example, the limitation of some systems in achieving simultaneous transmit and receive is leak through of amplified noise from the transmit path to the receive path. The leak through is often a problem despite the presence of a diplexer separating the transmit and receive paths due to the high output power level of the power amplifier in the transmit path. However, if the responses shown above were available to the system in the transmit path, large amounts of isolation between the transmit path and the receive path could be possible at targeted frequencies if the passband of the response was centered at the transmit band and the notch responses were centered at the receive bands to block amplified noise. In addition, there is a distinct advantage of the responses shown in this chapter over the responses shown in Chapter 5. The responses in Chapter 5 have additional passband insertion loss due to the source-to-load transmission line of the bandstop filters. The responses shown here have the same passband insertion loss whether or not notches are added to the stop band, leading to higher system sensitivity when compared with the responses in Chapter 5.

8.5 Resonator Array Design and Fabrication

Four devices were fabricated in Rogers TMM3 substrate to demonstrate the positive-to-negative inter-resonator coupling structure and its response enhancement capabilities. The devices were composed of substrate-integrated cavity resonators tuned with piezoelectric actuators [109], [27]. The first two devices are 6-resonator arrays with ports at each resonator and positive-to-negative coupling structures used to couple all resonators to all adjacent neighbors. A simulation model of these structures can be seen in Fig. 8.10 and a photograph can be seen in Fig. 8.11. Each positive-to-negative coupling structure contains four probes that each use a Skyworks SMP1340 PIN diode as a switch in the first design, and the second design uses 0 ohm resistors and open circuits for comparison. The PIN diode version would be useful to dynamically adapt to signals in the field, while the 0 ohm resistor version would be useful as a post-mass production shape-customizable filter since the surface-mount 0 ohm resistors can be easily added or removed with solder. The structure is 63 mm x 42 mm x 3.175 mm. The resonators and loading posts in all of the designs have radii of 7.5 mm and 2.1 mm, respectively, and the horizontal part of each probe is 1.2 mm wide by 7.8 mm long. The vertical parts of the probes are 0.8 mm diameter plated vias on one side and vertically mounted 68 pF RF bypass capacitors on the

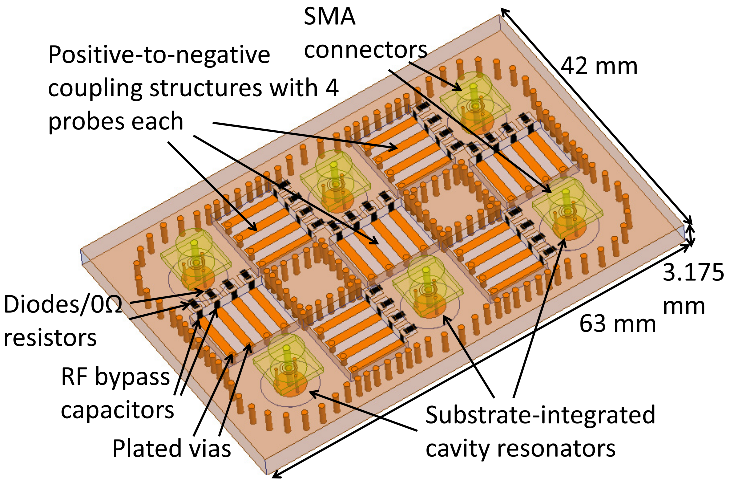

Fig. 8.10. Simulation model of 6-resonator array of tunable substrate-integrated cavity resonators and positive-to-negative coupling structures containing 4 probes each. Bias circuits not shown.

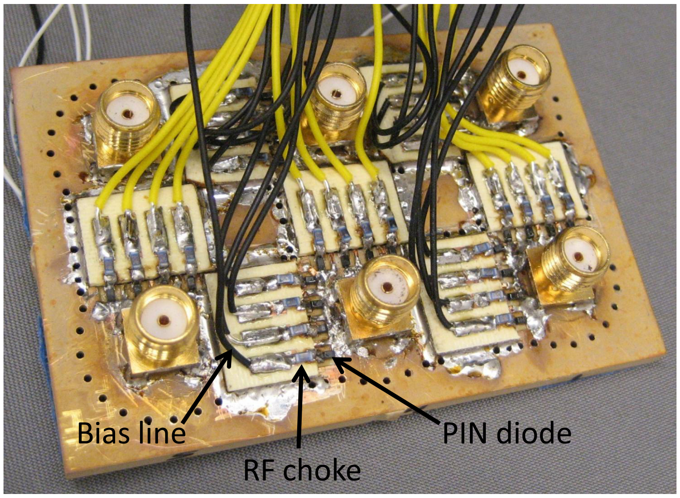

Fig. 8.11. Photograph of reconfigurable resonator array. PIN diodes switch inter-resonator coupling between positive, negative, and near-zero values. Black and yellow lines bias PIN diodes while white lines bias piezoelectric actuators that tune the center frequency of the resonators.

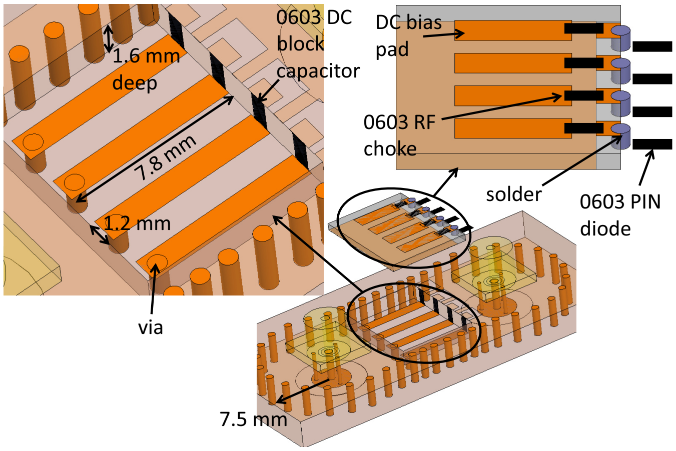

Fig. 8.12. Model of inter-resonator coupling structure and supplementary DC bias board. The DC bias board is soldered to the iris in the fabricated structure but raised in this figure for clarity.

other side. Fig. 8.12 shows closer views of the positive-to-negative inter-resonator coupling structure and supplementary DC bias circuit board. The DC bias board uses a 120 nH inductor in each bias circuit to block RF signal from propagating

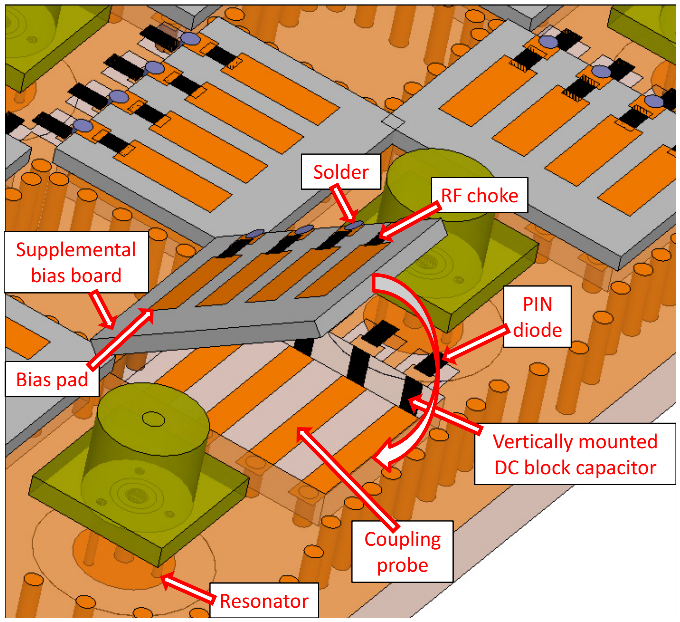

Fig. 8.13. Model of an inter-resonator coupling structure with the supplementary bias board rotated off of the cavity substrate to show internal structure. As PIN diodes are switched on, waveguide iris current is redirected, changing coupling values.

into the bias generator. Since the four PIN diodes in each inter-resonator coupling structure are connected in parallel, bias resistors on a separate breadboard were also used to equate the current in each branch of the parallel circuit. Another view of the positive-to-negative inter-resonator coupling structure and supplementary DC bias board is shown in Fig. 8.13.

A closer view of the loading post, which also forms the external coupling structure, is shown in Fig. 8.14. The top row of images in Fig. 8.14 show the dimensions of the loading post and its positional relationship with the SMA connector port above each resonator. The bottom row of images in Fig. 8.14 show the equivalent circuit of the external coupling circuit/loading post. The central plated via in the loading post connects to an isolated pad on the copper surface of the cavity substrate that is soldered to the center conductor of the SMA connector above each resonator. The ground housing of the SMA connectors is soldered to the rest of the copper surface

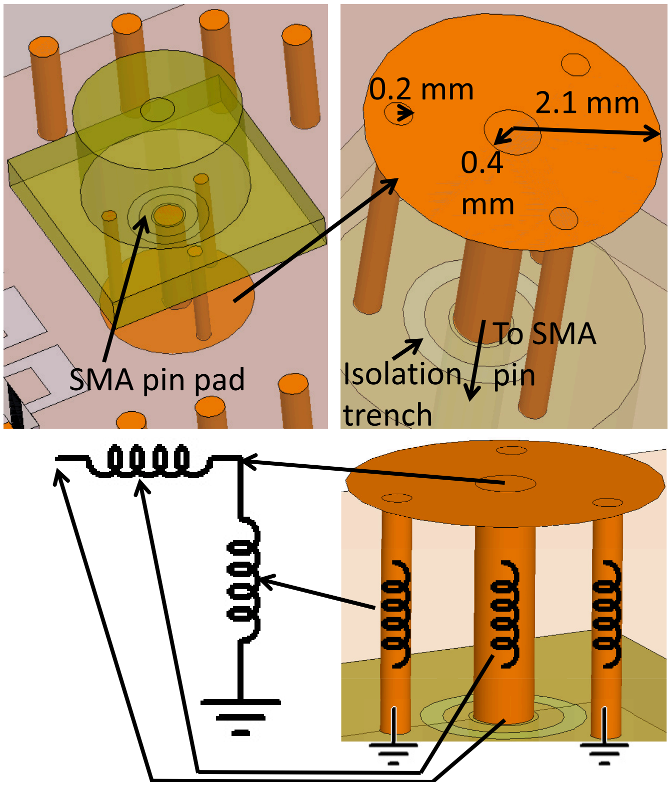

Fig. 8.14. External coupling circuit/loading post and equivalent circuit. Together, the vias in the loading post act as an inductive impedance transformer.

of the cavity substrate. The three outer vias in the loading post connect it to the copper surface of the cavity substrate and provide a DC path to ground. At RF, these three vias provide significant inductance to ground. Together, the vias in the post form an inductive impedance transformer. The radius and number of these vias can be adjusted to obtain various external coupling values.

The third and fourth fabricated structures are sets of two resonators with single positive-to-negative coupling structures between them. One of these structures has an inter-resonator coupling structure of the same dimensions as those of the 6-resonator arrays discussed above and weak external coupling. This structure was used to extract measured inter-resonator coupling values for use when switching coupling values in the larger array. The other structure with two resonators was designed with an inter-resonator coupling structure of the same concept as the others, but slightly different dimensions and near-critical external coupling. This structure was designed to work with Peregrine 42422 switches. Peregrine 42422 switches have much lower insertion loss than the Skyworks SMP1340 PIN diodes used in the original designs, and the purpose of the design with the Peregrine 42422 switches is to show that the positive-to-negative inter-resonator coupling structures described in this chapter can be used with minimal increase in filter insertion loss when modern, low-loss switches are integrated into the design.

8.6 Measured Results

During device operation, the SMA connectors that were not used as input and output ports were left open (unterminated). This is possible because the highly capacitively loaded resonators used in this design have a very low characteristic impedance. Therefore, termination with an open circuit approximates termination with a 50 ohm load. Leaving the port open can save volume and cost if such a filter was used in a production application.

Measurements of the two weakly-coupled resonators can be seen in Fig. 8.15 along with switch states and extracted M_{12} values. It can be seen that coupling values that would be useful in critically coupled responses, isolation paths between desired and undesired resonators, and cross-coupling paths with negative coupling can be obtained from the same electronically reconfigurable inter-resonator coupling structure. The measured coupling values are plotted graphically in Fig. 8.16. Fig. 8.17 shows measured 1.25% fractional bandwidth 2-pole responses from resonators 3 and 4 of the 6-resonator array that uses PIN diodes to electronically switch coupling. Measured insertion loss (IL) ranged from 3.11 dB to 3.96 dB over the tuning range. A similar 2-pole response from the device that uses 0 ohm resistors to mechanically switch coupling is also shown at 1.8 GHz to show the tradeoff between electronic reconfiguration capability and IL. The diodes added 1.06 dB IL. The silicon construction of these

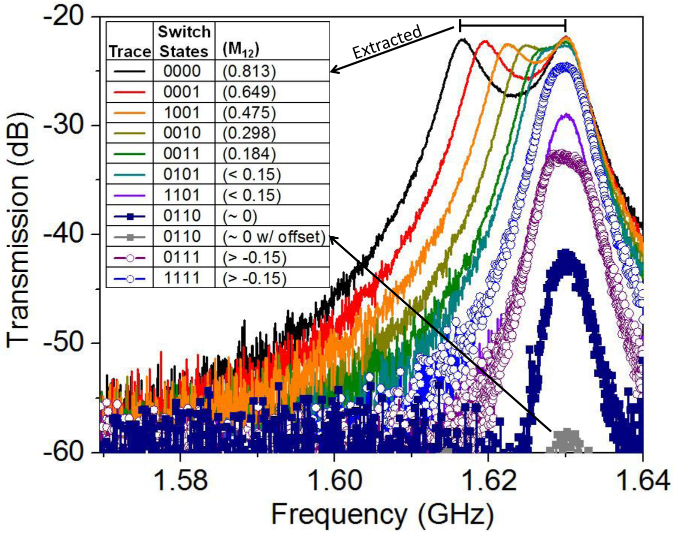

Fig. 8.15. Measured weakly-coupled 2-pole responses used for M_{12} coupling value extraction. The table shows PIN diode states, where 1 is on and 0 is off, and extracted M_{12} values for a 1.25% fractional bandwidth. Offset tuning the resonators results in minimal coupling.

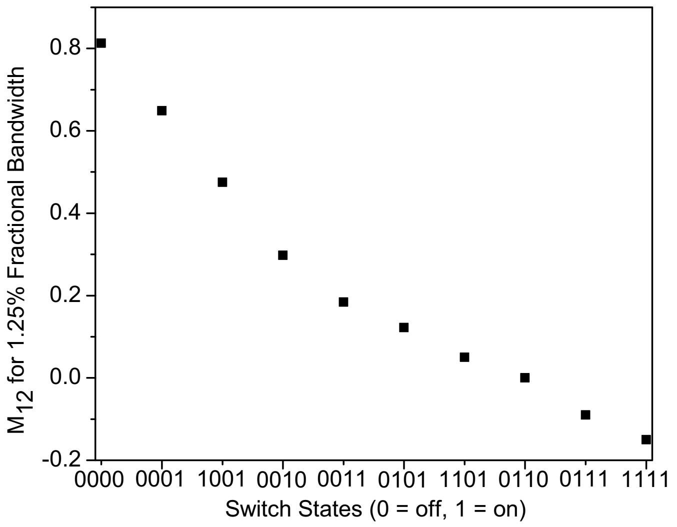

Fig. 8.16. Measured extracted inter-resonator coupling values from Fig. 8.15 for different switch/PIN diode states.

diodes was part of the reason for this additional loss. Lower loss diodes in the same package size are also available, but they have larger off state capacitance that would

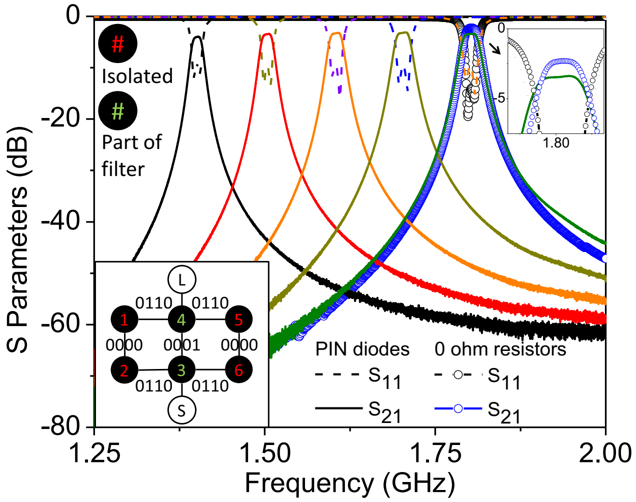

Fig. 8.17. Measured 2-pole responses obtained by isolating 4 resonators with the shown switch states. Solid lines show responses of the PIN diode version. Lines marked with white circles show a response of the 0 ohm resistor version for comparison.

limit the spurious free range of the FPFA. Another possible reason is that the complete recommended bias circuit in the diode's data sheet could not be implemented in the FPFA prototype shown in this chapter due to space constraints. Lower-loss switches such as RF MEMS devices could possibly reduce switching element insertion loss. Fig. 8.18 shows measured 1.02% fractional bandwidth 4-pole responses from resonators 1-4 of the 6-resonator array that uses 0 ohm resistors. Transmission zeros (TZs) are added and removed by toggling M_{34} between near-zero and negative values. IL ranged from 4.07 dB to 5.31 dB with TZs and 4.81 dB to 6.38 dB without TZs. The measured IL is within 1.3 dB of fullwave simulations. The first spurious response is at 3.86 GHz and is at -20.2 dB and -48.2 dB levels in the 2- and 4-pole cases, respectively. The spurious responses for both a 2-pole response and a 4-pole response can be seen in Fig. 8.19. The spurious modes are a result of the electrical length of the probes in the inter-resonator coupling structure, and their frequency does not change when the resonators are tuned across their tuning range.

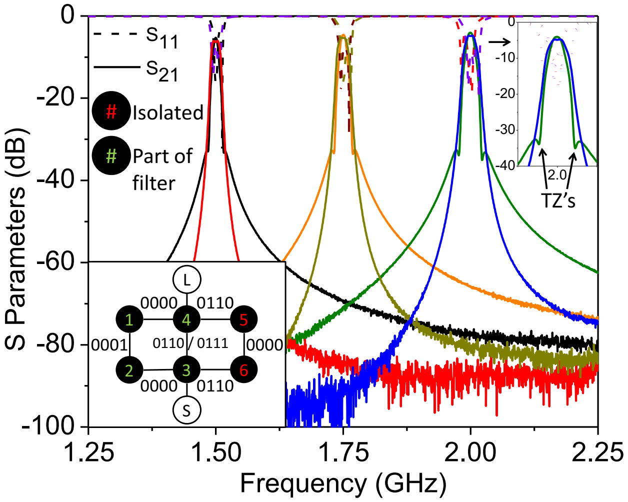

Fig. 8.18. Measured 4-pole responses with and without TZs obtained by isolating 2 resonators and toggling M_{34} between near-zero and negative values. All responses are from the 0 ohm resistor version.

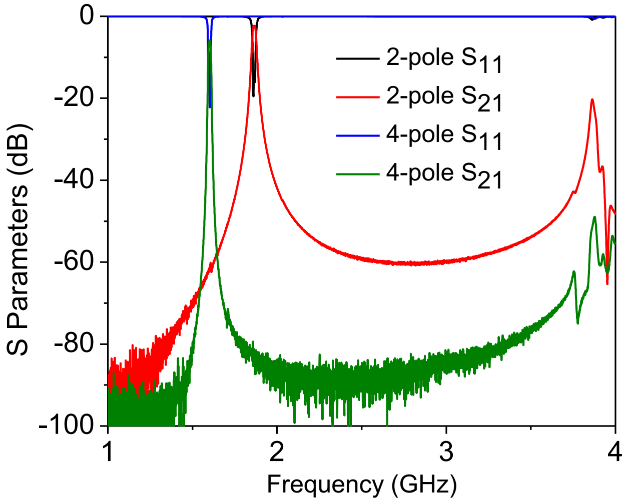

Fig. 8.19. Measured 2-pole and 4-pole responses showing the first spurious response in both states.

Measured superimposed results of the fabricated filter that show the destructive interference stopband enhancement technique can be seen in Fig. 8.20. One adjacent path through two resonators was activated in order to obtain the plots shown in Fig. 8.20. A tunable two-pole notch response can be seen at various locations in

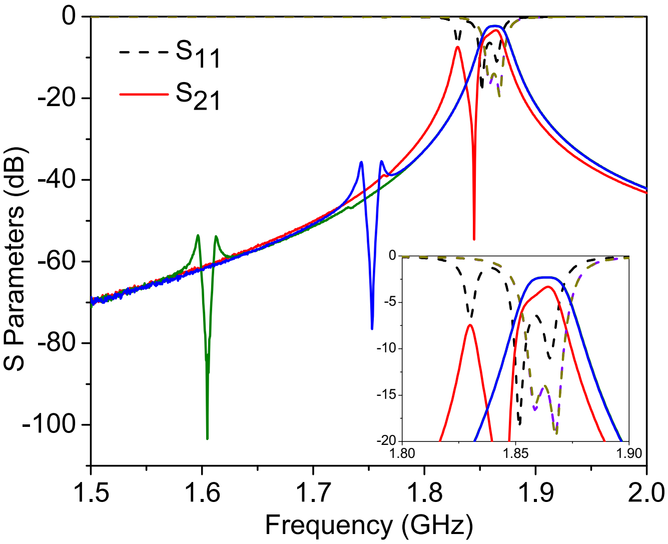

Fig. 8.20. Three superimposed measured results showing a two-pole passband response with one adjacent resonant path creating a tunable notch in the filter stopband.

the stopband of the two-pole passband response. The final two resonators of the device are isolated. When the notch is significantly far away from the passband, the filter exhibits 2.32 dB insertion loss and a 1.2% fractional bandwidth. Passband insertion loss increases as the notch is brought close to the passband due to the skirt reactance of the notch. Fig. 8.20 shows that when the notch is placed 20 MHz away from the passband at 1.8646 GHz, the minimum insertion loss of the filter degrades by 1 dB and the passband shape becomes distorted. The passband response was designed expecting 50 ohm terminations, and the input impedance of the notch at the passband frequency is not 50 ohms when it is tuned close to the passband. In order to mitigate this distortion, the passband response can be designed to expect a complex load [123]. However, the response would become distorted when the notch was far from the passband in this case unless the external coupling could also be tuned, which is not a capability of the fabricated example.

Fig. 8.21 shows measured superimposed responses when two adjacent paths are activated to create two 2-pole notches in the stopband of the two-pole passband

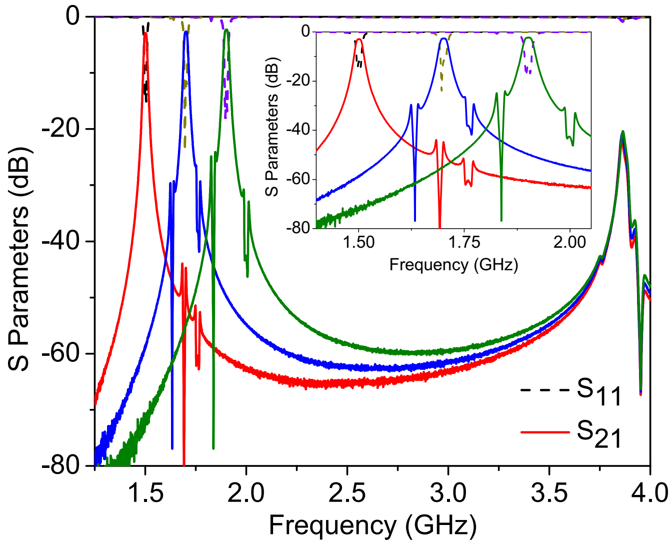

Fig. 8.21. Wideband measurement showing first spurious resonances and three superimposed two-pole passband responses with two adjacent resonant paths creating tunable notches in the filter stopbands. Inset shows closer view of the frequency range near the passband frequencies. Therefore, the addition of notches in the skirt of the passband does not change the first spurious resonance frequency.

response. The filter passband exhibits 2.93 dB to 2.30 dB insertion loss and a 1.2% fractional bandwidth over the tuning range shown. The two notches can be placed on opposite sides or the same side of the passband. In addition, Butterworth or equi-ripple notches are possible. Fig. 8.22 shows the response from Fig. 8.21 with a passband at 1.7 GHz along with a synthesized response using the coupling matrix

$$\begin{bmatrix} 0 & 0 & 0 & 0.841 & 0 & 0 & 0 & 0 \\ 0 & 6.820 & 0.649 & 0.649 & 0 & 0 & 0 & 0 \\ 0 & 0.649 & 6.820 & 0 & 0.649 & 0 & 0 & 0 \\ 0.841 & 0.649 & 0 & 0 & 0.649 & 0.649 & 0 & 0 \\ 0 & 0 & 0.649 & 0.649 & 0 & 0 & 0.649 & 0.841 \\ 0 & 0 & 0 & 0.649 & 0 & -5.270 & 0.649 & 0 \\ 0 & 0 & 0 & 0 & 0.649 & 0.649 & -6.370 & 0 \\ 0 & 0 & 0 & 0 & 0.841 & 0 & 0 & 0 \end{bmatrix} \tag{8.5}$$

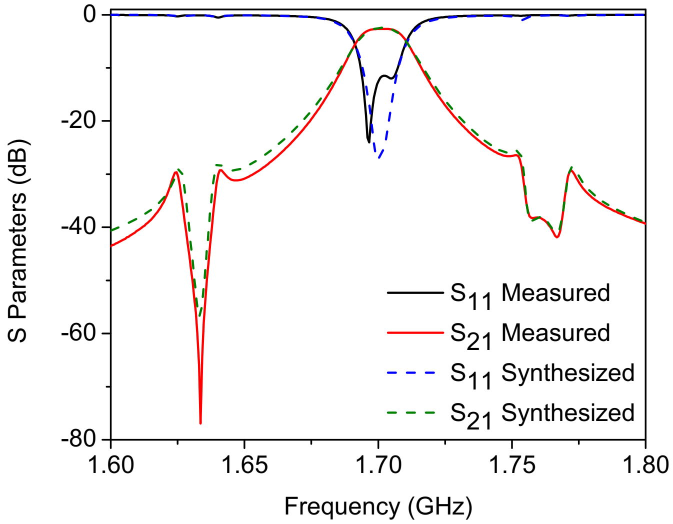

Fig. 8.22. Measured (blue S_{21} trace from Fig. 8.21) vs. synthesized response.

scaled to a center frequency of 1.7015 GHz where each self coupling term (M_{nn}, n is an integer from 1 to 6) also has a $-j0.185$ term to represent a 1.2% fractional bandwidth and Q of 450. The imaginary part of the self coupling terms was found according to the equation $-j/(Q * BW)$, where j is the square root of -1 and BW is the fractional bandwidth. 0.649 was used as an inter-resonator coupling value instead of 0.7071 as in the numerical example above because 0.649 is the closest discrete value to 0.7071 that is obtainable from the test structure [110]. While the narrowband approximation is used with the coupling matrix and the notches are away from the passband, approximate agreement between synthesized and measured results was obtained.

Measured results of the 2-pole, near critically coupled filter can be seen in Fig. 8.23. Compared with a measured result from the same structure with zero ohm resistors instead of Peregrine 42422 switches, the measured result with the Peregrine 42422 switches had only 0.2 dB more insertion loss. The filter shape is different in the two cases due to packaging parasitic effects, but this could be designed into the filter in the future. Therefore, using state-of-the-art switches, positive-to-negative inter-resonator coupling is achievable with minimal impact on filter insertion loss.

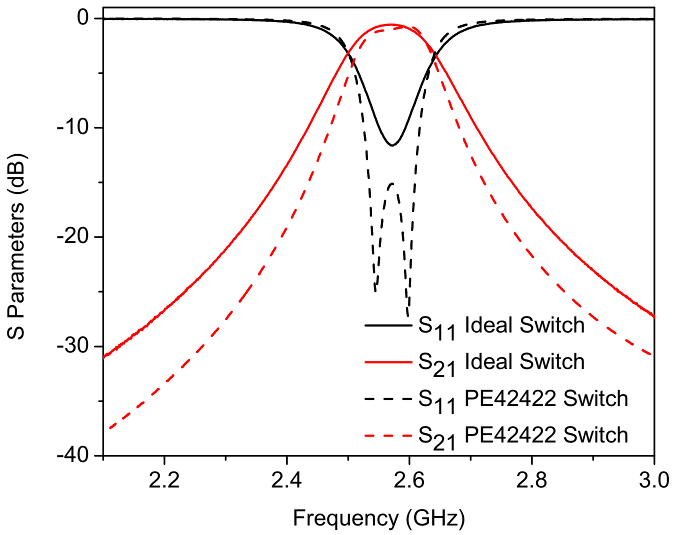

Fig. 8.23. Measured response of 2-pole, near critically coupled filter with Peregrine 42422 switches.

The OIP3 of the 6-resonator array with PIN diodes was measured in the two-pole passband configuration shown in Fig. 8.5 b) to determine the linearity of the device. While the linearity of such a device depends strongly on operating mode, switch/PIN diode selection, probe length, and probe position, it is important to understand the limitations of the actual fabricated device. An Agilent E4433B signal generator in multitone mode was used to create two 10 dBm tones at the filter input. The tone separation was 1 MHz, and the center frequency was 1.6 GHz. Each on PIN diode was biased with 15 mA current. The output fundamental tones were measured at 7.2 dBm using an Agilent E4408B spectrum analyzer, corresponding to a filter insertion loss of 2.8 dB. The output third order tones were measured at -54.0 dBm, corresponding to an OIP3 of 37.8 dBm. Using parameters from the Skyworks SMP1340 datasheet, common silicon hole and electron mobilities, and formulas shown in the Skyworks application note titled ”Design With PIN Diodes,” the expected IP3 was estimated to be 38.7 dBm, which is a close match to the measured value. It is important to note that these diodes were placed in the evanescent field region of the waveguide iris between the cavity resonators, so quality factor enhancement of the field magnitudes did not have as strong of an effect on the IP3 as it would have if the PIN diodes were placed inside the resonators. It is also important to note that PIN diodes with much higher IP3 values are available in the same package size. However, the SMP1340 diodes were chosen for their fast switching speed, which is often a tradeoff with linearity due to the narrow intrinsic zone widths and low carrier lifetime needed for fast switching speed in PIN diodes. The third order intermodulation products from the signal generator were measured at -78 dBm and assumed to be negligible.

The plots shown in this chapter are representative of numerous filter states that can be generated with the 6-resonator array, but they are not all-encompassing. The combination of many digitally addressable coupling states and tunable resonators provides the means to create a wide array of filter responses. However, there are still limitations to the responses of the FPFA prototype due to discretization of the inter-resonator coupling states, lack of source-to-load coupling, and static external coupling. While the discrete inter-resonator coupling structure used in the FPFA prototype did not limit its capability to add notches to the stop band at arbitrary frequencies, it does limit the number of possible passband shapes. Each unique shape and each order of each shape require different inter-resonator coupling values. Therefore, as FPFA's grow in number of resonators, more inter-resonator coupling values will be needed in order to fully utilize the capability of a large FPFA. The design of inter-resonator coupling structures that can provide many specific discrete values will be difficult because the position of each current probe affects multiple coupling states. In these cases, designing coupling structures with quasi-continuous tuning though the use of many discrete closely spaced coupling values may be the best design option. In contrast to these cases, the design of structures that switch between a few specific inter-resonator coupling values is useful for future systems that need a more limited amount of reconfiguration capability. For example, the inter-resonator coupling structure shown in this chapter has ten unique coupling values. One specific value was designed for a 2-pole response, two for a 4-pole response, one for zero coupling, and two for negative coupling. However, the remaining four unique values were left to be what naturally occurred after the first six values were obtained due to the difficulty in optimizing for ten specific values. Still, the FPFA was able to produce a multitude of responses.

The addition of tunable or switchable external coupling would enable both tunable bandwidth and further isolation of unused ports. When scaling the bandwidth of a filter, the external coupling must be scaled by the square root of the inverse of the bandwidth scaling factor. In addition, the sign of external coupling does not affect the magnitude response of 2-port bandpass filters. These two facts lead to the conclusion that external coupling values do not need to vary over the same range as inter-resonator coupling values (due to the square root factor) and only have to have one sign for most responses, making implementation somewhat easier. As in the inter-resonator coupling case for digitally controlled coupling values, there is a tradeoff between the number of possible responses and design complexity. If the external coupling was tunable or switchable to small values, it would limit the amount of coupling to unused ports. If a small enough value could be obtained, switches would not have to be used in the system to switch between ports. Tunable or switchable source-to-load coupling would enable further paths for group delay equalization, the addition of more transmission zeros, and/or the capability to switch between bandpass and bandstop responses, as shown in Chapter 6.

8.7 Conclusion

A wide spurious free range, positive-to-negative, digitally-addressable inter-resonator coupling structure was shown. The structure provides a wide range of reconfiguration capability while requiring relatively simple control and bias networks. Such control simplicity is integral to the future of practical reconfigurable arrays with a large number of resonators.

In systems that employ reconfigurable resonator arrays, it may not always be optimal to configure the device to operate with the largest possible filter order response due to the larger passband insertion loss associated with high order filters. This chapter showed a technique that locally enhances the stopband rejection of low order responses by more than 40 dB in the 1.4 GHz to 1.9 GHz frequency range through the use of adjacent resonators that would have otherwise been isolated from the circuit. In addition, analysis concerning the R_{on}-C_{off} tradeoff associated with switch selection when using the switchable coupling structure described in [110] was shown. Currently available switches can be used to implement the methods in this chapter with minimal resonator array performance degradation. These concepts create more frequency responses for more optimal interference adaptation and enable accurate design of reconfigurable resonator arrays, respectively.

9. INTERSECTING PARALLEL PLATE WAVEGUIDE LOADED CAVITIES FOR DUAL-MODE AND DUAL-BAND FILTERS

9.1 Introduction

The previous chapters focused on filters and synthesis techniques that enable reconfiguration between many filter shapes and responses. One of the limitations of the physical implementations of the filters in the previous chapters is their size. A method to help overcome their size limitations and make them desirable for use in more applications is to condense the number of physical resonators while retaining the same number of electrical resonances through the use of multi-mode resonances. This chapter will focus on a new dual-mode, dual band resonator and filter structure that provides multiple poles and passbands per resonator with tunable center frequencies. The new structure has a single fundamental resonance at a designed frequency, as well as a pair of two higher order resonances at another designed frequency, all from a single physical resonator that is of similar size as the resonators shown in previous chapters. The coupling to and between these three resonances can be controlled within some limitations, and many useful filtering capabilities are possible. In an FPFA, such a structure could be used to convert between a relatively wide band second order filter and a relatively narrow band fourth order filter, all while only using the physical volume of two resonators. This conversion could be obtained by tuning the fundamental modes away from the band of interest and the higher order modes to the band of interest. This concept is shown below in Fig. 9.1.

Dual-band, frequency-static filters are also used in applications where volume and weight are critical design parameters, including satellite and mobile systems [118]. The new structure shown in this chapter will also be useful for such applications.

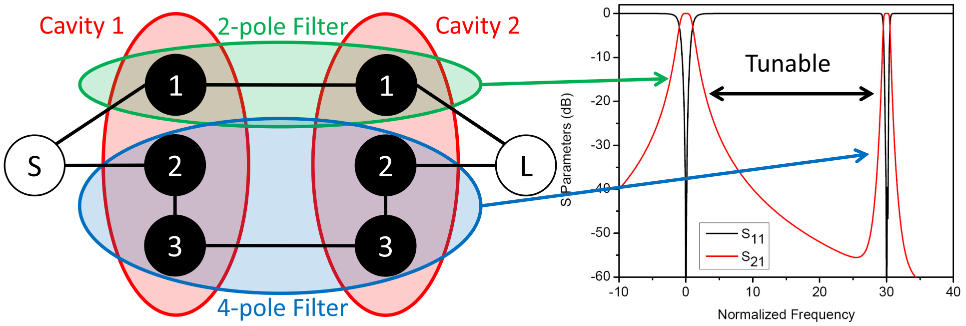

Fig. 9.1. Ideal coupling routing diagram of a 2-cavity filter with six resonances. Two resonances form a 2-pole bandpass filter, while the other four resonances form a narrower bandwidth 4-pole filter. Both responses tune together, allowing switching from a 2-pole response to a 4-pole response by simply tuning the center frequency of the resonances.

Past dual-mode filter structures have utilized rectangular [124], [125], circular [126], triangular [127], and other shaped planar resonators [128] as well as metal cavity [129], dielectric-resonator-loaded metal cavity [130], and strontium titanate resonators [131]. All of these structures offer their own respective advantages. Planar dual-mode structures can have comparatively low volume and weight compared with other dual-mode filter structures. In addition, the required surface area for a planar dual-mode filter can be further reduced using meandering [132]. In [132], 68% size reduction of a conventional square dual-mode resonator is shown through meandering. Dual-mode filters can also have frequency tuning capability through the use of varactors [133]. In [133], a 35% frequency tuning dual-mode bandpass filter is shown. However, tunable planar filters often have low resonator quality factors (Q) on the order of 20-200 due to substrate and tuning element losses.

The volume and weight of metal cavity dual-mode filters can be significantly reduced while retaining high resonator Q values on the order of 1,000-10,000 by using dielectric loading, rectangular ridge resonators [134], or transverse magnetic modes [135]. Substrate integrated waveguide (SIW) dual-mode filters [136]- [138] add simple integration of a filter with other system components at a slight cost to Q due to increased dielectric losses compared with an air filled cavity. However, these resonators are difficult to electronically tune due to their resonator field distributions. Additionally, while these technologies provide valuable volume and weight savings over single-mode, air-filled metal cavity filters, they still have dimensions that are significant fractions of a wavelength at their operating frequencies.

An additional feature of some dual-mode resonator structures is the capability to produce dual-band filter responses through the use of multiple sets of coupled resonances from the same resonator. Examples of dual-band filters that use dual-mode resonators can be seen in [118]- [126], [129], [139], [140], with most using resonators that belong to the planar or metal cavity categories described above. Planar dual-band filters where either one or both of the passbands are tunable have also been presented [141], [142]. In [141], the lower passband is tunable over a 22.2% frequency range, and the upper passband is tunable over a 19.6% frequency range. In [142], over 17% tuning of the upper passband is achieved while the lower passband remains static.

Currently, dual-mode and dual-band filter designers must choose between compact, tunable, low-Q planar designs or potentially bulky, static, high-Q cavity or dielectric resonator designs. In some applications it would be useful to have a resonator structure that has some of the compactness and tuning capability of past planar designs while retaining a Q approaching those of cavity-based designs. This chapter presents a new type of highly loaded coaxial cavity resonator filter that can fill this need. In contrast to previous highly loaded coaxial cavity resonator filters with wide spurious-free ranges [64]- [55], the proposed resonator has a loading post, the center conductor of the coaxial structure, that is split into multiple pieces to create new modes that can be used to create filter responses. While the new resonator structure can be made using any type of conductor-walled cavity such as machined bulk metal, the measured implementations shown in this chapter use plated via-defined, substrate-integrated cavities [64], [100], [55], [143]- [145]. However, substrate-integrated cavities are not required to use the resonator presented in this chapter. A dual-mode, two-pole filter using one of these resonators is shown in which the fundamental mode and both degenerate resonances can be tuned with a single actuator. This is a significant operational advantage over both past dual-mode filter designs and past single-mode highly loaded coaxial cavity resonator filters [64] because it simplifies potential control circuits. Finally, a tunable dual-band filter with a two-pole response in its lower band and a four-pole response in its higher band is shown that uses two of the new highly loaded coaxial cavity resonators. This structure is unique compared with previous dual-band filter implementations that use two resonances per physical resonator because the first band is created using the fundamental mode of the resonators and the second band is created using both of the next higher degenerate modes of the resonators for a total of three resonances per physical resonator.

9.2 Intersecting Parallel Plate Waveguide Loaded Resonators

Previously presented tunable coaxial cavity filters are tuned by physically modulating a small gap between the capacitive loading post and the wall of the cavity. In order to enable dual-band and dual-mode responses, the loading post of a coaxial cavity resonator is sliced into several wedge-shaped pieces in this chapter, creating degenerate modes in the resulting intersecting parallel plate waveguide sections inside the post. A model of a highly loaded coaxial cavity where the loading post has been sliced into four wedges can be seen in the left side of Fig. 9.2. The four wedge pieces create two orthogonal parallel plate waveguide sections inside the loading post. Fig. 9.2 shows important design parameters of the intersecting parallel plate waveguide loaded resonator, including the cavity radius (b), loading post radius (a), cavity height (h), span of the the gaps between wedge pieces (x), and gap between the four-wedge loading post and the top wall of the cavity (g). These design parameters can be used to manipulate the typical fundamental mode of the highly loaded coaxial cavity resonator as well as three new additional modes that are created through the division of the loading post into four wedge pieces. The right side of Fig. 9.2 shows

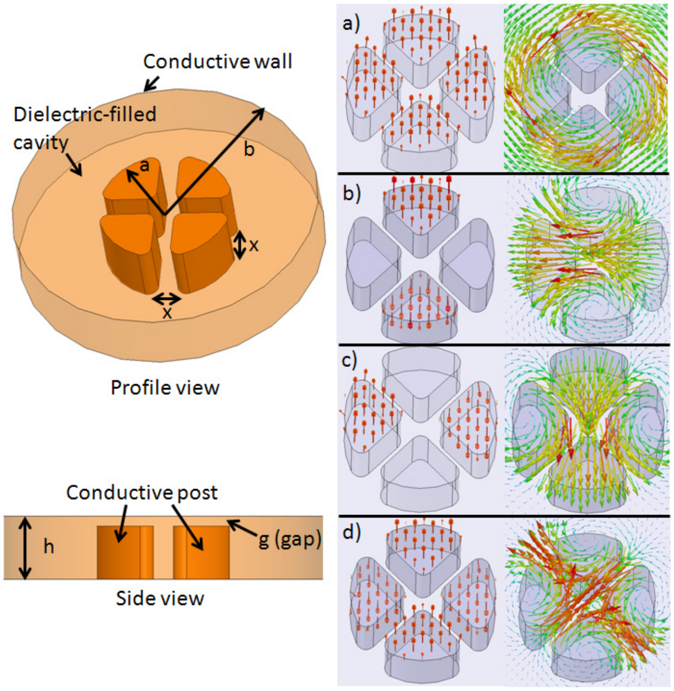

Fig. 9.2. Profile and side views of a four-wedge intersecting parallel plate waveguide loaded coaxial cavity resonator. E (left) and H (right) fields of a) fundamental mode. b) and c) degenerate modes. d) first spurious mode.

ANSYS HFSS simulated vector plots of the electric field (left) and magnetic field (right) of the fundamental a), degenerate b) and c), and first higher-order spurious d) modes of the resonator. The degenerate modes are orthogonal in space but share the same underlying geometry and boundary conditions. Therefore, in the absence of perturbation the degenerate modes occur at the same frequency.

An analytical model for fast approximation and theoretical understanding of the four modes shown in Fig. 9.2 can be constructed through expansion of the electromagnetic analysis in [146]. The fundamental mode (Fig. 9.2 a) frequency is modeled by approximating the cavity inductance as the inductance of a length $h-g$ of coaxial cable and the cavity capacitance as the parallel plate capacitance between the loading post wedges and the top wall of the cavity and the capacitance of a length $h-g$ of coaxial cable in parallel. The fundamental mode frequency in terms of the resonator geometry is

$$f_f = \frac{1}{2\pi}\sqrt{\frac{1}{LC}} = \frac{1}{2\pi}\sqrt{\frac{2\pi}{\mu(h-g)\ln(\frac{b}{a_{eff}})(C_{pp}+C_{coax})}}, \tag{9.1}$$

where C_{pp} is the parallel plate capacitance between the loading post top and cavity wall incorporating the fringing field approximation in [147] and given by

$$C_{pp} = \frac{\epsilon}{g}(\pi a_{eff}^2 + g a_{eff}\ln(\frac{16\pi a_{eff}}{g} - 1)), \tag{9.2}$$

and C_{coax} is the capacitance of a length $h-g$ of coaxial cable given by

$$C_{coax} = \frac{2\pi\epsilon(h-g)}{\ln(\frac{b}{a_{eff}})}. \tag{9.3}$$

Note that these formulas account for the reduction in parallel plate capacitor area caused by x by using an effective post radius a_{eff} given by

$$a_{eff} = \sqrt{a^2 - \frac{4ax}{\pi} + \frac{x^2}{\pi}}. \tag{9.4}$$

The same parallel plate capacitor model can be used to determine an expression for the energy stored in the electric field for the degenerate modes. However, the capacitance of the intersecting parallel plate waveguide sections inside the loading post, which is in parallel with the parallel plate capacitance between the post and cavity wall, must also be taken into account to accurately model the degenerate modes. The energy stored in the electric field of the degenerate modes can be written as

$$W_e = \frac{\epsilon}{4}\int\int\int_V \left|\bar{E}\right|^2 dV = \frac{\epsilon}{2} g A_{eff} E_0^2, \tag{9.5}$$

where E is the electric field, ϵ is the permittivity of the dielectric inside the cavity, A_{eff} is the effective area of the capacitance for the degenerate mode, and E_0 is the magnitude of the electric field. For the degenerate modes, the magnetic field concentration is much higher in the volume between the post wedges than in the volume exterior to the loading post if x is small relative to a, so it is also assumed that all of the current for this mode is flowing on the parallel-plate walls interior to the loading post. The magnetic field in the resonator can be calculated from the current density on the parallel-plate walls interior to the loading post. Therefore, the energy stored in the magnetic field of the degenerate modes can be written as

$$W_m = \frac{\mu}{4} \int \int \int_V \left|\bar{H}\right|^2 dV = \frac{\mu(h-g)x\epsilon^2 E_0^2 \omega^2 A_{eff}^2}{8a}, \tag{9.6}$$

where μ is the permeability of the dielectric inside the cavity, x is the gap between wedge pieces, and ω is radian frequency. Equating (9.5) and (9.6) at resonance yields the degenerate mode frequency, f_d, in terms of the resonator geometry

$$f_d = \frac{1}{2\pi}\sqrt{\frac{4a}{\mu(h-g)x(\frac{C_{pp}}{2} + C_{ppw})}}, \tag{9.7}$$

where C_{ppw} is the capacitance of one of the intersecting parallel plate waveguide sections inside the loading post and is defined as

$$C_{ppw} = \epsilon(2a - x)\left(\frac{(h-g)}{x} + \frac{1}{\pi} + \frac{1}{\pi}\ln\left(\frac{2\pi(h-g)}{x}\right)\right). \tag{9.8}$$

Note that the dimension h-g is the width of the parallel plate waveguide section, and the dimension x is its height. A fringing field approximation from [148] is also used in (9.8). An expression for the first higher-order spurious mode frequency can be obtained from (9.7) by reducing the effective area of the parallel plate capacitance by a factor of two. Therefore, the first higher-order spurious mode frequency is

$$f_s = \frac{1}{2\pi}\sqrt{\frac{4a}{\mu(h-g)x(\frac{C_{pp}}{4} + C_{ppw})}}. \tag{9.9}$$

Note that C_{ppw} is modeled to be the same for both f_d and f_s because the magnetic field curls around a single loading post wedge piece in the analysis of f_s. Although it encounters a bend along this path, it encounters the same length of parallel plate waveguide interior to the loading post as in the analysis of f_d where the magnetic field traverses the diameter of the loading post. The effect of the bend is only significant for large ratios of x and a that are beyond the scope of the design space focused on in this chapter.

Table 9.1
Design parameters of simulated dual-mode cavities.

Cavity	a (mm)	b (mm)	x (mm)	h (mm)	x/a (%)
1	2.0	8.0	0.4	3.0	20
2	3.0	8.0	0.9	3.0	30
3	4.0	8.0	1.6	3.0	40
4	5.0	8.0	2.5	3.0	50

In order to determine the accuracy of the model described above, it was checked against HFSS eigenmode simulations of dual-mode highly loaded coaxial cavities with the dimensions shown in Table 9.1. For all cases, the permittivity and permeability were set to their respective free-space values and b and h were kept constant to highlight the effects of varying values and ratios of a and x. Fig. 9.3 shows a comparison of the calculated resonant frequency vs. gap (g) from the analytical model and ANSYS HFSS eigenmode simulations for the four modes discussed above. Note that as the ratio of a and x changes, the ratio of the frequencies of the fundamental and degenerate modes changes. Using this ratio, the frequency spacing of the fundamental and degenerate modes can be set for dual-band filter design.

It can be seen that the resonant frequencies calculated by the analytical model are very close to those calculated by the eigenmode simulations for small gaps (g) and small x. The analytical model becomes less accurate for large g because the fringing field capacitance approximation used in (9.2) is not exact. Similarly, it becomes less accurate for large x because the effect of the fringing field approximation is magnified in this situation. While the analytical model has limitations at the extremes of the design space, it is accurate enough to be used to obtain a starting point for full-wave simulation and simple enough to provide understanding of the resonator's operation.

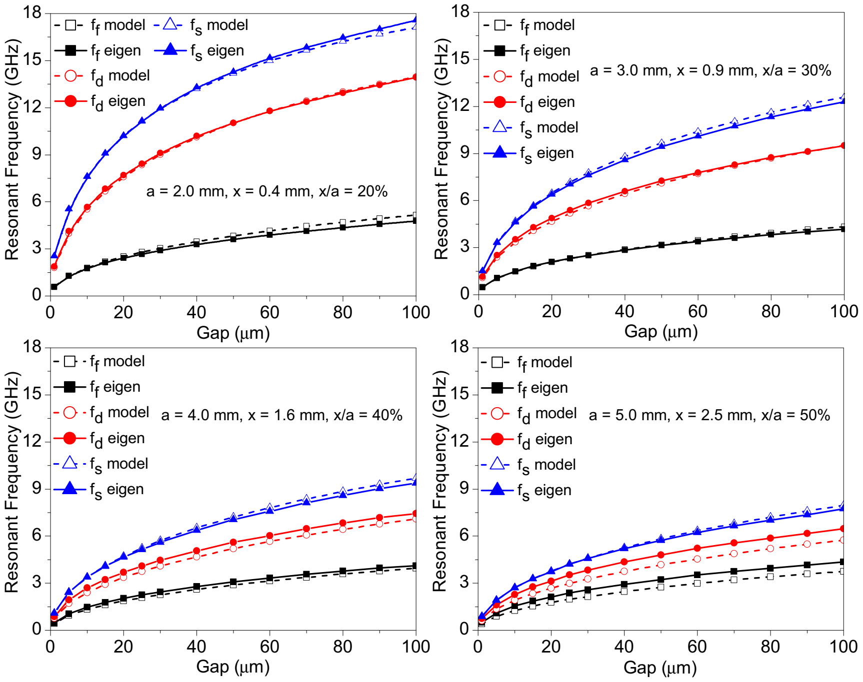

Fig. 9.3. Resonant frequencies calculated by the analytical model and ANSYS HFSS eigenmode simulation of the cavities described in Table 9.1.

9.3 Bandpass Filter Design Using Parallel Plate Waveguide Loaded Cavities

In order to design a filter with a specific type of resonator, external coupling and inter-resonator coupling values available from that resonator with particular coupling structures must be known and understood. This section will show design graphs of the simulated available coupling values of a parallel plate waveguide loaded coaxial cavity with specific coupling structures. These structures are meant to serve as examples and are not exclusive. Values for external coupling from a port to a resonator, intra-resonator coupling between two degenerate modes within a single cavity, and inter-resonator coupling between two cavities will be shown.

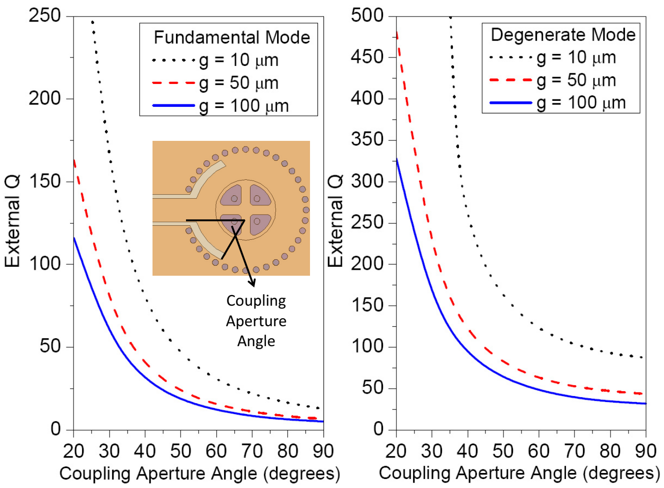

Fig. 9.4. External Q vs. coupling aperture sweep angle for the fundamental and degenerate modes of the proposed resonator.

9.3.1 External Coupling

Many highly loaded coaxial cavity resonators and filters use apertures to achieve external coupling, and aperture coupling can be used in parallel plate waveguide loaded coaxial cavities as well. A simulation model of a resonator with aperture coupling can be seen in the inset in Fig. 9.4. The aperture is created by sweeping the end of the insulated traces of a coplanar waveguide transmission line along an angle. The simulation model consists of an 8 mm radius substrate-integrated cavity defined by plated vias and a copper loading post of radius 3.55 mm cut into 4 wedges. Note that the geometry of this resonator is the same as that used in the fabricated example shown later in this chapter, and a more detailed description will be given in the next section. Additionally, while the analysis above assumed solid cavity walls and bulk metal loading post elements, the performance of highly loaded, via-defined geometries can still be well predicted by the analysis because the capacitance between the top of the loading post and the top wall of the resonator dominates the total capacitance. For less-loaded structures, bulk metal is recommended. For this study, the aperture sweep angle, defined graphically in Fig. 9.4, was swept from 20 degrees to 90 degrees.

External coupling values were extracted according the the method described in [75] for the fundamental and degenerate modes for gaps (g) of 10 μm, 50 μm, and 100 μm. Fig. 9.4 shows that the aperture sweep angle and gap (g) parameters can be used to obtain desired external coupling values. The ratio of the fundamental mode and degenerate mode external coupling values can be seen in Fig. 9.5 for different sizes of cavities. Three lines in Fig. 9.5 show ratios of the external coupling values shown in Fig. 9.4 for three values of g. The other two lines show ratios of the external coupling values of resonators with 25% larger or smaller outer diameters (b), respectively, with a g of 50 μm. Fig. 9.5 shows that the outer diameter (b) of the cavities can be designed to provide different ratios of external coupling, enabling the design of dual band filters with independant bandwidths. Such a change effectively changes the relative amount of capacitive loading in the cavity, or equivalently, the resonator's characteristic impedance at different frequencies. In summary, a filter designer can set the ratio of external coupling values using the technique shown in Fig. 9.5 and

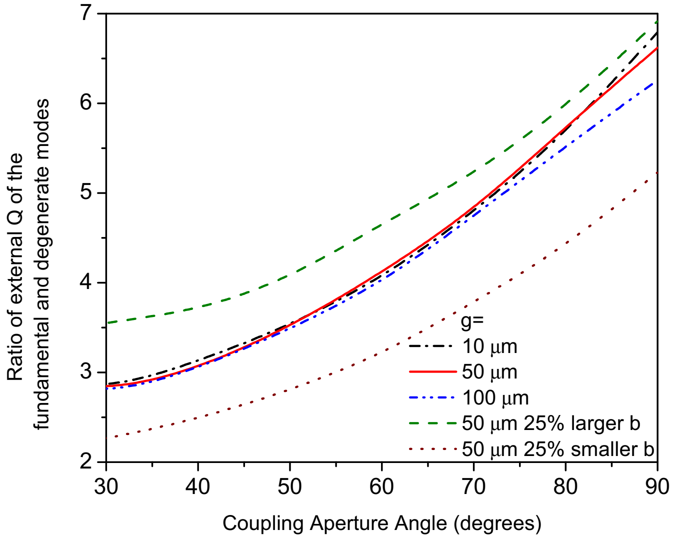

Fig. 9.5. Ratio of external Q of the fundamental and degenerate modes vs. coupling aperture sweep angle for resonators with various outer radii (b).

then set the absolute coupling values by using the coupling aperture sweep angle as shown in Fig. 9.4.

9.3.2 Intra-Resonator Coupling

Intra-resonator coupling refers to the coupling between degenerate modes inside a single cavity. It can be implemented with an additive or subtractive feature in one corner of the cavity's loading post. Alternatively, it can be implemented with a via or other conductive element that is located radially outward from the loading post. A mode splitting feature can be seen in the inset of Fig. 9.6 on the upper right corner of the loading post. Fig. 9.6 also shows k_{intra} values for mode splitting feature radii

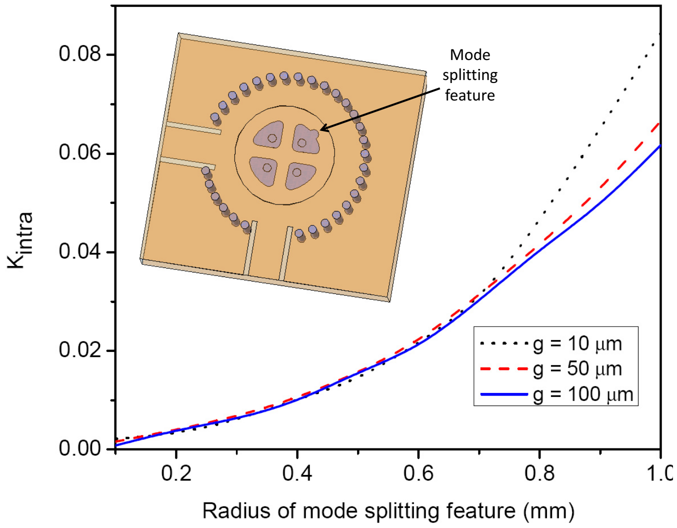

Fig. 9.6. Intra-resonator coupling, k_{intra}, vs. radius of mode-splitting post feature.

from 0.1 mm to 1 mm using a similar cavity as was used for the external coupling simulations above. k_{intra} is defined as

$$k_{intra} = \frac{f_b^2 - f_a^2}{f_b^2 + f_a^2}, \tag{9.10}$$

where f_b and f_a are the frequencies of the peaks seen in the transmission response when a pair of coupled resonances is coupled to the measurement ports using weak external coupling. Fig. 9.6 shows that relatively small perturbations to the loading post can produce a wide range of values of k_{intra} while not strongly affecting the fundamental mode frequency. Note also that k_{intra} is not a strong function of the gap (g) between the loading post and top wall of the cavity, allowing g to be used as a design parameter for external coupling.

9.3.3 Inter-Resonator Coupling

Inter-resonator coupling between cavity resonators can be implemented with waveguide irises. An example of a waveguide iris used to couple two parallel plate waveguide loaded, substrate-integrated cavities can be seen in the inset in Fig. 9.7. Fig. 9.7 also shows that inter-resonator coupling, k_{inter}, is a function of coupling iris width and g. k_{inter} is defined as

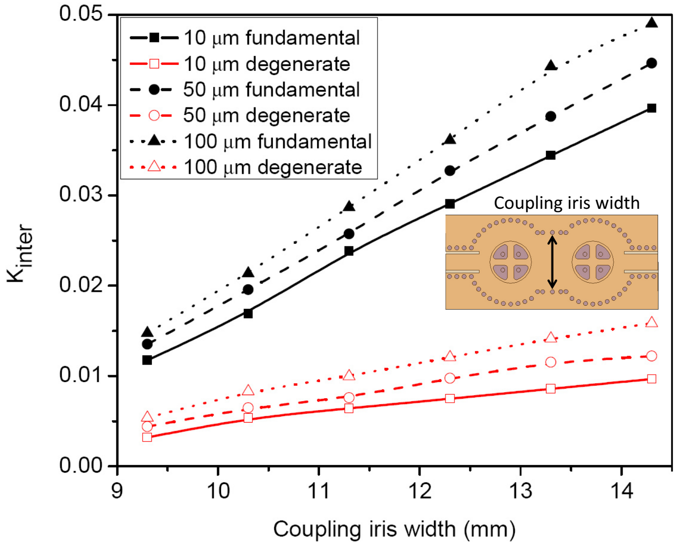

Fig. 9.7. Inter-resonator coupling, k_{inter}, vs. coupling iris width.

$$k_{inter} = \frac{f_b^2 - f_a^2}{f_b^2 + f_a^2}, \tag{9.11}$$

where f_b and f_a are the frequencies of the peaks seen in the transmission response when a pair of coupled resonances is coupled to the measurement ports using weak external coupling. Note that k_{inter} is also a function of the spacing between the coupled cavities and any perturbations in the iris, but these concepts will not be shown here. Additionally, low-pass or high-pass structures can be added in parallel with the iris to affect the frequency dependence of the coupling iris [64], effectively changing the ratio of inter-resonator coupling for the fundamental and degenerate modes of a pair of parallel plate waveguide loaded cavities since the fundamental and degenerate modes occur at different frequencies. Using waveguide irises, n-pole filters that use 2 degenerate modes per resonator can be designed, where n is an even integer. Now that the coupling values and example methods to manipulate them are understood, the next section will present design examples.

9.4 Design Examples

9.4.1 2-Pole, Single-Resonator Bandpass Filter

This subsection will provide an overview of the design and layout of a 1.2% 3 dB fractional bandwidth Butterworth 2-pole filter that is tunable about a frequency of 4.45 GHz and uses a single intersecting parallel plate waveguide loaded resonator. The coupling and routing diagram of the structure can be seen in Fig. 9.8. A coupling matrix will be shown later in the chapter to describe certain aspects of the measured responses. The design utilizes a fabrication procedure that has been used previously in this dissertation, and more detailed descriptions of the process can be found in [100], [73], and [149]. The resonator was designed as a substrate integrated

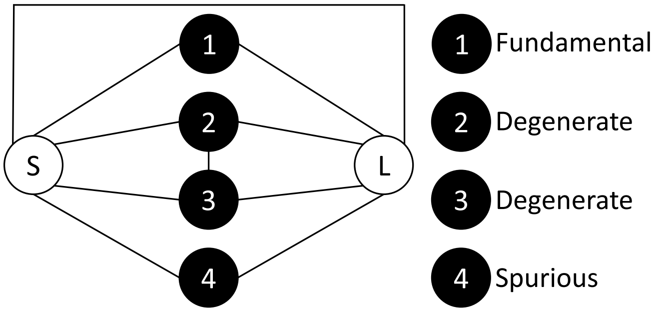

Fig. 9.8. Coupling-routing diagram for all four resonances of interest of the 2-pole, single-resonator bandpass filter.

resonator in 3.175 mm thick Rogers TMM3 (ϵ_r=3.27, tan(δ)=0.002 @ 10 GHz) substrate, and its simulation model can be seen in Fig. 9.9 along with simulation results of a weakly coupled forward transmission coefficient that shows the modes used for filtering. However, it is important to note that these resonators can be implemented using a multitude of fabrication techniques ranging from standard bulk metal machining to more complicated microfabrication techniques. The geometry shown in Fig. 9.9 was estimated using the design equations presented above and optimized using ANSYS HFSS software. In addition to what is shown in Fig. 9.9, the nominal gap (g) between the loading post and the top flexible wall of the cavity was designed to be 80 μm, and it was physically implemented by stacking three layers of 1 mil Dupont Pyralux LFO100 adhesive when laminating the flexible copper top wall of the cavity. Mechanically modulating g produces frequency tuning of the filter, and this modulation was done using 0.38 mm thick, 12.7 mm diameter piezoelectric disk actuators from Piezo Systems, Inc.

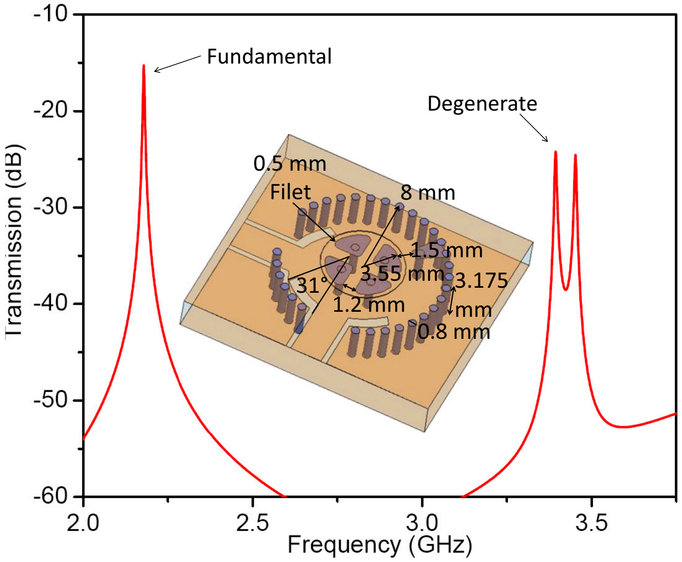

Fig. 9.9. Simulation model of the single-resonator, dual-mode filter and simulated weakly coupled forward transmission coefficient showing fundamental and degenerate modes used for filtering. Nominal g = 80 μm.

Another design aspect to note from Fig. 9.9 is that a plated via was used to obtain intra-resonator coupling instead of the mode-splitting feature on the loading post that was described above, which may be more or less favorable depending on the fabrication technologies available to the designer and the required value of intra-resonator coupling. For example, a small value of intra-resonator coupling would require a small and accurately sized feature to be added to the loading post that could be outside the fabrication tolerances of some manufacturing techniques. However, a relatively large plated via could be used to implement the same amount of intra-resonator coupling if it is placed far enough away from the loading post. The position of this via was determined through optimization in simulation using the method described in [25], and it has a similar relationship to k_{intra} as the post feature shown above. The external coupling structures are on separate conductor layers to aid in source-to-load out-of-band isolation, and their width is 1 mm. As shown in Fig. 9.9, the aperture sweep angle was determined to be 31 degrees by the method presented in [75]. Simulated and measured results of the 2-pole filter will be shown in the next section.

9.4.2 Double-Resonator, Dual-Band Bandpass Filter

This subsection will describe the design of a dual-band bandpass filter with a 2-pole, 5.5% 3 dB fractional bandwidth Butterworth filter at 2.5 GHz and a 4-pole, 2% 3 dB fractional bandwidth Butterworth filter at 4.1 GHz using the fundamental and degenerate modes of two intersecting parallel plate waveguide loaded resonators. A coupling-routing diagram of the structure can be seen in Fig. 9.10. The resonators are similar to the one described in the previous subsection, with coupling values and intra-resonator coupling structure physical implementation being the only changes. A simulation model of the structure with relevant geometrical properties labeled is shown in Fig. 9.11. Coupling structure geometries were determined using ANSYS HFSS simulation and the methods in [75], [25]. In contrast to the single resonator

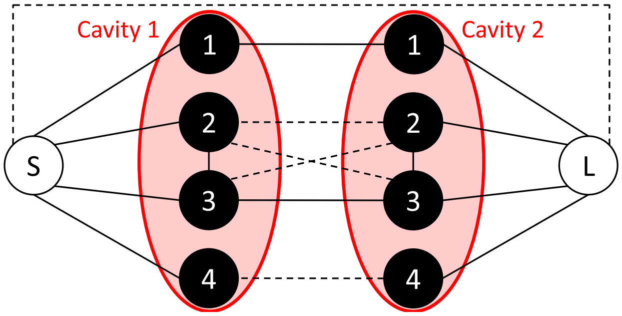

Fig. 9.10. Coupling-routing diagram for the double-resonator, dual-band bandpass filter. The resonances of each cavity are grouped together with red shaded ovals. Strong coupling values are denoted by solid lines. Weak coupling values that may have an effect on the response are denoted by dashed lines.

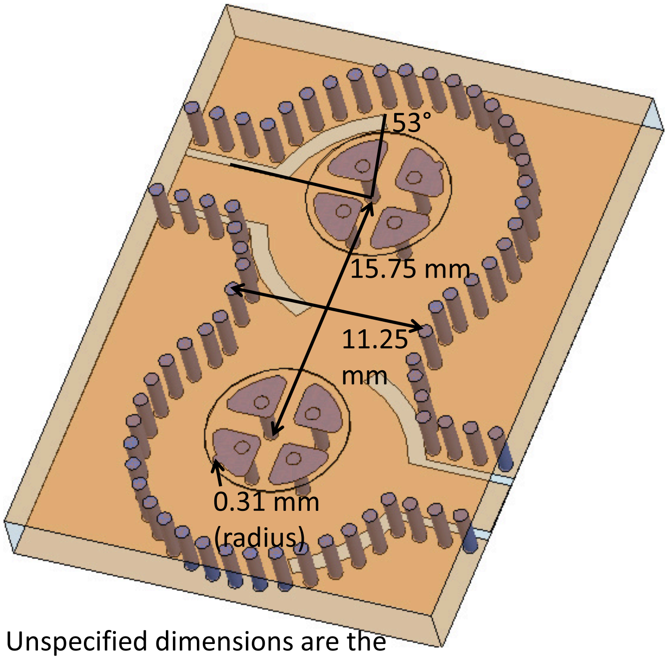

Unspecified dimensions are the same as those shown in Fig. 8.

Fig. 9.11. Simulation model of the double-resonator, dual-band filter. Nominal g = 80 μm.

design described in the previous subsection, an additive loading post feature was added to implement intra-resonator coupling instead of a plated via. One other interesting aspect of the design is that the resonators are physically rotated by 180 degrees with respect to each other as was originally shown in [150]. Designing the filter in this way has two desirable consequences. First, if coupling apertures are used to implement external coupling as they are in this design, the apertures will be further away from each other in space with this configuration. This reduces source-to-load coupling and provides more attenuation far away from the passbands of the filter. The second advantage to rotating the resonators 180 degrees with respect to each other is that the fundamental and degenerate modes in both cavities constructively couple, while the next spurious mode cancels due to the opposing direction of the magnetic fields of the spurious mode in the two resonators. This is a significant functional advantage that will be shown in the measured results in the next section.

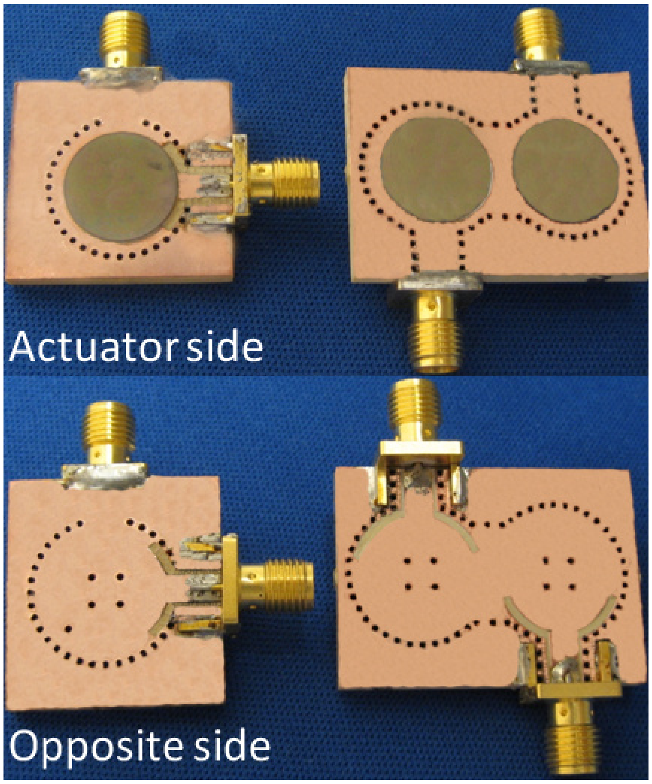

Fig. 9.12. Photograph showing both sides of both the 2-pole, single-resonator bandpass filter and the double-resonator, dual-band bandpass filter.

Photographs showing both sides of both the 2-pole, single-resonator bandpass filter and the double-resonator, dual-band bandpass filter can be seen in Fig. 9.12. The circular piezoelectric actuators can be seen in the top row of photographs with bias lines removed for clarity. The actuators are attached to the cavity resonators using silver epoxy. The plated vias that provide connection between the loading posts and the cavity walls, as well as the mode-splitting via used in the 2-pole, single-resonator filter can be seen in the bottom row of photographs.

9.5 Simulated and Measured Results

Measured vs. synthesized and full-wave simulation results of the single-resonator, 2-pole filter can be seen in Fig. 9.13 and Fig. 9.14. The measured fundamental mode is at 2.78 GHz and has 0.73 dB insertion loss. The fundamental mode can be filtered with a high pass filter if the 2-pole, dual-mode response is all that is desired. Alternatively, a low pass filter with a cutoff frequency between the fundamental and degenerate modes could be added between the ports of the filter that would act as a

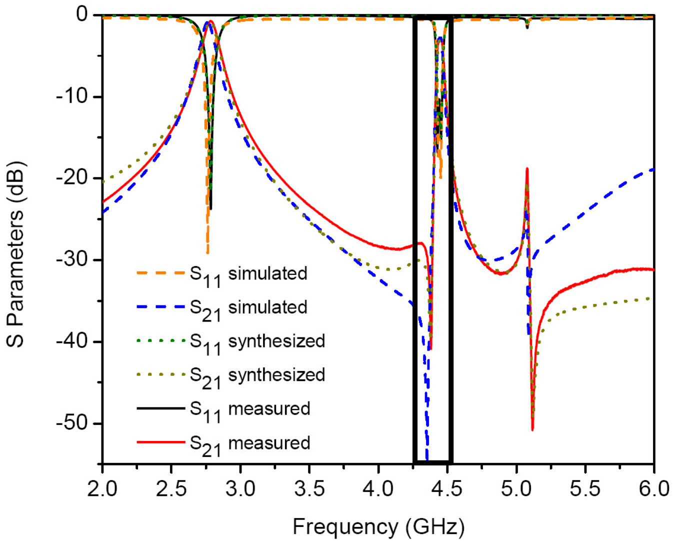

Fig. 9.13. Full-wave simulated vs. synthesized (with (9.12)) vs. measured results of the single-resonator, dual-mode filter. Fig. 9.14 shows a magnified view of the dual-mode passband.

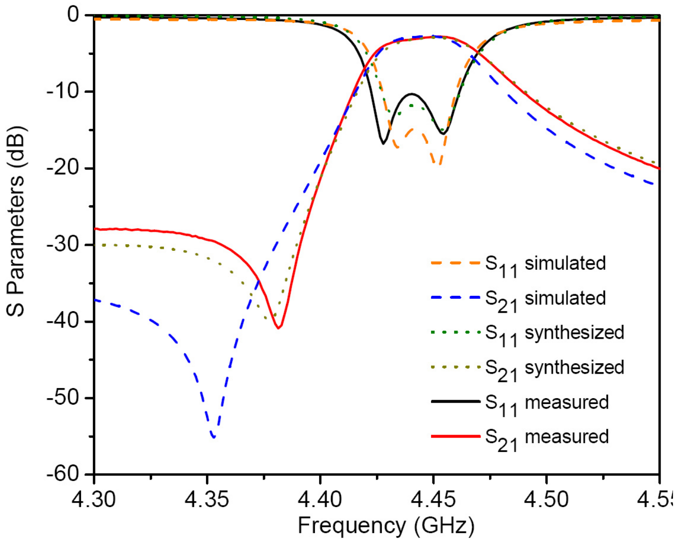

Fig. 9.14. Narrow band view of boxed frequency range in Fig. 9.13.

shunt (bandstop) feed for the fundamental mode and a series (bandpass) feed for the degenerate modes. However, the fundamental mode is shown here to demonstrate the behavior of the new resonator structure. The measured 2-pole, dual-mode response is at 4.45 GHz. It has 2.80 dB insertion loss and a 3 dB bandwidth of 52 MHz, corresponding to a fractional bandwidth of 1.2% (extracted Q = 360). The measured first spurious mode is at 5.08 GHz and has 18.75 dB insertion loss. This mode is undesired for this filter design, but it will be shown that it can be cancelled in higher-order filter structures that use the proposed resonator. While the responses in Fig. 9.2 match well, the largest difference is the location of the transmission zero on the lower-frequency side of the dual-mode, 2-pole filter response. This transmission zero is due to interaction of the apertures that provide external coupling and each aperture slightly coupling to the adjacent degenerate mode. These effects can be modeled in an $N+2 \times N+2$ coupling matrix that corresponds to the coupling and routing diagram in Fig. 9.8,

$$\begin{bmatrix} 0 & 0.675 & 0.386 & -0.052 & 0.064 & 0.019 \\ 0.675 & 0 & 0 & 0 & 0 & 0.675 \\ 0.386 & 0 & -22.07 & 0.199 & 0 & -0.052 \\ -0.052 & 0 & 0.199 & -22.07 & 0 & 0.386 \\ 0.064 & 0 & 0 & 0 & -29.05 & 0.064 \\ 0.019 & 0.675 & -0.052 & 0.386 & 0.064 & 0 \end{bmatrix}, \tag{9.12}$$

where -j0.082 was added to M_{11} and M_{44} to model the bandwidth and quality factor for the fundamental and spurious modes and -j0.065 was added to M_{22} and M_{33} to model the bandwidth and quality factor for the degenerate modes. The matrix in (9.12) was scaled to a center frequency of 2.783 GHz and a bandwidth of 122.3 MHz to correspond to the measured fundamental mode parameters. Although the coupling matrix incorporates the narrowband approximation, it still serves as a useful design tool here and describes the measured results well. Fig. 9.13 shows agreement between the synthesized and measured data. The discrepancy in transmission zero location in the simulated response could be attributed to slight manufacturing inaccuracies, differences between the simulation and bench top environments, and features that were not simulated such as solder since the coupling terms that most govern its location, M_{SL}, M_{S3}, and M_{2L}, are relatively small.

Fig. 9.15 shows measured results of the single-resonator, 2-pole filter tuning over a frequency range of 4.35 GHz to 4.65 GHz. All four modes of interest are controlled by the same actuator, but their tuning ranges are slightly different because the tunable capacitance created by g is a different percentage of the total capacitance associated with each mode. The shown 6.7% tuning range of the degenerate modes is much less than the octave or more tuning range that is common with highly loaded coaxial cavity filters. The cause is that a larger gap (g) was used between the loading post and top wall of the cavity in this design (80 μm) in order to achieve the coupling coefficients for the desired filter bandwidth, making the center frequency less sensitive

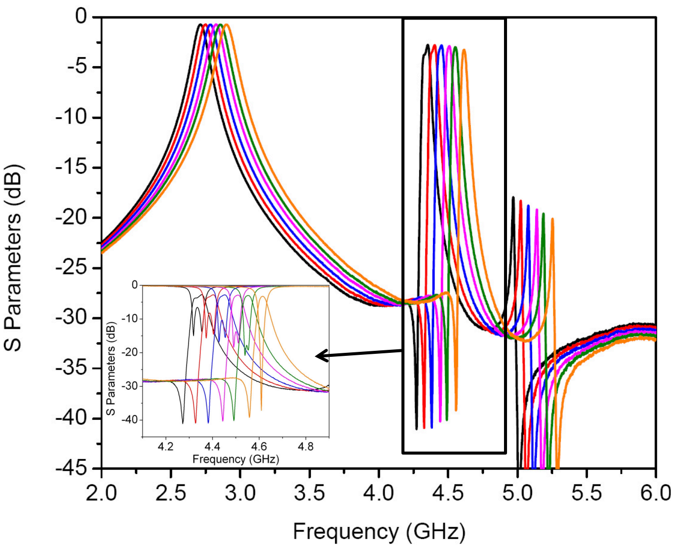

Fig. 9.15. Measured results of the single-resonator, dual-mode filter with a 2-pole response tunable about 4.5 GHz. Inset shows a magnified view of the tuning performance of the dual-mode, 2-pole response.

to small changes in g. Increasing this gap trades tuning range with a certain amount of actuator displacement for higher resonator impedance, higher power handling [151], and higher quality factor [55]. In a design with a larger g, an actuator with a larger range of physical motion could be used to achieve a wider tuning range. It is also worth noting that if all four modes are to be tuned together with a single actuator, the flexible copper membrane above the loading post must be relatively flat for a given g or the degenerate modes will tune at different rates. A larger g helps to mitigate this requirement.

Fig. 9.16 shows measured and simulated results for the double-resonator, dual-band filter with a 2-pole response that is tunable about 2.5 GHz and a 4-pole filter that is tunable about 4.1 GHz. The 2-pole response has an insertion loss of 1.26 dB and a 3 dB fractional bandwidth of 5.9%, and the 4-pole response has an insertion loss of 3.34 dB and a 3 dB fractional bandwidth of 2.1% (extracted Q = 400). Both measured responses are slightly overcoupled compared to their simulated results as can be seen in the return loss response plotted in the insets of Fig. 9.4, but they still prove the

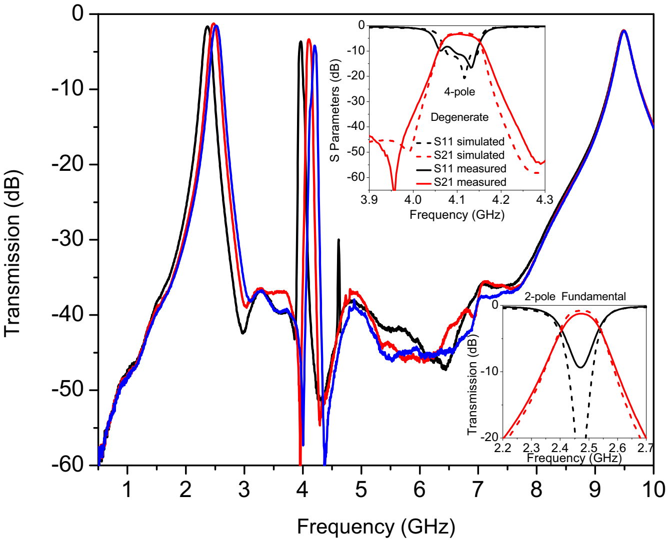

Fig. 9.16. Measured and simulated results of the filter with a 2-pole response tunable about 2.5 GHz and a 4-pole response tunable about 4.1 GHz. Solid lines represent measured results, and dashed lines represent simulated results.

concept of using multiple parallel-plate waveguide loaded coaxial cavity resonators to design higher-order filter responses. As described above, the first spurious mode cancels when the resonators are oriented as they are in Fig. 9.11, and the first spurious mode cannot be seen in two of the three responses shown in Fig. 9.16. However, the spurious mode starts to appear as the resonances are tuned to slightly offset frequencies as can be seen in the lowest-frequency response in Fig. 9.16.

Fig. 9.16 shows measurement data up to 10 GHz in order to show the second spurious mode of the structure. This mode is due to static features of the cavity and corresponds to the geometry between the loading post and the outer wall of the cavity. It was not a focus of this design, but the spurious mode can be moved higher in frequency or otherwise manipulated by removing or altering the dielectric material between the loading post and the outer wall of the cavity. While the mode looks like it is close to being critically coupled such that it could enable a triple-band response, this is a coincidence in this design. However, methods of manipulating coupling for this mode independent of the coupling for other modes used for filtering could be possible and could be the subject of future work. However, the mode would not be tunable in this configuration, at least without the addition of another tuning element.

9.6 Conclusion

A dual-mode resonator suitable for creating dual-mode and/or dual-band filter responses was shown. The structure used a multi-section loading structure in a highly loaded coaxial cavity to create degenerate modes that do not exist in typical highly loaded coaxial cavities. An analytical model of the structure was developed that can accurately predict the frequencies of the resonances over the proposed design space relative to full-wave simulation. A single-resonator, 2-pole filter, and a double-resonator, dual-band filter were designed and fabricated using the new structure to prove the concept. The proposed dual-mode resonator combines some of the compactness and tuning capability of previous planar dual-mode/dual-band filters while maintaining a Q that approaches those of static cavity and dielectric resonator filters. Additionally, the new dual-mode resonator enables the design of dual-mode filters with resonances that tune together with a single actuator. The combination of relatively high Q and reduced tuning complexity make the proposed dual-mode resonator a unique solution for future microwave systems.

10. CONCLUSIONS AND FUTURE WORK

The objective of this dissertation was to investigate novel synthesis techniques and electromagnetic structures that advance the state of the art of reconfigurable microwave filters. The synthesis techniques involved using the off resonance reactance of tunable resonators as well as tunable and/or able to be canceled coupling values to implement reconfiguration capability between many filter responses. It is notable that using the off resonance reactance of tunable resonators is a "'free"' capability if the resonators of a filter were already tunable for the purpose of shifting the center frequency of the filter, and modern switches and tuning elements enable coupling value tuning with minimal negative effects on filter responses. The electromagnetic structures described in this dissertation used impedance discontinuities, selective current redirection, relocation of field maximums, and multiple higher order modes to implement wider upper passband bandstop filters, tunable inter-resonator coupling, stronger bandstop filter external coupling for a given passband disturbance, and dual-mode resonator filters. Such innovations have progressed the state of the art of microwave filters in both theory and application, and several interesting use cases and future system level studies have been enabled.

10.1 List of Original Accomplishments Described in This Dissertation

- First use of tunable resonators to implement a reconfigurable bandstop filter array capable of providing several low-order notches or single higher-order notches of varying bandwidth.
- Widest frequency range non-Yttrium Iron Garnet (YIG) continuous notch coverage bandstop filter cascade to date (0.88-6.6 GHz).

- Widest upper passband tunable bandstop filter to date (17:1).
- First theoretical description of spurious resonance effects that can occur when cascading bandpass filters with bandstop filters for ultra-high isolation.
- Demonstration of 120 dB isolation of a 21 MHz bandwidth 16 % away from a low loss passband.
- First bandpass-to-bandstop reconfigurable filter without lossy tuning elements in its resonant path, which retains the high quality factor of the resonators.
- First switchless bandstop-to-all-pass reconfigurable filter.
- First wide spurious free range positive-to-negative inter-resonator coupling structure, enabling the most reconfigurable field programmable filter array (FPFA) to date.
- First demonstration of multi-order, reconfigurable transmission zeros using sets of parallel connected resonators.
- First dual-band filter that is tunable through the use of a single tuning element.

10.2 Future Work

In addition to the results shown in this dissertation, there are several opportunities for future work to utilize, supplement, and expand the state of the art in reconfigurable microwave filters. Some of these opportunities are outlined below.

1. **Ultra-wide tuning range reconfigurable and absorptive bandstop filters**: Some of the reconfigurable filter architectures described in this dissertation, for example the bandstop-to-all-pass filter, and some externally developed filter techniques, such as absorptive bandstop filters, rely on correct relationships between various coupling values in their networks to achieve maximum performance. When some of the coupling values are implemented using transmission lines of significant

electrical length, the coupling relationships only hold over a limited tuning range due to the change of the electrical length of the transmission lines with frequency. With innovative external coupling techniques, the required phase length of the transmission lines in these designs could be reduced to zero, removing the theoretical tuning range limitations of such filters. With a commensurate increase in resonator tuning range, multi-octave tuning absorptive and/or quasi-absorptive bandstop filters should be possible.

2. **MEMS tuners with air dielectric and improved attachment**: Silicon-based MEMS tuners have shown promising results toward being a faster-tuning, easier-to-control alternative to the piezoelectric actuators used to tune resonators described in this dissertation. However, dielectric charging limits both the tuning and life of MEMS tuners. In addition, the current MEMS tuner attachment methods, silver epoxy or compression using a mechanical fixture, result in lower than theoretically possible quality factors, difficult to control initial resonant frequencies, and/or addition of considerable bulk. New tuner fabrication techniques using air dielectric in the tuning field region and bonded metal-to-metal attachment would greatly advance MEMS tuners. Advances in laser ablation systems, which are currently capable of creating 50 μm features, and three dimensional printers, which are currently capable of 10 μm layer thickness, could also enable the use of new MEMS materials.

3. **Tunable filter control mechanisms and algorithms**: While significant tuning control accomplishments have been made, there is still no optimal way to automatically control many types of tunable resonators. Development of such methods would greatly increase the practicality of tunable filters, perhaps more than any other possible innovation.

4. **System capability benefits from tunable filters**: Most envisioned uses of tunable filters involve agile versions of protocols that are currently implemented with static filters. However, fast, controllable tunable filters could open up additional system operating modes that have not yet been envisioned. For example, imagine a transmitter with a purposely highly nonlinear power amplifier. Arbitrary or false

information could be sent on the fundamental frequency band, spoofing an eavesdropping receiver. Meanwhile, actual communication could be performed by the presence or blocking (with a tunable notch filter) of certain harmonics. The modulation of which harmonics are present during a symbol duration could be a form of covert communication.

5. **Multiplexer-tunable bandstop filter combinations for wideband systems**: As the performance of digital signal processing and analog to digital converters increases, more radio processing will be done in the digital domain. In addition, front ends in materials with high breakdown voltages and high thermal conductivity, such as Gallium Nitride, will allow a receiver to accept larger signals without being saturated. Therefore, as time progresses, receiver-saturating interference will be limited to only the highest power signals in the spectral environment. In such a scenario, a wide bandwidth front end with the capability to drop in notch filters on demand will offer the most efficient use and/or analysis of the current spectrum. Such capability will rely on innovations in both bandstop filter design and multiplexer design due to the difficulty of creating a bandstop filter with an ultra-wide passband.

6. **Analog signal processing and group delay engineering**: In current CMOS architectures, higher computation speed requires faster switching and therefore increased power consumption. If parts of computation-intensive processes could be done in the analog domain, power could potentially be saved and some sensor types could have increased use cases. While basic analog signal processing, for example an analog Fourier transform, has been accomplished, increased research into this domain could yield important results for computationally intensive tasks.

LIST OF REFERENCES

LIST OF REFERENCES

[1] Cisco, "Cisco visual networking index: Global mobile data traffic forecast update, 2011 to 2016," feb. 2012.

[2] I. Khalil, A. Liero, M. Rudolph, R. Lossy, and W. Heinrich, "Gan hemt potential for low-noise highly linear rf applications," *Microwave and Wireless Components Letters, IEEE*, vol. 18, pp. 605 –607, sept. 2008.

[3] W. Deal, X. Mei, K. Leong, V. Radisic, S. Sarkozy, and R. Lai, "Thz monolithic integrated circuits using inp high electron mobility transistors," *Terahertz Science and Technology, IEEE Transactions on*, vol. 1, pp. 25 –32, sept. 2011.

[4] T. young Choi, H. Sharifi, H. Sigmarsson, W. Chappell, S. Mohammadi, and L. Katehi, "3-d integration of 10-ghz filter and cmos receiver front-end," *Microwave Theory and Techniques, IEEE Transactions on*, vol. 55, pp. 2298 –2305, nov. 2007.

[5] R. Echevarria and L. Taylor, "Co-site interference tests of jtids, eplrs, sincgars, and mse (msrt)," in *Tactical Communications Conference, 1992. Vol. 1 Tactical Communications: Technology in Transition., Proceedings of the*, pp. 31 –39 vol.1, apr 1992.

[6] B. Perlman, J. Laskar, and K. Lim, "Fine-tuning commercial and military radio design," *Microwave Magazine, IEEE*, vol. 9, pp. 95 –106, aug. 2008.

[7] T. H. Lee, *Planar Microwave Engineering*. Cambridge, U.K.: Cambridge University Press, 2004.

[8] I. Reines, C. Goldsmith, C. Nordquist, C. Dyck, G. Kraus, T. Plut, P. Finnegan, I. Austin, F., and C. Sullivan, "A low loss rf mems ku-band integrated switched filter bank," *Microwave and Wireless Components Letters, IEEE*, vol. 15, pp. 74 – 76, feb. 2005.

[9] G. Matthaei, "Magnetically tunable band-stop filters," *Microwave Theory and Techniques, IEEE Transactions on*, vol. 13, pp. 203 – 212, mar 1965.

[10] A. Grichener, D. Merrier, and G. Rebeiz, "High-power high-reliability high-q switched rf mems capacitors," in *Microwave Symposium Digest, 2006. IEEE MTT-S International*, pp. 31 –34, june 2006.

[11] B.-W. Kim and S.-W. Yun, "Varactor-tuned combline bandpass filter using step-impedance microstrip lines," *Microwave Theory and Techniques, IEEE Transactions on*, vol. 52, pp. 1279 – 1283, april 2004.

[12] A. T. Wegener and W. Chappell, "Simultaneous transmit and receive with a small planar array," in *Microwave Symposium Digest (MTT), 2012 IEEE MTT-S International*, pp. 1–3, 2012.

[13] C. Andrews and A. Molnar, “A passive-mixer-first receiver with baseband-controlled rf impedance matching, $\leq$ 6db nf, and $\geq$ 27dbm wideband iip3,” in *Solid-State Circuits Conference Digest of Technical Papers (ISSCC), 2010 IEEE International*, pp. 46–47, 2010.

[14] C. Andrews and A. Molnar, “A passive mixer-first receiver with digitally controlled and widely tunable rf interface,” *Solid-State Circuits, IEEE Journal of*, vol. 45, no. 12, pp. 2696–2708, 2010.

[15] C. Andrews and A. Molnar, “Implications of passive mixer transparency for impedance matching and noise figure in passive mixer-first receivers,” *Circuits and Systems I: Regular Papers, IEEE Transactions on*, vol. 57, no. 12, pp. 3092–3103, 2010.

[16] A. Mirzaei, H. Darabi, and D. Murphy, “Architectural evolution of integrated m-phase high-q bandpass filters,” *Circuits and Systems I: Regular Papers, IEEE Transactions on*, vol. 59, no. 1, pp. 52–65, 2012.

[17] A. Ghaffari, E. Klumperink, and B. Nauta, “8-path tunable rf notch filters for blocker suppression,” in *Solid-State Circuits Conference Digest of Technical Papers (ISSCC), 2012 IEEE International*, pp. 76–78, 2012.

[18] C. Andrews, C. Lee, and A. Molnar, “Effects of lo harmonics and overlap shunting on n-phase passive mixer based receivers,” in *ESSCIRC (ESSCIRC), 2012 Proceedings of the*, pp. 117–120, 2012.

[19] T. Snow, C. Fulton, and W. Chappell, “Transmit and receive duplexing using digital beamforming system to cancel self-interference,” *Microwave Theory and Techniques, IEEE Transactions on*, vol. 59, no. 12, pp. 3494–3503, 2011.

[20] R. Cameron, “Advanced filter synthesis,” *Microwave Magazine, IEEE*, vol. 12, pp. 42 –61, oct. 2011.

[21] A. Atia, A. Williams, and R. Newcomb, “Narrow-band multiple-coupled cavity synthesis,” *Circuits and Systems, IEEE Transactions on*, vol. 21, pp. 649 – 655, sep 1974.

[22] R. J. Cameron, “General coupling matrix synthesis methods for chebyshev filtering functions,” *Microwave Theory and Techniques, IEEE Transactions on*, vol. 47, no. 4, pp. 433–442, 1999.

[23] R. J. Cameron, “Advanced coupling matrix synthesis techniques for microwave filters,” *Microwave Theory and Techniques, IEEE Transactions on*, vol. 51, no. 1, pp. 1–10, 2003.

[24] D. M. Pozar, *Microwave Engineering.* Hoboken, NJ: John Wiley & Sons, 2005.

[25] J.-S. Hong, *Microstrip Filters For RF/Microwave Applications.* Hoboken, NJ: John Wiley and Sons, Inc., second ed., 2011.

[26] R. J. Cameron, C. M. Kudsia, and R. R. Mansour, *Microwave Filters for Communication Systems: Fundamentals, Design, and Applications.* Hoboken, NJ: John Wiley and Sons, Inc., 2007.

[27] J. Lee, E. Naglich, H. Sigmarsson, D. Peroulis, and W. Chappell, “Tunable inter-resonator coupling structure with positive and negative values and its application to the field-programmable filter array (fpfa),” *Microwave Theory and Techniques, IEEE Transactions on*, vol. 59, pp. 3389 –3400, dec. 2011.

[28] D. Jachowski, “Passive enhancement of resonator q in microwave notch filters,” in *Microwave Symposium Digest, 2004 IEEE MTT-S International*, vol. 3, pp. 1315 – 1318 Vol.3, june 2004.

[29] E. Naglich, J. Lee, D. Peroulis, and W. Chappell, “Bandpass -bandstop filter cascade performance over wide frequency tuning ranges,” *Microwave Theory and Techniques, IEEE Transactions on*, vol. 58, pp. 3945 –3953, dec. 2010.

[30] I. Mitola, J. and J. Maguire, G.Q., “Cognitive radio: making software radios more personal,” *Personal Communications, IEEE*, vol. 6, pp. 13 –18, aug 1999.

[31] B. Carey-Smith and P. Warr, “Broadband configurable bandstop filter with composite tuning mechanism,” *Electronics Letters*, vol. 40, pp. 1587 – 1589, dec. 2004.

[32] A. Guyette, “Design of fixed- and varactor-tuned bandstop filters with spurious suppression,” in *Microwave Conference (EuMC), 2010 European*, pp. 288 –291, sept. 2010.

[33] I. Reines, S.-J. Park, and G. Rebeiz, “Compact low-loss tunable -band bandstop filter with miniature rf-mems switches,” *Microwave Theory and Techniques, IEEE Transactions on*, vol. 58, pp. 1887 –1895, july 2010.

[34] D. Jachowski and C. Rauscher, “Frequency-agile bandstop filter with tunable attenuation,” in *Microwave Symposium Digest, 2009. MTT ’09. IEEE MTT-S International*, pp. 649 –652, june 2009.

[35] S. Moon, H. Sigmarsson, H. Joshi, and W. Chappell, “Substrate integrated evanescent-mode cavity filter with a 3.5 to 1 tuning ratio,” *Microwave and Wireless Components Letters, IEEE*, vol. 20, pp. 450 –452, aug. 2010.

[36] J. Lee, E. Naglich, and W. Chappell, “Frequency response control in frequency-tunable bandstop filters,” *Microwave and Wireless Components Letters, IEEE*, vol. 20, pp. 669 –671, dec. 2010.

[37] SouthwestMicrowave, “The design & test of broadband launches up to 50 ghz on thin & thick substrates,” 2011.

[38] X. Liu, L. Katehi, W. Chappell, and D. Peroulis, “High- tunable microwave cavity resonators and filters using soi-based rf mems tuners,” *Microelectromechanical Systems, Journal of*, vol. 19, pp. 774 –784, aug. 2010.

[39] M. Win and R. Scholtz, “Ultra-wide bandwidth time-hopping spread-spectrum impulse radio for wireless multiple-access communications,” *IEEE Trans. Communications*, vol. 48, pp. 679 –689, Apr. 2000.

[40] T. Yucek and H. Arslan, “A survey of spectrum sensing algorithms for cognitive radio applications,” *IEEE Communications Surveys Tutorials*, vol. 11, no. 1, pp. 116 –130, 2009.

[41] B. Perlman, J. Laskar, and K. Lim, “Fine-tuning commercial and military radio design,” *IEEE Microw. Mag., IEEE*, vol. 9, pp. 95 –106, Aug. 2008.

[42] R. Levy, R. Snyder, and S. Shin, “Bandstop filters with extended upper passbands,” *IEEE Trans. Microw. Theory Tech.*, vol. 54, pp. 2503 –2515, June 2006.

[43] N. Yildirim, “Synthesis of bandstop filters with ultra wide upper passbands,” in *IEEE MTT-S Int. Microw. Symp. Dig.*, pp. 2109 –2112, June 2007.

[44] W. Fathelbab, “Two novel classes of band-reject filters realizing broad upper pass bandwidth;synthesis and design,” *IEEE Trans. Microw. Theory Tech.*, vol. 59, pp. 250 –259, Feb. 2011.

[45] G. Matthaei, “Magnetically tunable band-stop filters,” *IEEE Trans. Microw. Theory Tech.*, vol. 13, pp. 203 – 212, Mar. 1965.

[46] B. Carey-Smith and P. Warr, “Broadband configurable bandstop filter with composite tuning mechanism,” *Electronics Letters*, vol. 40, pp. 1587 – 1589, Dec. 2004.

[47] I. Reines, S.-J. Park, and G. Rebeiz, “Compact low-loss tunable X-band bandstop filter with miniature RF-MEMS switches,” *Microwave Theory and Techniques, IEEE Transactions on*, vol. 58, pp. 1887 –1895, July 2010.

[48] S. Hamzah, B. Ahmad, and P. W. Wong, “Multiband matched bandstop filter,” in *IEEE Asia-Pacific Conf. Applied Electromagnetics (APACE)*, pp. 1 –4, Nov. 2010.

[49] A. Guyette, I. Hunter, and R. Pollard, “Design of absorptive microwave filters using allpass networks in a parallel-cascade configuration,” in *IEEE MTT-S Int. Microw. Symp. Dig.*, pp. 733 –736, June 2009.

[50] G. Qiu, C. Tsai, B. Wang, and Y. Zhu, “A YIG/GGG/GaAs-based magnetically tunable wideband microwave band-pass filter using cascaded band-stop filters,” *IEEE Trans. Magnetics*, vol. 44, pp. 3123 –3126, Nov. 2008.

[51] A. Cismaru and R. Marcelli, “CPW cascaded magnetostatic-wave bandstop resonators,” *IEEE Tran.s Magnetics*, vol. 42, pp. 3347 –3349, Oct. 2006.

[52] C. Rauscher, “Varactor-tuned active notch filter with low passband noise and signal distortion,” *IEEE Trans. Microw. Theory Tech.*, vol. 49, pp. 1431 –1437, Aug. 2001.

[53] I. Reines, S.-J. Park, and G. Rebeiz, “Compact low-loss tunable X-band bandstop filter with miniature RF-MEMS switches,” *Microwave Theory and Techniques, IEEE Transactions on*, vol. 58, pp. 1887 –1895, July 2010.

[54] E. Naglich, J. Lee, D. Peroulis, and W. Chappell, “High-q tunable bandstop filters with adaptable bandwidth and pole allocation,” in *Microwave Symposium Digest (MTT), 2011 IEEE MTT-S International*, pp. 1 –4, june 2011.

[55] H. Joshi, H. Sigmarsson, D. Peroulis, and W. Chappell, “Highly loaded evanescent cavities for widely tunable high-Q filters,” in *IEEE/MTT-S Int. Microw. Symp. Dig.*, pp. 2133 –2136, June 2007.

[56] J.-S. Hong and B. Karyamapudi, "A general circuit model for defected ground structures in planar transmission lines," *IEEE Microw. Wireless Compon. Lett.*, vol. 15, pp. 706 – 708, Oct. 2005.

[57] C. O'Driscoll, M. Rao, D. Borio, E. Cano, J. Fortuny, F. Bastide, and D. Hayes, "Compatibility analysis between lightsquared signals and l1/e1 gnss reception," in *Position Location and Navigation Symposium (PLANS), 2012 IEEE/ION*, pp. 447–454, 2012.

[58] D. W. Bliss, P. A. Parker, and A. R. Margetts, "Simultaneous transmission and reception for improvedwireless network performance," in *Statistical Signal Processing, 2007. SSP '07. IEEE/SP 14th Workshop on*, pp. 478 –482, aug. 2007.

[59] "Simultaneous transmission of multiple signals through a shared array aperture," *Aerospace and Electronic Systems, IEEE Transactions on*, vol. 41, pp. 1457 – 1463, oct. 2005.

[60] E. Yalcin, C. Girard, M. Cabellic, M. Helier, G. Alquie, and J.-L. Montmagnon, "Modelling interference phenomena between cosite radiocommunication equipments to evaluate systems performance degradation," in *Intelligent Transport Systems Telecommunications,(ITST),2009 9th International Conference on*, pp. 249 –254, oct. 2009.

[61] E. Cottais and Y. Wang, "Spectrum estimation at the output of a nonlinear power amplifier with multicarrier signals," in *Digital Telecommunications, 2008. ICDT '08. The Third International Conference on*, pp. 23–26, 2008.

[62] D. Bang, S. Cheon, and J. Park, "Compact quintplexer module with meshed ground plane for us-cdma handset applications," in *Microwave Symposium Digest, 2009. MTT '09. IEEE MTT-S International*, pp. 1629–1632, 2009.

[63] R. Young, J. Adam, C. Vale, T. Braggins, S. Krishnaswamy, C. Milton, D. Bever, L. Chorosinski, L.-S. Chen, D. Crockett, C. Freidhoff, S. Talisa, E. Capelle, R. Tranchini, J. Fende, J. Lorthioir, and A. Tories, "Low-loss bandpass rf filter using mems capacitance switches to achieve a one-octave tuning range and independently variable bandwidth," in *Microwave Symposium Digest, 2003 IEEE MTT-S International*, vol. 3, pp. 1781 – 1784 vol.3, june 2003.

[64] H. Joshi, H. Sigmarsson, S. Moon, D. Peroulis, and W. Chappell, "High-q fully reconfigurable tunable bandpass filters," *Microwave Theory and Techniques, IEEE Transactions on*, vol. 57, pp. 3525 –3533, dec. 2009.

[65] Y. Murakami, T. Ohgihara, and T. Okamoto, "A 0.5-4.0-ghz tunable bandpass filter using yig film grown by lpe," *Microwave Theory and Techniques, IEEE Transactions on*, vol. 35, pp. 1192 – 1198, dec 1987.

[66] R. Snyder, S. Shin, and K. Keck, "Bandstop filter design using evanescent mode resonators," in *Microwave Symposium Digest, 2003 IEEE MTT-S International*, vol. 2, pp. 1073 – 1076 vol.2, june 2003.

[67] H. Joshi, H. H. Sigmarsson, and W. J. Chappell, "Analytical modeling of highly loaded evanescent-mode cavity resonators for widely tunable high-q filter applications," in *URSI National Radio Science Meeting 2008*, 2008.

[68] I. Hunter, *Theory and Design of Microwave Filters.* London, United Kingdom: Institution of Electrical Engineers, 2001.

[69] H. Bell, "The coupling matrix in low-pass prototype filters," *Microwave Magazine, IEEE*, vol. 8, pp. 70 –76, april 2007.

[70] S. Amari and U. Rosenberg, "New building blocks for modular design of elliptic and self-equalized filters," *Microwave Theory and Techniques, IEEE Transactions on*, vol. 52, pp. 721 – 736, feb. 2004.

[71] A. Abunjaileh and I. Hunter, "Tunable combline bandstop filter with constant bandwidth," in *Microwave Symposium Digest, 2009. MTT '09. IEEE MTT-S International*, pp. 1349 –1352, june 2009.

[72] W. Tang and J.-S. Hong, "Tunable microstrip quasi-elliptic function bandpass filters," in *Microwave Conference, 2009. EuMC 2009. European*, pp. 767 –770, 29 2009-oct. 1 2009.

[73] H. Sigmarsson, H. Joshi, S. Moon, D. Peroulis, and W. Chappell, "Substrate integration of widely tunable bandpass filters," in *Proceedings of International Symposium on Microelectronics, International Microelectronics and Packaging Society (IMAPS)*, pp. 711 –716, 2009.

[74] E. Naglich, J. Lee, D. Peroulis, and W. Chappell, "Tunable, substrate integrated, high q filter cascade for high isolation," in *Microwave Symposium Digest (MTT), 2010 IEEE MTT-S International*, pp. 1468 –1471, may 2010.

[75] R. Kwok and J.-F. Liang, "Characterization of high-q resonators for microwave filter applications," *Microwave Theory and Techniques, IEEE Transactions on*, vol. 47, pp. 111 –114, jan 1999.

[76] A. Khanna and Y. Garault, "Determination of loaded, unloaded, and external quality factors of a dielectric resonator coupled to a microstrip line," *Microwave Theory and Techniques, IEEE Transactions on*, vol. 31, pp. 261 –264, mar. 1983.

[77] W.-H. Tu, "Switchable microstrip bandpass filters with reconfigurable on-state frequency responses," *Microwave and Wireless Components Letters, IEEE*, vol. 20, pp. 259 –261, may 2010.

[78] M. Karim, A. Liu, A. Alphones, and A. Yu, "A novel reconfigurable filter using periodic structures," in *Microwave Symposium Digest, 2006. IEEE MTT-S International*, pp. 943 –946, june 2006.

[79] Y.-M. Chen, S.-F. Chang, C.-Y. Chou, and K.-H. Liu, "A reconfigurable bandpass-bandstop filter based on varactor-loaded closed-ring resonators [technical committee]," *Microwave Magazine, IEEE*, vol. 10, pp. 138 –140, february 2009.

[80] S. Amari, "Direct synthesis of folded symmetric resonator filters with source-load coupling," *Microwave and Wireless Components Letters, IEEE*, vol. 11, pp. 264 –266, june 2001.

[81] J. Lee and K. Sarabandi, "A miniaturized conductor-backed slot-line resonator filter with two transmission zeros," *Microwave and Wireless Components Letters, IEEE*, vol. 16, pp. 660 –662, dec. 2006.

[82] J. B. Muldavin and G. M. Rebeiz, “Novel dc-contact mems shunt switches and high-isolation series/shunt designs,” in *Microwave Conference, 2001. 31st European*, pp. 1 –3, sept. 2001.

[83] Peregrine, “Spdt ultracmos rf switch 103000 mhz, absorptive,” 2012.

[84] Avago, “Surface mount microwave schottky detector diodes,” 2012.

[85] I. Hunter, R. Ranson, A. Guyette, and A. Abunjaileh, “Microwave filter design from a systems perspective,” *Microwave Magazine, IEEE*, vol. 8, pp. 71 –77, oct. 2007.

[86] J. Slobodnik, A.J., G. Roberts, J. Silva, W. Kearns, J. Sethares, and T. Szabo, “Switchable SAW filter banks at UHF,” *Sonics and Ultrasonics, IEEE Transactions on*, vol. 26, pp. 120–126, Mar. 1979.

[87] J. Liu, S. He, S. Li, J. Liu, and Y. Liang, “P6G-3 switchable SAW filter bank with both narrow & wide channel bandwidth and 10 channels SAW filter bank,” in *Ultrasonics Symposium, 2007. IEEE*, pp. 2578–2581, Oct. 2007.

[88] X. Y. Zhang and Q. Xue, “High-selectivity tunable bandpass filters with harmonic suppression,” *Microwave Theory and Techniques, IEEE Transactions on*, vol. 58, pp. 964–969, Apr. 2010.

[89] L.-H. Hsieh and K. Chang, “Tunable microstrip bandpass filters with two transmission zeros,” *Microwave Theory and Techniques, IEEE Transactions on*, vol. 51, pp. 520–525, Feb. 2003.

[90] J. Nath, D. Ghosh, J.-P. Maria, A. Kingon, W. Fathelbab, P. Franzon, and M. Steer, “An electronically tunable microstrip bandpass filter using thin-film barium-strontium-titanate (BST) varactors,” *Microwave Theory and Techniques, IEEE Transactions on*, vol. 53, pp. 2707–2712, Sept. 2005.

[91] K. Entesari and G. Rebeiz, “A differential 4-bit 6.5-10-GHz RF MEMS tunable filter,” *Microwave Theory and Techniques, IEEE Transactions on*, vol. 53, pp. 1103–1110, Mar. 2005.

[92] W. Yan and R. Mansour, “Compact tunable bandstop filter integrated with large deflected actuators,” in *Microwave Symposium, 2007. IEEE/MTT-S International*, pp. 1611–1614, Jun. 2007.

[93] C. Tsai, G. Qiu, H. Gao, L. Yang, G. Li, S. Nikitov, and Y. Gulyaev, “Tunable wideband microwave band-stop and band-pass filters using YIG/GGG-GaAs layer structures,” *Magnetics, IEEE Transactions on*, vol. 41, pp. 3568–3570, Oct. 2005.

[94] C. Rodenbeck, S.-G. Kim, W.-H. Tu, M. Coutant, S. Hong, M. Li, and K. Chang, “Ultra-wideband low-cost phased-array radars,” *Microwave Theory and Techniques, IEEE Transactions on*, vol. 53, pp. 3697 – 3703, dec. 2005.

[95] K. Kobayashi, Y. C. Chen, I. Smorchkova, R. Tsai, M. Wojtowicz, and A. Oki, “A 2 watt, sub-db noise figure gan mmic lna-pa amplifier with multi-octave bandwidth from 0.2-8 ghz,” in *Microwave Symposium, 2007. IEEE/MTT-S International*, pp. 619 –622, june 2007.

[96] K. Raihn, N. Fenzi, G. Hey-Shipton, E. Saito, V. Loung, and D. Aidnik, “Adaptive high temperature superconducting filters for interference rejection,” *Microwave Theory and Techniques, IEEE Transactions on*, vol. 44, pp. 1374–1381, Jul. 1996.

[97] J. Rhodes, “Switched bandstop filters,” *International Journal of Circuit Theory and Applications*, vol. 22, pp. 107–120, 1994.

[98] A. Guyette, “Varactor-tuned bandstop filters with tunable center frequency and bandwidth,” in *Wireless Information Technology and Systems (ICWITS), 2010 IEEE International Conference on*, pp. 1–4, 28 2010-Sept. 3 2010.

[99] Z.-C. Hao, W. Hong, J.-X. Chen, X.-P. Chen, and K. Wu, “Compact super-wide bandpass substrate integrated waveguide (siw) filters,” *Microwave Theory and Techniques, IEEE Transactions on*, vol. 53, pp. 2968 – 2977, sept. 2005.

[100] E. Naglich, J. Lee, D. Peroulis, and W. Chappell, “Extended passband bandstop filter cascade with continuous 0.85 -6.6 ghz coverage,” *Microwave Theory and Techniques, IEEE Transactions on*, vol. 60, pp. 21 –30, jan. 2012.

[101] E. Naglich, J. Lee, D. Peroulis, and W. Chappell, “A tunable bandpass-to-bandstop reconfigurable filter with independent bandwidths and tunable response shape,” *Microwave Theory and Techniques, IEEE Transactions on*, vol. 58, pp. 3770 –3779, dec. 2010.

[102] D. Jachowski, “Compact, frequency-agile, absorptive bandstop filters,” in *Microwave Symposium Digest, 2005 IEEE MTT-S International*, pp. 513–516, Jun. 2005.

[103] M. Morgan and T. Boyd, “Theoretical and experimental study of a new class of reflectionless filter,” *Microwave Theory and Techniques, IEEE Transactions on*, vol. 59, pp. 1214–1221, May 2011.

[104] I. Hunter, A. Guyette, and R. Pollard, “Passive microwave receive filter networks using low-Q resonators,” *Microwave Magazine, IEEE*, vol. 6, pp. 46–53, Sept. 2005.

[105] A. Atia and A. Williams, “Measurements of intercavity couplings (short papers),” *Microwave Theory and Techniques, IEEE Transactions on*, vol. 23, pp. 519–522, Jun. 1975.

[106] C. Rauscher, “Reconfigurable bandpass filter with a three-to-one switchable passband width,” *Microwave Theory and Techniques, IEEE Transactions on*, vol. 51, no. 2, pp. 573–577, 2003.

[107] W. Fathelbab and M. Steer, “A reconfigurable bandpass filter for rf/microwave multifunctional systems,” *Microwave Theory and Techniques, IEEE Transactions on*, vol. 53, no. 3, pp. 1111–1116, 2005.

[108] M. Sanchez-Renedo, R. Gomez-Garcia, J. Alonso, and C. Briso-Rodriguez, “Tunable combline filter with continuous control of center frequency and bandwidth,” *Microwave Theory and Techniques, IEEE Transactions on*, vol. 53, no. 1, pp. 191–199, 2005.

[109] H. H. Sigmarsson, J. Lee, D. Peroulis, and W. Chappell, "Reconfigurable-order bandpass filter for frequency agile systems," in *Microwave Symposium Digest (MTT), 2010 IEEE MTT-S International*, pp. 1756–1759, 2010.

[110] E. Naglich, D. Peroulis, and W. Chappell, "Wide spurious free range positive-to-negative inter-resonator coupling structure for reconfigurable filters," in *Microwave Symposium Digest, 2013 IEEE MTT-S International*, june 2013.

[111] M. Sanchez-Renedo, R. Gomez-Garcia, and R. Loeches-Sanchez, "Microstrip filters with selectivity improvement using the new concept of signal-interference source/load coupling," in *Microwave Symposium Digest (MTT), 2013 IEEE MTT-S International*, 2013.

[112] G. Macchiarella, "Accurate synthesis of inline prototype filters using cascaded triplet and quadruplet sections," *Microwave Theory and Techniques, IEEE Transactions on*, vol. 50, no. 7, pp. 1779–1783, 2002.

[113] R. Snyder, "Inverted-resonator evanescent mode filters," in *Microwave Symposium Digest, 1996., IEEE MTT-S International*, vol. 2, pp. 465–468 vol.2, 1996.

[114] V. Walker and I. Hunter, "Design of cross-coupled dielectric-loaded waveguide filters," *Microwaves, Antennas and Propagation, IEE Proceedings*, vol. 148, no. 2, pp. 91–96, 2001.

[115] A. Fruehling, R. Pimpinella, R. Nordin, and D. Peroulis, "A single-crystal silicon dc-40 ghz rf mems switch," in *Microwave Symposium Digest, 2009. MTT '09. IEEE MTT-S International*, pp. 1633–1636, 2009.

[116] R. Stefanini, M. Chatras, P. Blondy, and G. Rebeiz, "Miniature rf mems metal-contact switches for dc-20 ghz applications," in *Microwave Symposium Digest (MTT), 2011 IEEE MTT-S International*, pp. 1–4, 2011.

[117] A. Menz and R. Hoper, "Micromechanical silicon rf switch with electroplated solid contacts for high reliability," in *Microwave Integrated Circuits Conference (EuMIC), 2012 7th European*, pp. 453–456, 2012.

[118] J. Lee, M. S. Uhm, and I.-B. Yom, "A dual-passband filter of canonical structure for satellite applications," *Microwave and Wireless Components Letters, IEEE*, vol. 14, pp. 271 – 273, june 2004.

[119] R. Levy, "Filters with single transmission zeros at real or imaginary frequencies," *Microwave Theory and Techniques, IEEE Transactions on*, vol. 24, no. 4, pp. 172–181, 1976.

[120] G. Pfitzenmaier, "Synthesis and realization of narrow-band canonical microwave bandpass filters exhibiting linear phase and transmission zeros," *Microwave Theory and Techniques, IEEE Transactions on*, vol. 30, no. 9, pp. 1300–1311, 1982.

[121] H. Bell, "L-resonator bandstop filters," *Microwave Theory and Techniques, IEEE Transactions on*, vol. 44, no. 12, pp. 2669–2672, 1996.

[122] H. Bell, "Narrow bandstop filters," *Microwave Theory and Techniques, IEEE Transactions on*, vol. 39, no. 12, pp. 2188–2191, 1991.

[123] H. Meng and K.-L. Wu, “Direct optimal synthesis of a microwave bandpass filter with general loading effect,” *Microwave Theory and Techniques, IEEE Transactions on*, vol. 61, no. 7, pp. 2566–2573, 2013.

[124] X. Y. Zhang and Q. Xue, “Novel dual-mode dual-band filters using coplanar-waveguide-fed ring resonators,” *Microwave Theory and Techniques, IEEE Transactions on*, vol. 55, pp. 2183 –2190, oct. 2007.

[125] T.-W. Lin, U.-H. Lok, and J.-T. Kuo, “New dual-mode dual-band bandpass filter with quasi-elliptic function passbands and controllable bandwidths,” in *Microwave Symposium Digest (MTT), 2010 IEEE MTT-S International*, pp. 576 –579, may 2010.

[126] S. Luo and L. Zhu, “A novel dual-mode dual-band bandpass filter based on a single ring resonator,” *Microwave and Wireless Components Letters, IEEE*, vol. 19, pp. 497 –499, aug. 2009.

[127] J.-S. Hong and S. Li, “Theory and experiment of dual-mode microstrip triangular patch resonators and filters,” *Microwave Theory and Techniques, IEEE Transactions on*, vol. 52, pp. 1237 – 1243, april 2004.

[128] R. Stefanini, M. Chatras, P. Blondy, and G. Rebeiz, “Compact 2-pole and 4-pole 2.4-2.8 ghz dual-mode tunable filters,” in *Microwave Symposium Digest (MTT), 2010 IEEE MTT-S International*, pp. 1480 –1483, may 2010.

[129] S. Amari and M. Bekheit, “A new class of dual-mode dual-band waveguide filters,” *Microwave Theory and Techniques, IEEE Transactions on*, vol. 56, pp. 1938 –1944, aug. 2008.

[130] S. Fiedziuszko, “Dual-mode dielectric resonator loaded cavity filters,” *Microwave Theory and Techniques, IEEE Transactions on*, vol. 30, pp. 1311 –1316, sep. 1982.

[131] A. Deleniv, A. Eriksson, and S. Gevorgian, “Design of narrow-band tunable band-pass filters based on dual mode srtio3 disc resonators,” in *Microwave Symposium Digest, 2002 IEEE MTT-S International*, vol. 2, pp. 1197 –1200, 2002.

[132] J. Hong and M. Lancaster, “Microstrip bandpass filter using degenerate modes of a novel meander loop resonator,” *Microwave and Guided Wave Letters, IEEE*, vol. 5, pp. 371 –372, nov 1995.

[133] L. Athukorala, D. Bondar, and D. Budimir, “Compact high linearity tunable dual-mode microstrip filters,” in *Microwave Conference (EuMC), 2010 European*, pp. 834 –837, sept. 2010.

[134] S. Bastioli, L. Marcaccioli, and R. Sorrentino, “A novel class of compact dual-mode rectangular waveguide filters using square ridge resonators,” in *Microwave Conference, 2008. EuMC 2008. 38th European*, pp. 626–629, 2008.

[135] S. Bastioli, C. Tomassoni, and R. Sorrentino, “A new class of waveguide dual-mode filters using tm and nonresonating modes,” *Microwave Theory and Techniques, IEEE Transactions on*, vol. 58, pp. 3909 –3917, dec. 2010.

[136] K. Ahn and I. Yom, "A ka-band multilayer ltcc 4-pole bandpass filter using dual-mode cavity resonators," in *Microwave Symposium Digest, 2008 IEEE MTT-S International*, pp. 1235 –1238, june 2008.

[137] W. Shen, X.-W. Sun, W.-Y. Yin, J.-F. Mao, and Q.-F. Wei, "A novel single-cavity dual mode substrate integrated waveguide filter with non-resonating node," *Microwave and Wireless Components Letters, IEEE*, vol. 19, pp. 368 –370, june 2009.

[138] D. Deslandes and K. Wu, "Substrate integrated waveguide dual-mode filters for broadband wireless systems," in *Radio and Wireless Conference, 2003. RAWCON '03. Proceedings*, pp. 385 – 388, aug. 2003.

[139] U. Rosenberg, "Multiplexing and double band filtering with common-multimode cavities," *Microwave Theory and Techniques, IEEE Transactions on*, vol. 38, pp. 1862 –1871, dec 1990.

[140] J.-T. Kuo, T.-H. Yeh, and C.-C. Yeh, "Design of microstrip bandpass filters with a dual-passband response," *Microwave Theory and Techniques, IEEE Transactions on*, vol. 53, pp. 1331 – 1337, april 2005.

[141] E. Djoumessi, M. Chaker, and K. Wu, "Varactor-tuned quarter-wavelength dual-bandpass filter," *Microwaves, Antennas Propagation, IET*, vol. 3, pp. 117 –124, february 2009.

[142] D. Girbau, A. Lazaro, A. Perez, E. Martinez, L. Pradell, and R. Villarino, "Tunable dual-band filters based on capacitive-loaded stepped-impedance resonators," in *Microwave Conference, 2009. EuMC 2009. European*, pp. 113 –116, 29 2009-oct. 1 2009.

[143] Y. Zheng, M. Sazegar, H. Maune, X. Zhou, J. Binder, and R. Jakoby, "Compact substrate integrated waveguide tunable filter based on ferroelectric ceramics," *Microwave and Wireless Components Letters, IEEE*, vol. 21, no. 9, pp. 477–479, 2011.

[144] V. Sekar, M. Armendariz, and K. Entesari, "A 1.2-1.6-ghz substrate-integrated-waveguide rf mems tunable filter," *Microwave Theory and Techniques, IEEE Transactions on*, vol. 59, no. 4, pp. 866–876, 2011.

[145] S. Adhikari, A. Ghiotto, and K. Wu, "Simultaneous electric and magnetic two-dimensionally tuned parameter-agile siw devices," *Microwave Theory and Techniques, IEEE Transactions on*, vol. 61, no. 1, pp. 423–435, 2013.

[146] H. Sigmarsson, A. Christianson, H. Joshi, S. Moon, D. Peroulis, and W. Chappell, "In-situ control of tunable evanescent-mode cavity filters using differential mode monitoring," in *Microwave Symposium Digest, 2009. MTT '09. IEEE MTT-S International*, pp. 633 –636, june 2009.

[147] L. Landau and E. Lifschitz, *Electrodynamics of Continuous Media.* Oxford, England: Permagon Press, 1987.

[148] H. B. Palmer, "The capacitance of a parallel-plate capacitor by the schwartz-christoffel transformation," *American Institute of Electrical Engineers, Transactions of the*, vol. 56, no. 3, pp. 363–366, 1937.

[149] H. Joshi, H. H. Sigmarsson, S. Moon, D. Peroulis, and W. Chappell, "High q narrow-band tunable filters with controllable bandwidth," in *Microwave Symposium Digest, 2009. MTT '09. IEEE MTT-S International*, pp. 629–632, 2009.

[150] S. Amari and F. Seyfert, "Design of dual-mode ridge cavity filters," in *Microwave Symposium Digest, 2009. MTT '09. IEEE MTT-S International*, pp. 1625–1628, 2009.

[151] X. Liu, L. P. B. Katehi, W. Chappell, and D. Peroulis, "Power handling of electrostatic mems evanescent-mode (eva) tunable bandpass filters," *Microwave Theory and Techniques, IEEE Transactions on*, vol. 60, no. 2, pp. 270–283, 2012.

VITA

VITA

Eric J. Naglich was born in Munster, IN in 1983. He received the B.S.E.C.E. degree in 2007 from Purdue University, West Lafayette. He is currently pursuing the Ph.D. degree in electrical and computer engineering at Purdue University in the IDEAS and ARES laboratories. He worked at GE Healthcare from 2007 to 2009, and he is a graduate of the Edison Engineering Development Program. His current research focuses on tunable filter synthesis and fabrication for widely tunable, adaptive RF front ends.

Mr. Naglich is a National Defense Science and Engineering Graduate (NDSEG) Fellow and a member of the IEEE Microwave Theory and Techniques Society (IEEE MTT-S). He is a past president of Purdue University's MTT-S Student Chapter and Beta Chapter of Eta Kappa Nu. His paper received the 2nd place award in the 2010 IEEE MTT-S International Microwave Symposium (IMS) Student Paper Competition. His project received the 2nd Place Award in the 2012 IEEE MTT-S IMS Power Amplifier Student Competition, and his paper was a finalist in the 2013 IEEE MTT-S IMS Student Paper Competition. He has authored 21 technical papers in international journals and conferences.